LIÈGE université Library

https://lib.uliege.be

https://matheo.uliege.be

Master's Dissertation : High-fidelity numerical modeling of dragonboat

Auteur : Sajjad, Muhammad Talha
Promoteur(s) : Andrianne, Thomas
Faculté : Faculté des Sciences appliquées
Diplôme : Master : ingénieur civil mécanicien, à finalité spécialisée en "Offshore Structure Modeling"
Année académique : 2025-2026
URI/URL : http://hdl.handle.net/2268.2/27800

Avertissement à l'attention des usagers :

Tous les documents placés en accès ouvert sur le site le site MatheO sont protégés par le droit d'auteur. Conformément aux principes énoncés par la "Budapest Open Access Initiative"(BOAI, 2002), l'utilisateur du site peut lire, télécharger, copier, transmettre, imprimer, chercher ou faire un lien vers le texte intégral de ces documents, les disséquer pour les indexer, s'en servir de données pour un logiciel, ou s'en servir à toute autre fin légale (ou prévue par la réglementation relative au droit d'auteur). Toute utilisation du document à des fins commerciales est strictement interdite.

Par ailleurs, l'utilisateur s'engage à respecter les droits moraux de l'auteur, principalement le droit à l'intégrité de l'oeuvre et le droit de paternité et ce dans toute utilisation que l'utilisateur entreprend. Ainsi, à titre d'exemple, lorsqu'il reproduira un document par extrait ou dans son intégralité, l'utilisateur citera de manière complète les sources telles que mentionnées ci-dessus. Toute utilisation non explicitement autorisée ci-avant (telle que par exemple, la modification du document ou son résumé) nécessite l'autorisation préalable et expresse des auteurs ou de leurs ayants droit.

UNIVERSITE DE LIEGE
FACULTE DES SCIENCES APPLIQUEES

High-fidelity Numerical Modeling of Dragon Boat

Muhammad Talha Sajjad
Student Number s2503470

Thesis presented to obtain the degree of
International Master of Science in Advanced Design of Sustainable Ships and Offshore Structures

Supervisor: Alban Leroyer (LHEEA, ECN)
Academic Supervisor: Thomas Andrianne (ULiège)

Academic year **2025 – 2026**

Summary

Numerical simulation is now a standard tool across industry and, increasingly, in sport, for evaluating and improving equipment and technique. This thesis develops a high-fidelity numerical model of one such application, dragon-boat paddling, a water sport practiced by millions of people worldwide. The stroke combines rapid paddle motion, blade entry and exit, free-surface deformation, and interaction with a translating hull, all of which are difficult to separate experimentally and have not previously been represented in a transient, free-surface computational model based on measured paddle motion. This study developed a numerical environment that converts field measurements into prescribed six-degree-of-freedom paddle kinematics and applies them in ISIS-CFD simulations of a standalone paddle, a bare hull, and a paddle–hull flow-interaction configuration.

A representative periodic stroke was reconstructed by phase averaging selected inertial-measurement and paddle-force data, followed by numerical integration of the acceleration signals to obtain the paddle motion. The resulting trajectory was imposed using an arbitrary Lagrangian–Eulerian overset-grid formulation. Adaptive grid refinement concentrated cells near the free surface, blade, hull, and resolved flow structures. The simulations comprised viscous and inviscid paddle cases, multiple AGR-threshold studies for the paddle and oscillating-surge hull, a calm-water hull-resistance sweep from 7 to 13 km/h, and a paddle–hull case with a single paddle alongside the hull. The measured force history was used as a reference for comparison. However, the absolute vertical position of the trajectory relative to the free surface could not be independently determined from the available measurements. A sensitivity study was therefore conducted to assess its influence, after which the vertical position was calibrated based on agreement with the measured forces. Consequently, the assessment should be regarded as calibration-informed rather than as an independent validation. Future experiments should directly measure the free-surface position to reduce this calibration dependence and enable more rigorous independent validation.

For the standalone paddle, viscosity changed the peak and root-mean-square blade loads by only 2.74% and 1.55%, respectively, indicating that pressure-dominated unsteady loading controls the integrated response for this prescribed stroke. The finest-grid paddle force had estimated grid-convergence uncertainties of 0.45% for the peak and 0.11% for the root-mean-square value. Hull resistance increased from 49.63 N at 7 km/h to 229.92 N at 13 km/h, while the frictional share decreased from 82.48% to 58.37% as wave-making became more important. Relative to the standalone inviscid paddle, the paddle–hull configuration increased peak and root-mean-square paddle force by 28.50% and 25.22%, respectively. Its propulsive impulse increased from 16.36 to 21.52 N s and its paddle-in-water ratio from 42.97% to 47.61%. The paddle wake convected downstream into the hull-side flow region, providing qualitative evidence of hydrodynamic interaction. The prescribed blade kinematics were identical between the paddle-only and paddle–hull configurations. The latter exhibited a locally elevated free surface due to the hull-generated wave system, leading to greater effective blade immersion and, consequently, increased paddle force.

The paddle motion governed the temporal resolution, with median time steps of 0.192 ms for the standalone paddle and 0.186 ms for the paddle–hull configuration. The paddle–hull simulation was more computationally expensive, primarily because adaptive refinement of the convecting paddle wake resulted in a 2.74-times larger mean cell count over the multiple-stroke simulations. In the present simulations, both paddle kinematics and hull surge motion were prescribed, providing a consistent framework for resolving the paddle-induced flow and its interaction with the hull. A separate appendix reports a proof-of-concept structural coupling between the CFD solver and the geometrically exact beam model, BeamDyn. The coupling is benchmarked against closed-form solutions and verified through an eleven-case kinematic and added-mass campaign. The study demonstrates its load- and motion-transfer capabilities without applying CFD-generated loads to a flexible paddle. The resulting framework provides a reproducible basis for comparing athlete techniques and establishes a foundation for future extensions toward independent validation, dynamically coupled hull surge driven by computed paddle-induced forces, and simulations involving multiple paddles.

Acknowledgements

I would like to express my sincere gratitude to all those who contributed to my studies and to the completion of this thesis. My deepest thanks go to Prof. Alban Leroyer of the LHEEA Laboratory at École Centrale Nantes for supervising this work. His expertise in computational fluid dynamics, fluid–structure interaction, and high-performance computing, together with his advice and the resources he provided, was instrumental in developing the numerical workflow, conducting the analysis, and interpreting the results. I particularly appreciate his technical input and the many valuable discussions throughout this work. I also acknowledge the LHEEA Laboratory at École Centrale Nantes and the Centre National de la Recherche Scientifique (CNRS) for providing the research environment, facilities, and computational resources that made this work possible.

I would also like to thank Prof. Thomas Andrianne, my academic supervisor, Prof. Philippe Rigo of the Université de Liège, and Prof. Evert Lataire of Ghent University, coordinator of the programme, for their guidance during my academic journey. I am honoured to have had the opportunity to pursue my EMSHIP Master's degree through the Erasmus Mundus Joint Masters programme. I also thank Prof. Stéphane Redonnet of the Hong Kong University of Science and Technology (HKUST) for providing the experimental dataset used in this thesis and for his assistance with the data. I am especially thankful to Prof. Florin Păcuraru of the Universitatea Dunărea de Jos din Galați for teaching CFD during my first year and supervising my summer internship. His teaching provided an important foundation for this work.

Finally, I would like to thank my friends for the experiences, discussions, and memories we shared throughout this journey. I am especially grateful to Sohaib Tariq, Mateen Iftikhar, and Ahmad Hassan for their friendship, encouragement, and support over the years. I am deeply grateful to my family for their constant presence and encouragement, especially my father for his unwavering support and my brother, Muzzammil, for always believing in me.

Contents

1 Introduction **1**
- 1.1 Research context and motivation . . . 1
- 1.2 Scope and contribution . . . 2
- 1.3 Objectives . . . 2
- 1.4 Thesis structure . . . 3

2 Literature Review **4**
- 2.1 Measured Technique and Its Limits . . . 4
- 2.2 Unsteady Free-Surface Blade Hydrodynamics . . . 4
- 2.3 Paddle Trajectory from Field Measurements . . . 5
- 2.4 Computational Framework and Numerical Verification . . . 5
- 2.5 Research Gap and Thesis Scope . . . 5

3 Theoretical Background **8**
- 3.1 Mathematical Formulation . . . 8
  - 3.1.1 Conservation Equations and Turbulence Closure . . . 8
  - 3.1.2 Two-Phase Flow and Volume-of-Fluid Tracking . . . 9
- 3.2 Reference Frames and Rigid-Body Kinematics . . . 9
  - 3.2.1 Reference Frames and Orientation Conventions . . . 9
- 3.3 Rigid-Body Dynamics . . . 11
- 3.4 Prescribed Motion and Advance Laws . . . 11
- 3.5 Dimensionless Parameters . . . 11
- 3.6 Numerical Resolution of Moving Free-Surface Flows . . . 12
  - 3.6.1 Combined Adaptive Grid-Refinement Criteria . . . 12
  - 3.6.2 Overset Interpolation and Cell-Size Continuity . . . 13
  - 3.6.3 Time-Step Resolution and Courant Limits . . . 13
  - 3.6.4 Verification on Adaptively Refined Meshes . . . 14

4 Methodology **15**
- 4.1 Software and simulation environment . . . 15
- 4.2 Description of experimental setup . . . 16
- 4.3 Paddle trajectory construction . . . 17
  - 4.3.1 Frame transformation and gravity compensation . . . 17
  - 4.3.2 Stroke segmentation and phase averaging . . . 18
  - 4.3.3 Numerical integration . . . 20
- 4.4 Trajectory export for CFD . . . 20
- 4.5 Computational framework and settings . . . 23
  - 4.5.1 Geometry preparation . . . 23
  - 4.5.2 Physical models, body definitions, and simulation types . . . 24
  - 4.5.3 Computational domains and mesh . . . 26
  - 4.5.4 Temporal discretisation and convergence controls . . . 31

4.5.5 Simulation case matrix . . . 32
4.5.6 Output definitions and post-processing . . . 32
4.5.7 Grid-convergence analysis . . . 36
4.6 CFD workflow automation . . . 37
4.6.1 Paddle and paddle-hull configuration cases (Type 1 and Type 3) . . . 37
4.6.2 Boat-only resistance and oscillating-surge cases (Type 2) . . . 38
4.6.3 Execution and automated post-processing . . . 38

5 Results and discussion **40**
5.1 Reconstructed trajectory and limitations . . . 40
5.1.1 Raw sensor data, selection, and analysis window . . . 40
5.1.2 Phase averaging and numerical integration . . . 42
5.1.3 Integrated paddle motion . . . 42
5.1.4 Immersion-depth calibration . . . 44
5.1.5 Heading correction and reference alignment . . . 46
5.1.6 Boat-speed and paddle-motion representation . . . 46
5.1.7 CFD-ready trajectory and vertical datum . . . 47
5.1.8 Uncertainty in the reconstructed trajectory . . . 48
5.1.9 Limitations of trajectory reconstruction and experimental requirements . . . 49
5.2 Type 1 simulations: CFD of paddle . . . 50
5.2.1 Free-surface and wake development . . . 50
5.2.2 Standalone paddle force, kinematic response, and turbulence modeling . . . 51
5.2.3 Discussion of the force–acceleration phase relationship . . . 54
5.2.4 Inviscid force history and grid-convergence uncertainty . . . 57
5.2.5 Gomory and Galipeau stroke descriptors . . . 60
5.3 Type 2 simulations: CFD of Boat . . . 61
5.3.1 Calm-water resistance speed sweep . . . 61
5.3.2 Calm-water free-surface patterns across the resistance-test speed range . . . 62
5.3.3 Oscillating-surge hull response . . . 64
5.3.4 Bare-hull discussion . . . 67
5.4 Type 3 simulation: CFD of paddle and hull interaction . . . 67
5.4.1 Phase definition and stroke-start detection . . . 68
5.4.2 Paddle force, immersion, and wetted area in the paddle-hull configuration . . . 68
5.4.3 Hull pressure-force comparison for standalone-versus-paddle-hull . . . 72
5.4.4 Numerical scope and limits of the paddle-hull configuration . . . 76
5.4.5 Paddle-hull flow interaction, discussion and scope . . . 79

6 Conclusions and future work **82**
6.1 Conclusions . . . 82
6.2 Future work . . . 84

Bibliography **88**

A Computational cost summary **89**

B IMU processing and validation results **90**
B.1 Sensor quality and data conditioning . . . 90
B.2 Left-sensor failure pattern . . . 94
B.3 Stroke-to-stroke variability of the selected paddle signal set . . . 96

C Immersion-depth sensitivity **97**
C.1 Immersion-depth and advance speed sensitivity of the peak paddle-normal force . . . 97

D Supplementary results **99**
D.1 Grid convergence of the impulse and positive-mean metrics . . . 99
D.2 Boat heave and pitch during the oscillating-surge and paddle–hull cases . . . 100
D.3 Supplementary standalone-paddle . . . 102

E IMU error-propagation derivations **104**
E.1 IMU attitude and integration-uncertainty propagation . . . 104

F BeamDyn and ISIS-CFD coupling proof of concept **107**
F.1 Benchmark and verification cases . . . 107
F.2 Coupling frame convention . . . 108
F.3 Closed-form reference solutions . . . 110
F.4 Full verification case matrix . . . 110
F.5 BeamDyn benchmark response histories . . . 111
F.6 ISIS-CFD–BeamDyn frame-transfer illustrations . . . 111
F.7 Added-mass verification table . . . 113

List of Figures

3.1 Paddle and boat initial configuration and reference frames. This figure defines the boat-aligned ISIS-CFD frame convention (origin, axis directions, and paddle lever arms) adopted throughout this thesis. . . . 10
3.2 Intrinsic and extrinsic paddle rotation sequences. . . . 11
3.3 Conceptual illustrations of overset grids and adaptive grid refinement. Reproduced from the FINE/Marine User Guide [1]. . . . 13

4.1 Schematic overview of thesis workflow . . . 15
4.2 Instrumented paddle and sensor mounting locations. . . . 16
4.3 Procedure used to reconstruct the prescribed paddle motion from the IMU and force measurements. . . . 18
4.4 Three-view comparison of the actual hull geometry with the simplified hull. . . . 23
4.5 Prescribed paddle motion used in the CFD simulations, defined in the global frame for Type 1 and relative to the boat translation in T_x for Type 3. . . . 26
4.6 Initial mesh for Type 1 (standalone paddle). The full-tank background domain B0 contains the paddle overset mesh. . . . 27
4.7 Near-wall paddle mesh at the mid-plane of the paddle face ($z = -0.731$ m). . . . 28
4.8 Initial mesh for Type 2 (boat alone). The boat is contained within the half-tank background domain B1 with mirror symmetry at the centreplane. . . . 29
4.9 Initial mesh for Type 3 (paddle-hull configuration). The half-tank background domain B2 contains the boat hull and paddle overset mesh. . . . 29
4.10 AGR-region configurations for the three simulation types. . . . 30

5.1 Raw paddle-IMU histories and selected analysis window. . . . 41
5.2 Detected stroke boundaries and phase resampling . . . 42
5.3 Effect of periodic spline interpolation near the stroke-period boundary, with the lower panel showing a magnified view of the stroke boundary. . . . 43
5.4 Measured and phase-averaged kinematic and paddle-force histories over the five stroke intervals. . . . 43
5.5 Acceleration, velocity, and position integration stages. . . . 44
5.6 Phase-averaged paddle velocity and displacement after endpoint-drift correction. . . . 45
5.7 Phase-averaged paddle force and reconstructed paddle-tip elevation for the selected vertical datum. . . . 45
5.8 Earth-fixed and boat-aligned frames used for the heading correction. . . . 46
5.9 Boat speed history and prescribed oscillating-surge velocity law. . . . 47
5.10 Paddle trajectory relative to the boat. Dashed lines indicate the paddle trajectory during boat advance. . . . 47
5.11 Paddle trajectory relative to the free surface and boat reference. . . . 48
5.12 Paddle trajectory relative to the boat, showing zero relative translational velocity between the paddle and hull. . . . 48

5.13 Standalone-paddle free-surface elevation at four stroke phases. Each column shows the side view above the oblique three-dimensional view. The free surface is colored by its elevation. . . . 51
5.14 AGR for the standalone-paddle configuration. . . . 52
5.15 Paddle-normal force (dashed lines) and instantaneous wetted area (dotted lines) as functions of stroke phase for the viscous and Euler simulations, together with the experimentally measured force. Force is shown on the primary vertical axis and wetted area S_w on the secondary vertical axis. . . . 53
5.16 Normalised paddle-normal force, linear acceleration, and angular acceleration magnitudes for the Euler case at the reference grid resolution $T_{rH}/L = 0.20$ (case 1, Table 4.10). The reference values are $F_{\text{ref}} = 107.265$ N, $a_{\text{ref}} = 40.922\ \text{m s}^{-2}$, and $\alpha_{\text{ref}} = 313.942\ \text{rad s}^{-2}$. . . 55
5.17 Paddle-normal force over one stroke for the four standalone-paddle Euler refinement levels. 58
5.18 Grid-convergence assessment of the peak and RMS paddle-normal force. . . . 59
5.19 Numerical evolution of the standalone-paddle simulations showing (a) instantaneous cell count and (b) adaptive time step as functions of stroke phase for the four Euler refinement levels. The viscous $T_{rH}/L = 0.20$ case is included for comparison. . . . 60
5.20 Calm-water resistance and its pressure and viscous components. . . . 62
5.21 Calm-water free-surface pattern (two views) at the seven resistance-test speeds. . . . 63
5.22 Hull mesh before and after AGR for the 12 km.h^{-1} calm-water case. . . . 64
5.23 Hull-force comparison across mesh and time-stepping variants. . . . 66
5.24 Free-surface Courant number near the hull leading edge, fixed time step (top) versus adaptive Courant-controlled time step (bottom), at the same spatial resolution and the same instant. . . . 66
5.25 Oscillating-surge hull mesh before and after AGR at $T_{rH}/L = 0.20$. . . . 67
5.26 AGR for the paddle-hull configuration. . . . 68
5.27 Aligned paddle-normal force with and without the hull. . . . 70
5.28 Paddle-tip elevation against paddle-normal force (upper panel) and wetted area (lower panel), comparing the standalone paddle with the paddle-and-hull computation. . . . 71
5.29 Front-view standalone and paddle-hull states from approach through drive. . . . 72
5.30 Front-view comparison of standalone and hull-adjacent paddle flow from late drive, through release, to late recovery. . . . 73
5.31 Top-view comparison of standalone and hull-adjacent paddle wakes over the same eight stroke instants as Figures 5.29 and 5.30. . . . 74
5.32 Paddle force and positive hull resistance in the paddle-hull configuration, using all available stroke data, with vertical lines marking five-percent phase intervals. . . . 75
5.33 Paddle-tip elevation against paddle and hull force for all available paddle-hull-configuration stroke data. . . . 75
5.34 Hull pressure-force comparison for standalone and paddle-hull configurations. . . . 76
5.35 Top-view free-surface contours at six paddle-hull boat-force spikes. . . . 77
5.36 Paddle and hull pressure at six paddle–hull boat-force spikes. . . . 78
5.37 Side-view free-surface contours at six paddle-hull boat-force spikes. . . . 78
5.38 Cell-count and time-step histories for the paddle-hull and standalone cases. . . . 79

B.1 Reconstructed and sensor-reported quaternions, checked for the double-cover consistency distance e_q. . . . 91
B.2 Consistency between the quaternion- and Euler-angle-derived attitude, confirming the two representations agree. . . . 91
B.3 Gravity-compensation stages, from raw specific force to the earth-frame acceleration used in the trajectory integration. . . . 92
B.4 Sensor-frame magnetometer components, used to evaluate the magnitude coefficient of variation CV_H of Equation (B.1). . . . 92

B.5 Static gravity-compensation residual over the reference window, quantifying the bias floor r_g of Equation (B.3). . . . 93
B.6 Earth-frame vertical acceleration and low-frequency bias, tracked with the rolling mean of Equation (B.4). . . . 93
B.7 Gravity-compensated specific-force direction, used to check the attitude correction before integrating the trajectory. . . . 94
B.8 Left-IMU Euler-angle glitches and detection thresholds, showing the jerk-and-reset pattern used to identify the sensor malfunction. . . . 95
B.9 IMU attitude-rate glitch counts, comparing the left- and right-sensor detection rates behind Table B.1. . . . 96

C.1 Peak paddle-normal force across exploratory immersion-depth and inflow-speed cases. . . . 97

D.1 Grid-convergence assessment of the blade-force impulse and positive mean, the two metrics omitted from the main peak and RMS comparison of Chapter 5. . . . 99
D.2 Boat heave T_z (top) and pitch R_y (bottom) relative to their value at $t = 15$ s, oscillating-surge bare-hull case, uniform time step (left) and adaptive time step (right), across the four T_{rH}/L mesh levels. . . . 100
D.3 Boat heave T_z (top) and pitch R_y (bottom) relative to their value at $t = 15$ s, at $T_{rH}/L = 0.20$, for the paddle-hull case, the bare hull with adaptive time step, and the bare hull with uniform time step. . . . 101
D.4 Paddle force and normalised acceleration in the sensor/paddle frame, supplementing the force-acceleration discussion of Section 5.2.3. . . . 102
D.5 Paddle force and normalised acceleration in the ISIS-CFD frame, the fixed-frame version of Figure D.4. . . . 103

F.1 BeamDyn benchmark configurations. The labels denote the local loading directions used in the archived tests. . . . 107
F.2 Paddle dimensions and axis correspondence between the ISIS-CFD and BeamDyn frames, origin at the IMU location on the shaft, used for the coupling exercise. . . . 109
F.3 BeamDyn benchmark response histories for the straight and curved beam configurations. The transient responses converge toward their corresponding closed-form static solutions. 111
F.4 ISIS-CFD–BeamDyn frame-transfer check for the straight beam at the initial orientation. 112
F.5 ISIS-CFD–BeamDyn frame-transfer check for the curved beam at the initial orientation. . 112

List of Tables

1.1 Objectives and the case series and thesis sections that address them. . . . 3

2.1 Representative studies informing the present investigation . . . 6

4.1 Paddle and boat instrumentation suite. . . . 17
4.2 Common fluid properties, numerical controls, and computational parameters used in the CFD simulations. . . . 24
4.3 Degree-of-freedom treatment of the paddle and boat bodies. . . . 25
4.4 Background-domain specifications and boundary conditions for the three simulation types. B0 is used for Type 1, B1 for Type 2, and B2 for Type 3. . . . 26
4.5 Relationship between simulation type, background domain, body treatment, overset treatment, and analysed cases. . . . 27
4.6 Paddle overset-mesh specifications for Types 1 and 3. . . . 28
4.7 Background-domain motion and deformation treatment. . . . 30
4.8 Adaptive grid-refinement criteria and controls by simulation type. . . . 31
4.9 Prescribed speeds and recommended nominal time steps for the calm-water resistance cases. 32
4.10 CFD cases considered in the analysis and their principal numerical controls. . . . 33
4.11 Numerical model selection and scope of the resulting analysis. . . . 33

5.1 Stroke statistics used to assess the representative cycle. . . . 44
5.2 Peak paddle-normal force at $z_{fs} = -0.80$ m across the tested advance-speed range, one settled stroke, versus the measured PaddleMate peak. . . . 46
5.3 Viscous-versus-Euler comparison over the first stroke. . . . 53
5.4 Grid-convergence series for the standalone-paddle paddle-normal force over the four Euler refinement levels $T_{rH}/L = 0.20, 0.15, 0.10, 0.05$. Here, ϕ_i is the computed value, ϕ_{fit} is the least-squares fitted value at the assumed convergence order, U_ϕ is the estimated discretisation uncertainty obtained using the Eça–Hoekstra procedure, and $U_\phi/|\phi_1|$ is the uncertainty relative to the finest-grid value. . . . 59
5.5 Stroke descriptors calculated from the CFD histories using the phase definitions of Gomory (2018) and the time-to-peak and paddle-in-water descriptors reported by Galipeau (2018). Time-based descriptors are reported as a percentage of the stroke period T_s (phase τ) rather than in seconds, consistent with the phase convention used throughout this chapter. 61
5.6 Whole-hull resistance from the time-weighted final 2% of each run. The half-hull force is sign-corrected and multiplied by two. . . . 62
5.7 Time-aligned standalone and paddle-hull-configuration paddle-force statistics. . . . 69
5.8 Spatial and temporal workload descriptors over the common post-acceleration interval. . . 77

A.1 Core-hour usage summary of the analysed CFD simulations, ordered according to the computational matrix. . . . 89

B.1 Left- versus right-sensor attitude-rate glitch pattern over the full trial ($n_\sigma = 4$ threshold). "Worst deviation" is the logged angle at the most severe detected glitch on that channel. . 94

B.2 Phase-resolved variability of the signals used for the representative stroke. 96

C.1 Peak paddle-normal force over one settled stroke, exploratory immersion-depth and inflow-speed CFD runs, versus the measured PaddleMate peak. 98

F.1 BeamDyn benchmark results compared with closed-form reference responses. 108
F.2 Fixed axis convention between the ISIS-CFD (fluid) frame and the BeamDyn (beam) frame, read as $\mathbf{x}_{\text{BeamDyn}} = \mathbf{R}\,\mathbf{x}_{\text{ISIS-CFD}}$ with $\mathbf{R}$ the matrix of table entries. 108
F.3 Full eleven-case kinematic verification matrix. Cases marked † additionally inject a tension or torsion load through the coupling dynamic library rather than relying on prescribed rotation alone. 111
F.4 Added mass coefficient comparison – Curved Beam, 45°, Rotation. 113

Abbreviations

AGR	adaptive grid refinement
ALE	arbitrary Lagrangian–Eulerian
CFD	computational fluid dynamics
EFD	experimental fluid dynamics
GCI	grid-convergence index
ENU	east–north–up frame
IMU	inertial measurement unit
RMS	root mean square
VOF	volume of fluid

Roman symbols

$\mathbf{a}, \boldsymbol{\alpha}$	linear and angular acceleration
C_D	quasi-static drag coefficient (Morison-type decomposition)
C_T, C_R, C_F	total, residual and reference-friction coefficients
Co_{fs}, Co_{os}	free-surface and overset Courant targets
$F_n \equiv F_z^B$	paddle-normal force
$\overline{F_z^{B+}}$	conditional-positive mean paddle-normal force (loaded time only)
$\overline{F}_{\text{prop}}$	cycle-averaged propulsive force (zero-clipped, full stroke period)
Fn	Froude number based on the reference length, $v/\sqrt{gL}$
Fr	Froude number based on draft, $v^2/(gd)$
F_s	safety factor of the discretisation-uncertainty estimate
g	gravitational acceleration
$\mathbf{g}$	gravity vector
$\widehat{h}_i$	dimensionless Hessian-refinement coordinate, $T_{rH,i}/L_{\text{ref}}$
$h_{fs}, h_{os}, h_{\min}$	free-surface, overset-interface and minimum cell sizes
I_z^B	signed paddle-normal impulse
L	reference length
N_s	number of strokes in an ensemble
p	pressure, also fitted convergence order where stated
q_0, q_1, q_2, q_3	unit-quaternion components of sensor attitude

e_q	quaternion consistency (double-cover) distance
Q	dynamic-pressure force scale, $\frac{1}{2}\rho v_{\text{boat}}^2 S$
Re	Reynolds number
R_{ES}	sensor-to-earth rotation matrix
R_T, R_P, R_V, R_F	total, pressure, viscous and reference-friction resistance magnitudes
R_x, R_y, R_z	elementary rotation matrices
S	hull wetted surface area used in the resistance coefficients
S_w	paddle wetted area
t, T_s	time and stroke period
t'	time measured from the end of the paddle-hull acceleration stage, $t - 15$ s
t_a	staging (acceleration-stage) duration of the paddle-hull advance law
T_{rH}/L	dimensionless Hessian-refinement threshold
T_{rS}	free-surface refinement threshold
$\mathbf{u}, \mathbf{u}_m$	fluid and mesh velocity
$U(S_i)$	discretisation uncertainty
v_{boat}	boat advance speed
$v_{\min}, v_{\max}$	lower and upper bounds of the advance law
$\bar{v}, v_a$	mean and amplitude of the prescribed advance speed
y_{offset}	lateral shift placing the blade tip clear of the hull
$\widehat{q}$	signal normalised by its own peak magnitude
$\forall$	displaced volume
z_{fs}	free-surface elevation, general symbol
z_{fs}^{IMU}	free-surface datum in the IMU measurement frame, -0.8 m
z_{fs}^{CFD}	free-surface datum on the CFD side, 0 m
z_{tip}	paddle-tip elevation
$\Delta_{\text{peak}}, \Delta_{\text{RMS}}$	viscous–inviscid relative peak and RMS force difference
$\delta(\tau), \overline{\delta}_m$	phase-local and phase-binned viscous–inviscid relative difference
Γ_v	viscous-stress share of total paddle-normal force
t_{start}	paddle-hull stroke-start time from immersion minimum
CV_H	magnetometer magnitude coefficient of variation
n_σ	glitch-detection threshold, in standard deviations

r_g	static-window specific-force residual against gravity
w	rolling-mean window length, in samples
σ_g, σ_a	gyroscope and accelerometer noise standard deviations
σ_ϑ	propagated Euler-angle uncertainty

Greek symbols and superscripts

α	water volume fraction
$\Delta t, \Delta$	time step and local cell size
ν	kinematic viscosity
ϕ, θ, ψ	roll, pitch and yaw Euler angles
ρ	fluid density
$\boldsymbol{\sigma}_v$	viscous stress tensor
τ	stroke phase, reported in percent
τ_c	unwrapped stroke phase of the paddle-hull configuration, in percent
ψ_{boat}	boat heading used in the earth-to-boat rotation
φ_v	phase offset of the advance-speed law
$(\cdot)^B, (\cdot)^E, (\cdot)^S$	blade, earth and sensor frames

Chapter 1

Introduction

1.1 Research context and motivation

Numerical simulation is an increasingly useful and widely used tool across all branches of industry for designing and improving product performance. The same trend can be observed in sports, particularly in those that involve equipment. This project aims to develop a high-fidelity numerical model of a water sport practiced by millions of people around the world, namely dragon boat [2].

Dragon-boat paddling ranges from recreational participation to competitive international racing. Understanding the hydrodynamics of paddling is therefore relevant both to the interpretation of athlete performance and to the development of paddle and boat configurations. Experimental measurements have provided valuable information on paddle loads and stroke characteristics, but they provide limited access to the detailed flow structures and free-surface processes that produce those loads.

Computational fluid dynamics (CFD) has become a widely used approach for investigating complex unsteady flows and provides a means of examining the flow around a paddle and hull in greater detail than is generally possible with on-water measurements alone. CFD can resolve the evolution of the free surface, blade entry and exit, flow separation, ventilation, and the interaction between the paddle-generated flow and the hull. It also allows different configurations and operating conditions to be investigated under controlled conditions. Despite the extensive use of CFD in fluid mechanics, numerical studies of dragon-boat paddling remain limited compared with the available experimental work.

This capability has already been applied at LHEEA to rowing for several years [3–5], reviewed in Chapter 2, and provides the numerical basis this thesis builds on. The objective here is the same in kind, applied to a different sport. It is to resolve the flow around both the hull and the paddle, and thereby improve the knowledge, efficiency, and performance available to dragon-boat paddling. The methodology is built on ISIS-CFD, the CFD solver developed at LHEEA and distributed worldwide by Cadence Design Systems as FineMarine [1], together with a trajectory-generation procedure that converts on-water paddle-motion data provided by HKUST into the representative periodic stroke prescribed in the simulations (Section 1.2).

The difficulty is that dragon-boat paddling involves a strongly unsteady interaction between the paddle, free surface, and moving hull. During each stroke, the blade enters and exits the water while undergoing simultaneous translation, rotation, and acceleration. The resulting force therefore depends on the prescribed paddle motion, blade geometry and orientation, immersion, free-surface deformation, and hull motion. A numerical treatment must consequently represent both the physical unsteadiness of the stroke and the numerical requirements associated with a moving body crossing a free surface.

Studies of related oar and canoe blades demonstrate the importance of this unsteady treatment. Leroyer et al. [3] prescribed measured oar kinematics in a transient free-surface calculation and showed that unsteady effects and free-surface deformation strongly influence the integrated blade load. Robert et al. [5] incorporated adaptive refinement and highlighted the importance of temporal resolution in resolving the free-surface flow. Grift et al. [6] measured the flow around an oar blade and identified acceleration-

dependent added-mass effects that cannot be represented by a quasi-steady drag model. Within dragon boating, Campbell Ritchie and Bin Selamat [7] combined experimental measurements with CFD, but considered a fixed, fully submerged blade. Their configuration therefore does not represent the blade entry and exit processes that characterise an actual dragon-boat stroke.

The numerical treatment of a complete dragon-boat stroke therefore remains relatively underdeveloped. In particular, there is limited numerical work that combines measured paddle kinematics, a resolved free surface, and a moving dragon-boat hull, together with an assessment of the numerical sensitivity of the predicted paddle loads. The present work aims to address this gap through a CFD investigation of dragon-boat paddling. Measured stroke kinematics are reconstructed and prescribed in the numerical model, and the resulting paddle loads and flow are examined for standalone-paddle and paddle-hull configurations. The study also evaluates grid sensitivity and discretisation uncertainty where the available refinement data permit a formal assessment.

1.2 Scope and contribution

This work is a collaborative project between the LHEEA Laboratory (Centrale Nantes) and the Hong Kong University of Science and Technology (HKUST). HKUST conducted the on-water measurement campaign in Hong Kong, instrumenting paddle-mounted inertial and shaft-force sensors and providing the resulting dataset for this thesis. LHEEA, where the present numerical study was carried out, reconstructed the measured paddle kinematics, developed the CFD workflow, and performed the transient free-surface simulations reported in this thesis. Five selected strokes define a periodic six-degree-of-freedom motion. ISIS-CFD prescribes that motion with an arbitrary Lagrangian–Eulerian formulation, an overset grid around the blade, and Hessian-driven adaptive refinement. The campaign progresses from an isolated paddle to a bare hull and then to one paddle beside the hull. Python scripts generate and post-process the cases under common numerical settings. The resulting workflow links field measurements to prescribed CFD motion, quantifies selected load sensitivities, and resolves the flow around a measured dragon-boat stroke beside a hull. The standalone paddle and the bare hull each carry a systematic multi-level grid-convergence series with a discretisation-uncertainty estimate, and are the two cases in this thesis supported by that level of numerical verification. The paddle-hull configuration uses a single grid, and its results are reported as single-grid observations without a matching uncertainty estimate.

The scope remains narrow. One athlete's data and one phase-averaged stroke define a repeatable reference motion, and they do not describe dragon-boat technique in general. The inertial data did not recover the blade's absolute vertical position. The model selected that datum by matching computed and measured peak load, so the load-level comparison is calibration-informed. The hull follows a prescribed surge law, and the paddle-hull study uses one paddle and one grid. The results cannot predict self-propelled speed, crew-level propulsive efficiency, or athlete-to-athlete variation. Chapter 6 sets out the work required to address those questions.

1.3 Objectives

The present work has five objectives.

(a) to reconstruct a continuous, periodic, six-degree-of-freedom paddle trajectory from selected field measurements,

(b) to develop an automate workflow and numerical environment for converting the reconstructed motion into reproducible CFD cases,

(c) to characterise the transient free-surface hydrodynamics of the standalone paddle and quantify the sensitivity of paddle loads to the flow model and mesh resolution,

(d) to quantify bare-hull resistance, assess temporal-resolution effects under prescribed oscillating surge, and investigate the hydrodynamic interaction between a prescribed paddle and the hull, and

(e) to compare the computed paddle-load history with the available experimental force history while explicitly distinguishing calibration, verification, and validation.

Beyond these five objectives, Appendix F reports a feasibility check of structural and rigid-body coupling between ISIS-CFD and BeamDyn, a geometrically exact beam solver, in preparation for a future flexible-paddle extension of objective (b). The coupling is benchmarked against closed-form structural solutions and verified through an eleven-case kinematic and added-mass campaign, reported in the same appendix. It verifies selected transfer operations rather than providing a hydroelastic prediction, and its results are not used to support the load and flow-field claims of Chapter 5. Because it stands on its own as a proof of concept rather than a step in the main CFD chain, it is reported with the appendices rather than as its own chapter.

Table 1.1 maps each objective to the case series and thesis section that address it. The corresponding results, quantitative outcomes, and their interpretation limits are reported in Chapter 5 and summarised in Chapter 6.

Table 1.1: Objectives and the case series and thesis sections that address them.

Obj.	Case series and data	Addressed in
(a)	Five phase-aligned strokes from the selected right-paddle inertial history	§5.1
(b)	Automated geometry, motion, mesh and computation workflow	Ch. 4
(c)	Standalone paddle, viscous–Euler pair and a four-level Euler refinement series	§5.2
(d)	Bare hull, seven-speed calm-water sweep and four-level oscillating-surge series, and one paddle–hull configuration	§5.3, §5.4
(e)	Computed paddle-normal load against the phase-averaged measured history, with a force-selected vertical datum	§5.1.4

1.4 Thesis structure

Chapter 2 reviews paddle measurements, unsteady blade hydrodynamics, moving-grid CFD, and numerical verification. Chapter 3 defines the frames, force measures, free-surface formulation, and convergence concepts used in the analysis. Chapter 4 documents the measurements, trajectory reconstruction, numerical models, mesh approaches, and post-processing. Chapter 5 reports the motion, standalone-paddle loads, hull results, and paddle-hull response. Chapter 6 returns to the objectives, limits the claims to the available data, and identifies the next experiments and calculations. Appendix F reports the BeamDyn benchmarking and coupling feasibility exercise introduced above. It does not provide a hydroelastic prediction and does not affect the CFD results of Chapter 5.

Chapter 2

Literature Review

2.1 Measured Technique and Its Limits

Dragon-boat studies have measured the athlete and paddle more often than the surrounding flow. Instrumented paddles and video quantify stroke kinematics, shaft force, and propulsive efficiency [8, 9]. They do not resolve the transient free-surface flow that produces blade load. Campbell Ritchie and Bin Selamat [7] combined CFD with water-tunnel measurements, but modelled fixed blade geometries. Their method cannot represent blade entry and exit, changing orientation and immersion, or a moving paddle beside a hull. These limitations motivate a transient model based on measured paddle motion.

Comparison with measured paddling behaviour requires a consistent set of kinematic and force-based descriptors. The descriptors reported by Gomory [9] and Galipeau [10] fall into three groups. Rate measures describe how quickly load is built and released, namely the 20–80% rate of force development during the catch and the 20%–zero reduction rate at exit. Integral measures describe how much impulse the stroke delivers, namely catch, drive and propulsive impulses, average drive force, drive-force quality defined as the mean divided by the peak, and impulse rate. Timing measures describe where in the cycle that load acts, namely time to peak from water contact, paddle-in-water ratio, stroke rate, and the catch, drive and recovery durations. Galipeau [10] additionally resolves the propulsive, lateral and vertical blade-force components and reports stroke-to-stroke standard deviations, which the present phase-averaged treatment deliberately removes. These three groups define the reporting basis adopted in Chapter 5. Propulsive efficiency, by contrast, requires force, velocity and work transfer to be evaluated for a dynamically responding boat. A prescribed-surge calculation therefore determines force and timing descriptors but cannot determine efficiency, because the boat response and the mechanical work transfer are not solved.

2.2 Unsteady Free-Surface Blade Hydrodynamics

Paddle loading changes throughout the stroke. Rowing studies link the load to blade acceleration, ventilation, added mass, and vortex development as well as instantaneous speed and angle of attack [3, 6, 11]. Sprint-canoe measurements and calculations associate the catch and draw with the growth of tip and side vortices [12, 13]. A sequence of steady blade positions or fixed lift and drag coefficients cannot reproduce the entry-to-exit cycle. Rowing and canoeing remain the closest hydrodynamic analogue, although their boats and blade constraints differ from a dragon boat.

CFD studies of oar blades have progressed from fixed-blade calculations [14] to moving free-surface simulations [15, 16] and measured blade kinematics combined with adaptive mesh refinement [4, 5]. Leroyer et al. [3] demonstrated that unsteadiness and free-surface deformation govern the integrated oar load, whereas viscosity has limited influence for their configuration. Robert et al. [5] subsequently showed that the treatment of the free-surface interface also affects computational cost. Their compressive BRICS scheme required a local free-surface Courant number below 0.3, and volume-fraction sub-cycling was introduced to prevent this restriction from being applied to every equation. These findings motivate three

checks in the present work, namely that the prescribed motion must preserve the measured phase content, that the interface must remain temporally resolved, and that the difference between viscous and inviscid loads must be quantified for the present paddle rather than inferred from the oar literature.

2.3 Paddle Trajectory from Field Measurements

Field measurements offer the best route to athlete-driven paddle motion. Laboratory experiments can repeat a trajectory, but it may miss features of a stroke performed on water. Sprint-canoe studies have combined paddle-mounted inertial sensing with shaft-force measurement [10]. Inertial reconstruction has a known weakness, because gravity-compensated acceleration must be integrated twice, so attitude error and drift affect position [17, 18]. Stroke periodicity provides a useful constraint. The present method resamples individual strokes to a common phase, averages them, and enforces consistent endpoint conditions. Chapter 4 documents the resulting representative trajectory, its uncertainty, and the CFD-calibrated vertical datum.

2.4 Computational Framework and Numerical Verification

The simulations involve prescribed six-degree-of-freedom paddle motion, an air–water interface, and, in the paddle-hull configuration, a nearby hull. The computational framework must therefore accommodate substantial body motion while limiting mesh distortion and preserving adequate free-surface resolution. The present study uses an arbitrary Lagrangian–Eulerian moving-mesh formulation, interface capturing, and an overset-grid treatment. These methods have been applied in ISIS-CFD to simulate ship free surfaces and moving bodies [19, 20]. Adaptive mesh refinement is also employed because the dominant flow structures move with the blade and include free-surface deformation [21], strong pressure gradients and wake structures [22], and the moving blade itself [4, 5]. The combined multi-criterion metric used here follows Wackers et al. [23].

Previous studies indicate that metric-based adaptation can support convergence of integrated forces and wake features when the refinement criterion accounts for the free surface, pressure gradients, boundary layer, and wake [23, 24]. The refinement threshold should not, however, be interpreted as an equivalent uniform mesh spacing. Mesh subdivision occurs discretely, refined regions expand as the threshold is reduced, and newly resolved flow features can modify the adaptation metric. Where a systematic refinement series is available, the present study applies a multi-level least-squares power-law fit to estimate discretisation uncertainty [24, 25]. This procedure is applied to the standalone-paddle series for the selected integral-load quantities. Only one mesh is used for the paddle-hull configuration, so the paddle-hull results do not support a mesh-convergence assessment or a discretisation-uncertainty estimate. The adaptive-grid formulation and used parameters are described in Section 4.5.3.

2.5 Research Gap and Thesis Scope

Dragon-boat field studies report paddle force, orientation, water-entry timing, and impulse, but they do not resolve the transient flow that generates blade loading. Rowing and sprint-canoe studies show that blade motion, free-surface deformation, and vortex development govern that loading, yet their blade geometries, oar-lock constraints, and operating conditions differ from those of a dragon boat. The remaining literature addresses moving-body numerics, inertial trajectory reconstruction, and discretisation uncertainty separately.

This review did not identify a study that combines athlete-measured dragon-boat motion, transient free-surface CFD, and a nearby hull in one investigation. This thesis addresses that gap with a standalone paddle, a bare hull, and a single prescribed paddle beside the hull. Numerical verification through a multi-level grid-convergence assessment is achieved for the standalone paddle, where a systematic refinement

series is available. The paddle-hull configuration uses a single grid, so it is examined through force histories and flow structures without a matching discretisation-uncertainty estimate. It also does not predict complete dragon-boat propulsion, because the vertical trajectory datum is calibration-informed, boat surge is prescribed, and neither a full crew nor a dynamically solved propulsive balance is included. A self-propelled extension would require stable load–motion exchange in the presence of added-mass effects [26]. Table 2.1 identifies the studies that supply the experimental measures, physical mechanisms, and numerical methods used in the present work.

Table 2.1: Representative studies informing the present investigation. The attribute column shows, for each group, whether the blade or hull moves (M), whether a free surface is resolved (FS), whether measured athlete kinematics are prescribed (K), and whether a discretisation-uncertainty estimate is reported (V). A dash denotes an attribute that the group does not address.

Study group and references	Application and method	Attributes (M/FS/K/V)	Relevance to the present work
Dragon-boat measurements [8–10]	On-water video, shaft-force and inertial measurement of athletes	M yes (athlete) FS – K measured V –	Define the stroke descriptors that a numerical model must reproduce, but report an integrated load only and resolve no flow field.
Dragon-boat and canoe-paddle hydrodynamics [7, 12, 13]	Water-tunnel measurement with steady CFD, and transient canoe-blade CFD	M fixed or partial FS partial K – V –	Establish blade-level pressure and vortex behaviour, but the fixed, fully submerged blade of [7] excludes water entry and exit.
Rowing-oar hydrodynamics [3–6, 11, 14–16]	Unsteady free-surface CFD with measured blade kinematics, and PIV and force experiments	M yes FS resolved K measured V partial	This is the closest available comparison. Unsteadiness, added mass and free-surface deformation govern the integrated load [3, 6], and the interface imposes a Courant limit near 0.3 [5]. The oar-lock is fixed and no hull is present.
Paddle-motion reconstruction [10, 17, 18, 27]	Attitude estimation, gravity compensation and inertial navigation	M n/a FS – K measured V error bounds	Supply the attitude and drift treatment needed to convert inertial histories into a six-degree-of-freedom blade path, and the growth laws that bound its uncertainty.
Moving-body and free-surface numerics [19, 20, 28]	ALE motion, interface capturing and overset grids in ISIS-CFD	M yes FS resolved K prescribed V –	Provide the solver components used for the moving paddle, the deforming free surface and the nearby hull.
Adaptive refinement and verification [21–25, 29]	Metric-based adaptive refinement, and least-squares power-law uncertainty estimation	M yes FS resolved K – V reported	Give the refinement criterion used here and the procedure for estimating discretisation uncertainty when refinement is non-uniform, which is the basis of the four-level series in §5.2.4.

The following chapters reconstruct prescribed paddle motion from synchronised field measurements, resolve the transient free surface around the moving paddle, and assess mesh, time-step, and viscous-

model sensitivity for the case series that permit those tests. The paddle-hull calculation examines local paddle-hull interaction, but it does not predict complete dragon-boat propulsion.

Chapter 3

Theoretical Background

This chapter presents the flow, rigid-body-motion, and nondimensional foundations used in the methodology and results chapters.

3.1 Mathematical Formulation

The incompressible arbitrary Lagrangian–Eulerian (ALE) form of the Navier–Stokes equations provides the basis for two-phase flow calculations involving air and water. The governing equations are mass conservation, momentum conservation, and volume-fraction transport, combined with a turbulence model where viscous stresses are resolved. This formulation and its ALE treatment are consistent with the ISIS-CFD methodology reported by Queutey et al. [19] and Leroyer and Visonneau [20].

3.1.1 Conservation Equations and Turbulence Closure

Let $\mathbf{u}$ denote fluid velocity, ρ fluid density, p pressure, $\mathbf{g}$ gravitational acceleration (with $g = 9.81$ m/s^2), and $\mathbf{u}_m$ mesh velocity. The continuity equation (mass conservation) is

$$\nabla \cdot \mathbf{u} = 0, \tag{3.1}$$

The momentum equation in ALE form is

$$\frac{\partial(\rho \mathbf{u})}{\partial t} + \nabla \cdot [\rho \mathbf{u} \otimes (\mathbf{u} - \mathbf{u}_m)] = -\nabla p + \nabla \cdot \boldsymbol{\sigma}_v + \rho \mathbf{g}, \tag{3.2}$$

where $\boldsymbol{\sigma}_v$ is the viscous stress tensor. For a Newtonian fluid,

$$\boldsymbol{\sigma}_v = 2\mu \mathbf{S}, \quad \text{where} \quad \mathbf{S} = \frac{1}{2}\left(\nabla \mathbf{u} + (\nabla \mathbf{u})^T\right), \tag{3.3}$$

and μ is the dynamic viscosity. The term $2\mu\mathbf{S}$ represents viscous diffusion of momentum.

The governing equations are discretised by a cell-centred finite-volume method. Convective and diffusive terms use second-order spatial schemes, pressure and velocity are co-located at cell centres, and a pressure-correction procedure enforces mass conservation. The viscous stress $\boldsymbol{\sigma}_v$ is evaluated at cell faces to maintain a consistent diffusive flux. The symbol τ is therefore reserved elsewhere in this thesis for stroke phase.

The Euler formulation neglects viscous stress ($\mu = 0$). Where viscous effects are resolved, the k–ω SST two-equation turbulence model of Menter [30] represents the effective viscosity as a function of the flow state. The case-specific selection is given in the methodology.

3.1.2 Two-Phase Flow and Volume-of-Fluid Tracking

To represent the water–air interface, the volume-of-fluid (VOF) method is employed. This interface-capturing approach follows the VOF formulation of Hirt and Nichols [31]. Let α denote the water volume fraction in a cell. The transport equation for α is

$$\frac{\partial \alpha}{\partial t} + \nabla \cdot (\alpha \mathbf{u}) = 0, \tag{3.4}$$

The convective discretisation must keep the transition between $\alpha = 0$ and $\alpha = 1$ sharp while the paddle pierces the interface. ISIS-CFD uses a bounded compressive scheme for this purpose. Robert et al. [5] identify this interface treatment as a governing temporal constraint in a closely related rowing-blade calculation. Their BRICS scheme kept its full compressive behaviour only while the local free-surface Courant number remained below 0.3. The precise admissible value depends on the solver version and the selected interface scheme, but the mechanism is general. If the interface crosses too many cells in one step, boundedness limiting reduces compression, the air–water transition spreads, and the predicted ventilation and impact loads can change. The present calculations therefore control the time step from local free-surface and overset Courant numbers rather than from the stroke period alone.

where $\alpha = 1$ denotes pure water, $\alpha = 0$ denotes pure air, and the interface is defined by the contour $\alpha = 0.5$. Density is computed as a function of α at each cell, $\rho(\alpha) = \alpha\rho_w + (1-\alpha)\rho_a$, where ρ_w is water density and ρ_a is air density. The dynamic viscosity is computed in the same manner as the density.

The physical properties used in a particular calculation and the corresponding numerical controls are specified in the methodology.

3.2 Reference Frames and Rigid-Body Kinematics

3.2.1 Reference Frames and Orientation Conventions

The boat-aligned CFD frame is right handed. Its x axis is positive forward along the centreline, y is positive to port, and z is positive upward. The undisturbed free surface is $z = 0$. Roll ϕ, pitch θ, and yaw ψ are rotations about x, y, and z, respectively. Positive pitch raises the bow and positive yaw is counterclockwise when viewed from above.

Paddle orientation is reconstructed between sensor frame S with IMU axes X, Y, and Z and earth frame E (East, North, Up) using Euler angles (roll ϕ, pitch θ, yaw ψ) and unit quaternions. The rotation-matrix and quaternion conventions follow standard rigid-body kinematics, while the fused attitude is treated as the output of an inertial/magnetic sensor filter [18, 32]. Each inertial unit reports orientation as fused Euler angles (ϕ, θ, ψ) and a fused quaternion $\vec{q}_{\text{sensor}} = (q_0, q_1, q_2, q_3)$, both derived internally from the same gyroscope, accelerometer, and magnetometer filter. The processing sequence uses Euler angles as the primary representation. The quaternion serves as an independent internal-consistency check by recomputing it from the Euler angles and comparing against the sensor's fused output (Appendix B). Because both are derived from the same raw sensor data, close agreement confirms mutual consistency without implying absolute correctness against ground truth (no external motion capture was available).

The sensor-to-earth transformation uses the intrinsic z–y–x (yaw–pitch–roll) sequence with elementary rotations

$$\mathbf{R}_x(\phi) = \begin{bmatrix} 1 & 0 & 0 \\ 0 & \cos\phi & -\sin\phi \\ 0 & \sin\phi & \cos\phi \end{bmatrix}, \quad \mathbf{R}_y(\theta) = \begin{bmatrix} \cos\theta & 0 & \sin\theta \\ 0 & 1 & 0 \\ -\sin\theta & 0 & \cos\theta \end{bmatrix}, \quad \mathbf{R}_z(\psi) = \begin{bmatrix} \cos\psi & -\sin\psi & 0 \\ \sin\psi & \cos\psi & 0 \\ 0 & 0 & 1 \end{bmatrix}. \tag{3.5}$$

The composite rotation matrix is built as

$$\mathbf{R}(\phi, \theta, \psi) = \mathbf{R}_z(\psi)\, \mathbf{R}_y(\theta)\, \mathbf{R}_x(\phi), \tag{3.6}$$

which expands to

$$\mathbf{R} = \begin{bmatrix} \cos\psi\cos\theta & \cos\psi\sin\theta\sin\phi - \sin\psi\cos\phi & \cos\psi\sin\theta\cos\phi + \sin\psi\sin\phi \\ \sin\psi\cos\theta & \sin\psi\sin\theta\sin\phi + \cos\psi\cos\phi & \sin\psi\sin\theta\cos\phi - \cos\psi\sin\phi \\ -\sin\theta & \cos\theta\sin\phi & \cos\theta\cos\phi \end{bmatrix}. \tag{3.7}$$

This product $\mathbf{R}_z(\psi)\,\mathbf{R}_y(\theta)\,\mathbf{R}_x(\phi)$ is equivalently an extrinsic fixed-axis X–Y–Z rotation or an intrinsic moving-axis Z–Y'–X'' rotation (Figures 3.1–3.2). A sensor-frame vector transforms to earth frame via

$$\mathbf{q}^E = \mathbf{R}(\phi,\theta,\psi)\,\mathbf{q}^S, \tag{3.8}$$

where $\mathbf{q}^S$ is an arbitrary vector in frame S and $\mathbf{q}^E$ is the same vector in frame E.

The fused Euler angles are converted to an equivalent unit quaternion using half-angle formulas,

$$\vec{q}_{\text{Euler}}(\phi,\theta,\psi) = \begin{bmatrix} \cos(\phi/2)\cos(\theta/2)\cos(\psi/2) + \sin(\phi/2)\sin(\theta/2)\sin(\psi/2) \\ \sin(\phi/2)\cos(\theta/2)\cos(\psi/2) - \cos(\phi/2)\sin(\theta/2)\sin(\psi/2) \\ \cos(\phi/2)\sin(\theta/2)\cos(\psi/2) + \sin(\phi/2)\cos(\theta/2)\sin(\psi/2) \\ \cos(\phi/2)\cos(\theta/2)\sin(\psi/2) - \sin(\phi/2)\sin(\theta/2)\cos(\psi/2) \end{bmatrix}, \tag{3.9}$$

with q_0 as the scalar part and (q_1, q_2, q_3) the vector part. This reconstructed quaternion is compared component-wise against $\vec{q}_{\text{sensor}}$ as documented in Appendix B.

Extraction of ϕ and ψ from a known rotation matrix uses the quadrant-aware, two-argument arctangent,

$$\text{Atan2}(y,x) = \begin{cases} \arctan(y/x) & x > 0 \\ \pi + \arctan(y/x) & x < 0,\ y \geq 0 \\ -\pi + \arctan(y/x) & x < 0,\ y < 0 \\ \pi/2 & x = 0,\ y > 0 \\ -\pi/2 & x = 0,\ y < 0 \end{cases} \tag{3.10}$$

ensuring the returned angle lies in the correct quadrant. All subsequent two-argument inverse tangents refer to this definition by name.

For a fixed sensor-frame lever arm $\mathbf{r}_P^S$ to point P on the paddle, rigid-body transformation gives

$$\mathbf{x}_P^E(t) = \mathbf{x}_S^E(t) + \mathbf{R}(t)\,\mathbf{r}_P^S, \qquad P \in \{\text{tip}, \text{handle}\}. \tag{3.11}$$

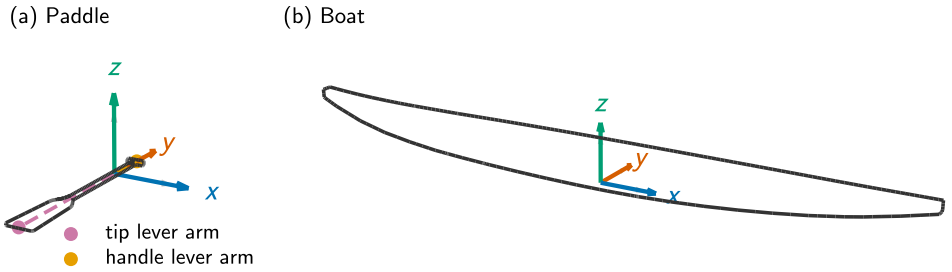

Figure 3.1: Paddle and boat initial configuration and reference frames. This figure defines the boat-aligned ISIS-CFD frame convention (origin, axis directions, and paddle lever arms) adopted throughout this thesis.

The paddle-tip elevation z_{tip} is the third component of $\mathbf{x}_{\text{tip}}^E$, used throughout for immersion analysis with the free surface set to $z = 0$. Lever arms measured from paddle CAD are $\mathbf{r}_{\text{tip}}^S = (0, -0.988, 0)$ m and $\mathbf{r}_{\text{handle}}^S = (0, +0.262, 0)$ m, giving a total paddle length of 1.25 m.

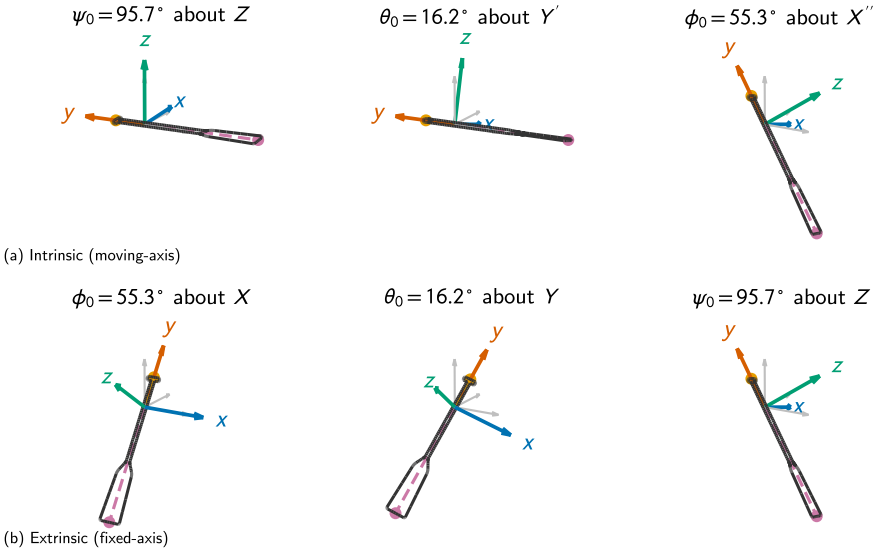

Figure 3.2: Intrinsic and extrinsic paddle rotation sequences.

3.3 Rigid-Body Dynamics

A body subject to hydrodynamic forces evolves according to Newton's second law. If $\mathbf{F}$ is the total hydrodynamic force and $\mathbf{M}$ is the total hydrodynamic moment, the equations of motion are

$$m\ddot{\mathbf{x}}_{\mathrm{CoG}} = \mathbf{F} + m\mathbf{g}, \tag{3.12}$$

$$\mathbf{I}\dot{\boldsymbol{\omega}} + \boldsymbol{\omega} \times (\mathbf{I}\boldsymbol{\omega}) = \mathbf{M}, \tag{3.13}$$

where m is body mass, $\mathbf{x}_{\mathrm{CoG}}$ is the position of the centre of gravity, $\mathbf{I}$ is the inertia tensor, and $\boldsymbol{\omega}$ is the angular velocity. Hydrostatic restoring forces and moments are included in $\mathbf{F}$ and $\mathbf{M}$.

These equations distinguish imposed degrees of freedom from those solved as part of the rigid-body response. The implementation used for each case is specified in the methodology.

3.4 Prescribed Motion and Advance Laws

A periodic forward velocity can be represented by

$$v_{\mathrm{advance}}(t) = v_{\mathrm{mean}} + v_{\mathrm{amp}} \cos(\omega_s t), \tag{3.14}$$

where v_{mean} is the mean speed, v_{amp} the velocity amplitude, and ω_s the angular frequency. The constant-speed limit follows when $v_{\mathrm{amp}} = 0$. The prescribed motions and degrees of freedom selected for this study are defined in Chapter 4.

3.5 Dimensionless Parameters

The key dimensionless parameters characterizing the flow regime are given below.

$$Fn = \frac{v}{\sqrt{gL}}, \quad Re = \frac{vL}{\nu}, \quad Fr = \frac{v^2}{gd}, \tag{3.15}$$

where v is the characteristic velocity, L is the reference length, g is gravitational acceleration, d is the characteristic depth, and ν is kinematic viscosity. The Froude number Fn governs wave-making

resistance, the Reynolds number Re governs viscous effects, and the Froude number based on draft Fr governs shallow-water effects if applicable. The reference values used for the dragon boat are specified in the methodology.

3.6 Numerical Resolution of Moving Free-Surface Flows

The present class of problem combines a moving air–water interface, strong local pressure and velocity gradients, and relative motion between overlapping grids. A numerical approach must therefore control both where resolution is placed and how far the relevant interface moves during one time step. The following formulation provides the scientific basis for the combined AGR criteria and time-step controls used later in the methodology.

3.6.1 Combined Adaptive Grid-Refinement Criteria

Adaptive grid refinement is expressed through a symmetric positive metric tensor $\mathbf{C}(\mathbf{x})$. A local edge vector $\boldsymbol{\ell}$ is adequately resolved when

$$\boldsymbol{\ell}^{\mathsf{T}}\mathbf{C}(\mathbf{x})\boldsymbol{\ell} \leq 1. \tag{3.16}$$

The tensor encodes both the desired local cell size and the preferred refinement direction. The multisurface (MS) criterion fixes the target spacing normal to the free surface. It can be combined with the tensorial pressure-Hessian (PH) criterion,

$$\mathbf{C}_{\mathrm{MS+PH}} = \max_{\mathrm{metric}} \left(\mathbf{C}_{\mathrm{MS}},\ w_P\mathbf{C}_{\mathrm{PH}}\right), \tag{3.17}$$

where $\mathbf{C}_{\mathrm{PH}}$ is obtained from second spatial derivatives of pressure. This criterion adds directional refinement at pressure peaks, stagnation regions, and vortex cores while keeping controlled free-surface spacing. It is therefore appropriate when wave pattern and pressure-driven hull loading are the principal targets.

The multisurface–flux-component-Hessian (MSFCH) criterion extends this combination by replacing the pressure-only Hessian with a metric based on the second spatial derivatives of pressure and velocity, as follows.

$$\mathbf{C}_{\mathrm{MSFCH}} = \max_{\mathrm{metric}} \left(\mathbf{C}_{\mathrm{MS}},\ w_H\mathbf{C}_{\mathrm{FCH}}\right). \tag{3.18}$$

Here w_H is the internal weighting associated with the Hessian threshold. The metric maximum preserves the more restrictive directional requirement of the two criteria. Thus, the multisurface component resolves the interface, while the flux-component Hessian adds refinement at pressure peaks, shear layers, boundary layers, and wakes. This physical division is important because the free-surface criterion alone does not necessarily resolve the wake or blade-induced pressure gradients, whereas the Hessian criterion alone does not impose a controlled interface-normal spacing [23]. The case-specific selection between MS+PH and MSFCH is stated in the methodology.

For a reference length L_{ref}, the dimensional Hessian threshold is written as

$$T_{rH} = \alpha_H L_{\mathrm{ref}}, \qquad \widehat{h} = \frac{T_{rH}}{L_{\mathrm{ref}}}, \tag{3.19}$$

where the non-dimensional multiplier α_H controls the sensitivity to flow features. Decreasing this threshold increases the number of cells, but does not by itself establish convergence. The case-specific threshold series belongs to the methodology, while the resulting convergence assessment is reported in the results.

The interface threshold and minimum adapted cell size are implementation controls. Their values and their relation to the initial free-surface spacing are stated with the computational setup.

3.6.2 Overset Interpolation and Cell-Size Continuity

An overset method decomposes the fluid domain into independently meshed, overlapping subdomains. At a given time, cells are active, blanked, or interpolated. The governing equations are solved in active cells, blanked cells are excluded, and interpolated cells obtain their state from active donor cells in another domain. This permits large prescribed body motion without the mesh distortion that would accompany a single deforming mesh.

The additional interpolation step is not neutral. Repeated transfer between grids can affect local mass conservation and may generate convergence difficulties or force oscillations if overlap, donor quality, or cell-size continuity is inadequate. Cadence/FineMarine therefore recommends a tensorial combined refinement criterion for overset free-surface applications. The MSFCH criterion in Equation (3.18) satisfies this requirement. It resolves the free surface and flow features while allowing AGR to reduce abrupt size changes across the interpolation region. The associated overset-continuity control keeps cell sizes at the overlap from differing by more than a factor of two. Overset use is consequently justified here by the large paddle displacement, but its interpolation diagnostics remain part of the numerical basis required for any subsequent validation claim.

Figure 3.3 illustrates the two operations as implemented in FineMarine. The overset method transfers the solution across the overlap between an independently meshed moving region and the background domain. AGR instead subdivides selected existing cells according to the solution criterion and can coarsen them again as an unsteady feature moves. They solve different numerical problems and are used together here, as overset motion prevents paddle-induced mesh distortion, while AGR follows the moving free surface and local flow gradients.

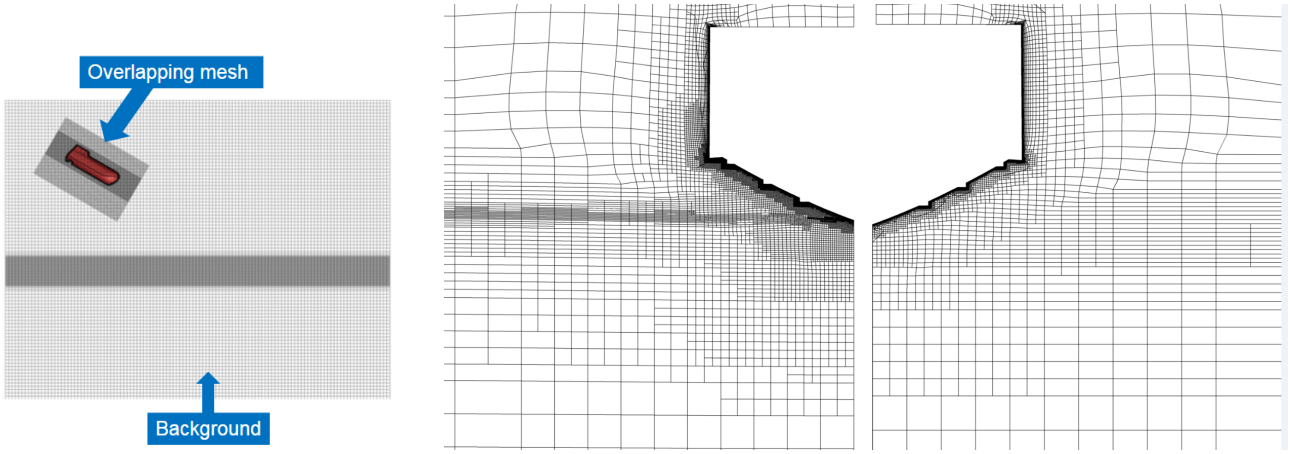

(a) Overlapping moving and background grids.

(b) Adapted grid (left) and its initial grid (right).

Figure 3.3: Conceptual illustrations of overset grids and adaptive grid refinement. Reproduced from the FINE/Marine User Guide [1].

3.6.3 Time-Step Resolution and Courant Limits

The free-surface and overset Courant numbers are

$$Co_{\mathrm{fs}} = \frac{|u_n|\,\Delta t}{h_{\mathrm{fs}}}, \qquad Co_{\mathrm{os}} = \frac{|u_{\mathrm{rel}}|\,\Delta t}{h_{\mathrm{os}}}, \tag{3.20}$$

where u_n is the velocity normal to the free surface, u_{rel} is the relative velocity at the overset interface, and h_{fs} and h_{os} are the respective local cell sizes. The resulting admissible time step is

$$\Delta t \le \min\left(\frac{Co^{\star}_{\mathrm{fs}} h_{\mathrm{fs}}}{|u_n|}, \frac{Co^{\star}_{\mathrm{os}} h_{\mathrm{os}}}{|u_{\mathrm{rel}}|}, \Delta t_{\max}\right). \tag{3.21}$$

Courant targets of order unity limit the interface motion and the relative overset motion to approximately one local cell width per step. Cadence/FineMarine also gives approximately 100 steps per period as a general time-accurate starting point. For a paddle entering and leaving the free surface, the local Courant limits can be more restrictive and therefore govern the selected time step. The selected time step for each case is reported in the methodology.

3.6.4 Verification on Adaptively Refined Meshes

For an independently generated AGR series, a response S_i can be represented by the power-law model

$$S_i = S_0 + c\widehat{h}_i^{\,p}, \tag{3.22}$$

where S_0 is the extrapolated response, c is a coefficient, p is the observed order, and $\widehat{h}_i$ is the Hessian-threshold coordinate from Equation (3.19). The least-squares procedure of Eça and Hoekstra estimates these quantities from the full refinement series [25].

With fit offset $\delta_i = S_i^{\mathrm{fit}} - S_0$, data range ΔS, and residual scatter σ, the associated uncertainty is

$$U(S_i) = \begin{cases} F_s|\delta_i| + \sigma + |S_i - S_i^{\mathrm{fit}}|, & \sigma < \Delta S, \\ F_s \dfrac{\sigma}{\Delta S}\left(|\delta_i| + \sigma + |S_i - S_i^{\mathrm{fit}}|\right), & \sigma \geq \Delta S, \end{cases} \tag{3.23}$$

where $F_s = 1.25$ is used for a reliable fit and $F_s = 3$ otherwise. This method supports a numerical-uncertainty statement only for configurations with a genuine refinement series. It cannot transfer a convergence bound automatically to a different paddle-hull configuration.

Chapter 4

Methodology

4.1 Software and simulation environment

The methodology comprises an automated workflow linking experimental paddle measurements, CFD simulation, and subsequent analysis of the numerical result as shown in Figure 4.1. IMU and PaddleMate measurements were processed to reconstruct the paddle trajectory and prescribe its six-degree-of-freedom motion for each simulation case. The paddle and hull geometries were prepared in Rhino, assigned surface names in CADfix, and subsequently used into the CFD computational domains.

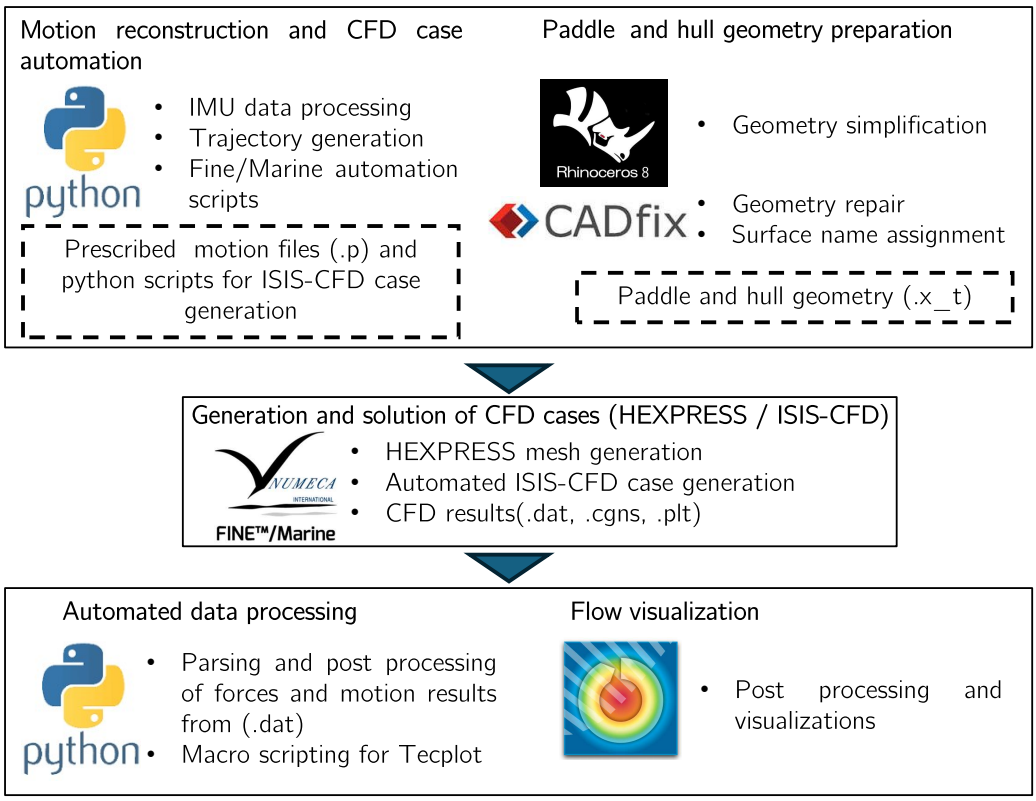

Figure 4.1: Schematic overview of thesis workflow

Python scripts were used to automate the generation of CFD cases within the FineMarine framework [1]. The automated workflow included mesh generation with HEXPRESS, specification of the flow model and fluid properties, definition of body motion (prescribed, fixed, or solved), boundary conditions, AGR and overset-grid settings, time-step controls, and solver parameters. During post-processing, Python

scripts were used to parse the `.dat` files containing motion and effort data and to generate driver scripts for the automated creation of Tecplot macros (`.mcr`) used for assembling CFD dataset for comparison. The resulting macros were executed in Tecplot 360 to generate mesh visualisations, contours, and flow-field plots. The workflow was managed in a Linux environment, with the CFD simulations executed on the Phileas high-performance computing cluster of the GLiCID facility [33].

4.2 Description of experimental setup

The dataset used in this study was collected by the collaborating partner, HKUST, during an outdoor dragon-boat training session in Hong Kong, and provided to LHEEA for the reconstruction and CFD analysis presented in this thesis (Section 1.2). The dataset was collected for two front-row athletes. Each athlete's paddle was equipped with a PaddleMate force sensor and a WitMotion inertial measurement unit (IMU). A DJI Osmo system captured the motion of the boat. The sensor specifications used in the uncertainty analysis were taken from the manufacturer's documentation [34]. The instrumented paddle and sensor arrangement are shown in Figure 4.2.

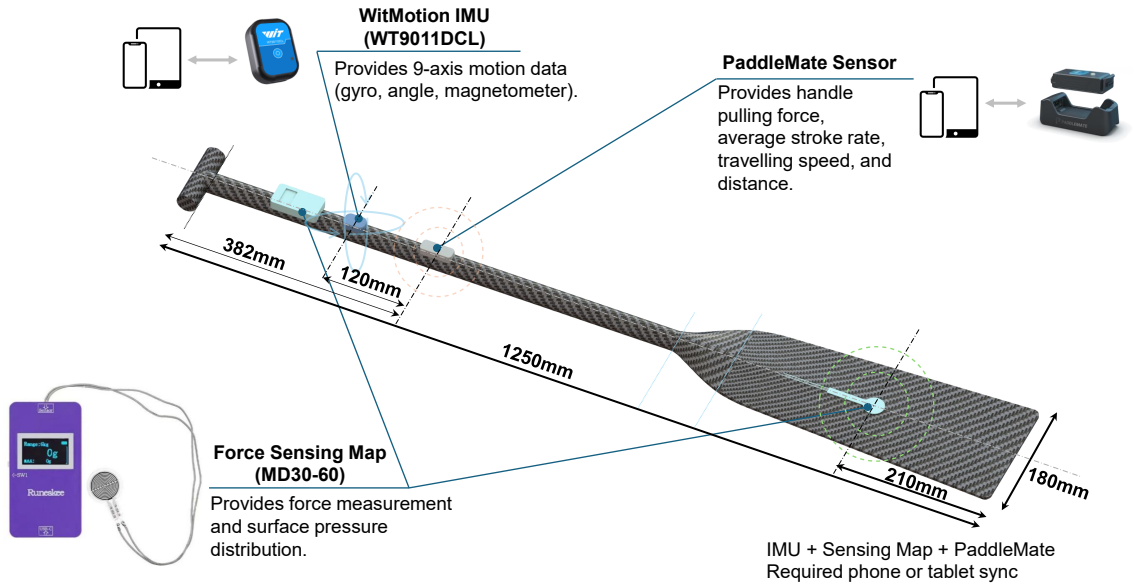

Figure 4.2: Instrumented paddle and sensor mounting locations.

The PaddleMate and WitMotion datasets shared a 100 Hz sampling, whereas the DJI Osmo operated on an independent 60 Hz. In the analysed trial, the clocks of PaddleMate, WitMotion and boat GPS were not synchronized. The time offset between the PaddleMate and boat GPS with respect to the WitMotion IMU was 13.99 s and 10.0 s, respectively. This offset was applied during preprocessing to align the force, GPS and IMU data. The instrumentation and sampling rates are summarised in Table 4.1.

The complete duration of the trial was almost 34 s. The interval from 25 to 30 s was selected for phase averaging and trajectory reconstruction because it contained five complete strokes and excluded the transients at the beginning and end of the trial. During the selected interval, the GPS data indicated northward and eastward displacements of approximately 85.7 m and 30.9 m, respectively, corresponding to a straight-line displacement of approximately 91 m, with an average heading of approximately 22 ° from the true north. This heading was used in the further processing of the data. Separately from the trajectory-reconstruction workflow, a second interval towards the end of the trial, ranging from 33.25 to

Table 4.1: Paddle and boat instrumentation suite.

System	Sensor	Quantity	Sample rate
Paddle motion	Sensor 1 (PaddleMate)	Force (N)	100 Hz
		GPS (lat., long.)	10 Hz[a]
	Sensors 2–3, WitMotion WT9011DCL (raw)	Acceleration XYZ (m/s^2)	100 Hz[b]
		Angular rate XYZ (deg/s)	100 Hz
		Euler angles (deg)	100 Hz[c]
		Magnetic field (μT)	100 Hz
	WitMotion (fused)	Quaternion	5 Hz[a]
Boat motion	Boat IMU	Acceleration XYZ (m/s^2)	60 Hz
		Quaternion	60 Hz
	Boat GPS	GPS (lat., long.)	60 Hz
		Velocity ($km\,h^{-1}$)	10 Hz[d]

[a] Not used for trajectory reconstruction.
[b] Accelerations are in sensor-fixed reference frame
[c] Euler angles are in earth-fixed reference frame with intrinsic order of rotations (yaw, pitch, roll).
[d] Not used, boat speed was computed from the 60 Hz GPS instead.

33.75 s, was selected in which the paddle was stationary for the data quality and sensor-health checks described in Section B.1.

4.3 Paddle trajectory construction

Dragon-boat paddling exhibits inherent stroke-to-stroke variability in paddle kinematics, arising from both the athlete's paddling technique and measurement noise. Simulating multiple measured strokes would capture this variability but would require substantial computational resources. A representative periodic stroke was therefore derived using phase averaging over a selected time interval during which the measured motion was approximately periodic. The flowchart summarizing the steps included in the paddle trajectory generation from IMU data is presented in Figure 4.3.

An interval, based on visual inspection of the measured motion signal, was selected for phase averaging. The interval excludes the transient portions at the beginning and end of the trial and contains multiple complete strokes. The trajectory was computed using the Euler angles available at 100 Hz for rotations instead of quaternions, which were logged at a lower rate of 5 Hz.

4.3.1 Frame transformation and gravity compensation

The IMU accelerations were reported in the sensor frame fixed to the paddle and included the static gravitational acceleration. The measured accelerations were therefore transformed from the sensor frame to the earth-fixed frame before gravity compensation and phase averaging. This order ensures that gravity removal is performed using the instantaneous orientation of each measured stroke, rather than an averaged orientation that could introduce a residual gravity component.

The initial paddle configuration corresponding to zero Euler angles is defined in Section 3.2.1. The Euler angles are earth-fixed with intrinsic order of rotations (yaw, pitch, roll).

For every sample, the sensor-frame acceleration was rotated to the earth-fixed frame and compensated for gravity.

$$\mathbf{a}^E(t) = \mathbf{R}_{SE}(t)\,\mathbf{a}^S(t) - \mathbf{g}^E, \tag{4.1}$$

where $\mathbf{a}^S(t)$ is the measured sensor-frame acceleration, including gravity, $\mathbf{R}_{SE}(t)$ is the sensor-to-earth rotation matrix, and $\mathbf{g}^E$ is the gravitational acceleration vector. For an earth-fixed frame with positive

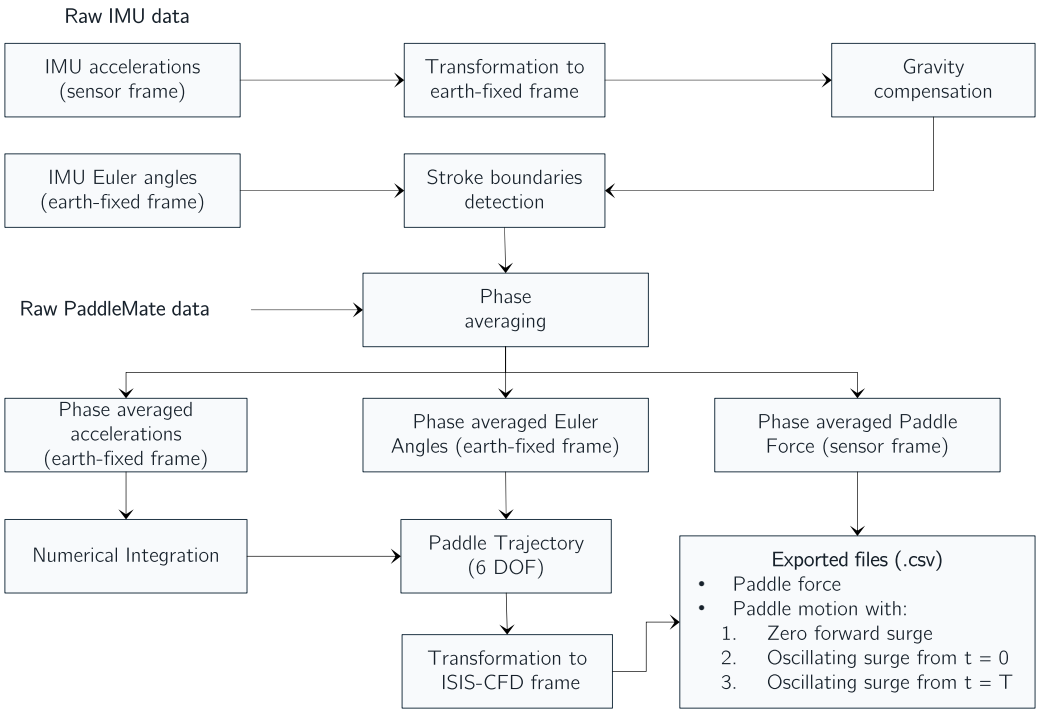

Figure 4.3: Procedure used to reconstruct the prescribed paddle motion from the IMU and force measurements.

vertical direction upward, $\mathbf{g}^E = (0, 0, g)^\mathsf{T}$, where $g = 9.81\,\mathrm{m\,s^{-2}}$. The rotation matrix was constructed as

$$\mathbf{R}_{SE}(t) = \mathbf{R}_z\big(\psi(t)\big)\,\mathbf{R}_y\big(\theta(t)\big)\,\mathbf{R}_x\big(\phi(t)\big). \tag{4.2}$$

The procedure was checked using the stationary-paddle interval described in Appendix B. During this interval, the rotated acceleration before gravity removal should be approximately $(0, 0, g)^\mathsf{T}$, whereas the gravity-compensated acceleration should be approximately $\mathbf{0}$.

4.3.2 Stroke segmentation and phase averaging

The phase-averaging procedure was applied within the selected analysis window to the three Euler-angle components, the three gravity-compensated acceleration components, and the paddle-force signal. One of the six kinematic signals was selected as the segmentation criterion. Local crests and troughs were identified in this criterion using a prominence of 25 in the native units of the selected signal and a minimum separation of 40 samples.

Depending on the selected phase reference, either successive crests or successive troughs defined the common stroke boundaries for all kinematic and force signals. Consequently, the phase origin, $\tau = 0\,\%$, corresponds to the selected extremum of the criterion signal, whereas $\tau = 100\,\%$ corresponds to the subsequent occurrence of the same extremum type. Algorithm 1 summarises the phase-averaging procedure.

For each interval, the stroke period was calculated from the timestamps of its two boundaries. The mean period, $\overline{T}$, was then calculated over all identified intervals and used to define a representative time grid containing N_p equally spaced points.

For every signal and every stroke interval, both boundary samples were kept. As the measured histories were nearly periodic but exhibited small endpoint differences, the first and final signal values were replaced

by their mean before fitting a periodic cubic spline [35]. This small endpoint adjustment enforces the equal boundary values required for the periodic spline condition. The resulting interpolant is continuous together with its first and second derivatives across the representative-cycle boundary, providing C^2 continuous motion for stable prescription in the CFD simulations.

Algorithm 1 Phase averaging based on a selectable kinematic criterion.

Require: Time-resolved data set, selected kinematic criterion, selected phase reference, number of phase points N_p

Ensure: Phase-averaged Euler angles, gravity-compensated accelerations, and paddle force, together with individual and mean stroke periods

$\mathcal{V}_{\text{kin}} \leftarrow \{\theta_i, a_i\}_{i=1}^{3}$ ▷ Euler-angle and gravity-compensated acceleration components
$\mathcal{V} \leftarrow \mathcal{V}_{\text{kin}} \cup \{F\}$ ▷ kinematic signals and paddle force
Select criterion signal $y_{\text{crit}} \in \mathcal{V}_{\text{kin}}$
$(\mathcal{C}, \mathcal{T}) \leftarrow \text{LocateExtrema}(y_{\text{crit}}, \text{prominence} = 25, \text{distance} = 40)$
if the selected phase reference is a crest **then**
    $\mathcal{B} \leftarrow \mathcal{C}$
else
    $\mathcal{B} \leftarrow \mathcal{T}$
end if ▷ successive stroke boundaries
$N_s \leftarrow |\mathcal{B}| - 1$
for $k = 1$ to N_s **do**
    $T_k \leftarrow t_{\mathcal{B}_{k+1}} - t_{\mathcal{B}_k}$
end for
$\overline{T} \leftarrow \text{mean}(\{T_k\}_{k=1}^{N_s})$
$\bar{\mathbf{t}} \leftarrow \text{linspace}(0, \overline{T}, N_p)$
for each signal $v \in \mathcal{V}$ **do**
    for $k = 1$ to N_s **do**
        Extract $\mathbf{t}_k$ and $\mathbf{v}_k$, including both stroke-boundary samples
        $N_k \leftarrow |\mathbf{t}_k|$
        $v_{\text{m}} \leftarrow \frac{1}{2}(\mathbf{v}_k[1] + \mathbf{v}_k[N_k])$
        $\mathbf{v}_k[1] \leftarrow v_{\text{m}}$
        $\mathbf{v}_k[N_k] \leftarrow v_{\text{m}}$
        Fit periodic cubic spline $S_{v,k}$ to $(\mathbf{t}_k, \mathbf{v}_k)$
        $\hat{\mathbf{t}}_k \leftarrow \text{linspace}(\mathbf{t}_k[1], \mathbf{t}_k[N_k], N_p)$
        $\mathbf{V}_{v,\cdot,k} \leftarrow S_{v,k}(\hat{\mathbf{t}}_k)$
    end for
    $\bar{\mathbf{v}} \leftarrow \text{mean}(\mathbf{V}_v, \text{axis} = 2)$
    $\mathbf{v}^{\min} \leftarrow \min(\mathbf{V}_v, \text{axis} = 2)$
    $\mathbf{v}^{\max} \leftarrow \max(\mathbf{V}_v, \text{axis} = 2)$
    $\boldsymbol{\sigma}_{\text{v}} \leftarrow \text{std}(\mathbf{V}_v, \text{axis} = 2)$
end for
return phase statistics for all signals, individual stroke periods, mean stroke period, and representative time grid

Each spline was evaluated at N_p equally spaced points over the physical duration of the corresponding stroke. Although individual strokes may have different durations, the resampled histories can therefore be represented on the common normalised phase coordinate

$$\tau_j = 100\frac{j-1}{N_p - 1}, \qquad j = 1, \ldots, N_p. \tag{4.3}$$

For each parameter $v \in \mathcal{V}$, the phase-averaged history was calculated at every phase location as

$$\overline{v}(\tau_j) = \frac{1}{N_s} \sum_{k=1}^{N_s} v_k(\tau_j), \qquad v \in \mathcal{V}, \tag{4.4}$$

where $v_k(\tau_j)$ is the value of parameter v for stroke k at phase location τ_j, and N_s is the number of stroke intervals. The minimum, maximum, and standard deviation were calculated analogously at each phase location for every parameter. The points at $\tau = 0\,\%$ and $\tau = 100\,\%$ represent the periodic boundaries of the resampled stroke.

The paddle-force signal was segmented, resampled, and phase-averaged using the same kinematic stroke boundaries. It was not used to reconstruct the paddle trajectory. Instead, it was used subsequently as the calibration-informed comparison reference for the CFD computed paddle forces (Section 5.1.4).

4.3.3 Numerical integration

The paddle displacements were obtained by double integration of the phase-averaged accelerations using trapezoidal law. The initial conditions used were zero initial velocity and zero initial displacement $\mathbf{v}_0 = \mathbf{0}$ and $\mathbf{x}_0 = \mathbf{0}$.

$$\mathbf{v}_i = \mathbf{v}_{i-1} + \frac{\mathbf{a}_i + \mathbf{a}_{i-1}}{2} (t_i - t_{i-1}) . \tag{4.5}$$

Accelerometer bias and attitude uncertainty introduce errors in the resolved acceleration, which accumulate through numerical integration and result in velocity and position drift [17, 18]. The velocity endpoint mismatch was removed by applying a linear correction.

$$\mathbf{v}_i^{\mathrm{p}} = \mathbf{v}_i - \frac{t_i - t_0}{t_N - t_0} (\mathbf{v}_N - \mathbf{v}_0) , \tag{4.6}$$

such that $\mathbf{v}_N^{\mathrm{p}} = \mathbf{v}_0^{\mathrm{p}}$. This correction removes the accumulated velocity drift by imposing a periodic endpoint constraint. It does not provide an independent estimate of the true inertial velocity. Equivalently, the linear velocity correction corresponds to subtracting a constant acceleration from the integrated acceleration.

The corrected velocity was then integrated to obtain an intermediate position history.

$$\mathbf{x}_i^{\mathrm{int}} = \mathbf{x}_{i-1}^{\mathrm{int}} + \frac{\mathbf{v}_i^{\mathrm{p}} + \mathbf{v}_{i-1}^{\mathrm{p}}}{2} (t_i - t_{i-1}) . \tag{4.7}$$

The mean velocity required to enforce zero net displacement over the cycle was then removed.

$$\mathbf{v}_i^{\mathrm{c}} = \mathbf{v}_i^{\mathrm{p}} - \frac{\mathbf{x}_N^{\mathrm{int}} - \mathbf{x}_0^{\mathrm{int}}}{t_N - t_0} . \tag{4.8}$$

The final paddle position was obtained by integrating the corrected velocity.

$$\mathbf{x}_i^{\mathrm{c}} = \mathbf{x}_{i-1}^{\mathrm{c}} + \frac{\mathbf{v}_i^{\mathrm{c}} + \mathbf{v}_{i-1}^{\mathrm{c}}}{2} (t_i - t_{i-1}) . \tag{4.9}$$

The periodicity evident in the measured acceleration was used as a constraint on the integration. The resulting trajectory satisfies $\mathbf{v}_N = \mathbf{v}_0$ and $\mathbf{x}_N = \mathbf{x}_0$ over the representative stroke, while the corrections compensate for accumulated drift associated with inertial integration.

4.4 Trajectory export for CFD

The trajectory reconstruction used the following sequence of reference frames.

$$S \xrightarrow{\mathrm{R}_{SE}} E \xrightarrow{\mathrm{R}_{EB}} B \equiv \text{ISIS-CFD},$$

where S denotes the sensor frame fixed to the paddle, E the earth-fixed East–North–Up frame, and B the boat-aligned surge–sway–heave frame. The ISIS-CFD frame coincides with B, as the hull and paddle geometries are defined along the surge, sway, and heave directions, following the axis and origin convention established in Section 3.2 and Figure 3.1.

The transformation from the earth-fixed to the boat-aligned frame was defined as a yaw rotation through the boat heading, using Equation (4.12). The transformation was applied consistently to the reconstructed position, velocity, and acceleration.

$$\mathbf{q}^{B}(t) = \mathbf{R}_{EB}\,\mathbf{q}^{E}(t), \qquad \mathbf{q} \in \{\mathbf{r}, \mathbf{v}, \mathbf{a}\}, \tag{4.10}$$

where $\mathbf{r}$, $\mathbf{v}$, and $\mathbf{a}$ denote position, velocity, and acceleration, respectively. Paddle orientation was transformed using the corresponding rotation-matrix composition.

$$\mathbf{R}_{PB}(t) = \mathbf{R}_{EB}\,\mathbf{R}_{PE}(t), \tag{4.11}$$

where $\mathbf{R}_{PE}(t)$ and $\mathbf{R}_{PB}(t)$ denote the paddle orientation in the earth-fixed and boat-aligned frames, respectively. With the adopted yaw–pitch–roll convention, the transformation changes the yaw reference by $-\psi_{\text{boat}}$, while roll and pitch are unchanged.

The phase-averaged trajectory of the IMU reference point was then combined with the corresponding phase-averaged attitude and the fixed lever arms between the IMU, paddle handle, and blade tip. The lever arms were obtained from the paddle CAD model, thereby defining the six-degree-of-freedom motion of the paddle.

The reconstructed trajectory was transformed from the earth-fixed reference frame to the boat-aligned CFD reference frame using the rotation matrix given below. The heading convention was defined consistently with this transformation.

$$\mathbf{R}_{EB} = \begin{bmatrix} \cos\psi_{\text{boat}} & \sin\psi_{\text{boat}} & 0 \\ -\sin\psi_{\text{boat}} & \cos\psi_{\text{boat}} & 0 \\ 0 & 0 & 1 \end{bmatrix}. \tag{4.12}$$

The complete transformation was expressed as

$$\mathbf{r}_{\text{tip}}^{\text{CFD}}(t) = \mathbf{R}_{EB}\,\mathbf{r}_{\text{tip}}^{E,\text{rel}}(t) + \begin{bmatrix} x_{\text{boat}}(t) + x_0 \\ y_{\text{offset}} \\ 0 \end{bmatrix}, \tag{4.13}$$

where $\mathbf{r}_{\text{tip}}^{E,\text{rel}}$ is the reconstructed paddle-tip trajectory relative to the selected earth-fixed origin, x_0 is the initial longitudinal location, and y_{offset} defines the lateral blade clearance from the hull. The lateral blade location was prescribed using the minimum clearance between the blade tip and the hull.

$$y_{\text{offset}} = \begin{cases} -\left(b_{1/2} + c\right) - \max_{\tau} y_{\text{tip}}(\tau), & \text{starboard}, \\ \left(b_{1/2} + c\right) - \min_{\tau} y_{\text{tip}}(\tau), & \text{port}, \end{cases} \tag{4.14}$$

where $b_{1/2}$ is the hull half-beam and c is the prescribed clearance margin (used 0.2 m).

Preparing the Trajectory for CFD

The reconstructed paddle motion was exported in three forms. Let $\mathbf{r}_p(t)$ and $\mathbf{R}_p(t)$ denote the periodic translational trajectory and attitude of the paddle reconstructed from the measured data, respectively. The representative stroke period was defined as

$$T = T_s = \overline{T}. \tag{4.15}$$

For cases including forward advance, the prescribed boat speed was defined by

$$v_{\text{boat}}(t) = \bar{v} + v_a \cos\left[2\pi\left(\frac{t}{T} + \varphi_v\right)\right], \qquad \bar{v} = \frac{v_{\max} + v_{\min}}{2}, \qquad v_a = \frac{v_{\max} - v_{\min}}{2}, \tag{4.16}$$

where φ_v is the phase offset expressed as a fraction of the stroke period.

Export 1, paddle motion without forward advance. For Export 1, no forward advance was applied to the reconstructed paddle motion. The prescribed paddle translation and attitude were therefore

$$\mathbf{r}_p^{(1)}(t) = \mathbf{r}_p(t), \qquad \mathbf{R}_p^{(1)}(t) = \mathbf{R}_p(t), \qquad x_{\text{boat}}^{(1)}(t) = 0. \tag{4.17}$$

Export 2, oscillating-surge advance from $t = 0$. For Export 2, the oscillating-surge motion was applied from the beginning of the prescribed paddle motion. The corresponding longitudinal boat translation was obtained from

$$x_{\text{boat}}^{(2)}(t) = \int_0^t v_{\text{boat}}(s)\,\mathrm{d}s. \tag{4.18}$$

The paddle translation and attitude were then prescribed as

$$\mathbf{r}_p^{(2)}(t) = \mathbf{r}_p(t) + \begin{bmatrix} x_{\text{boat}}^{(2)}(t) \\ 0 \\ 0 \end{bmatrix}, \qquad \mathbf{R}_p^{(2)}(t) = \mathbf{R}_p(t). \tag{4.19}$$

Export 3, paddle motion following boat acceleration. For Export 3, the boat was first accelerated from rest over a prescribed interval $T_{\text{acc}} = 15$ s, while the paddle remained fixed relative to the boat. The periodic paddle motion and oscillating-surge motion commenced at $t = T_{\text{acc}}$. The boat speed was prescribed as

$$v_{\text{boat}}^{(3)}(t) = \begin{cases} [\bar{v} + v_a \cos(2\pi\varphi_v)]\,\min[\tanh(t), 1]\,, & 0 \le t < T_{\text{acc}}, \\ v_{\text{boat}}(t - T_{\text{acc}}), & t \ge T_{\text{acc}}, \end{cases} \tag{4.20}$$

where t is evaluated in seconds within the hyperbolic-tangent ramp. The first branch accelerates the boat towards the initial value of the oscillating-surge law, $v_{\text{boat}}(0)$.

The corresponding longitudinal translation was obtained by integration.

$$x_{\text{boat}}^{(3)}(t) = \int_0^t v_{\text{boat}}^{(3)}(s)\,\mathrm{d}s. \tag{4.21}$$

During the acceleration stage, the paddle kept its initial position and orientation relative to the boat. Its prescribed surge was

$$\mathbf{r}_p^{(3)}(t) = \begin{cases} \mathbf{r}_p(0) + \begin{bmatrix} x_{\text{boat}}^{(3)}(t) \\ 0 \\ 0 \end{bmatrix}, & 0 \le t < T_{\text{acc}}, \\ \mathbf{r}_p(t - T_{\text{acc}}) + \begin{bmatrix} x_{\text{boat}}^{(3)}(t) \\ 0 \\ 0 \end{bmatrix}, & t \ge T_{\text{acc}}, \end{cases} \tag{4.22}$$

and its attitude was prescribed as

$$\mathbf{R}_p^{(3)}(t) = \begin{cases} \mathbf{R}_p(0), & 0 \le t < T_{\text{acc}}, \\ \mathbf{R}_p(t - T_{\text{acc}}), & t \ge T_{\text{acc}}. \end{cases} \tag{4.23}$$

Since $\tanh(15) \approx 1$, the hand-off speed is effectively equal to $v_{\text{boat}}(0)$. Thus, the paddle initially translated with the accelerating boat while maintaining its initial pose. Periodic paddle motion was then introduced. Only Exports 2 and 3 were used in the CFD simulations presented in the results.

4.5 Computational framework and settings

This section describes the numerical methodology used to simulate the dragon boat and paddle configurations. A common CFD framework was adopted for all cases, while the domain arrangement, body-motion treatment, and prescribed paddle trajectory were varied according to the simulation objective. The following subsections describe the computational domains, mesh generation, physical models, numerical settings, and motion definitions.

4.5.1 Geometry preparation

The paddle and hull geometries were provided by HKUST. The geometries were repaired and prepared using Rhino and CADfix before being exported as clean Parasolid files for HEXPRESS. The geometry preparation ensured compliance with the requirements of the meshing workflow, including watertight surfaces, absence of duplicate or self-intersecting faces, and valid edge connectivity.

Hull geometry

The hull considered in this study is a standard 20-seater IDBF dragon boat, in accordance with the 2025 ICF Dragon Boat Competition Rules [36]. The original CAD geometry was simplified in Rhino by removing non-essential structural details while keeping the hydrodynamically relevant geometry. The simplified geometry was then imported into CADfix, where the hull and deck surfaces were defined as named groups. Figure 4.4 compares the original and simplified geometries. The resulting model was used for the Type 2 (boat-alone) and Type 3 (paddle-hull configuration) simulations.

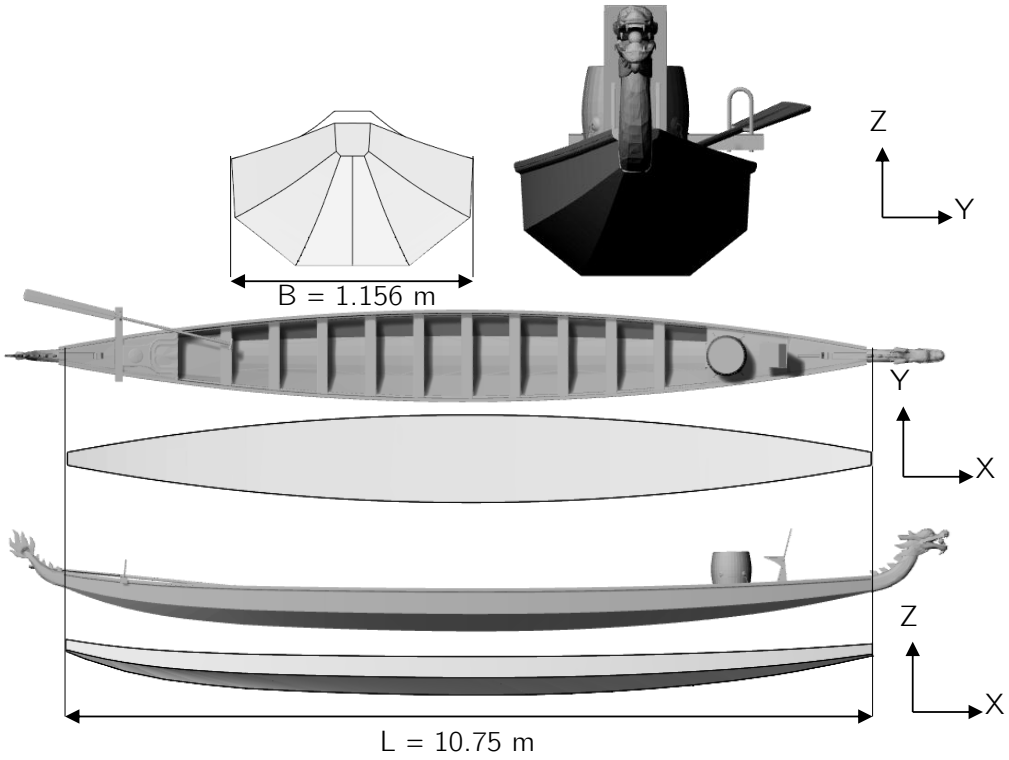

Figure 4.4: Three-view comparison of the actual hull geometry with the simplified hull.

Paddle geometry

The paddle geometry used in the simulations is shown in Figure 4.2. The paddle surfaces were divided into named groups according to their location, including the front face, back face, side edge, shaft, and handle. These groups provided consistent patch definitions for mesh generation and CFD case setup, enabling automated and reproducible mesh generation and case setup across all simulations.

4.5.2 Physical models, body definitions, and simulation types

Common fluid and numerical parameters

The fluid properties, numerical controls, and reference quantities common to all CFD cases are summarised in Table 4.2.

Table 4.2: Common fluid properties, numerical controls, and computational parameters used in the CFD simulations.

Quantity	Value
Fluid model	Two-phase (air/water)
Water density ρ_w	1000 kg/m^3
Kinematic viscosity ν	1.0×10^{-6} m^2/s
Target y^+ (viscous-layer cases)	50
Residual convergence criterion	3 orders of magnitude
Free-surface Courant target	1.0
Overset Courant target	1.0
Hull reference length L_{OA}	10.7507 m
Paddle reference length L_{paddle}	0.514 m

Simulation types and analysed cases

Three simulation types were defined to separate the paddle, boat, and paddle-hull responses. Their principal characteristics are described below, with the case-specific numerical settings given subsequently in Table 4.10 of Section 4.5.5.

Type 1, standalone paddle. Type 1 isolates the hydrodynamic response of the paddle. The paddle follows the prescribed measured six-degree-of-freedom trajectory. Cases 1–5 in Table 4.10 belong to this type.

Type 2, boat alone. Type 2 isolates the hydrodynamic response of the boat. Surge motion is prescribed, while heave and pitch are solved dynamically. Cases 6–20 in Table 4.10 belong to this type and comprise the calm-water resistance and oscillating-surge series.

Type 3, paddle-hull configuration. Type 3 combines the prescribed six-degree-of-freedom paddle trajectory with the boat. Boat surge is prescribed, while heave and pitch are solved dynamically. Case 21 in Table 4.10 belongs to this type.

Boat mass, CFD datum, and hydrostatic equilibrium

The following properties define the boat body used in Types 2 and 3. The coordinate and rotation conventions are defined in Section 4.4. The total boat-system mass was specified as 980 kg, with the

centre of gravity located at $z_{\mathrm{CoG}} = 0.1613$ m above the undisturbed free surface in the CFD reference frame.

The specified mass was combined with the simplified hull geometry to determine the hydrostatic equilibrium and the rigid-body inertial properties required for the boat-body definition. Because the FineMarine `domhydro` plugin does not support lumped masses, the 980 kg total mass was represented by an equivalent uniform surface density over the simplified hull. This provided the mass distribution and inertia tensor used by the dynamic rigid-body model. Hydrostatic equilibrium was first computed in constrained-equilibrium mode, with roll, pitch, and yaw fixed at zero. The resulting equilibrium draft was $d = 0.238$ m. The hull was then translated vertically so that the undisturbed free surface coincided with $z_{\mathrm{fs}} = 0$ in the CFD reference frame. A final `domhydro` evaluation was performed using the translated hull to obtain the hydrostatic and inertial properties used in the boat-body definition.

At equilibrium, the centre of buoyancy relative to the centre of gravity is

$$\mathbf{r}_{\mathrm{CoB}}^{\mathrm{rel}} = \begin{pmatrix} -2.840368 \times 10^{-6} \\ 0 \\ 0.1492866 \end{pmatrix} \mathrm{m}. \tag{4.24}$$

The inertia tensor evaluated at the centre of gravity is

$$\mathbf{I}_{\mathrm{CoG}} = \begin{pmatrix} 221.19 & 0 & 9.262 \\ 0 & 5566.9 & 0 \\ 9.262 & 0 & 5478.6 \end{pmatrix} \mathrm{kg\,m^2}. \tag{4.25}$$

Body definitions, degrees of freedom, and prescribed motions

The paddle body is used in Types 1 and 3 with all six degrees of freedom prescribed from the processed measured trajectory. The boat body is used in Types 2 and 3, with prescribed surge and dynamically solved heave and pitch, while sway, roll, and yaw are fixed. The resulting degree-of-freedom treatment is summarised in Table 4.3.

Table 4.3: Degree-of-freedom treatment of the paddle and boat bodies.

	Paddle	Boat
Simulation types	Type 1, Type 3	Type 2, Type 3
Surge T_x	Prescribed	Prescribed
Sway T_y	Prescribed	Fixed
Heave T_z	Prescribed	Solved
Roll R_x	Prescribed	Fixed
Pitch R_y	Prescribed	Solved
Yaw R_z	Prescribed	Fixed
Mass	–	980 kg
Mass distribution	–	Uniform surface density

The boat surge follows the advance law defined in Equation (4.16). For the paddle-hull calculation, the 15 s acceleration stage defined in Equation (4.22) precedes the periodic paddle stroke.

The prescribed paddle motion used in Types 1 and 3 are shown in Figure 4.5. For Type 1, the motion is imposed directly in the global reference frame. In Type 3, the paddle follows the boat translation in the T_x direction, with the prescribed paddle motion therefore applied relative to the advancing hull.

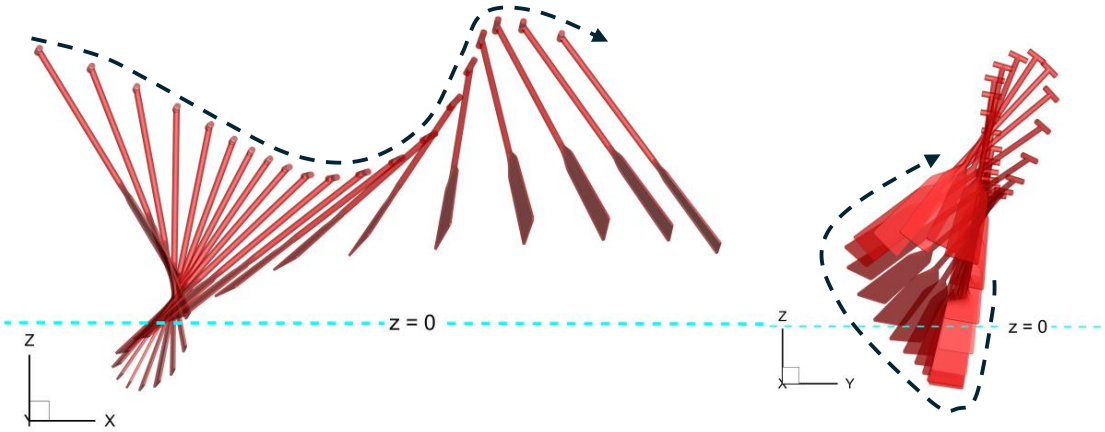

Figure 4.5: Prescribed paddle motion used in the CFD simulations, defined in the global frame for Type 1 and relative to the boat translation in T_x for Type 3.

4.5.3 Computational domains and mesh

Background domains and boundary conditions

Three background domains were used. B0 is the full-tank domain for the standalone-paddle cases, while B1 and B2 are half-tank domains for the boat-alone and paddle-hull configuration cases, respectively. Mirror symmetry is applied at the $y = 0$ centreplane in the half-tank domains.

The lateral and longitudinal boundaries use far-field conditions, while the upper and lower boundaries use prescribed-pressure conditions. The domain dimensions, base-cell distributions, and boundary treatments are summarised in Table 4.4.

Table 4.4: Background-domain specifications and boundary conditions for the three simulation types. B0 is used for Type 1, B1 for Type 2, and B2 for Type 3.

Property	B0 (Type 1)	B1 (Type 2)	B2 (Type 3)
Domain type	Full tank	Half tank	Half tank
Extent $x \times y \times z$	$30.72 \times 10.24 \times 10.24$ m	$5.5L_{OA} \times 2.0L_{OA} \times 2.5L_{OA}$	$30.72 \times 5.12 \times 10.24$ m
Base cells	$24 \times 8 \times 8$	$24 \times 4 \times 8$	$24 \times 4 \times 8$
Centreplane	None	Mirror	Mirror
Top/bottom	Prescribed pressure	Prescribed pressure	Prescribed pressure
Sides/front/back	Far field	Far field	Far field
Initial cell count	64,528	205,061	143,528

For Types 1 and 3, the background-domain dimensions and base-cell counts produce a uniform base-cell size of 1.28 m in all three coordinate directions. Seven global refinement levels were selected so that the initial free-surface mesh has a vertical cell size of

$$h_{fs} = \frac{1.28}{2^7} = 0.010 \text{ m}. \tag{4.26}$$

Table 4.5 provides an overview of the background domains used for each simulation type.

Type 1, standalone paddle mesh

Type 1 combines the B0 full-tank background domain with a rigid paddle overset mesh. The background domain translates with the prescribed paddle surge, while the paddle follows the complete measured six-

Table 4.5: Relationship between simulation type, background domain, body treatment, overset treatment, and analysed cases.

Property	Type 1	Type 2	Type 3
Configuration	Standalone paddle	Boat alone	Paddle-hull
Background domain	B0	B1	B2
Domain	Full tank	Half tank	Half tank
Paddle	Prescribed 6-DOF	–	Prescribed 6-DOF
Boat	–	Prescribed surge, solved heave/pitch	Prescribed surge, solved heave/pitch
Overset mesh	Yes	No	Yes
Cases	1–5	6–20	21

degree-of-freedom trajectory. The overset formulation therefore accommodates the prescribed paddle motions without deforming the background mesh. The mesh for this case is shown in Figure 4.6.

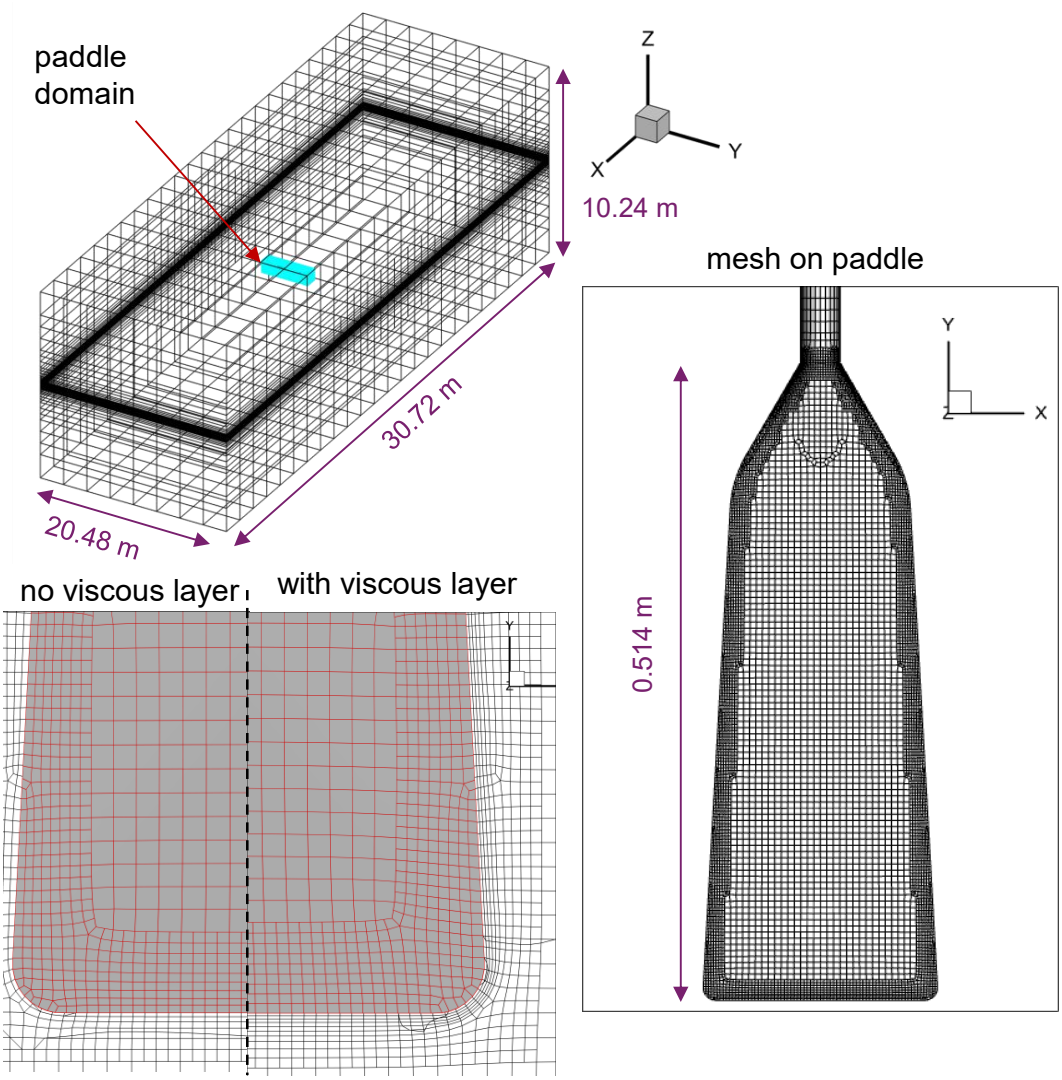

Figure 4.6: Initial mesh for Type 1 (standalone paddle). The full-tank background domain B0 contains the paddle overset mesh.

The same paddle overset mesh is used in Type 3. Its dimensions, base-cell distribution, and surface

treatments are given in Table 4.6. Type 2 contains no overset mesh because the boat hull is represented directly in the background mesh.

Table 4.6: Paddle overset-mesh specifications for Types 1 and 3.

Property	Euler	k–ω SST
Simulation type	Type 1, Type 3	Type 1
Extent $x \times y \times z$	$0.64 \times 2.56 \times 0.64$ m	
Base cells	$8 \times 32 \times 8$	
Outer boundaries	Overset	
Paddle faces	Slip wall	Wall function, $y^+ = 50$
Paddle shaft and handle	Slip wall	Slip wall
Initial cell count	179,656	260,937

The Euler cases use a slip-wall paddle surface without prism layers. The viscous Type 1 case uses prism layers on the paddle with a wall function corresponding to a target $y^+ = 50$. The resulting near-wall meshes are compared in Figure 4.7.

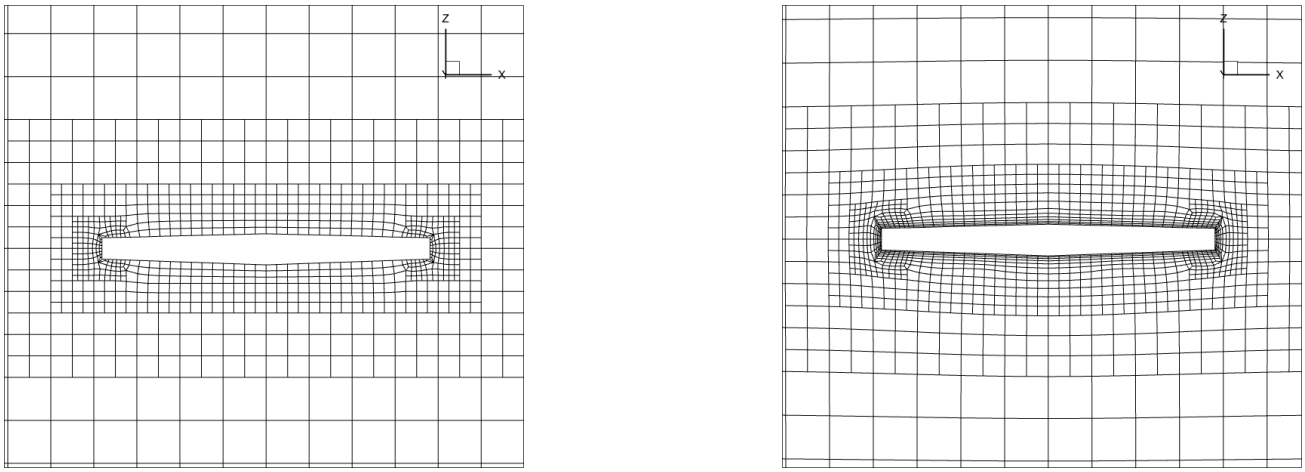

(a) Euler mesh. **(b)** k–ω SST mesh.

Figure 4.7: Near-wall paddle mesh at the mid-plane of the paddle face ($z = -0.731$ m).

Type 2, boat-alone mesh

Type 2 uses the B1 half-tank background domain with mirror symmetry at $y = 0$. The boat hull is represented directly in the background mesh, so no overset region is required. Its longitudinal motion is prescribed by the resistance or oscillating-surge advance law, while heave and pitch are solved dynamically. The resulting Type 2 mesh is shown in Figure 4.8.

Type 3, paddle-Hull configuration mesh

Type 3 combines the B2 half-tank background domain, the boat hull, and the paddle overset mesh defined for Type 1. The paddle follows its prescribed six-degree-of-freedom trajectory relative to the translating boat domain. Boat surge is prescribed, whereas heave and pitch are solved dynamically.

Figure 4.9 shows the resulting paddle-hull mesh arrangement.

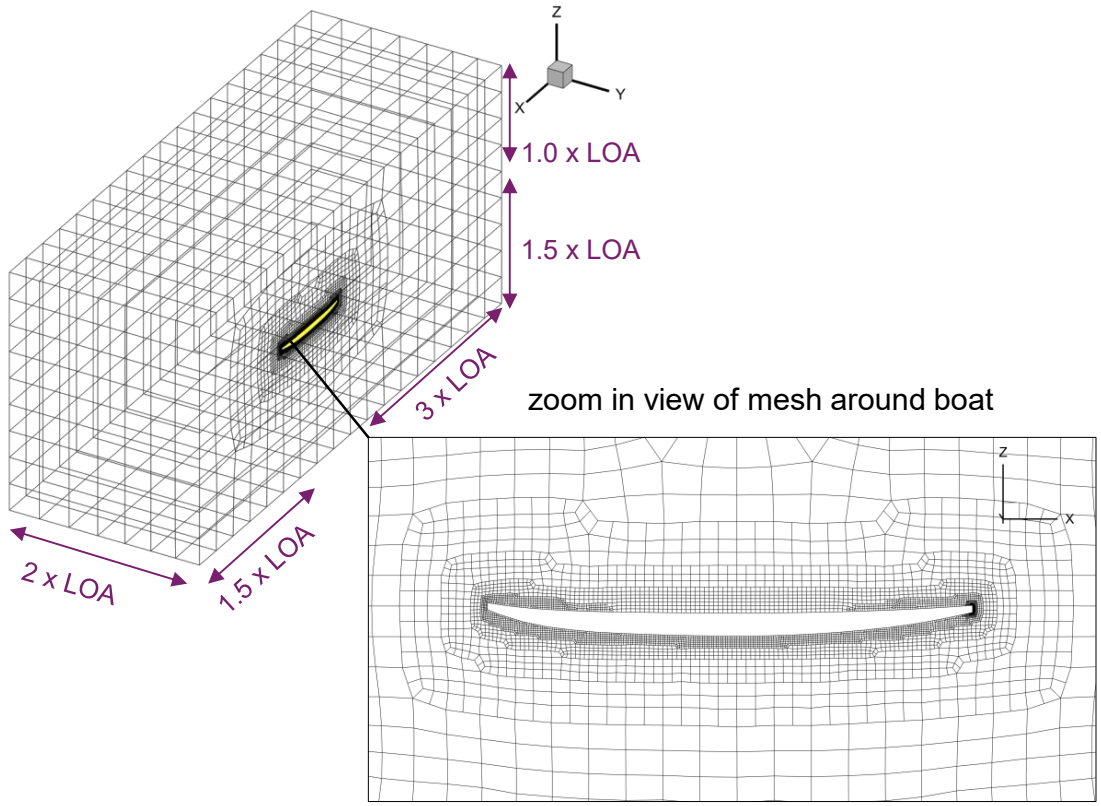

Figure 4.8: Initial mesh for Type 2 (boat alone). The boat is contained within the half-tank background domain B1 with mirror symmetry at the centreplane.

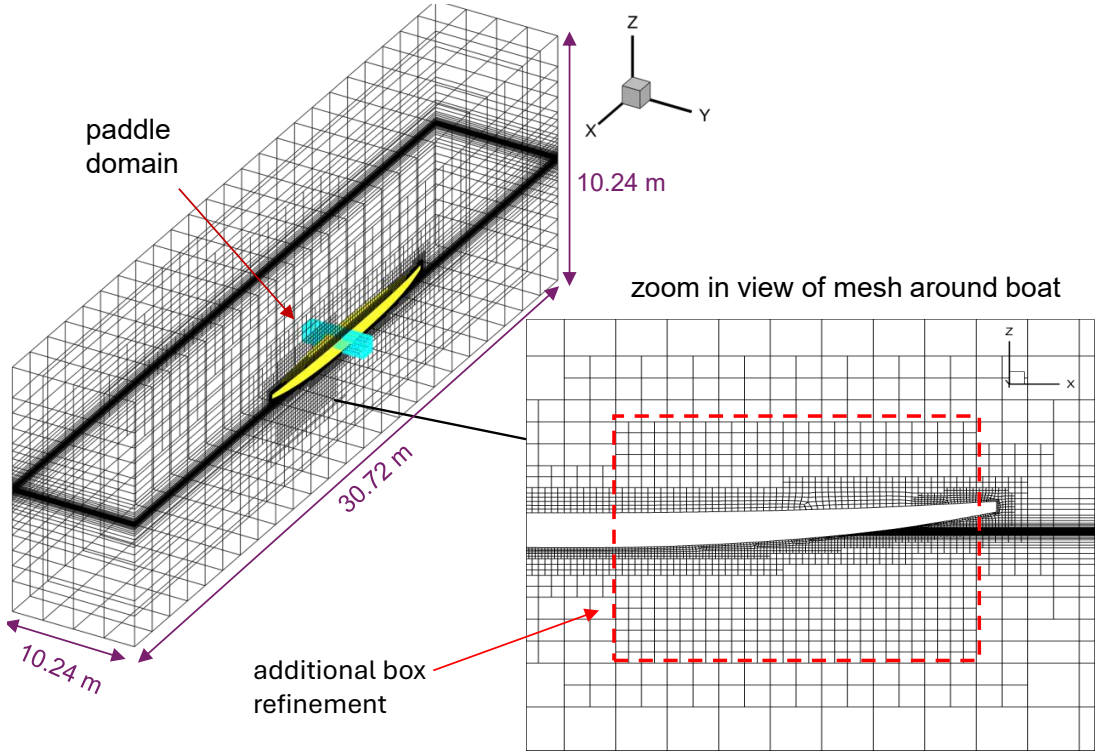

Figure 4.9: Initial mesh for Type 3 (paddle-hull configuration). The half-tank background domain B2 contains the boat hull and paddle overset mesh.

Domain motion and mesh deformation

The mesh-motion treatment follows directly from the three configurations. For Type 1, paddle surge is applied to the B0 background domain. For Types 2 and 3, the prescribed boat motion is applied to the corresponding background domain. The paddle overset mesh keeps its prescribed rigid six-degree-of-freedom motion in Types 1 and 3. For boat-containing cases, vertical translation and pitch rotation are accommodated through weighted mesh deformation. The remaining imposed background-domain motions are rigid. Table 4.7 summarises the treatment.

Table 4.7: Background-domain motion and deformation treatment.

Configuration	Motion source	Deformation	Paddle overset
Type 1	Paddle surge	Rigid	6-DOF
Type 2	Boat motion	Weighted vertical translation and pitch	–
Type 3	Boat motion	Weighted vertical translation and pitch	6-DOF

Adaptive grid refinement

A moving adaptive grid refinement (AGR) region localises refinement around the hydrodynamically active flow region. The AGR region follows the relevant background-domain motion, following the paddle in Type 1, surrounding the boat in Type 2, and encompassing both paddle and boat in Type 3. The three configurations are shown in Figure 4.10.

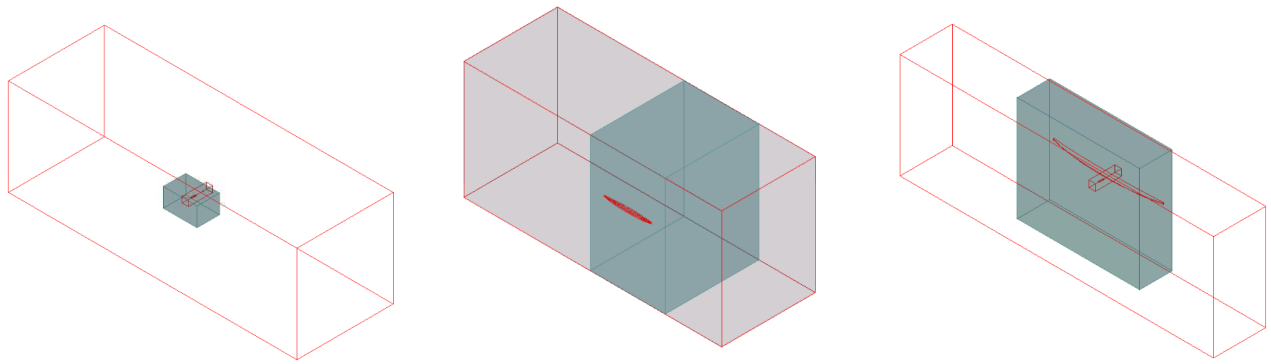

(a) Type 1, paddle. **(b)** Type 2, boat. **(c)** Type 3, paddle and boat.

Figure 4.10: AGR-region configurations for the three simulation types.

The paddle, oscillating-surge hull, and paddle-hull configurations use the multisurface–flux-component-Hessian (MSFCH) criterion defined in Section 3.6.1. Its tensorial formulation is compatible with overset interpolation and provides a continuous cell-size transition across the overlap. The calm-water resistance cases use the multisurface plus pressure-Hessian (MS+PH) criterion.

The refinement procedure is evaluated every three time steps. Each AGR level is generated independently from the same base mesh rather than by continuing from a previously adapted mesh. The threshold levels therefore represent separate adapted meshes.

For the paddle and paddle-hull configurations,

$$T_{rS} = 1.1\frac{h_{\mathrm{fs}}}{2}, \qquad h_{\min} = 0.8T_{rS}, \tag{4.27}$$

where h_{fs} is the initial free-surface cell height, T_{rS} is the interface threshold, and $h_{\min}$ limits local refinement. The case-specific AGR parameters are given in Table 4.8.

The AGR threshold serves a different role for the paddle configurations (Types 1 and 3) than for the boat-alone configuration (Type 2). For Types 1 and 3, the free surface is already refined within the base

Table 4.8: Adaptive grid-refinement criteria and controls by simulation type.

Quantity	Type 1 & 3	Type 2
Refinement criterion	MSFCH	Oscillating surge, MSFCH Resistance, MS+PH
Surface-layer cell height h_{sl}	0.01 m	–
Initial free-surface cell height h_{fs}	h_{sl}	No initial free surface refinement
Free-surface aspect ratio AR_{FS}	300	120
Interface threshold T_{rS}	$1.1h_{sl}/2$	$L_{\mathrm{OA}}/2000$
Minimum adapted cell size $h_{\min}$	$0.8T_{rS}$	$0.8T_{rS}$
Refinement-zone target cell size	$(AR_{FS}/5)h_{sl}$	–
Hessian threshold levels T_{rH}/L_{ref}	0.20, 0.15, 0.10, 0.05	Oscillating surge, 0.20, 0.15, 0.10, 0.05 Resistance, 0.20
Buffer layers, full / fractional	4 / 4	4 / 2
Time steps between AGR calls	3	3

mesh, to the target cell size $h_{\mathrm{fs}} = 0.010$ m of Equation (4.26) (Section 4.5.3), before AGR is applied. The interface threshold $T_{rS} = 1.1h_{sl}/2$ of Equation (4.27) is set relative to this already-fine surface-layer cell height $h_{sl} = h_{\mathrm{fs}} = 0.010$ m (Table 4.8), so that AGR need only add one further level of refinement at the free-surface interface beyond the base mesh, concentrating the additional AGR on the paddle, its wake, and the pressure-gradient regions identified by the Hessian criterion rather than on establishing the free-surface resolution itself. For Type 2, the base mesh does not pre-refine the free surface, so AGR is instead responsible for the complete free-surface refinement, starting from the coarser initial mesh (Table 4.8). The reported Type 2 AGR settings therefore represent the entire free-surface refinement rather than a single level added to an already-refined base mesh.

Wackers et al. [21–24] provide the formulation and verification basis for this AGR approach. The AGR threshold defines a refinement coordinate rather than a uniform grid-spacing ratio because refinement occurs through discrete cell subdivision. Consequently, a single adapted mesh does not establish grid independence. The four-level fits used in this study follow the least-squares procedure described by Wackers et al. [24].

4.5.4 Temporal discretisation and convergence controls

The time step is controlled by the free-surface and, where applicable, overset Courant limits defined in Section 3.6.3. The temporal settings applied to the simulations are summarised below.

Courant-controlled time stepping

The paddle and oscillating-surge cases use adaptive time stepping with a free-surface Courant target of unity and, where an overset grid is present, an overset Courant target of unity. The time step is reduced when required to satisfy the applicable free-surface and overset Courant constraints. Type 2 cases without an overset grid are therefore subject only to the free-surface constraint.

Fixed time stepping and resistance restarts

The Type 2 calm-water resistance cases use fixed time steps following the Cadence/FineMarine recommended procedure. Seven prescribed advance speeds were considered, with each case after the lowest speed initialised by restart from the preceding converged calculation. The acceleration-ramp and maximum calculation durations were assigned according to the same procedure.

The nominal time step was selected from the hull length and prescribed speed as

$$\Delta t = \frac{L_{\mathrm{OA}}}{200V}, \tag{4.28}$$

where $L_{\mathrm{OA}} = 10.7507$ m and V is the prescribed boat speed. The resulting time steps and execution settings are given in Table 4.9.

Table 4.9: Prescribed speeds and recommended nominal time steps for the calm-water resistance cases.

CFD case	6	7	8	9	10	11	12
Speed [km h^{-1}]	7	8	9	10	11	12	13
Recommended Δt [s]	0.0276	0.0242	0.0215	0.0194	0.0176	0.0161	0.0149

Paddle-hull configuration simulation stages (Type 3)

The Type 3 paddle-hull calculation uses two stages. The acceleration stage is run without probes. The subsequent stroke stage restarts from the converged acceleration solution, activates probes, and uses Courant-controlled stepping. Refinement is not reinitialised at the restart. Probe output is written every $T_s/20 = 0.041$ s.

Solver convergence

The maximum nonlinear iterations per time step are case-dependent. Type 1 cases use 20 iterations per step, while Type 2 and Type 3 cases use 30 iterations per step. All cases use a residual convergence criterion of three orders of magnitude. The nonlinear-iteration limit represents the maximum allowed iterations, not a separate convergence criterion.

4.5.5 Simulation case matrix

Table 4.10 summarises the CFD cases considered in the analysis, together with their motion prescriptions, flow models, spatial refinement levels, and temporal controls. The four-level AGR sequence is applied where a grid-convergence series is specified, and each level uses a distinct Hessian threshold while keeping the same base mesh and solver settings. Exports 2 and 3 correspond to the motion prescriptions defined in Section 4.4. Export 2 applies the oscillating-surge motion from $t = 0$, whereas Export 3 introduces the same surge motion after the 15 s acceleration stage.

Model-selection basis and scope of claims

Table 4.11 states the modelling decision for each case group before the results are interpreted. The associated scope defines the claim that can subsequently be made.

4.5.6 Output definitions and post-processing

The paddle force is reported in the ISIS-CFD inertial frame and transformed to the paddle reference frame before the normal force is evaluated. The force transformation is

$$\mathbf{F}^B = \mathbf{R}_{IB}^{\mathsf{T}} \mathbf{F}^I, \tag{4.29}$$

where the paddle-normal force is defined as

$$F_n = F_z^B. \tag{4.30}$$

Table 4.10: CFD cases considered in the analysis and their principal numerical controls.

Sr. No.	Simulation type	Surge motion	Flow model	T_{rH}/L
Type 1, Single paddle (domain B0)				
1–4	Paddle grid-convergence series	Export 2	Euler	[0.20, 0.15, 0.10, 0.05]
5	Viscous paddle	Export 2	k–ω SST	0.20
Type 2, Boat alone (domain B1)				
6–12	Boat resistance	Ramp to prescribed velocity	k–ω SST	0.20
13–16	Boat oscillating surge, fixed Δt	Export 3	k–ω SST	[0.20, 0.15, 0.10, 0.05]
17–20	Boat oscillating surge, fixed Δt	Export 3	k–ω SST	[0.20, 0.15, 0.10, 0.05]
Type 3, Paddle-hull (domain B2)				
21	Paddle-hull	Export 3	Euler	0.20

Note. The AGR values listed in brackets denote the refinement levels used within the corresponding grid-convergence series. Common Courant targets, nonlinear-iteration limits, and convergence criteria are specified in Table 4.2.

Table 4.11: Numerical model selection and scope of the resulting analysis.

Case	Numerical model	Selection basis	Scope of analysis
Standalone paddle	Euler, with one viscous comparison	Isolate free-surface and inertial paddle loading, and assess model-form sensitivity separately	Configuration-specific integral-load analysis with a four-level Euler refinement series
Bare-hull resistance	k–ω SST with MS+PH refinement	Capture viscous hull resistance and resolve pressure and wave-system features	Resistance and hull-response analysis for the specified prescribed-motion cases
Oscillating-surge hull	k–ω SST with MSFCH refinement	Resolve unsteady free-surface and hull-force response	Unsteady hull-only analysis with a four-level refinement series
Paddle-hull configuration	Euler with overset motion and MSFCH refinement	Demonstrate the prescribed-motion interaction framework within available cost	Qualitative interaction analysis, with no paddle-hull grid-convergence, viscous, or propulsion prediction

The paddle orientation follows the ISIS Cardan sequence

$$\mathbf{R}_{IB} = R_z(\psi)R_y(\theta)R_x(\phi), \tag{4.31}$$

and the paddle-tip elevation is evaluated as

$$z_{\text{tip}} = T_{z0} - 0.988\cos\theta\sin\phi. \tag{4.32}$$

The corresponding paddle-frame lever arm is

$$\mathbf{r}^B_{\text{tip}} = (0, -0.988, 0)\,\text{m}. \tag{4.33}$$

For a stroke interval $[t_a, t_b]$, the following paddle-normal force measures are evaluated as

$$F^B_{z,\max} = \max_{t_a \le t \le t_b} |F^B_z(t)|, \qquad F^B_{z,\text{RMS}} = \left[\frac{1}{t_b - t_a}\int_{t_a}^{t_b} (F^B_z)^2\,\mathrm{d}t\right]^{1/2}, \qquad I^B_z = \int_{t_a}^{t_b} F^B_z\,\mathrm{d}t, \tag{4.34}$$

together with the conditional-positive mean force

$$\overline{F_z^{B+}} = \frac{\displaystyle\int_{F_z^B>0} F_z^B \, \mathrm{d}t}{\displaystyle\int_{F_z^B>0} \mathrm{d}t}. \tag{4.35}$$

Peak force, RMS force, impulse, and conditional-positive mean force are evaluated over the defined stroke interval. The RMS calculation is time-weighted to account for non-uniform CFD output. Paddle-tip elevation is obtained from the prescribed motion, while wetted area is taken from the solver output on the corresponding time axis.

For shape comparisons between traces, each signal is normalised by its own maximum absolute value,

$$\widehat{q}(t) = \frac{q(t)}{\max_t |q(t)|}. \tag{4.36}$$

Dimensional force and acceleration values are used for all quantitative comparisons.

Gomory and Galipeau stroke descriptors

Table 5.5 (Section 5.2.5) expresses the computed force history through a set of scalar descriptors rather than through the full force history. Two sources define these descriptors. Gomory [9] defines a set of timing, rate, and impulse descriptors for the paddle force during a single stroke. Galipeau [10] reports a matching time-to-peak and paddle-in-water descriptor for an instrumented sprint-canoe paddle. Both are descriptive hydrodynamic-stroke metrics, not measures of athlete efficiency, and neither requires an independently defined mechanical work input.

Let $F(t)$ denote the paddle-normal force over one stroke of period T_s, and let t_c denote the water-contact (catch) time, identified from the first crossing of the reconstructed paddle-tip elevation through the free surface, $z_{\mathrm{tip}}(t_c^-) > 0 \geq z_{\mathrm{tip}}(t_c^+)$, with a force-threshold crossing at 15% of the peak force used as a fallback when no such crossing is present in the analysed window. Let t_p denote the time of the force peak after contact,

$$t_p = \arg\max_{t \geq t_c} F(t), \qquad F_{\max} = F(t_p), \tag{4.37}$$

and let t_0 denote the end of the drive, defined as the first zero-force crossing after the peak, $F(t_0^-) > 0 \geq F(t_0^+)$.

Timing descriptors. The catch-to-peak time and its expression as a percentage of the stroke period (Galipeau's time-to-peak descriptor, reported here in the phase convention used throughout this thesis) are

$$\Delta t_{\mathrm{peak}} = t_p - t_c, \qquad \tau_{\mathrm{peak}} = 100 \, \frac{\Delta t_{\mathrm{peak}}}{T_s} \ [\%]. \tag{4.38}$$

The paddle-in-water ratio (also used by Galipeau [10]) is the fraction of the stroke period over which the blade carries a non-zero force,

$$R_{\mathrm{water}} = 100 \, \frac{t_0 - t_c}{T_s} \ [\%]. \tag{4.39}$$

Rate descriptors. Gomory's force-development rate is the average slope of the rising force between the 20% and 80% crossings of the peak force, and the force-reduction rate is the corresponding slope on the falling side between the peak and the 20% crossing,

$$\dot{F}_{20\text{–}80} = \frac{0.60 \, F_{\max}}{t_{80} - t_{20}}, \qquad \dot{F}_{20\text{–}0} = -\frac{0.20 \, F_{\max}}{t_0 - t_{20}^{\downarrow}}, \tag{4.40}$$

where t_{20} and t_{80} are the times at which the rising force first reaches 20% and 80% of $F_{\max}$, and $t_{20}^{\downarrow}$ is the time at which the falling force returns to 20% of $F_{\max}$. Both are linear (constant-rate) approximations to a generally nonlinear rise and fall, and are reported in $\mathrm{N\,s^{-1}}$.

Impulse and average-force descriptors. The catch, drive, and propulsive impulses are the time integrals of the force over the corresponding sub-intervals of the stroke,

$$I_{\text{catch}} = \int_{t_c}^{t_p} F(t)\,\mathrm{d}t, \qquad I_{\text{drive}} = \int_{t_p}^{t_0} F(t)\,\mathrm{d}t, \qquad I_{\text{prop}} = \int_{t_c}^{t_0} \max(F(t), 0)\,\mathrm{d}t, \tag{4.41}$$

where I_{prop} clips the integrand to its positive part so that any small negative force interval during catch or exit does not offset the propulsive impulse. The average drive force and Gomory's drive-force quality (the ratio of the average to the peak drive force, bounded between 0 and 1 and largest for a steady, plateau-like force profile) are

$$\overline{F}_{\text{drive}} = \frac{I_{\text{drive}}}{t_0 - t_p}, \qquad Q_{\text{drive}} = \frac{\overline{F}_{\text{drive}}}{F_{\max}}. \tag{4.42}$$

Finally, the impulse rates normalise the drive and propulsive impulses by the full stroke period rather than by the drive duration, giving a cycle-averaged force,

$$i_{\text{drive}} = \frac{I_{\text{drive}}}{T_s}, \qquad i_{\text{prop}} = \frac{I_{\text{prop}}}{T_s}, \qquad f_s = \frac{60}{T_s}\ [\text{strokes min}^{-1}]. \tag{4.43}$$

All of the above are evaluated directly on the raw, un-resampled CFD force history for each case, using the case's own detected t_c, t_p, and t_0, and no descriptor is interpolated onto a common phase grid before these scalar quantities are extracted (see the discussion of Table 5.3 in Section 5.2.2 for why this distinction matters).

Cycle-averaged positive paddle-normal force

The conditional-positive mean force in Equation (4.35) describes the average force only during the portion of the stroke for which $F_z^B > 0$. It therefore does not represent the average positive force over the complete stroke period. A separate cycle-averaged quantity is defined as

$$\overline{F}_{\text{prop}} = \frac{1}{T_s} \int_0^{T_s} \max\big(F_z^B(t), 0\big)\ \mathrm{d}t, \tag{4.44}$$

where T_s is the stroke period. The positive part of the paddle-normal force is integrated over the complete stroke, including the portions for which the blade is out of the water or the force is negative. These portions therefore contribute zero to the numerator while remaining part of the averaging period.

Equation (4.44) is evaluated directly from the raw stroke history. It is not obtained from the stroke descriptors defined in Section 4.5.6, which describe athlete technique rather than cycle-averaged force. When the integration is restricted to the detected catch-to-end-of-drive interval, the corresponding zero-clipped integral gives the propulsive impulse rate i_{prop} defined by Equation (4.43). The two calculations are performed independently and provide a consistency check on the force integration and the identified drive interval.

Hull resistance

The hull simulations use a half-hull computational domain with a symmetry plane. The force reported by the solver therefore represents one half of the physical hull. For forward motion, the solver force is negative when it opposes the direction of travel. The whole-hull resistance is thus defined as

$$R_T = 2\left|F_x^{I,\text{half}}\right|, \qquad Fn = \frac{v_{\text{boat}}}{\sqrt{gL}}, \tag{4.45}$$

where R_T is the whole-hull resistance, Fn is the Froude number, v_{boat} is the prescribed boat speed, $g = 9.81\ \text{m s}^{-2}$, and $L = 10.7507$ m is the hull waterline length.

For the time-dependent oscillating-surge simulations, the instantaneous whole-hull resistance is defined as

$$R_T(t) = -2F_x^{l,\mathrm{half}}(t). \tag{4.46}$$

The negative sign converts the solver convention to a positive resistance for forward motion. The magnitude form in Equation (4.45) is used for the steady resistance results, while Equation (4.46) is used for the time-dependent force history.

Resistance is reported using both dimensional force and nondimensional coefficients. The Reynolds number and reference friction relation are

$$Re = \frac{v_{\mathrm{boat}} L}{\nu}, \qquad C_F^{\mathrm{ref}} = \frac{0.075}{(\log_{10} Re - 2)^2}, \qquad R_F = \frac{1}{2}\rho v_{\mathrm{boat}}^2 S C_F^{\mathrm{ref}}, \tag{4.47}$$

where ν is the kinematic viscosity, C_F^{ref} is the reference friction coefficient, R_F is the corresponding friction resistance, ρ is the water density, and S is the wetted surface area used for the reference calculation.

With

$$Q = \frac{1}{2}\rho v_{\mathrm{boat}}^2 S, \tag{4.48}$$

the reported resistance coefficients are

$$C_T = \frac{R_T}{Q}, \qquad C_F = \frac{R_F}{Q}, \qquad C_R = C_T - C_F, \tag{4.49}$$

where C_T, C_F, and C_R denote the total, reference-friction, and residual resistance coefficients, respectively.

The solver also provides pressure and viscous contributions, allowing the total resistance to be decomposed as

$$R_T = R_P + R_V, \tag{4.50}$$

where R_P and R_V are the pressure and viscous resistance contributions, respectively. The reference friction resistance R_F is distinct from the solver viscous resistance R_V. Consequently, $C_R = C_T - C_F$ is not a nondimensional form of the solver pressure contribution.

These definitions are applied consistently to the steady resistance sweep and the oscillating-surge hull simulations.

4.5.7 Grid-convergence analysis

All simulations use adaptive grid refinement (AGR). Formal grid-convergence analysis is applied only to four-level refinement series for which the reported quantity is appropriate for assessing spatial discretisation. The Type 1 standalone-paddle Euler series satisfies this requirement and is therefore analysed using the grid-convergence index (GCI) procedure described below. The Type 2 boat-alone oscillating-surge k–ω SST series is instead used to assess the sensitivity of the results to grid refinement, without applying the formal GCI procedure.

The Type 2 resistance cases use the same B1 base mesh, hull representation, and AGR formulation, but no separate four-level refinement sequence was generated for the resistance conditions. Formal GCI analysis is therefore not applied to these cases. The Type 1 viscous and Type 3 cases likewise use AGR but do not have the four-level refinement data required for formal grid-convergence analysis.

The uncertainty expressions are defined in Section 3.6.4. For the four-level grid-convergence series, the Hessian threshold is varied while the base mesh, motion, and remaining numerical controls are held fixed. The admissible least-squares fit with the smallest residual scatter is then selected. The detailed least-squares implementation follows Eça and Hoekstra [25].

4.6 CFD workflow automation

The CFD workflow converts the measured paddling motion into reproducible, documented CFD cases. Modular Python scripts automate geometry and motion preparation, mesh generation, hydrostatic evaluation, body and boundary condition definitions, overset interpolation, adaptive grid refinement (AGR), case creation, and post-processing. Changes to input quantities, such as the athlete trajectory, free-surface datum, or mesh-refinement threshold, are therefore propagated consistently through the dependent setup stages without repeating unrelated procedures.

Two complementary approaches were used to generate the CFD cases. Boat-only resistance and oscillating-surge cases were based on projects generated using C-Wizard, with additional FineMarine scripts used to apply settings not exposed through the C-Wizard interface. Standalone-paddle and paddle-hull configuration cases were generated directly using FineMarine and HEXPRESS.

4.6.1 Paddle and paddle-hull configuration cases (Type 1 and Type 3)

The selected analysis configuration defines the geometry, motion data, domain type, flow model, body properties, mesh settings, refinement thresholds, and computational controls. Processed IMU data are converted into prescribed paddle-motion files containing all six degrees of freedom. Where applicable, the corresponding boat surge motion is generated consistently with the selected trajectory-export option.

The background mesh is generated first, together with the required edge, surface, free-surface, and volume-refinement groups. Paddle overset meshes are then generated and assembled with the background domain. The named surfaces defined during CAD preparation are used throughout the setup to apply mesh refinement, define bodies, assign boundary conditions, and prescribe body motion.

For paddle-hull configurations, the hull is positioned consistently with the CFD free-surface datum. With the free surface fixed at $z = 0$, an initial `domhydro` calculation determines the equilibrium draft for the prescribed hull mass. The resulting vertical translation is applied to the hull before the background mesh is regenerated. A final hydrostatic evaluation is then performed on the translated geometry to obtain the hydrostatic and inertial properties used in the dynamic hull-body definition. The mesh, hydrostatic calculation, and body definition therefore use the same vertical reference.

Algorithm 2 summarises the direct workflow.

Algorithm 2 Direct FineMarine/HEXPRESS setup of paddle and paddle-hull configuration cases.

1: Load the selected analysis configuration, geometry paths, motion data, and mesh settings.
2: Validate the selected sweep and AGR-study options.
3: Convert the processed paddle kinematics into FineMarine motion files for all six degrees of freedom, including the vertical-datum transformation.
4: Generate the background mesh and associated edge- and surface-refinement groups.
5: **if** the configuration includes a hull **then**
6: Run `domhydro` to determine the equilibrium draft for the specified hull mass.
7: Apply the resulting vertical hull translation and regenerate the background mesh.
8: Perform a final `domhydro` evaluation to obtain the hydrostatic and inertial properties for the hull body.
9: **end if**
10: Generate the paddle overset mesh and replicate it for additional paddles where required.
11: Assemble the background and overset meshes and link the completed mesh to FineMarine.
12: Define bodies and boundary conditions using the named CADfix surfaces, and assign prescribed motions, solved degrees of freedom, overset treatment, AGR, probes, and solver controls.
13: Create the required motion, AGR, mesh-convergence, or staged acceleration–oscillating-surge computations.
14: Save the FineMarine project and associated mesh, motion, and computation files.

The same setup structure generates standalone-paddle, paddle-hull configuration, and multiple-paddle cases. Refinement and motion studies can therefore be generated from the same geometry, body definitions, and prescribed-motion inputs without manually reconstructing each case.

4.6.2 Boat-only resistance and oscillating-surge cases (Type 2)

Boat-only cases were generated from a C-Wizard resistance template and then completed with FineMarine scripts for settings not exposed directly through C-Wizard. Two workflows were used, namely a calm-water resistance sweep and a transient workflow consisting of an acceleration stage followed by prescribed oscillating surge.

For the transient workflow, the hull first accelerated from rest to the initial speed of the prescribed oscillating-surge law and then followed the periodic surge motion. The complete surge-displacement history was written as a single absolute-time motion file. Restarted computations therefore continued from the same motion history without resetting the surge phase. Surge was prescribed in all boat-only cases and was not solved dynamically.

The resistance workflow generated one C-Wizard computation for each selected speed. The transient workflow generated an acceleration computation followed by a restart computation for each selected AGR refinement threshold. The acceleration calculation used fixed time stepping and ended before the prescribed oscillating-surge interval. Its corresponding restart used Courant-controlled time stepping and continued from the refined mesh produced by the acceleration calculation. Algorithm 3 summarises the procedure.

The procedure generates the required Type 2 computations from the same C-Wizard and FineMarine setup. Changes to the target speed, acceleration law, or AGR threshold can therefore be applied without manually rebuilding the complete case setup.

4.6.3 Execution and automated post-processing

Case-specific solver settings are assigned according to Table 4.10. For restart-based calculations, the workflow creates the required sequence of restarts, carries forward the inherited solution and refinement state, and logs the completion status and final simulated time. Batch-submission scripts execute the configured cases and log convergence information, mesh-motion diagnostics, and overset-interpolation warnings.

Following completion, the force histories are extracted using consistent processing windows for the relevant simulation type. Peak, RMS, impulse, and conditional-positive-mean force measures are then evaluated automatically. The corresponding entry-point, mesh-hydrostatics, and per-computation procedures are given by Algorithms 2 and 3 above.

Algorithm 3 C-Wizard and FineMarine setup of boat-only resistance and oscillating-surge cases.

Load the selected boat geometry, fluid properties, hull mass, mesh settings, AGR settings, solver controls, and prescribed-motion parameters.
Select either the calm-water resistance workflow or the transient acceleration–oscillating-surge workflow.
Validate the selected workflow and refinement settings.
if the calm-water resistance workflow is selected **then**
    Insert the selected speed range into the C-Wizard resistance template.
    Generate the C-Wizard input file and create the FineMarine project.
    for each generated speed computation **do**
        Apply the common box-confined multisurface Hessian AGR definition and selected refinement threshold.
        Apply the selected iteration and residual-reduction controls while preserving the C-Wizard computation duration and output frequency.
    end for
else
    Construct the absolute-time surge motion from a hyperbolic-tangent acceleration stage followed by the periodic oscillating-surge law.
    Write the surge-displacement motion file.
    Determine the acceleration and transient computation durations and their corresponding time-step settings.
    Generate the C-Wizard input file at the hand-off speed and create the FineMarine project.
    for each selected AGR refinement threshold **do**
        if the threshold is the first in the sequence **then**
            Use the C-Wizard computation as the acceleration calculation.
        else
            Duplicate the preceding transient calculation and reset it to uniform initial conditions.
        end if
        Apply box-confined multisurface Hessian AGR with the selected threshold.
        Define the acceleration calculation with fixed time stepping and the prescribed surge motion.
        Create a transient restart from the corresponding acceleration calculation.
        Apply Courant-controlled time stepping to the restart and disable AGR reinitialisation after its first step.
        Continue the same absolute-time surge motion in the restart.
    end for
end if
Save the FineMarine project, C-Wizard input file, motion file, AGR patches, solver-control patches, and all generated computations.

Chapter 5

Results and discussion

This chapter establishes the reconstructed paddle motion as the kinematic input for the CFD calculations and presents results for the standalone-paddle, bare-hull, and paddle-hull configurations. The standalone-paddle and bare-hull cases provide reference blade-load, resistance, and unsteady hull-force results, while the coupled paddle-hull case examines the resulting paddle and hull response when both bodies undergo the prescribed advance motion. Spatial and temporal resolution effects are assessed for the relevant cases, and the final comparisons relate the computed paddle loading to the bare-hull resistance and provide an indicative assessment of the potential for the calculated propulsive force to overcome the hull resistance.

5.1 Reconstructed trajectory and limitations

A periodic six-degree-of-freedom paddle trajectory was reconstructed from the available IMU history and expressed in the boat-aligned CFD frame. The resulting trajectory provides the prescribed paddle motion used in the CFD simulations.

The reconstruction comprised stroke segmentation, phase averaging, integration of the measured motion, selection of the vertical datum, and alignment to the CFD reference frame. The resulting trajectory was checked for cycle-to-cycle repeatability and for consistency after drift correction. These checks establish whether the reconstructed stroke provides a sufficiently repeatable kinematic input for the numerical simulations.

The available camera footage was not sufficient to independently establish the absolute vertical position of the paddle relative to the water surface. The reconstructed motion therefore defines the paddle displacement and orientation, while the absolute vertical datum was determined separately through the CFD calibration described below. In particular, the paddle immersion was prescribed as $z = -0.8$ m in the measurement frame. This datum was selected by comparison with the phase-averaged experimental force and is therefore a calibration choice rather than an independently measured quantity.

Wearable inertial sensing is nevertheless well established for capturing cyclic paddle-sport motion outside the laboratory. Shaft- or paddle-mounted IMUs have been used to identify stroke phase and quantify paddle kinematics in flatwater kayaking [37] and canoeing [38], while hull-mounted accelerometers have been used to recover stroke-cycle kinematics in rowing [39]. These studies support the use of inertial measurements for reconstructing cyclic water-sport motion, although the present application differs in its objective. The reconstructed trajectory is used directly as a continuous, periodic six-degree-of-freedom motion for CFD simulations rather than for stroke classification or athlete performance monitoring.

5.1.1 Raw sensor data, selection, and analysis window

Figure 5.1 shows the raw time histories of paddle-IMU throughout the trial. The right-paddle exhibits smooth, periodic stroke motion, whereas the left-paddle history contains abrupt changes in attitude and

repeated resets. The reconstruction therefore uses the right-paddle history over the marked 25–30 s analysis window.

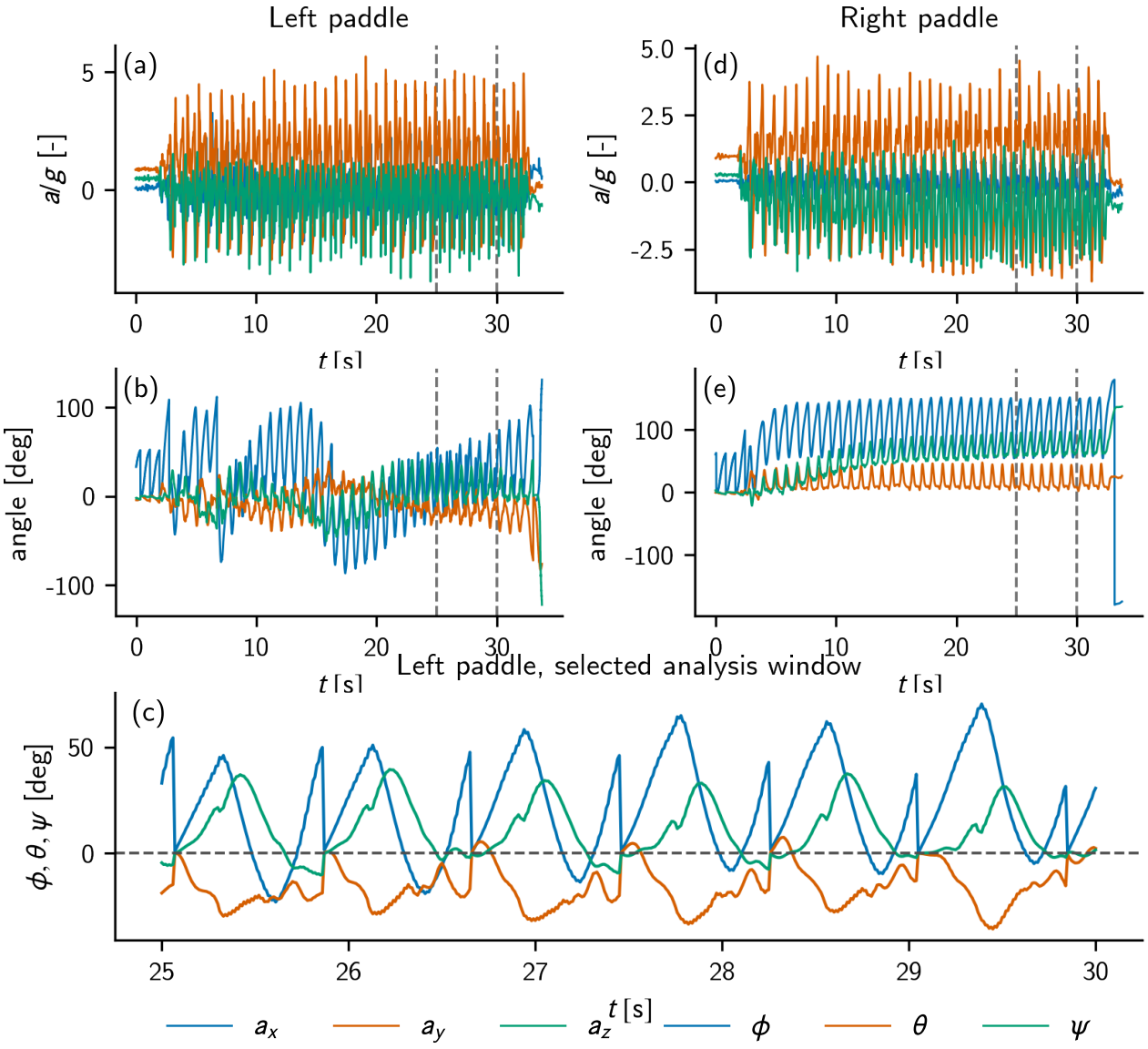

Figure 5.1: Raw paddle-IMU histories and selected analysis window.

The reconstruction uses the 100 Hz Euler-angle channels for paddle attitude. The reduced-rate quaternion output is not used because it is available only at 5 Hz, owing to sensor logging frequency issue.

The right-paddle IMU data remain periodic throughout the selected window. In contrast, the left-paddle data contain anomalous changes in angles and elevated attitude-rate fluctuations. At several points in the trial, the left-paddle roll and pitch angles abruptly return towards zero within one or two samples, rather than following the smooth stroke motion observed on the right paddle. Correspondence with HKUST indicated that a malfunction in the sensor's internal drift-correction algorithm was the underlying cause of these anomalous left-paddle readings (Section 5.1.9). The right-paddle sensor did not exhibit this fault. Appendix B documents the event counts and angle histories. The left sensor exhibited more frequent and larger deviations than the right sensor and was therefore excluded from the kinematic reconstruction. Thus, the present study was unable to perform a comparative assessment of paddling technique.

5.1.2 Phase averaging and numerical integration

The stroke boundaries were defined from the crests and troughs of the angle ϕ signal. For this dataset, the trough corresponds to the highest paddle position above the water, while the crest corresponds to the deepest paddle position in the water. The crests were therefore used as the segmentation criterion for defining individual stroke intervals and reinterpolating the IMU data onto a common sampling grid. Figure 5.2 identifies the five consecutive stroke intervals and the common resampling grid, and only a subset of the resampled points is shown for clarity.

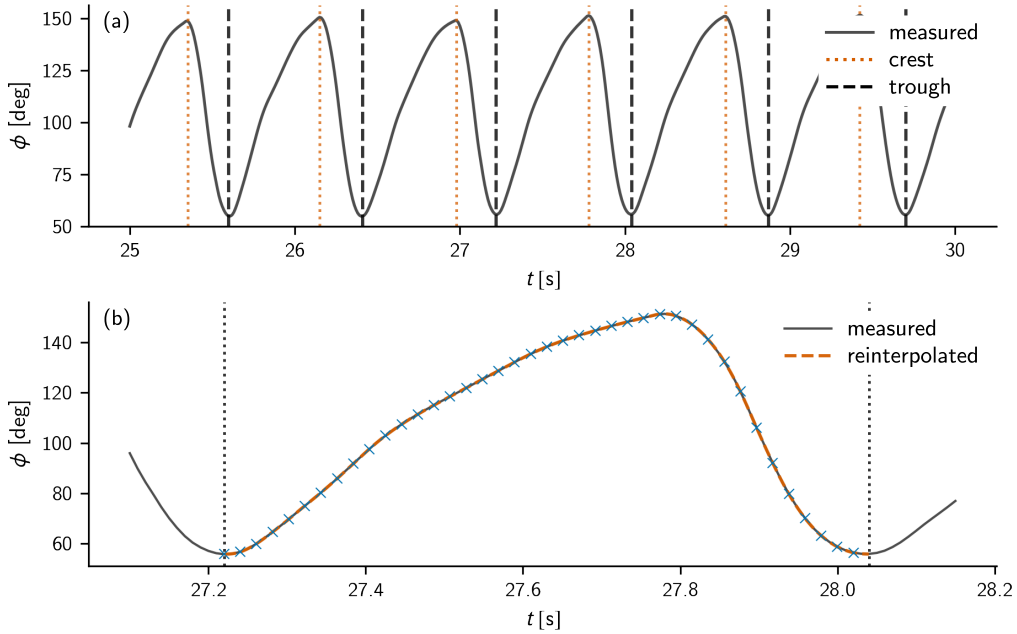

Figure 5.2: Detected stroke boundaries and phase resampling

Figure 5.3 shows the effect of applying a periodic boundary condition to the spline interpolation. Each stroke period was reinterpolated using 1000 equally spaced points. This density was selected to provide sufficient temporal resolution for the small CFD time steps while maintaining a smooth representation of the prescribed paddle motion. A coarser grid would produce a less smooth prescribed trajectory. The lower panel in Figure 5.3 is a magnified view of the corresponding region in the upper panel, highlighting the differences near the stroke-period boundary.

Table 5.1 summarises the resulting stroke statistics. The mean period is 0.820 s with a standard deviation of 0.009 s, while the peak-force coefficient of variation is 5.0%. The period coefficient of variation is 1.1%, comparable to the low cycle-to-cycle timing variability reported for phase-locked IMU segmentation of paddle-sport strokes over similarly short analysis windows [37, 39]. This supports treating the five strokes as repetitions of one underlying cycle rather than as distinct stroke types. The larger 5.0% variation in peak force indicates that load amplitude varies more than stroke timing, consistent with the sensitivity of peak force to small differences in paddle entry and boat motion. The selected window is therefore adequate for constructing one representative cycle, but is too short to characterise athlete-to-athlete or session-to-session variability.

5.1.3 Integrated paddle motion

The acceleration history is integrated in two stages to obtain paddle velocity and displacement. Figure 5.5 shows the resulting integration sequence from acceleration through velocity to displacement.

Double integration of acceleration is sensitive to small measurement biases, which accumulate as drift in the integrated velocity and displacement. Unlike foot-mounted inertial navigation, where zero-velocity

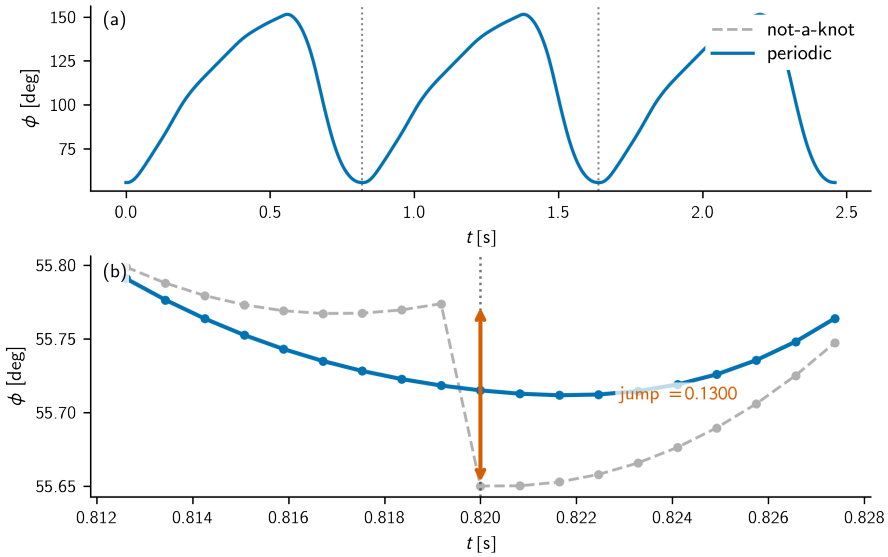

Figure 5.3: Effect of periodic spline interpolation near the stroke-period boundary, with the lower panel showing a magnified view of the stroke boundary.

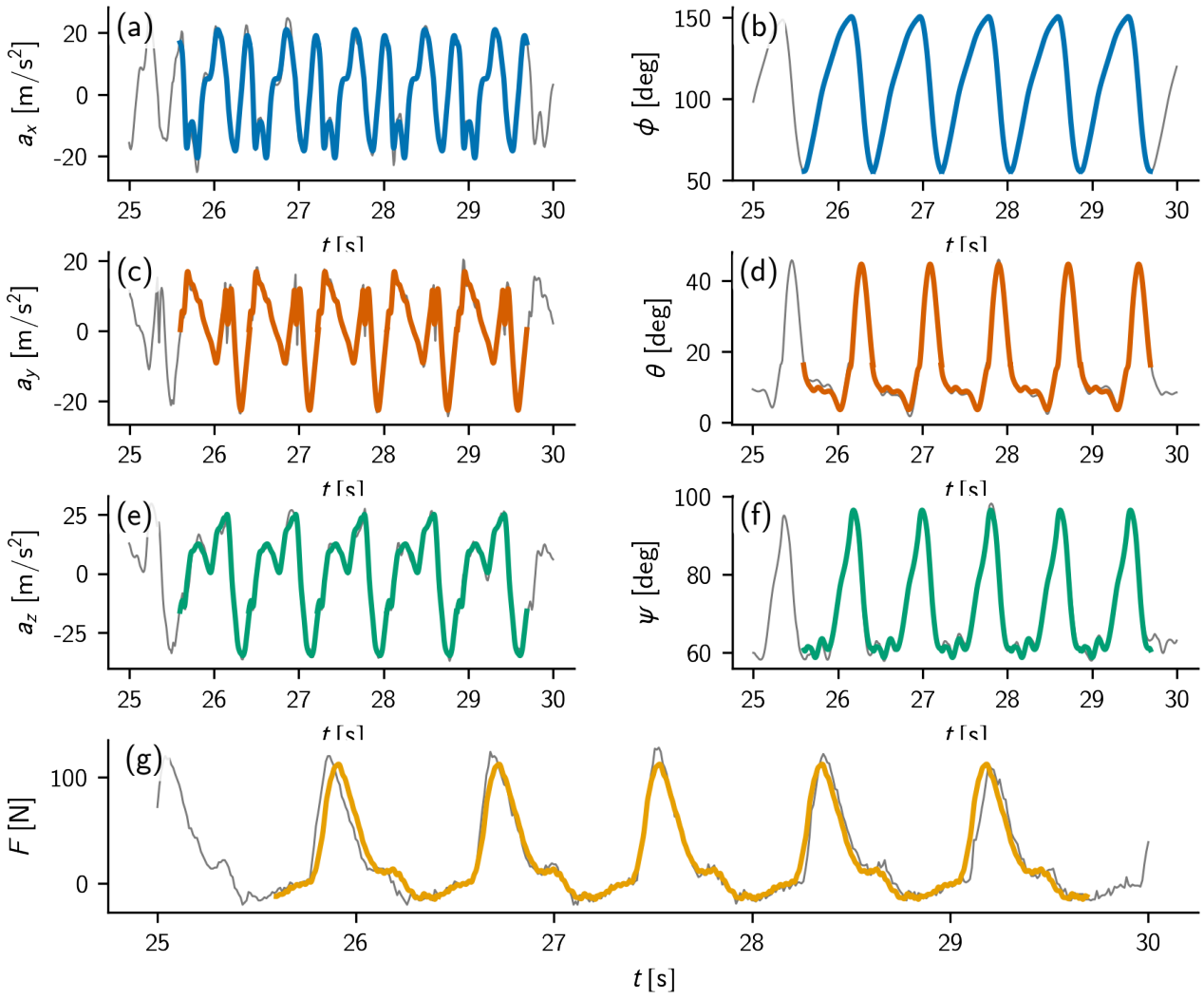

Figure 5.4: Measured and phase-averaged kinematic and paddle-force histories over the five stroke intervals.

Table 5.1: Stroke statistics used to assess the representative cycle.

Stroke	Period [s]	Peak force [N]	
1	0.8100	120.65	
2	0.8100	124.30	
3	0.8200	128.08	
4	0.8300	122.03	
5	0.8300	110.11	
Mean ± std	0.8200 ± 0.0089	121.03 ± 6.01	CV= 5.0%

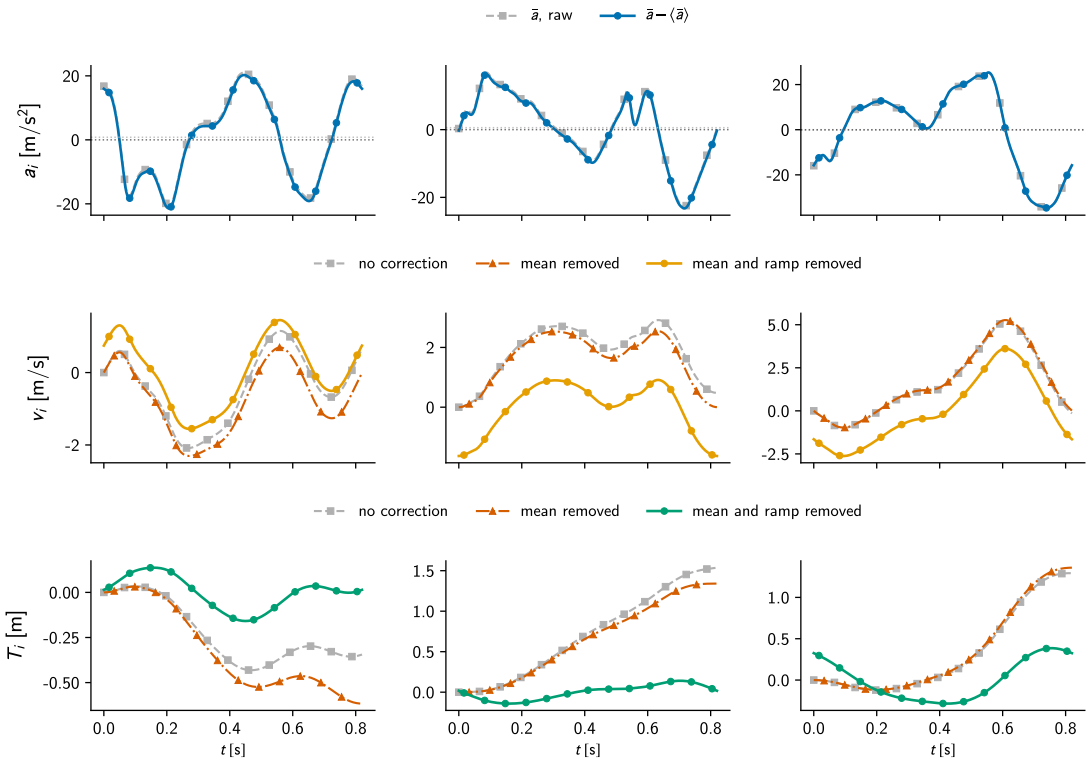

Figure 5.5: Acceleration, velocity, and position integration stages.

updates can reset the integration during known stationary periods, a paddle stroke contains no equivalent interval of zero velocity [40]. The present reconstruction therefore uses the periodicity of the stroke as the kinematic constraint. Velocity and displacement are required to return to consistent values at the beginning and end of each cycle. A linear correction is applied to the integrated velocity so that $v^c(t_0) = v^c(t_1) = 0$ at the cycle boundaries, with the corresponding correction propagated to displacement. The resulting uncertainty is quantified in Section 5.1.8.

Figure 5.6 shows the phase-averaged velocity and displacement after this endpoint-drift correction. The reconstructed motion therefore defines the paddle displacement relative to the selected cycle boundaries.

5.1.4 Immersion-depth calibration

The reconstructed motion gives relative paddle displacement but not its absolute height above the water, for the camera-coverage reasons noted in Section 5.1. A vertical datum was therefore prescribed for the CFD calculation and assessed against the phase-averaged experimental force.

Candidate vertical offsets were evaluated in the Type 1 CFD configuration. The selected datum, $z_{\mathrm{fs}} = -0.8$ m in the measurement frame, produced the closest peak paddle-normal force to the phase-averaged measurement. The sensitivity cases were used only to establish this working datum and were

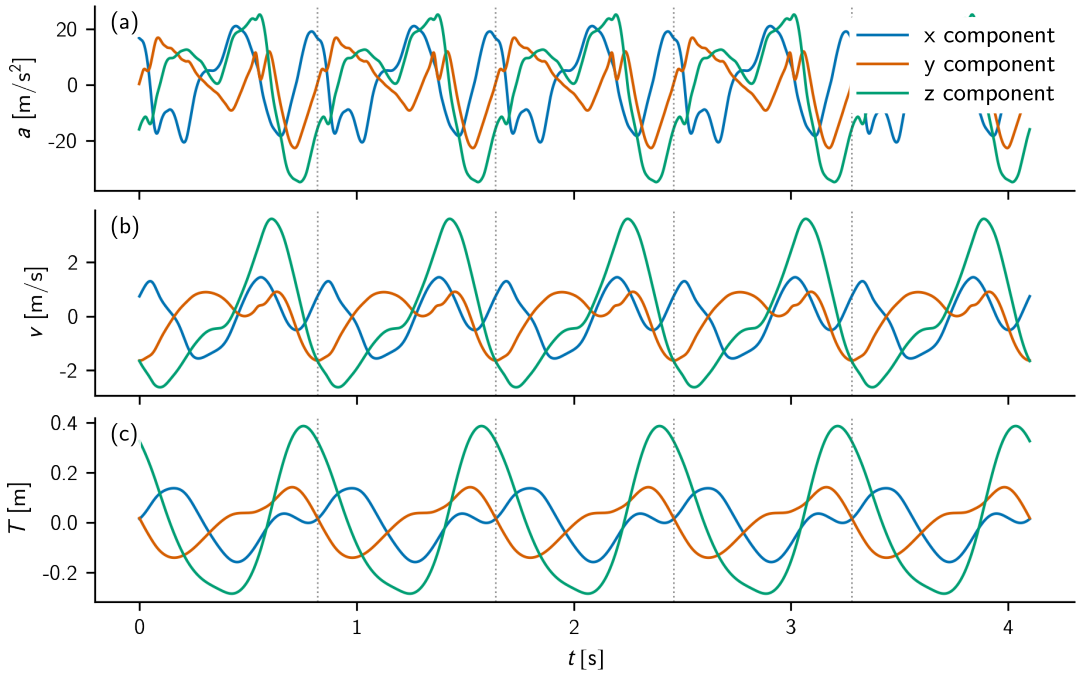

Figure 5.6: Phase-averaged paddle velocity and displacement after endpoint-drift correction.

not intended as an investigation of paddle hydrodynamics.

Figure 5.7 shows the force comparison and the corresponding reconstructed paddle-tip elevation for the selected datum. The corresponding sensitivity values are reported in Table 5.2.

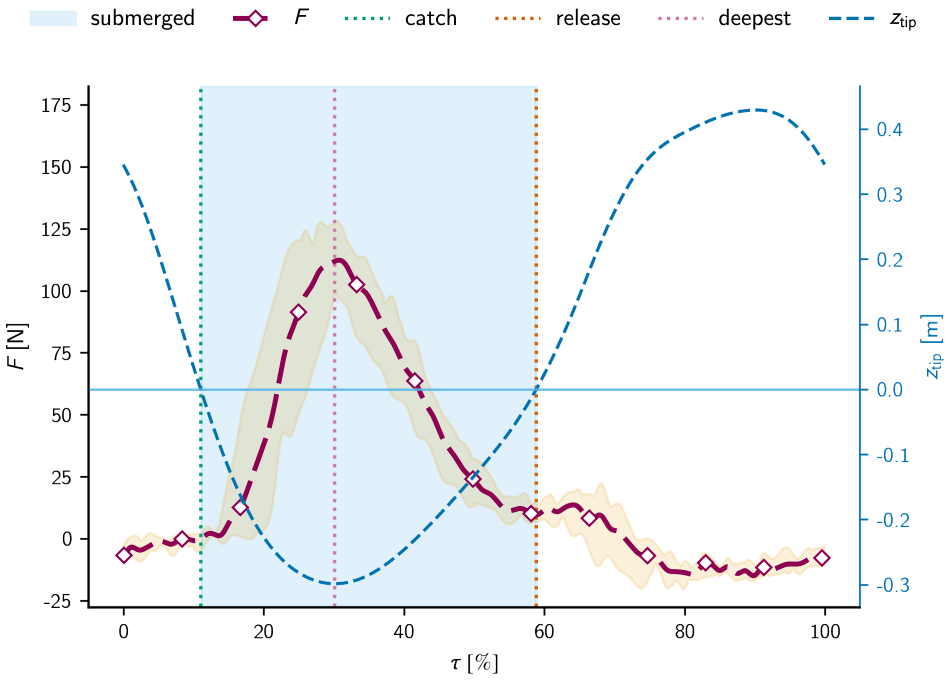

Figure 5.7: Phase-averaged paddle force and reconstructed paddle-tip elevation for the selected vertical datum.

The comparison provides calibration support for the selected vertical datum, not independent validation, because the same experimental force measurement was used to select the datum. After applying the selected vertical datum, the free surface is defined as $z_{fs} = 0$. The maximum tip immersion is 0.2988 m,

Table 5.2: Peak paddle-normal force at $z_{fs} = -0.80$ m across the tested advance-speed range, one settled stroke, versus the measured PaddleMate peak.

Case	Condition	Speed	z_{fs} [m]	Peak force [N]
PaddleMate (measured)	measured	-	-	112.4
advance 10-12 kph, z=-0.80 m (2-stroke export)	advancing	10-12 kph	-0.80	198.0
inflow, 12 kph, z=-0.80 m	inflow	12 kph	-0.80	87.5
advance 9-10 kph, z=-0.80 m	advancing	9-10 kph	-0.80	152.7
advance 10-11 kph, z=-0.80 m	advancing	10-11 kph	-0.80	134.0
advance 11-12 kph, z=-0.80 m	advancing	11-12 kph	-0.80	115.1
advance 10-12 kph, z=-0.80 m	advancing	10-12 kph	-0.80	155.4

with catch and release occurring at $\tau = 11.0\%$ and 58.8% of the stroke, respectively.

5.1.5 Heading correction and reference alignment

The reconstructed motion is initially expressed in the earth-fixed reference frame. The boat heading obtained from the GPS data was approximately 22° from north and was used to establish the orientation of the boat reference. The reconstructed paddle trajectory, however, remained offset from the boat by an approximately constant yaw angle. An additional rotation of 103° about the vertical axis was therefore applied to the paddle trajectory to align it with the boat. This yaw offset was subsequently confirmed by HKUST to have resulted from the sensor mounting. The resulting motion was then expressed in the boat-aligned CFD frame. Figure 5.8 defines the earth-fixed and boat-aligned frames and the associated transformation, consistent with the boat-aligned ISIS-CFD frame convention established in Section 3.2 and Figure 3.1.

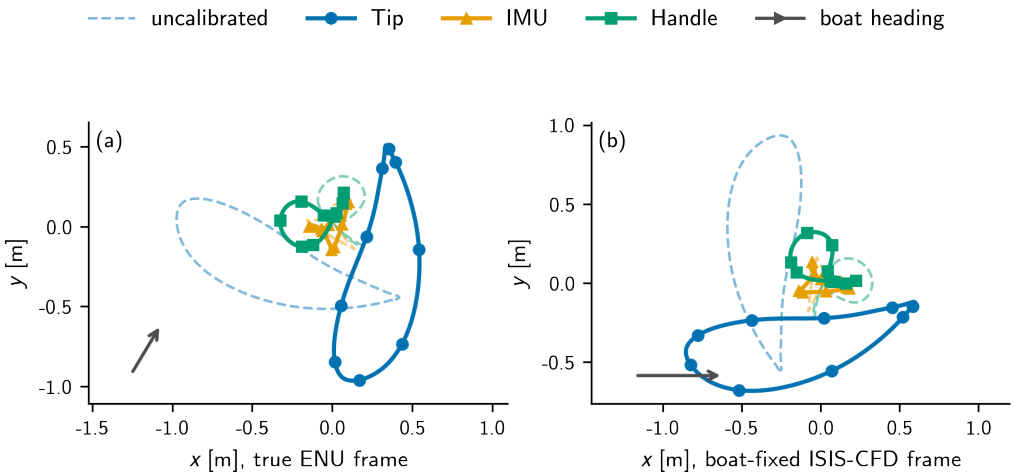

Figure 5.8: Earth-fixed and boat-aligned frames used for the heading correction.

5.1.6 Boat-speed and paddle-motion representation

The boat translation and prescribed paddle motion are defined from the processed experimental data. The boat translation is prescribed using the oscillating-surge law defined in Equation (4.16), with the velocity parameters based on the same calibration adopted for the vertical-datum sensitivity analysis. Figure 5.9 compares the prescribed velocity law with the GPS-derived PaddleMate boat speed over the trial and

selected analysis window. The prescribed paddle motion is obtained from the reconstructed six-degree-

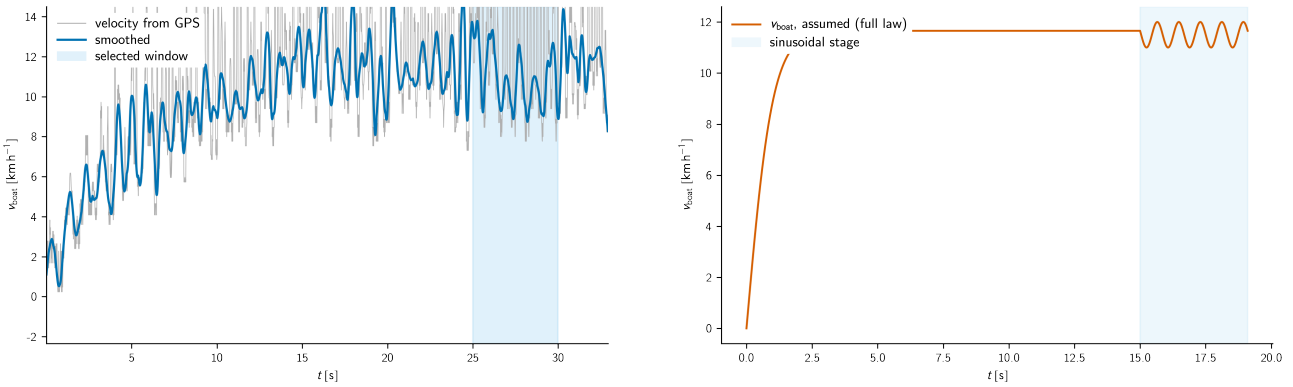

(a) GPS-derived boat speed. **(b)** Prescribed oscillating-surge velocity law.

Figure 5.9: Boat speed history and prescribed oscillating-surge velocity law.

of-freedom trajectory described in the preceding sections. Following the heading correction, the paddle is positioned relative to the boat using the prescribed lateral offset. Figure 5.10 shows the resulting paddle trajectory relative to the boat in the earth-fixed (ENU) and boat-aligned CFD frames.

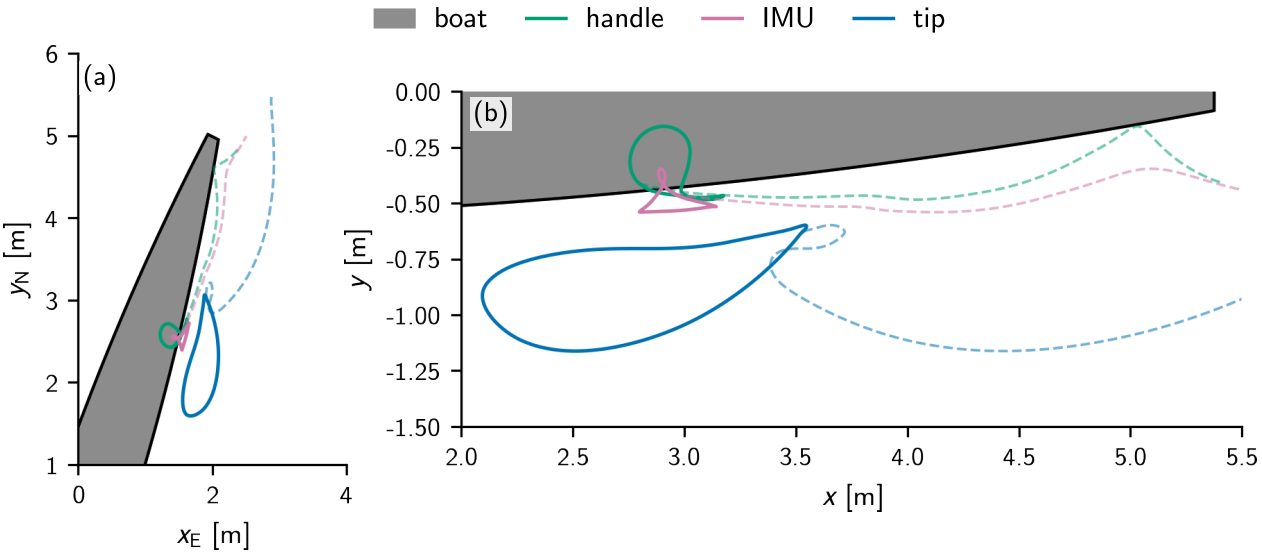

Figure 5.10: Paddle trajectory relative to the boat. Dashed lines indicate the paddle trajectory during boat advance.

5.1.7 CFD-ready trajectory and vertical datum

The final trajectory is exported as prescribed six-degree-of-freedom motion for the Type 1 and Type 3 simulations. The measurement-frame free-surface datum is $z_{fs}^{IMU} = -0.8$ m, while the CFD free-surface datum is $z_{fs}^{CFD} = 0$. The corresponding vertical translation is

$$T_z^{CFD} = T_z^{IMU} + z_{fs}^{CFD} - z_{fs}^{IMU}. \tag{5.1}$$

For Type 3, the same prescribed six-degree-of-freedom paddle motion is applied relative to the advancing boat domain.

Figures 5.11 and 5.12 show the final paddle placement relative to the free surface and hull.

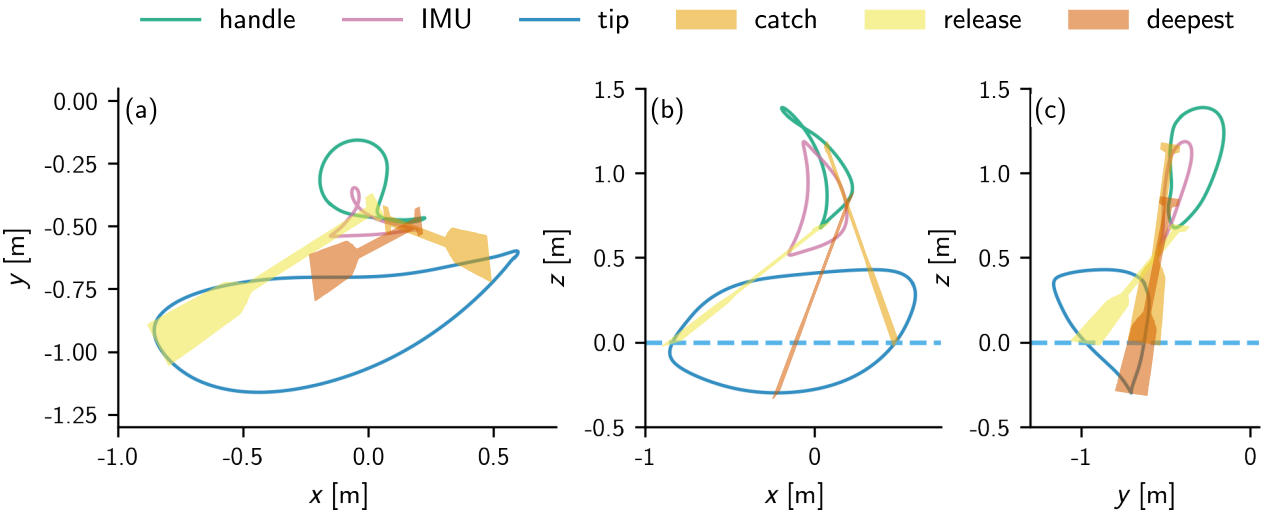

Figure 5.11: Paddle trajectory relative to the free surface and boat reference.

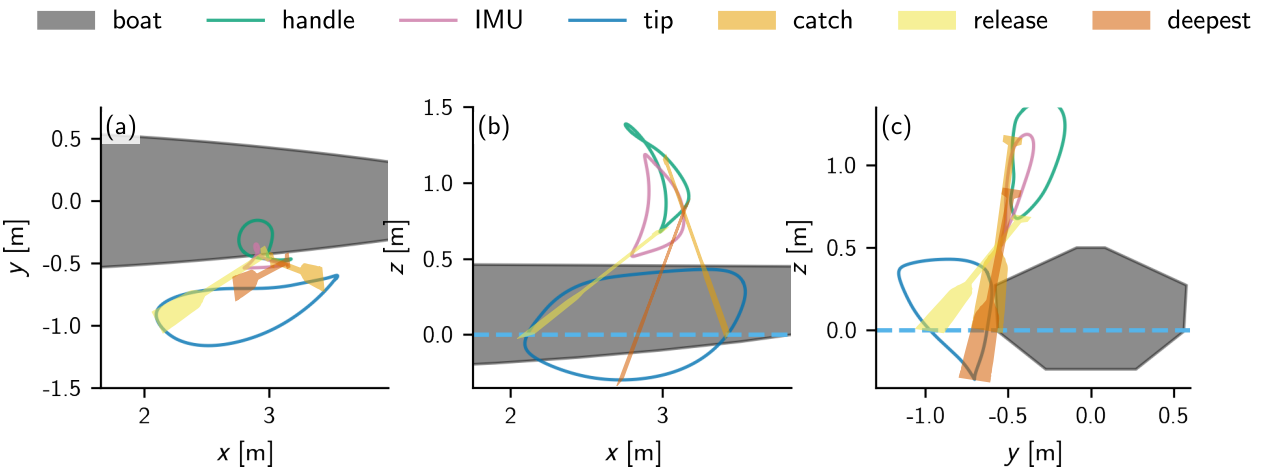

Figure 5.12: Paddle trajectory relative to the boat, showing zero relative translational velocity between the paddle and hull.

5.1.8 Uncertainty in the reconstructed trajectory

The reconstructed trajectory should be interpreted as a calibrated CFD input rather than as an independently measured paddle path. The vertical datum is determined by force matching (Section 5.1.4), whereas the uncertainty considered here arises from sensor noise and its propagation through the double-integration procedure. These are distinct sources of uncertainty. Sensor noise affects the reconstructed relative motion, while the absolute vertical position remains dependent on the selected calibration datum. The full derivation is given in Appendix E, Section E.1 (Equations (E.1)–(E.11)). Only the resulting bounds are evaluated here.

Attitude uncertainty arising from gyroscope and accelerometer noise propagates through the Euler-angle solution according to Equation (E.1). For the WITMOTION WT9011DCL-BT5.0 sensor, the manufacturer specifications give $\sigma_g \approx 0.05^\circ\,\mathrm{s}^{-1}$ and $\sigma_a \approx 0.005\,g$, together with quoted static accuracies of 0.05° for roll and pitch and 1° for yaw after magnetic calibration.

For trapezoidal integration of a noisy acceleration signal, the unconstrained velocity and position errors increase approximately as $\sigma_v \propto n^{1/2}$ and $\sigma_x \propto n^{3/2}$ over an N-sample stroke, as given by Equations (E.4)

and (E.8). The periodic endpoint correction used in the reconstruction limits this growth. The corrected velocity satisfies

$$\sigma_v^c(n) \leq 2\,\sigma_v(N), \qquad 0 \leq n \leq N, \tag{5.2}$$

according to Equation (E.11). Applying the same construction to the position integral gives

$$\sigma_x^c(n) \leq 2\,\sigma_x(N). \tag{5.3}$$

These bounds are imposed once per stroke by the endpoint correction and are not obtained by adjusting the trajectory to the noise model.

Numerical bound for the representative stroke

The mean stroke period of 0.820 s corresponds to approximately $N = 82$ samples at the 100 Hz sampling rate. Using $\sigma_a \approx 0.005\,g \approx 0.049\ \mathrm{m\,s^{-2}}$ and $\Delta t = 0.01$ s in Equations (E.4) and (E.8) gives

$$\sigma_v(N) \approx 4.4\ \mathrm{mm\,s^{-1}}, \qquad \sigma_x(N) \approx 2.1\ \mathrm{mm}.$$

The corresponding endpoint-corrected bounds are therefore

$$\sigma_v^c \leq 8.9\ \mathrm{mm\,s^{-1}}, \qquad \sigma_x^c \leq 4.2\ \mathrm{mm}$$

within one stroke.

The position bound is approximately 1.4% of the reconstructed maximum paddle-tip immersion of 0.2988 m. Thus, for the present reconstruction, double-integration noise is small compared with the uncertainty associated with the absolute vertical datum. The latter cannot be reduced by refining the integration procedure because the available measurements do not establish the paddle height relative to the free surface. An independent measurement of paddle position and free-surface elevation would be required to resolve this uncertainty.

5.1.9 Limitations of trajectory reconstruction and experimental requirements

The reconstructed motion provides the relative paddle displacement and orientation over a stroke, but not its independently measured absolute position relative to the free surface. The selected datum, $z_{\mathrm{fs}} = -0.8$ m, is therefore based on calibration rather than an independent measurement of paddle immersion.

The reconstruction also relies on the right-paddle IMU. The left-paddle history contains anomalous pitch behaviour and attitude-rate glitches relative to the right-paddle history (Figures B.8 and B.9). These measurements were therefore excluded from the CFD kinematic input. Post-experiment investigation by HKUST identified a malfunction in the sensor's internal drift-correction algorithm as the source of the anomalous angle measurements observed for the left IMU. The right IMU did not exhibit this behaviour, but its yaw reference was found to be miscalibrated. Although the sensors had been calibrated before the trial, the calibration was not verified at the time of data collection. HKUST subsequently confirmed that the yaw offset in the right IMU was attributable to the sensor mounting.

As noted in Section 5.1.4, the camera footage could not resolve the paddle–water interface well enough to check this height independently. A repeat experiment should therefore include at least two calibrated cameras positioned at non-collinear viewing angles, with hardware-synchronised timing with the IMU and force measurements, enabling an independent three-dimensional reconstruction of the paddle trajectory and an independent check of the prescribed paddle motion.

Boat motion should also be measured independently using a boat-mounted GNSS/INS system providing surge, heading, heave, and pitch on the same time base as the paddle measurements, removing the need for the manually selected heading correction and separating paddle motion from boat motion. The instantaneous free surface should likewise be measured in the camera views or with synchronised level sensors near the paddle, so that immersion depth is measured directly rather than inferred from CFD force

matching. The force measurements also need an independent calibration procedure. Repeating the experiment with verified paddle sensors and multiple athletes separates sensor uncertainty from stroke-to-stroke and athlete-to-athlete variability. Together, these additional measurements supply independent kinematic, immersion, and force data, allowing the CFD force predictions to be evaluated against experimental measurements that are not used to define the paddle kinematics or immersion, giving a more rigorous validation of the predicted hydrodynamic loads. The additional measurements could be incorporated directly into the trajectory-processing framework developed in this study, preserving the established methodology while providing a more robust experimental basis for the prescribed CFD kinematics.

5.2 Type 1 simulations: CFD of paddle

This section presents and discusses the CFD results for the standalone paddle before the hull is introduced. The results first characterise the flow development and free-surface response associated with the prescribed paddle motion, followed by an assessment of the paddle-normal force in relation to the paddle kinematics, immersion, and wetted area. The calculated paddle-normal force is compared with the phase-averaged experimental force, and the viscous and inviscid formulations are compared to quantify the influence of viscous stresses and establish the hydrodynamic model adopted for the subsequent paddle-hull simulations. The force–acceleration phase relationship is then examined to give a physical, added-mass-based account of the observed force fluctuations. The selected inviscid formulation is next assessed for sensitivity to spatial discretisation through a four-level grid-convergence study, after which the same standalone-paddle results are re-expressed through the literature stroke descriptors of Gomory and Galipeau. Together, these results provide the physical basis for interpreting the paddle force, establish the flow model selection, and quantify the numerical uncertainty associated with the standalone-paddle predictions before the coupled paddle-hull configuration is considered.

5.2.1 Free-surface and wake development

The evolution of the free surface and the wake generated by the paddle is examined at four phases of the standalone-paddle stroke, as shown in Figure 5.13. The results are computed with the Euler formulation at the reference grid resolution $T_{rH}/L = 0.20$ (case 1, Table 4.10). Side and oblique three-dimensional views are presented to illustrate the development of the flow from paddle entry, through the immersed drive phase, and into paddle extraction.

At $\tau \approx 20\%$, after the catch at $\tau = 11.0\%$, the blade is immersed and its interaction with the surrounding water produces a localized deformation of the free surface. The initial disturbance is concentrated around the blade and is associated with the displacement and acceleration of water as the paddle enters the active part of the stroke. This deformation creates the conditions for air entrainment near the blade and the initial development of the paddle wake.

At $\tau \approx 35\%$, the paddle is within the drive phase and a more distinct wake has developed behind the blade. The free-surface disturbance becomes more pronounced and extends over a larger region around and downstream of the paddle. The deformation of the free surface around the blade is accompanied by air entrainment, indicating the development of ventilation during the drive phase.

At $\tau \approx 50\%$, the paddle remains within the drive phase and the wake extends farther downstream. The free surface around the blade remains strongly deformed, with ventilation persisting as the paddle continues to displace and accelerate the surrounding water. The wake and free-surface disturbance extend well beyond the immediate vicinity of the blade.

At $\tau \approx 65\%$, after the release at $\tau = 58.8\%$, the blade is undergoing extraction from the water. The direct interaction between the paddle and the surrounding water decreases as the immersed blade area is reduced. Nevertheless, the wake generated during the drive phase remains clearly visible downstream, together with the residual free-surface deformation and ventilation around the extracting blade. The disturbed free surface and entrained air therefore remain present during the early extraction phase..

The four phases were selected from the CFD results available at 5% phase intervals. The first three phases lie within the catch-to-release interval identified in Section 5.1.4, whereas the final phase represents the early extraction period. These phases provide an overview of the formation, development, and persistence of the paddle-induced wake and free-surface disturbance throughout the active part of the stroke.

The wake generated by the paddle travels downstream, however, because the AGR was confined to a box surrounding the paddle (Figure 4.10), the wake eventually exits the refined region and is subsequently damped as it propagates into the coarser mesh. The implications of this effect are discussed further in comparison with the paddle–hull configuration in Section 5.4.

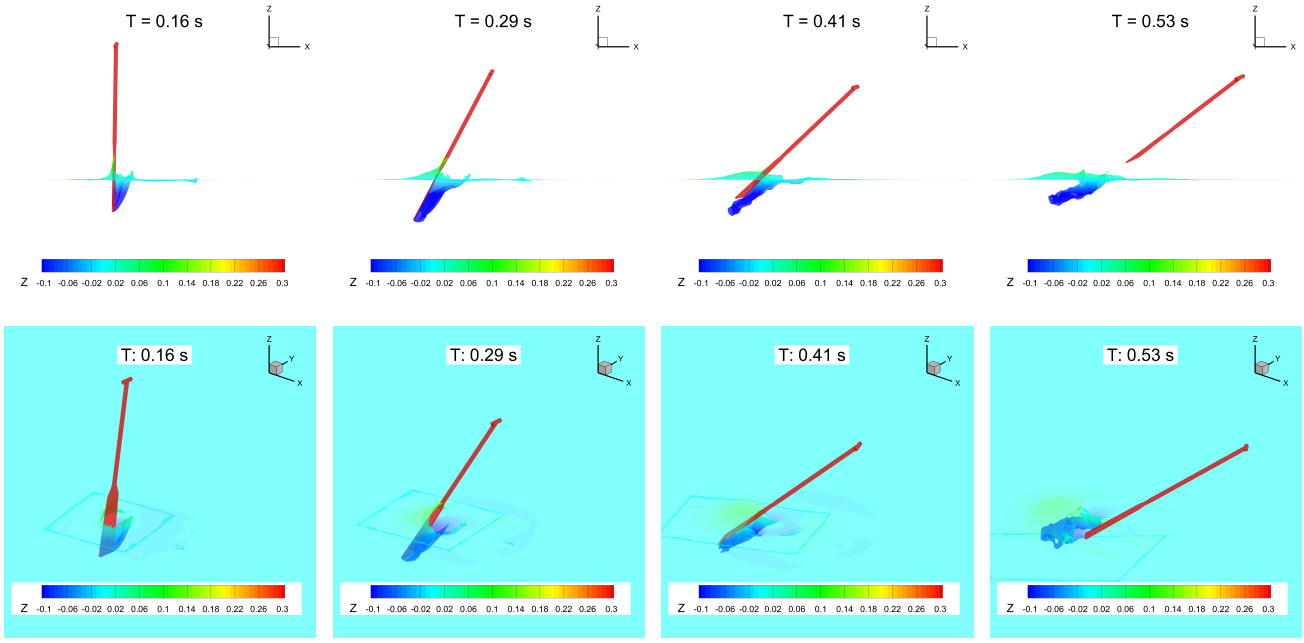

(a) $\tau \approx 20\%$ **(b)** $\tau \approx 35\%$ **(c)** $\tau \approx 50\%$ **(d)** $\tau \approx 65\%$

Figure 5.13: Standalone-paddle free-surface elevation at four stroke phases. Each column shows the side view above the oblique three-dimensional view. The free surface is colored by its elevation.

Figure 5.14 illustrates the adaptive grid refinement (AGR) for the standalone-paddle configuration using a refinement threshold of 0.20. The side view shows the overset grid surrounding the paddle and its interaction with the background mesh, with locally increased resolution around the moving blade and the overset-grid interface. The top view shows the refinement generated in the free-surface region, where the mesh adapts to resolve the evolving interface and the paddle-induced flow structures. In both views, the refinement remains concentrated in regions of strong solution gradients, while progressively coarser cells are retained away from the paddle and the disturbed free surface. This localized refinement provides increased spatial resolution in the regions governing the paddle hydrodynamics without requiring a uniformly fine mesh throughout the computational domain.

5.2.2 Standalone paddle force, kinematic response, and turbulence modeling

The standalone-paddle analysis considers the paddle-normal force obtained from the experimental measurements and CFD post-processing. Both the viscous and Euler cases discussed in this section are run at the reference grid resolution $T_{rH}/L = 0.20$ (cases 1 and 5, Table 4.10), with the effect of further spatial refinement addressed separately in Section 5.2.4. The measured paddle kinematics are prescribed identically in the viscous and Euler simulations, so the paddle trajectory, immersion, entry phase, and extraction phase are the same in both calculations. This allows differences between the two numerical force histories to be attributed to the turbulence model.

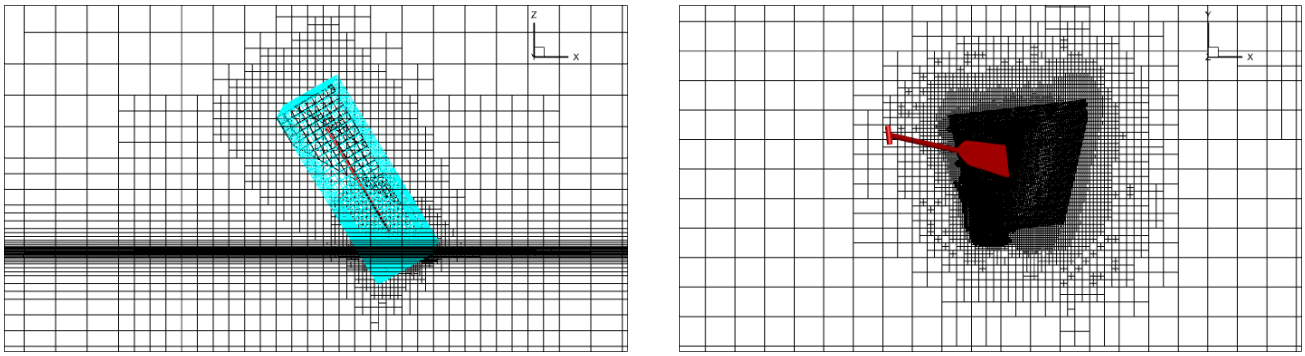

(a) Overset grid (x–z view). **(b)** Free surface (top view).

Figure 5.14: AGR for the standalone-paddle configuration.

The instantaneous wetted area $S_w(t)$ is examined together with the force histories to relate the hydrodynamic loading to the portion of the blade in contact with the water. The paddle-tip elevation z_{tip} is used separately to identify the geometric entry and extraction phases, while the linear and angular accelerations are considered later to examine the relationship between the prescribed paddle motion and the force response.

Figure 5.15 compares the experimentally measured paddle-normal force with the viscous (k–ω SST) and Euler CFD predictions, together with the corresponding wetted-area histories. During paddle entry, the wetted area increases rapidly as a progressively larger portion of the blade becomes submerged. The paddle-normal force increases concurrently and reaches its maximum during the early part of the immersed drive phase.

The viscous and Euler force histories are very similar during the initial loading phase and both reproduce the principal rise and peak observed experimentally. After the force maximum, the computed force decreases while the wetted area continues to increase and reaches its maximum later in the stroke. The maximum force therefore does not coincide with the maximum wetted area. This indicates that the instantaneous paddle-normal load is not governed by wetted area alone, but also depends on the translational and rotational motion of the blade and the associated unsteady response of the surrounding fluid.

During the later part of the drive, larger differences develop between the viscous and Euler force histories. The corresponding wetted-area histories also diverge, despite the identical prescribed paddle trajectory and immersion. The difference in $S_w(t)$ therefore reflects differences in the free-surface and local flow response predicted by the two flow models. As the paddle approaches release, the wetted area decreases and eventually returns to zero. The CFD predicted force decreases correspondingly, whereas the experimental force exhibits a broader decay and remains higher over part of the late-drive and release phases.

The same standalone-paddle calculations are also used to determine whether the viscous formulation is required for the subsequent paddle-hull simulations. Both calculations use the same prescribed paddle trajectory, immersion, translational and rotational kinematics, advance velocity, computational mesh, and numerical setup. The principal difference is therefore the inclusion or omission of viscous stresses.

The quantitative comparison is based first on the peak and RMS paddle-normal forces. For viscous and inviscid force histories $F_v(\tau)$ and $F_i(\tau)$,

$$\Delta_{\text{peak}} = 100\frac{|F_{v,\max} - F_{i,\max}|}{F_{i,\max}}, \qquad \Delta_{\text{RMS}} = 100\frac{|F_{v,\text{RMS}} - F_{i,\text{RMS}}|}{F_{i,\text{RMS}}}. \tag{5.4}$$

A phase-resolved comparison is additionally obtained from

$$\delta(\tau) = \frac{|F_v(\tau) - F_i(\tau)|}{F_{i,\max}}, \qquad \overline{\delta}_m = \frac{1}{N_m}\sum_{\tau \in \text{bin } m} \delta(\tau). \tag{5.5}$$

The stroke is divided into ten successive 10% phase intervals. This metric distinguishes differences

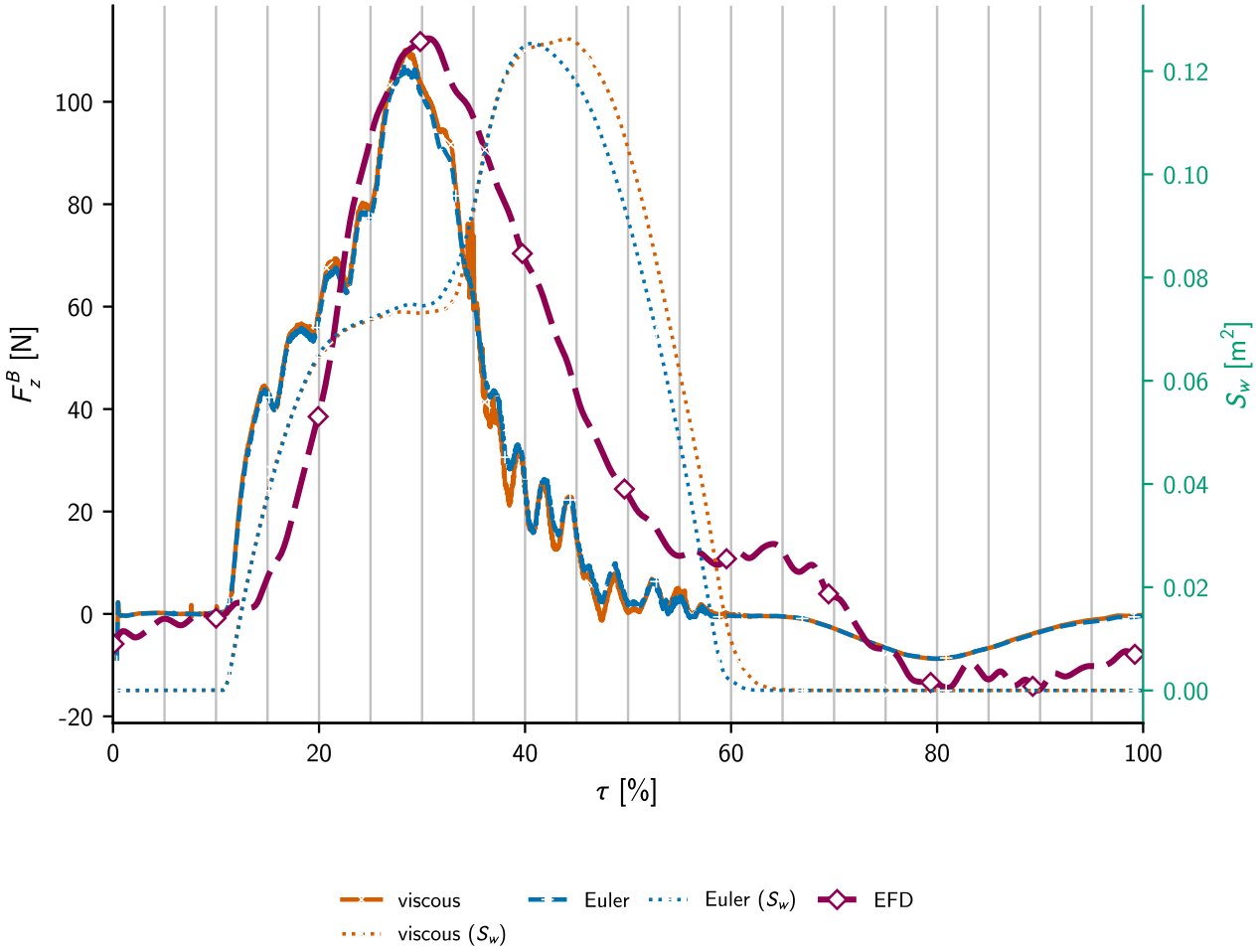

Figure 5.15: Paddle-normal force (dashed lines) and instantaneous wetted area (dotted lines) as functions of stroke phase for the viscous and Euler simulations, together with the experimentally measured force. Force is shown on the primary vertical axis and wetted area S_w on the secondary vertical axis.

concentrated within a particular part of the stroke from systematic differences in the overall force magnitude.

The direct viscous contribution is also evaluated from the force decomposition provided by the solver,

$$\Gamma_v(\tau) = \frac{F_{z,V}^B(\tau)}{F_z^B(\tau)}. \tag{5.6}$$

where $F_{z,V}^B$ is the viscous contribution to the paddle-normal force and F_z^B is the corresponding total force in the viscous calculation. The quantity Γ_v therefore provides a direct measure of the contribution of viscous stresses to the total paddle-normal load.

Table 5.3: Viscous-versus-Euler comparison over the first stroke.

Metric	Euler	Viscous	Difference [%]
Peak F_z^B [N]	107.249	110.190	2.74
RMS F_z^B [N]	37.232	37.808	1.55

The viscous k–ω SST calculation is treated as the reference because it retains both pressure and

viscous contributions to the hydrodynamic load. During the catch and the initial rise towards peak force, the two numerical solutions remain very close. The maximum paddle-normal force is 107.2 N for the Euler calculation and 110.2 N for the viscous calculation, corresponding to a difference of only 2.74%. The RMS force differs by 1.55%, as shown in Table 5.3. The corresponding catch-to-peak phases are also very similar, occurring at 17.32% and 17.64% of the stroke for the Euler and viscous calculations, respectively.

Larger differences occur during the subsequent drive phase. The phase-resolved metric defined by Equation (5.5) reaches its maximum between 30% and 40% of the stroke. Over the complete drive interval, the mean paddle-normal force is 37.4 N for the Euler case and 47.4 N for the viscous case, corresponding to a difference of approximately 27%. This difference is substantially larger than either the peak-force or RMS-force difference and therefore cannot be represented adequately by global force measures alone.

Part of this difference is associated with the wetted-area histories. Although the geometric immersion and prescribed paddle motion are identical, the duration for which the calculated wetted area remains non-zero differs between the two simulations. The reported in-water duration is defined from the interval for which $S_w > 0$ and is therefore a wetted-duration metric, rather than a measure of geometric paddle immersion. Using this definition, the wetted duration is 36.3% of the stroke period for the viscous calculation and 43.0% for the Euler calculation.

Despite this difference in wetted duration and mean force, the integrated propulsive impulses are nearly identical, 16.21 N s for the viscous calculation and 16.36 N s for the Euler calculation, corresponding to a difference of approximately 0.9%. A similar total impulse is therefore accumulated in both cases, while its distribution over the stroke differs. Because the mean drive force is evaluated over the interval of non-zero wetted area, the shorter wetted duration in the viscous case produces a higher mean drive force. The corresponding drive-force quality is 0.430 for the viscous calculation and 0.348 for the Euler calculation.

The comparison therefore shows that the choice of viscous or Euler formulation has only a small influence on the peak paddle-normal force, RMS force, and integrated propulsive impulse, while larger differences occur locally during the drive phase. The close agreement in peak force and impulse indicates that the overall paddle-normal loading is governed primarily by pressure and unsteady inertial effects, consistent with the oar-blade results of Leroyer et al. [3] and the modelling discussion of Robert et al. [5]. Viscous effects remain measurable, particularly in the phase-resolved force and wetted-area response, but their contribution to the overall loading is comparatively small. On this basis, the Euler formulation is selected for the subsequent paddle-hull simulations, providing a reduced computational model while retaining the dominant hydrodynamic loading characteristics observed in the standalone-paddle analysis.

5.2.3 Discussion of the force–acceleration phase relationship

The normalised hydrodynamic force, linear acceleration, and angular acceleration of the paddle are compared over one stroke in Figure 5.16. Each quantity is normalised by its own maximum, so the figure is intended to compare their relative timing rather than establish a quantitative force–acceleration relationship. This subsection interprets these temporal relationships in the context of the unsteady, added-mass component of the hydrodynamic load and quantifies where the force and angular-acceleration fluctuations coincide and where they do not.

Kinematic origin of the coupling

The paddle is a rigid body that translates and rotates simultaneously. The acceleration of a material point P on the paddle, located at $\mathbf{r}_P$ relative to a body-fixed reference point, is

$$\mathbf{a}_P = \mathbf{a}_O + \boldsymbol{\alpha} \times \mathbf{r}_P + \boldsymbol{\omega} \times (\boldsymbol{\omega} \times \mathbf{r}_P)\,, \tag{5.7}$$

where $\mathbf{a}_O$ is the acceleration of the reference point, $\boldsymbol{\omega}$ and $\boldsymbol{\alpha}$ are the paddle's angular velocity and angular acceleration, and the last term is the centripetal contribution. Equation (5.7) shows that the local fluid acceleration relative to the paddle surface (the quantity that sets the instantaneous added-mass reaction)

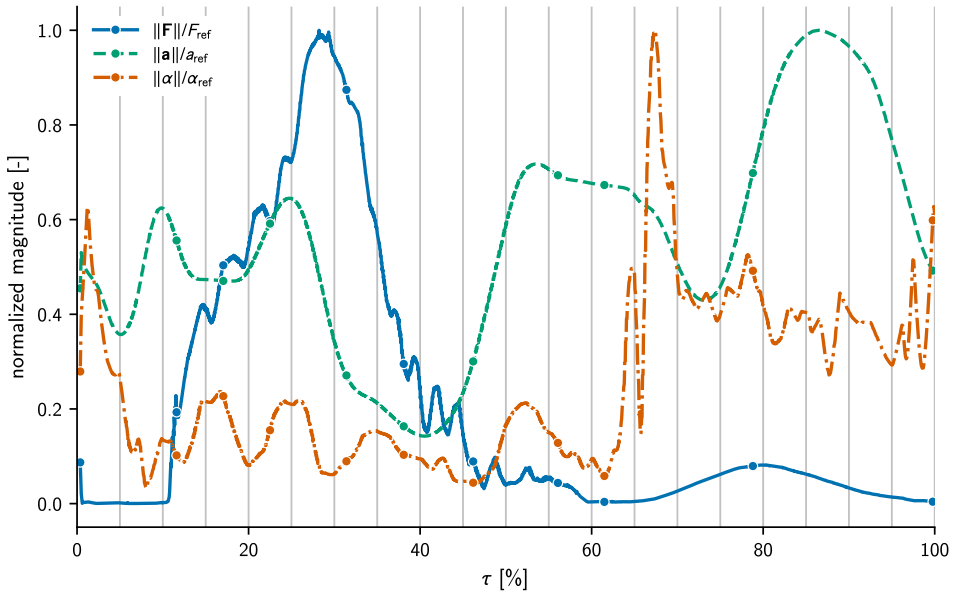

Figure 5.16: Normalised paddle-normal force, linear acceleration, and angular acceleration magnitudes for the Euler case at the reference grid resolution $T_{rH}/L = 0.20$ (case 1, Table 4.10). The reference values are $F_{\text{ref}} = 107.265$ N, $a_{\text{ref}} = 40.922\ \text{m s}^{-2}$, and $\alpha_{\text{ref}} = 313.942\ \text{rad s}^{-2}$.

depends on $\boldsymbol{\alpha}$ through a term that scales with the lever arm $\mathbf{r}_P$. A paddle element far from the axis of rotation (as the outboard tip is) is therefore comparatively more sensitive to angular acceleration than one close to it, even under an identical translational motion.

Why the added-mass reaction tracks acceleration without a resolvable phase lag

The force–acceleration coupling just derived carries a further, testable implication. Within the incompressible-flow regime used by the solver, the added-mass reaction is expected to track the body acceleration essentially without phase lag. Taking the divergence of the incompressible momentum equation and using $\nabla\cdot\mathbf{u} = 0$ removes the time-derivative of velocity and leaves a Poisson equation for pressure,

$$\nabla^2 p = -\rho\,\nabla\cdot[(\mathbf{u}\cdot\nabla)\mathbf{u}]\,, \tag{5.8}$$

with the no-penetration condition on the moving paddle surface, $\partial p/\partial n = -\rho\,\mathbf{a}_P\cdot\mathbf{n}$, supplying the boundary forcing from Equation (5.7). Equation (5.8) is elliptic. Unlike the wave-type (hyperbolic) equations that govern compressible or free-surface gravity-wave propagation, an elliptic equation has no finite signal speed, so a change in the instantaneous boundary acceleration $\mathbf{a}_P$ is felt everywhere in the pressure field at the same computational time step, not after a convection or diffusion delay. This is the precise sense in which the added-mass pressure reaction is "instantaneous" because it is fixed by the current kinematic state alone, in contrast to the viscous (vorticity diffusion) contribution to the load, which develops over the boundary-layer diffusion time scale δ^2/ν and therefore carries genuine memory of the recent flow history. This distinction is consistent with the standalone viscous-versus-Euler comparison of Section 5.2.2, where removing the viscous terms changes the peak and RMS paddle-normal force by only a few percent (Table 5.3), because the pressure-dominated, essentially memoryless added-mass and quasi-static contributions of Equation (5.10) already account for most of the load, while the comparatively small viscous correction is the part of the signal that does carry a diffusive time lag.

Unsteady force decomposition

Robert et al. [5] formalise this coupling for the same class of flow (an oar blade undergoing combined translation and rotation with a deforming free surface) by splitting the instantaneous hydrodynamic load

into a quasi-static part, which depends on the instantaneous relative velocity and incidence and is written with an overline, and an added-mass part, which depends linearly on the body acceleration through the added-mass matrix M_A,

$$\begin{pmatrix} \mathbf{F} \\ \mathbf{M} \end{pmatrix} = \begin{pmatrix} \overline{\mathbf{F}} \\ \overline{\mathbf{M}} \end{pmatrix} - M_A \begin{pmatrix} \ddot{\mathbf{x}} \\ \ddot{\boldsymbol{\vartheta}} \end{pmatrix}, \tag{5.9}$$

where $\ddot{\mathbf{x}}$ and $\ddot{\boldsymbol{\vartheta}}$ collect the linear and angular acceleration components and M_A is the 6×6 added-mass matrix obtained from the added fluid mass distributed around the paddle. Restricting Equation (5.9) to the paddle-normal force and the moment about the paddle axis, and keeping only the dominant diagonal and cross-coupling terms identified by Robert et al. [5] (their Equation 5, restricted to the normal degree of freedom f and its associated moment),

$$F_y = \overline{F}_y - M_{A22}\,\ddot{f}, \qquad M_z = \overline{M}_z - M_{A22} L_e\,\ddot{f}, \tag{5.10}$$

where $\ddot{f}$ is the acceleration normal to the paddle and L_e is the outboard lever. Equation (5.10) was derived by Robert et al. for the oar-shaft bending problem, but the underlying physical statement is general. Any structural or hydrodynamic model that must reproduce the instantaneous blade load has to include a force contribution proportional to blade acceleration, separate from the velocity-dependent quasi-static term. Because the normal acceleration $\ddot{f}$ of an outboard paddle element itself contains an $\boldsymbol{\alpha} \times \mathbf{r}$ contribution (Equation (5.7)), fluctuations in angular acceleration are, through this mechanism, a physically expected source of fluctuation in the paddle-normal force, provided the paddle is submerged, so that an added mass of water is actually present to react against.

This is consistent with the classical unsteady-force formulation used for bluff and lifting bodies in oscillatory flow (the Morison-type decomposition), where the total in-line force is written as the sum of a velocity-squared drag term and an acceleration-proportional inertia term,

$$F(t) = \tfrac{1}{2}\rho C_D A\,|V_r|V_r + \rho C_M \forall\,\dot{V}_r, \tag{5.11}$$

with V_r the relative flow velocity, $\forall$ the displaced volume, and C_M an inertia (added-mass) coefficient. Equation (5.11) is not fitted to the present CFD results. It is quoted only to show that the force–acceleration coupling invoked here is the same structural feature found throughout unsteady hydrodynamics, not a feature specific to this case.

Where the force and angular-acceleration fluctuations overlap, and where they do not

Direct inspection of the standalone-paddle history (case 1, Table 4.10) shows that the paddle is wetted ($S_w > 0$) between $\tau \approx 9\%$ and $\tau \approx 67\%$ of the stroke, consistent with the catch-to-exit interval reported in Table 5.5. Two distinct regimes follow from Equation (5.10).

First, while the paddle is submerged, the dominant force peak ($\|\mathbf{F}\|/F_{\text{ref}} = 1$ at $\tau \approx 28\%$) occurs where the normalised linear-acceleration magnitude is moderate ($\|\mathbf{a}\|/a_{\text{ref}} \approx 0.48$) and the normalised angular-acceleration magnitude is small ($\|\boldsymbol{\alpha}\|/\alpha_{\text{ref}} \approx 0.08$). The principal force peak is therefore governed mainly by the velocity-dependent quasi-static term $\overline{F}_y$ of Equation (5.10) (consistent with the rapid rise of relative velocity and incidence through the catch, described in Section 5.2.2) rather than by the added-mass term. The smaller force ripples that follow the main peak, over approximately $\tau = 30$–45%, occur while the paddle is still wetted and coincide with the secondary, lower-amplitude oscillations of both $\|\mathbf{a}\|$ and $\|\boldsymbol{\alpha}\|$ visible over the same interval in Figure 5.16. This is where the added-mass contribution of Equation (5.10) is expected to be most visible as a modulation superimposed on the decaying quasi-static load.

Second, and more decisively, the largest single feature in the angular acceleration history ($\|\boldsymbol{\alpha}\|/\alpha_{\text{ref}} \approx 1$ at $\tau \approx 67\%$) occurs immediately after the paddle has left the water. At that phase the total force has already fallen to $\|\mathbf{F}\|/F_{\text{ref}} \approx 0.01$. This is a direct numerical confirmation of the mechanism implied by Equation (5.10). The added-mass term requires both a non-zero acceleration *and* a submerged paddle area for the surrounding fluid to react against. Once the paddle is out of the water, the large kinematic angular

acceleration associated with the recovery reversal produces no corresponding force response, because M_{A22} collapses toward zero as $S_w \to 0$. The force and angular-acceleration fluctuations therefore overlap in the sense required by Equation (5.10) (coincident, modest fluctuations while the paddle is wetted), but they visibly decouple once the paddle is unwetted, which is itself consistent with the added-mass mechanism rather than a contradiction of it.

This reading is consistent with Leroyer et al. [3], who found that the unsteadiness of the blade motion (following Kinoshita and Kobayashi's earlier finding for a rotating blade in uniform flow) and the free-surface deformation are the two physical effects that quasi-static models omit and that dominate the departure from a quasi-static force law, while viscous stresses remain a secondary contribution. The present comparison narrows that statement. The unsteady departure from quasi-static behaviour is not uniform over the stroke. It is concentrated in the submerged portion of the cycle, where the added-mass term of Equation (5.10) is active, and it is this submerged-only coupling (not a generic correlation between force and angular acceleration over the whole cycle) that Figure 5.16 should be read as showing.

Taken together, the standalone-paddle force signal can therefore be read back almost entirely in terms of the prescribed kinematics, namely a velocity-dependent quasi-static term that follows the oscillatory advance and incidence of the stroke, and a pressure-dominated added-mass term that follows the acceleration of the wetted paddle with no resolvable lag. Neither the large rigid-body translation and rotation of the stroke motion nor the free-surface deformation at entry and exit introduces a force feature that falls outside this two-term picture, and the residual, unmodelled part of the signal (the "noise" that Equation (5.10) does not account for) is small in comparison, consistent with the under-3% sensitivity of the peak and RMS force to removing the viscous terms entirely (Table 5.3).

5.2.4 Inviscid force history and grid-convergence uncertainty

Once the inviscid formulation has been selected, the remaining numerical question is whether the predicted paddle loads are sufficiently insensitive to spatial discretisation. Four adaptive-grid refinement levels are considered,

$$T_{rH}/L = 0.20,\ 0.15,\ 0.10,\ 0.05,$$

here lower values of T_{rH}/L correspond to progressively finer spatial resolution. The Eça–Hoekstra procedure described in Chapter 4, Section 4.5.7, is used to evaluate the grid dependence of the force predictions. The quantities considered are the peak paddle-normal force, RMS force, propulsive impulse, and conditional-positive mean force. The full force histories are also compared across the refinement levels to examine changes in the phase-resolved loading that may not be captured by these scalar metrics alone. Figure 5.17 compares the paddle-normal force histories obtained with the four Euler refinement levels. The overall force response is consistent across the grid sequence, with only minor differences in magnitude. The rapid increase in force following paddle entry, the main force peak, and the subsequent decay during the drive are reproduced at all refinement levels. The higher-frequency fluctuations that develop during the later part of the drive are also present on all four meshes, indicating that their occurrence is not eliminated by spatial refinement. Examining the complete force histories is therefore necessary in addition to the single-valued convergence metrics, since agreement in peak, RMS, or integral quantities alone does not ensure convergence of the phase-resolved force response. The differences between the four solutions remain small compared with the overall force level. The most noticeable deviations are confined to the vicinity of the main force peak and to the oscillatory decay later in the stroke, while the overall shape and phase of the force histories remain largely unchanged. This suggests that the dominant hydrodynamic loading characteristics are already resolved on the coarser grids, with further refinement producing only limited changes in the local force response.

The convergence of the individual force metrics is examined in Figure 5.18, where the values obtained at the four refinement levels are compared with the fitted asymptotic solution and the corresponding discretisation uncertainty. The peak force shows only a weak dependence on grid refinement. The finest-

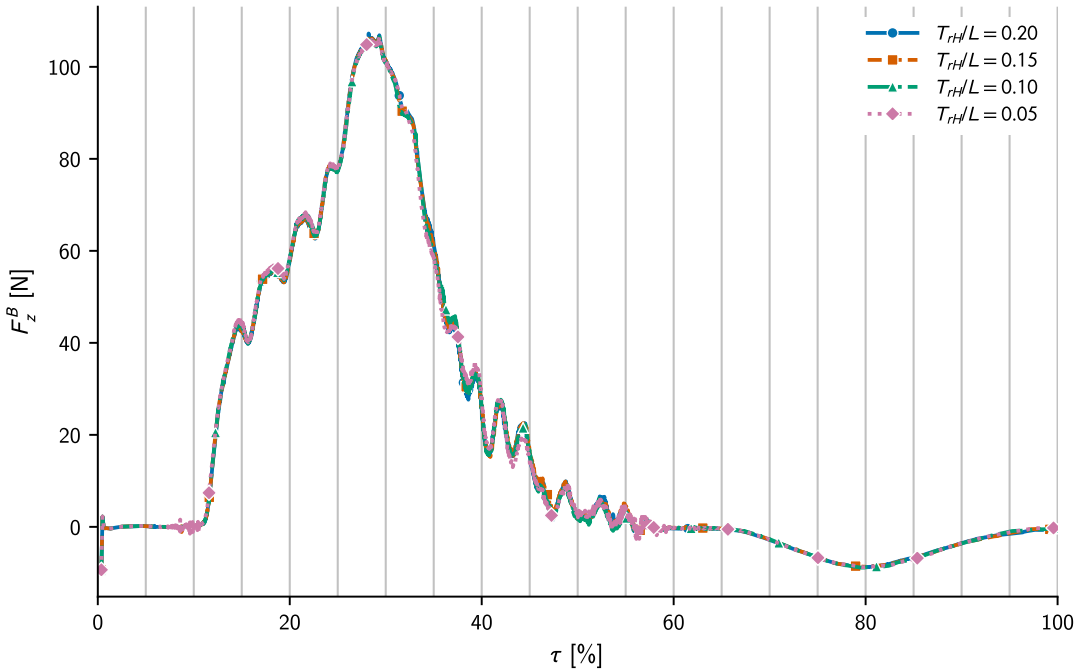

Figure 5.17: Paddle-normal force over one stroke for the four standalone-paddle Euler refinement levels.

grid value is approximately 106.5 N, compared with a fitted limiting value of approximately 106.4 N, while the estimated uncertainty on the finest grid is approximately 0.45%.

The RMS force is even less sensitive to spatial refinement. Across the four grid levels, it varies only from approximately 37.14 N to 37.23 N, and the estimated relative discretisation uncertainty remains below 0.5% in all cases. This lower sensitivity is consistent with the RMS force being a stroke-integrated measure, which is less affected by local variations in the instantaneous force history than the peak value.

Table 5.4 extends the convergence assessment to the propulsive impulse and conditional-positive mean force. The estimated discretisation uncertainty varies noticeably between the different quantities. The RMS force is the least sensitive to grid refinement, with $U_\phi/|\phi_1| < 0.5\%$ at all four levels. The peak-force uncertainty is also small, increasing from approximately 0.45% on the finest grid to 2.16% on the coarsest grid.

The propulsive impulse shows a somewhat greater sensitivity, with the estimated uncertainty reaching approximately 3–4% on the intermediate and coarser grids. However, the corresponding impulse values remain tightly grouped between 15.08 and 15.16 N s. The conditional-positive mean is the most grid-sensitive quantity, with relative uncertainties of approximately 4–5%. This is consistent with its definition, since it is evaluated only over the portion of the stroke for which the paddle-normal force is positive. It is therefore more sensitive to small grid-dependent shifts in the onset and decay of positive loading near paddle entry and extraction than metrics evaluated over the complete stroke.

The evolution of the computational mesh and adaptive time step provides additional insight into the numerical behaviour of the four refinement levels. Figure 5.19 shows the instantaneous cell count N_c and time step Δt over the stroke. As the refinement threshold is reduced, the number of computational cells increases substantially. The finest $T_{rH}/L = 0.05$ case shows the largest increase in cell count as AGR responds to the evolving free surface and paddle-induced flow structures, whereas the coarser refinement levels require considerably fewer cells.

The cell count varies throughout the stroke because the adaptive mesh evolves with the instantaneous flow field. The increase in N_c during the drive reflects the larger spatial extent of regions satisfying the AGR criterion. This effect becomes more pronounced at lower refinement thresholds, leading to a considerable increase in computational cost even though the resulting changes in the principal force metrics remain relatively small.

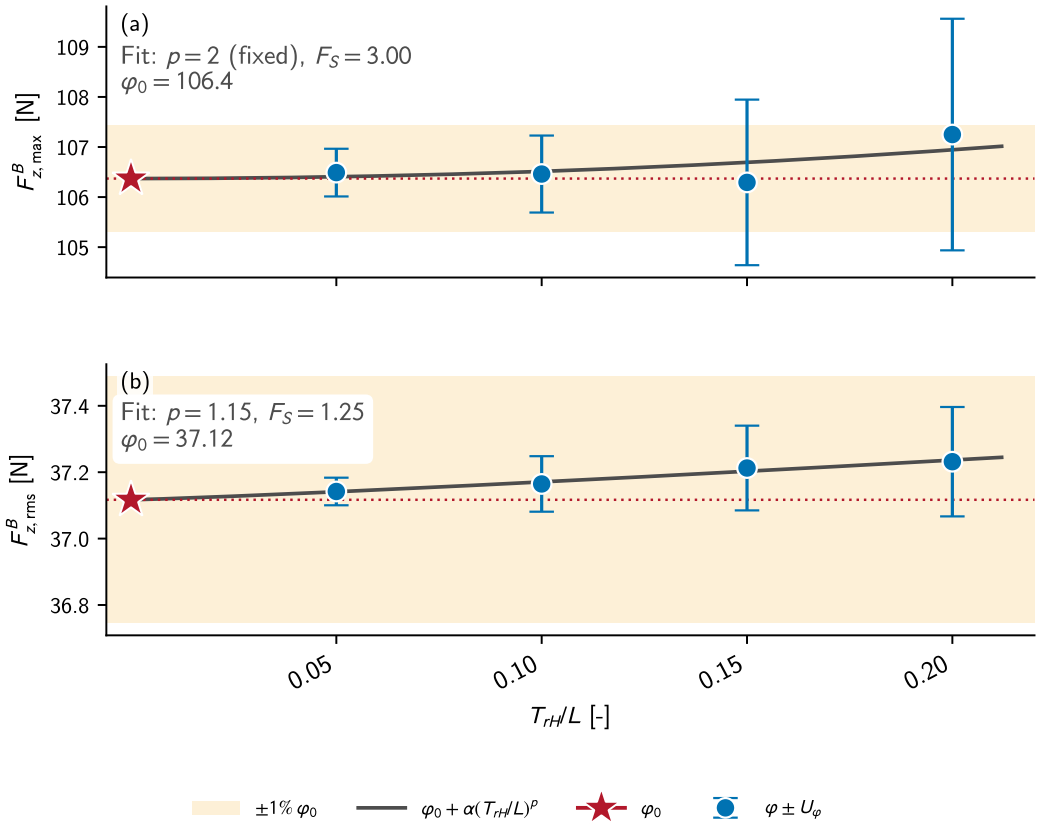

Figure 5.18: Grid-convergence assessment of the peak and RMS paddle-normal force.

Table 5.4: Grid-convergence series for the standalone-paddle paddle-normal force over the four Euler refinement levels $T_{rH}/L = 0.20, 0.15, 0.10, 0.05$. Here, ϕ_i is the computed value, ϕ_{fit} is the least-squares fitted value at the assumed convergence order, U_ϕ is the estimated discretisation uncertainty obtained using the Eça–Hoekstra procedure, and $U_\phi/|\phi_1|$ is the uncertainty relative to the finest-grid value.

Metric	T_{rH}/L	ϕ_i	ϕ_{fit}	U_ϕ	$U_\phi/\lvert\phi_1\rvert$ [%]
Peak $F^B_{z,\max}$ [N]	0.05	106.5	106.4	0.4760	0.4500
	0.10	106.5	106.5	0.7690	0.7200
	0.15	106.3	106.7	1.653	1.560
	0.20	107.2	106.9	2.313	2.160
RMS $F^B_{z,\mathrm{RMS}}$ [N]	0.05	37.14	37.14	0.04200	0.1100
	0.10	37.17	37.17	0.08400	0.2200
	0.15	37.21	37.20	0.1280	0.3400
	0.20	37.23	37.24	0.1650	0.4400
Impulse I^B_z [N s]	0.05	15.10	15.10	0.2910	1.930
	0.10	15.08	15.11	0.4610	3.060
	0.15	15.16	15.12	0.5930	3.910
	0.20	15.11	15.13	0.5440	3.600
Conditional-positive mean $\overline{F^{B+}_z}$ [N]	0.05	38.31	38.45	1.545	4.030
	0.10	38.63	38.41	2.059	5.330
	0.15	38.28	38.34	1.690	4.410
	0.20	38.24	38.24	1.865	4.880

The lower panel of Figure 5.19 shows the corresponding adaptive time-step histories. The time step varies in response to the Courant-number constraint and the local mesh resolution. As smaller cells are introduced by AGR, particularly around the paddle and the disturbed free surface, a smaller time step is required to maintain the prescribed Courant-number limit. The spatial and temporal discretisations are therefore closely coupled, with the finer refinement levels requiring both more cells and smaller time steps.

The viscous $T_{rH}/L = 0.20$ case is included for reference. Although it uses the same AGR threshold as the corresponding Euler case, the additional near-wall resolution modifies the total cell count and the adaptive time-step response. It is therefore not treated as part of the Euler grid-convergence sequence.

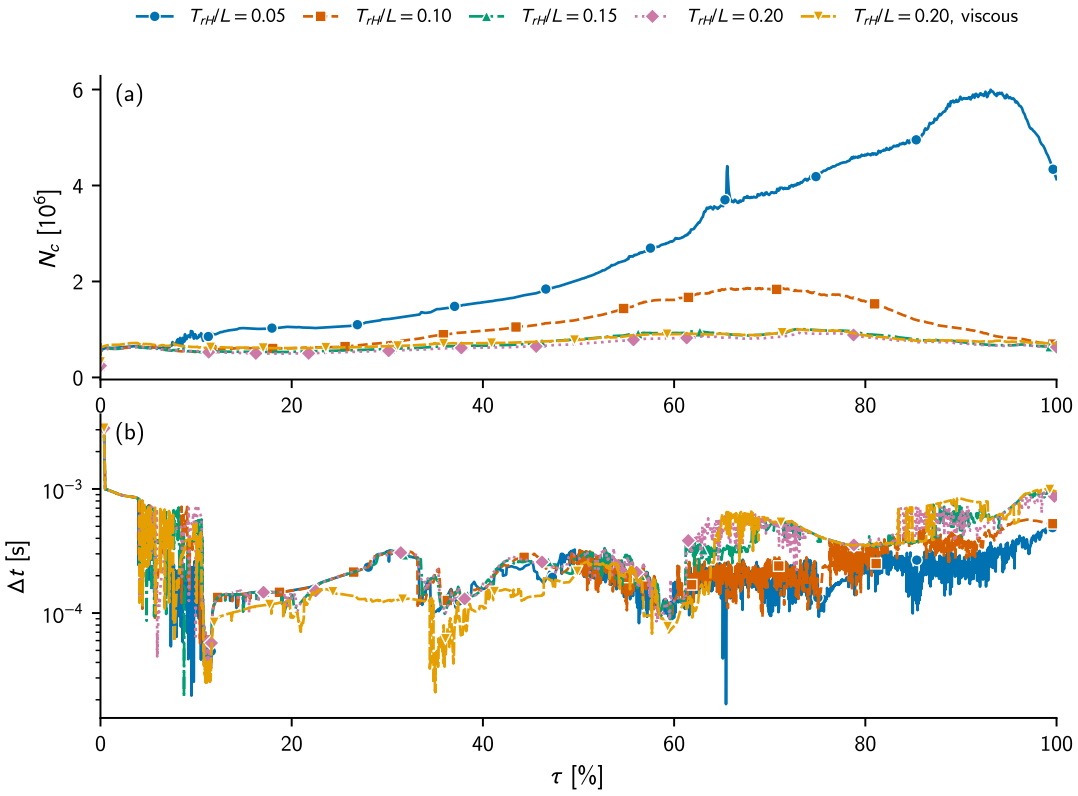

Figure 5.19: Numerical evolution of the standalone-paddle simulations showing (a) instantaneous cell count and (b) adaptive time step as functions of stroke phase for the four Euler refinement levels. The viscous $T_{rH}/L = 0.20$ case is included for comparison.

Taken together, the phase-resolved force histories, single-valued convergence metrics, and mesh evolution indicate that the principal paddle-normal loading is only weakly dependent on further spatial refinement over the range considered. The finest meshes substantially increase the cell count and require smaller adaptive time steps, while producing only limited changes in the peak and RMS force. The larger uncertainty associated with the impulse and conditional-positive mean shows that quantities influenced by the duration and phase limits of the loading interval are more sensitive to spatial discretisation and should therefore be interpreted together with their estimated numerical uncertainty.

5.2.5 Gomory and Galipeau stroke descriptors

The Gomory and Galipeau stroke descriptors defined in Section 4.5.6 (Section 4.5.6) are evaluated for the standalone-paddle cases in Table 5.5.

Table 5.5 expresses the same histories through the descriptors defined by Gomory [9] and Galipeau [10]. The Euler and viscous paddles reach their maxima at 17.32% and 17.64% of the stroke period after water contact and have similar 20–80% force-development rates (576 and 591 $\mathrm{N\,s^{-1}}$). Viscosity changes the

falling branch more than the rising branch, as the 20%–zero reduction rate increases in magnitude from 188 to 301 $\mathrm{N\,s^{-1}}$, while the propulsive impulses remain 16.36 and 16.21 N s. Thus the principal model-form effect lies in the distribution of load during the drive and exit, not in the stroke-integrated impulse.

Table 5.5: Stroke descriptors calculated from the CFD histories using the phase definitions of Gomory (2018) and the time-to-peak and paddle-in-water descriptors reported by Galipeau (2018). Time-based descriptors are reported as a percentage of the stroke period T_s (phase τ) rather than in seconds, consistent with the phase convention used throughout this chapter.

Metric	Paddle Euler	Paddle viscous	Paddle+hull Euler
Time from contact to peak, τ_{peak} [%]	17.32	17.64	17.53
Peak force [N]	107.2	110.2	137.8
20–80% development rate [$\mathrm{N\,s^{-1}}$]	576	591	702
Average drive force [N]	37.4	47.4	42.0
Drive force quality [-]	0.348	0.430	0.305
Propulsive impulse [N s]	16.36	16.21	21.52
Propulsive impulse rate [N]	19.69	19.51	25.90
Paddle-in-water ratio [%]	43.0	36.3	47.6

These results justify the Euler formulation for the integrated force and impulse comparisons made in the paddle-hull configuration. They do not show that viscosity is absent from the local flow, and they do not transfer an uncertainty bound to the hull boundary layer or the paddle-hull wake.

5.3 Type 2 simulations: CFD of Boat

The bare-hull simulations characterise the hydrodynamic response of the hull independently of the paddle. Two sets of cases are considered, a calm-water resistance sweep from 7 to 13 $\mathrm{km.h^{-1}}$ and a Type 2 oscillating-surge case representing time-varying advance. The former defines the variation of whole-hull resistance with speed, while the latter provides the corresponding unsteady force response. These results provide the reference bare-hull behaviour for comparison with the coupled paddle-hull simulations in Section 5.4. The force definitions and post-processing follow Section 4.5.6, while the computational setup is described in Chapter 4.

5.3.1 Calm-water resistance speed sweep

The calm-water simulations predict the bare-hull resistance over the speed range of 7–13 $\mathrm{km.h^{-1}}$. The steady resistance at each speed is obtained from the time-weighted mean over the final 2% of the simulated time. This averaging interval excludes the initial transient and provides a consistent basis for comparison across all seven resistance cases.

The resistance calculations use the same B1 domain and hull geometry as the Type 2 oscillating-surge simulations, but apply the MS+PH refinement criterion rather than the MSFCH criterion used for the oscillating-surge case (Section 4.5.7). The four-level grid-convergence study performed for the oscillating-surge case is used to assess the numerical behaviour of this computational setup under unsteady loading, and a separate grid-convergence study is not performed at each calm-water speed.

The half-hull force reported by the solver is converted to the positive drag convention and doubled according to Equation (4.46). The pressure and viscous components are subjected to the same half-hull correction so that their sum is consistent with the reported whole-hull resistance.

The resulting resistance curve and its pressure and viscous components are presented in Figure 5.20, while the corresponding numerical values are reported in Table 5.6. The total resistance increases continuously over the investigated speed range, from approximately 50 N at 7 $\mathrm{km.h^{-1}}$ to more than 200 N at 13 $\mathrm{km.h^{-1}}$. Both the pressure and viscous contributions increase with speed, although their relative

importance changes across the range. The increase in pressure resistance becomes particularly pronounced at the higher Froude numbers, reflecting the increasing contribution of free-surface wave generation to the total hydrodynamic resistance.

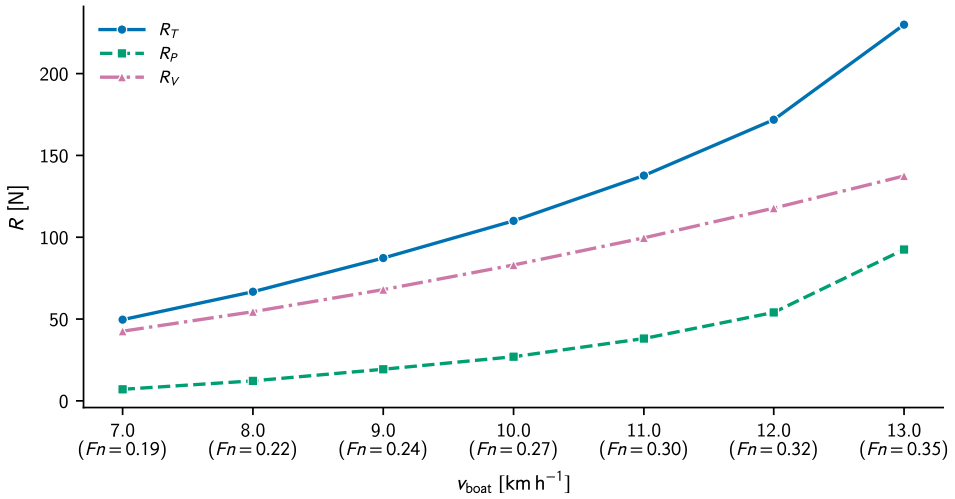

Figure 5.20: Calm-water resistance and its pressure and viscous components.

Table 5.6: Whole-hull resistance from the time-weighted final 2% of each run. The half-hull force is sign-corrected and multiplied by two.

v_{boat} [km h^{-1}]	Fn	R_T [N]	R_F/R_T [%]	$10^3 C_T$	$10^3 C_R$	$10^3 C_F$
7	0.19	49.6	82.5	3.26	0.57	2.69
8	0.22	66.7	79.2	3.32	0.69	2.63
9	0.24	87.3	75.6	3.41	0.83	2.58
10	0.27	110.0	73.3	3.46	0.92	2.54
11	0.30	137.7	70.3	3.55	1.05	2.50
12	0.32	171.8	66.8	3.69	1.23	2.46
13	0.35	229.9	58.4	4.17	1.74	2.43

5.3.2 Calm-water free-surface patterns across the resistance-test speed range

Figure 5.21 presents the calm-water free-surface response for all seven resistance-test speeds. As the speed and Froude number increase, the wave system generated by the hull becomes progressively more pronounced. The diverging and transverse components of the wake become increasingly distinct, together with stronger free-surface deformation in the bow and stern regions. At the highest investigated speeds, the disturbance associated with the transom region also becomes more prominent.

The resistance decomposition in Figure 5.20 reports the pressure and viscous forces obtained directly from the CFD solution. The reference-friction quantity reported separately in Table 5.6 is therefore not equivalent to the solver viscous contribution. The Froude number and resistance coefficients provide additional nondimensional measures for interpreting the variation of resistance with speed without considering the dimensional force increase alone.

AGR mesh at 12 km.h^{-1}

The initial and final mesh for calm-water resistance case is shown in Figure 5.22. The initial mesh is based on the B1 background domain defined in Chapter 4, Section 4.5.3. During the calculation, AGR introduces

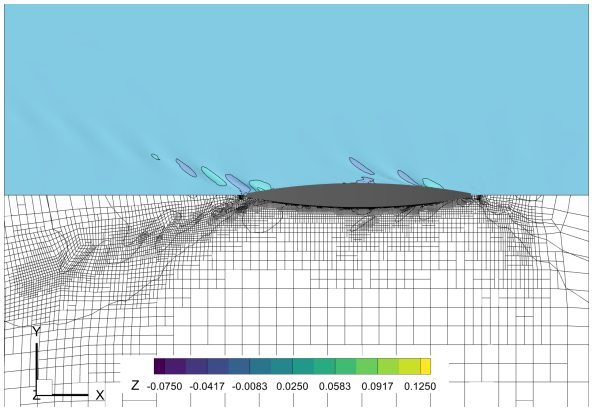

(a) 7 km h^{-1} ($Fn = 0.19$).

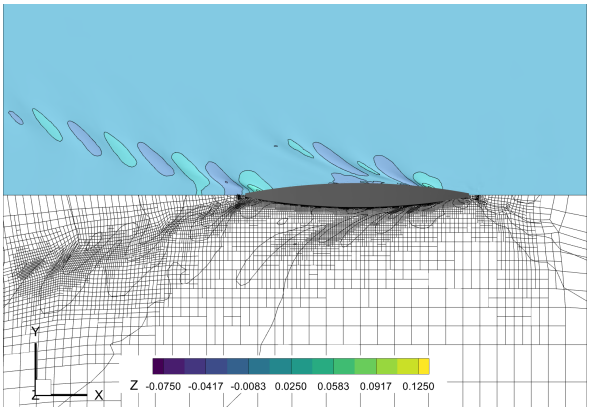

(b) 8 km h^{-1} ($Fn = 0.22$).

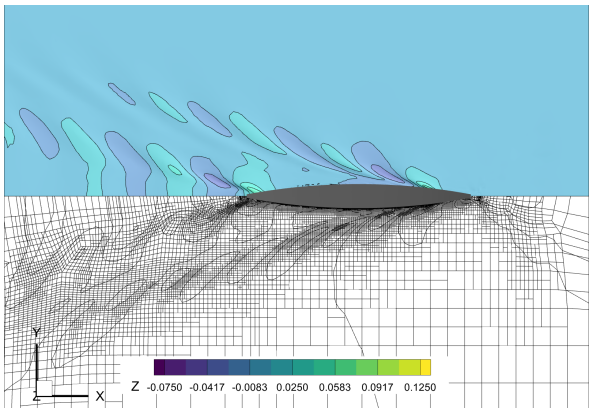

(c) 9 km h^{-1} ($Fn = 0.24$).

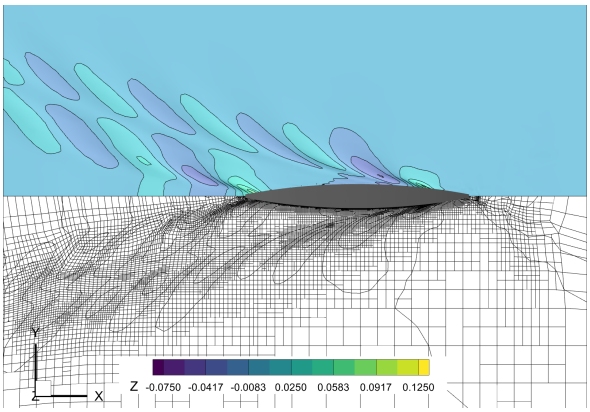

(d) 10 km h^{-1} ($Fn = 0.27$).

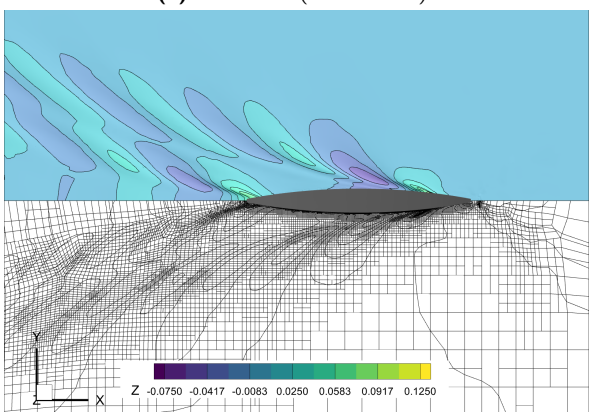

(e) 11 km h^{-1} ($Fn = 0.30$).

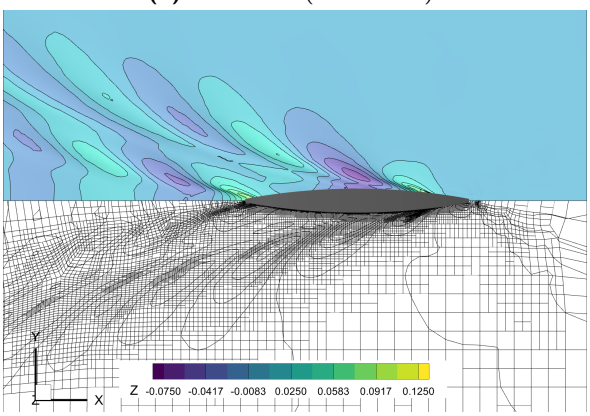

(f) 12 km h^{-1} ($Fn = 0.32$).

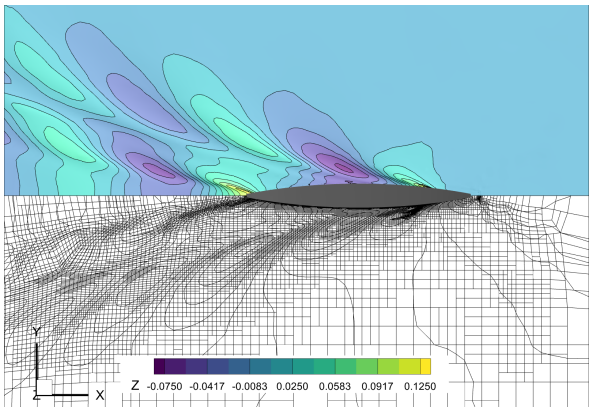

(g) 13 km h^{-1} ($Fn = 0.35$).

Figure 5.21: Calm-water free-surface pattern (two views) at the seven resistance-test speeds.

additional resolution in regions identified by the refinement criterion, with refinement concentrated around the hull and the evolving free surface.

The top view in Figure 5.22(a) compares the free-surface mesh before and after AGR, showing how the refinement is concentrated around the hull-induced free-surface disturbance. The second view, Figure 5.22(b), shows the mesh at the mid-section of the hull and illustrates the local refinement around the waterline and hull surface. In both views, the refined cells remain confined to regions of interest, while a coarser mesh is retained farther from the hull and free surface.

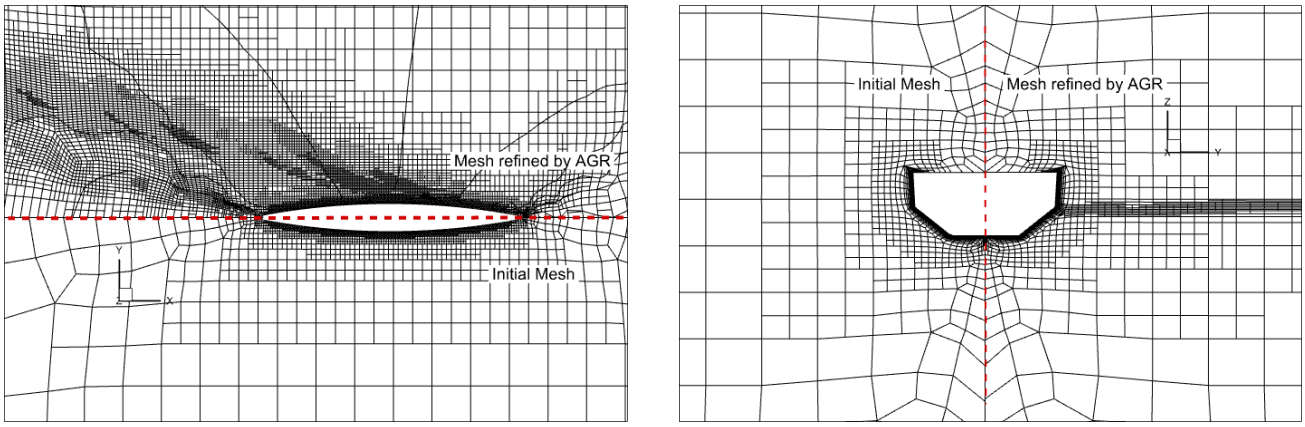

(a) Mesh on the free surface. **(b)** Mesh at mid-section of the boat.

Figure 5.22: Hull mesh before and after AGR for the 12 km.h^{-1} calm-water case.

The mesh comparison illustrates how AGR redistributes the spatial resolution during the resistance calculation. It is intended to document the local mesh adaptation around the hull and free surface rather than to provide an independent grid-convergence assessment. The discretisation uncertainty is therefore not inferred from this visual comparison.

5.3.3 Oscillating-surge hull response

The second set of bare-hull simulations considers prescribed oscillating-surge advance. Unlike the steady resistance sweep, the boat speed varies with time according to the prescribed advance law. The hull remains uncoupled from the paddle, so the resulting force history represents the response of the bare hull to the imposed nonlinear forward motion.

The oscillating-surge stage begins at the prescribed transition time $t = 15$ s. Consistent with the acceleration-stage convention defined in Section 4.4, only the history for $t \geq 15$ s is used in the subsequent comparison. The displayed time origin is shifted to the beginning of this analysis window where appropriate.

The simulation isolates the hull-force response to continuously changing advance speed. It supplies the unsteady hull-only reference for the paddle-hull calculation, where paddle forcing and hull motion occur simultaneously.

Considered grid levels

Four spatial refinement levels are considered, expressed using $T_{rH}/L = 0.20$, 0.15, 0.10, and 0.05. Figure 5.23 compares the resulting hull-force histories. The corresponding boat heave and pitch motion histories, including the paddle-hull case, are reported for reference in Appendix D.

The force histories provide a direct comparison of the influence of spatial refinement on the unsteady hull loading. The four refinement levels are compared in terms of force amplitude, phase, and the local structure of the response throughout the imposed surge cycle. The comparison is therefore used to assess the sensitivity of the predicted hull force to the spatial resolution of the adaptive mesh.

Adaptive and uniform time stepping

The temporal discretisation is examined separately from the spatial mesh. Adaptive Courant-controlled stepping is compared with a uniform time step at fixed spatial resolution, using the coarsest mesh, $T_{rH} = 0.20$. This mesh exhibits the largest short-period force fluctuations among the four spatial levels and therefore provides the more demanding case for assessing the temporal discretisation. It is also the refinement level used for the oscillating-surge calculations presented below.

Figure 5.23 contains the corresponding force comparisons. The upper panels show the force histories for the four spatial mesh levels, with the short-period force fluctuations decreasing as the mesh is refined. The temporal comparison is therefore shown at $T_{rH} = 0.20$, where these fluctuations are most pronounced. The adaptive and uniform time-stepping approaches produce different levels of short-period variation in the force history. This indicates that the temporal discretisation influences the resolved instantaneous force response. However, these differences should not be interpreted directly as differences in the underlying hydrodynamic behaviour, since the short-period variations may also be influenced by numerical dissipation.

Discussion about spikes in force signal

The difference has a specific numerical origin in the treatment of the captured volume-of-fluid interface. A compressive interface scheme maintains a sharp transition only when the interface moves by approximately one cell or less per time step. If a uniform time step advances the interface across several cells, the boundedness limiter shifts the flux towards a more upwind formulation and the interface becomes more diffuse. Spatial refinement alone may therefore be insufficient if the time step is not reduced accordingly.

The time step also affects pressure–velocity coupling. In a collocated finite-volume formulation, the momentum-interpolation correction used to construct face fluxes depends on the transient coefficient of the momentum equation. A larger time step weakens this coefficient and increases pressure smoothing. Together with the more diffuse volume-fraction field, this reduces the resolved short-period free-surface dynamics and their feedback on the pressure force. The uniform-step force history is therefore smoother because part of the interface dynamics is numerically filtered, not because the physical hull response is intrinsically steadier.

Since the hull force in Figure 5.23 is obtained by integrating the hydrodynamic pressure over the wetted hull surface, this smoothing also affects the resolved force features directly. The adaptive-step calculation preserves sharper free-surface and pressure gradients around regions such as the bow wave, which appear as sharper short-period variations in the force history. The uniform-step calculation smooths these gradients before integration, producing a noticeably quieter force response despite the identical prescribed hull motion.

The force histories in Figure 5.23 provide the direct basis for the force-domain comparison. A matched free-surface Courant-number contour is available for the two temporal approaches and provides direct local support for the mechanism argued above.

Figure 5.24 shows the free-surface Courant number for the fixed and adaptive time-stepping approaches at the same spatial resolution and instant. Under the fixed step, the elevated Courant number ($Co \geq 2$–5) is spread over a broad, spatially diffuse region extending well away from the surface. This is exactly the pattern predicted by the compressive-interface argument above. The fixed step repeatedly advances the interface across more than the one-cell-per-step limit that the compressive scheme needs to hold a sharp transition, so the boundedness limiter reverts to its diffusive upwind branch over an extended region, consistent with the finding of Robert et al. [5] that the compressive scheme imposes a local free-surface Courant limit near 0.3. The adaptive scheme, by construction, keeps the local Courant number close to its target everywhere on the free surface, which keeps the diffusive branch confined to a narrow layer and is the local analogue of the sharper, less-smoothed pressure field invoked above to explain the short-period force structure. This behaviour is consistent with the numerical diffusion discussed by Leroyer et al. [3], who attributed the late-stroke convergence of their free-surface-resolved oar solution towards the no-free-surface reference to insufficient resolution of the interface dynamics. The present comparison similarly

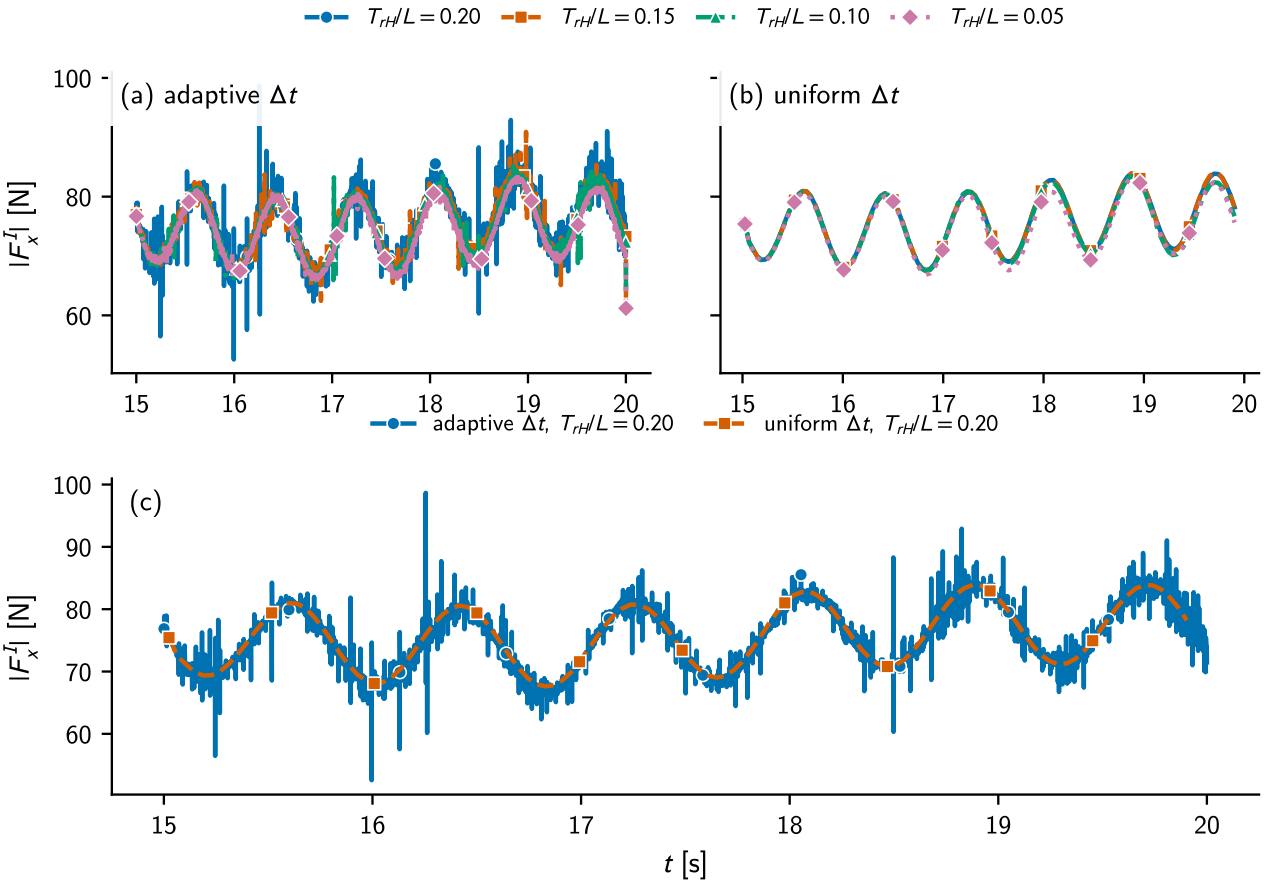

Figure 5.23: Hull-force comparison across mesh and time-stepping variants.

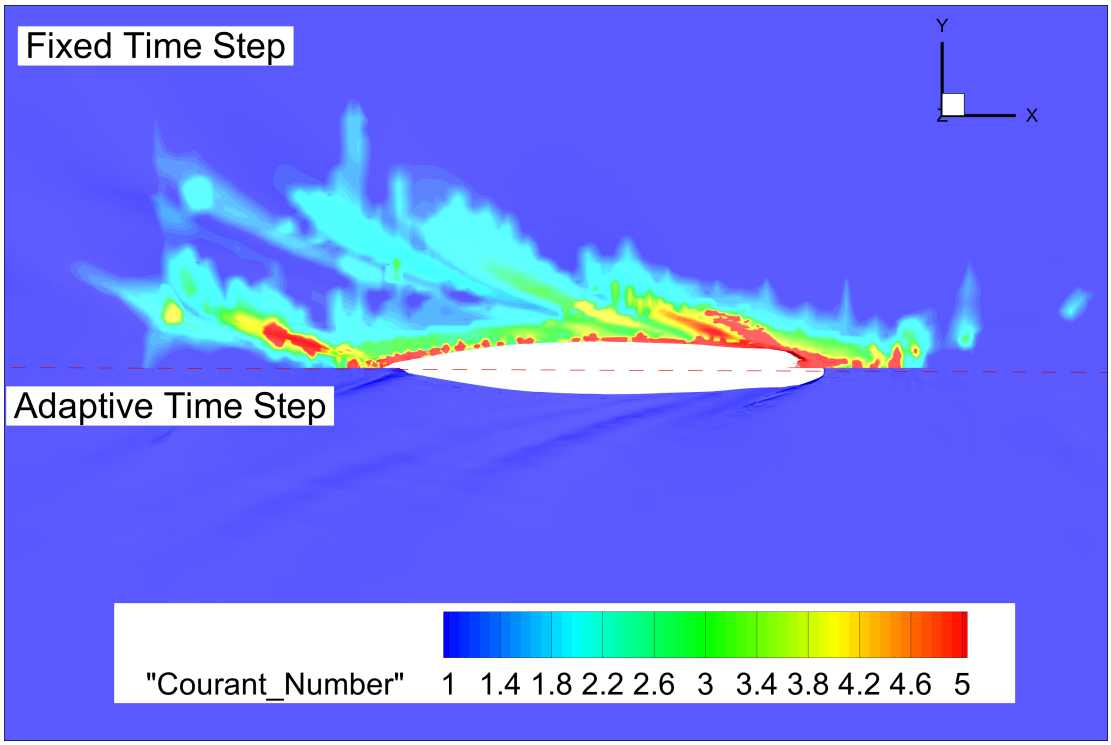

Figure 5.24: Free-surface Courant number near the hull leading edge, fixed time step (top) versus adaptive Courant-controlled time step (bottom), at the same spatial resolution and the same instant.

suggests that the differences between the adaptive and uniform time-stepping results arise primarily from temporal resolution and the associated interface diffusion.

AGR mesh for the oscillating-surge case

The spatial mesh corresponding to the finest oscillating-surge case is shown in Figure 5.25. The figure compares the mesh before and after AGR activation during the oscillating-speed stage.

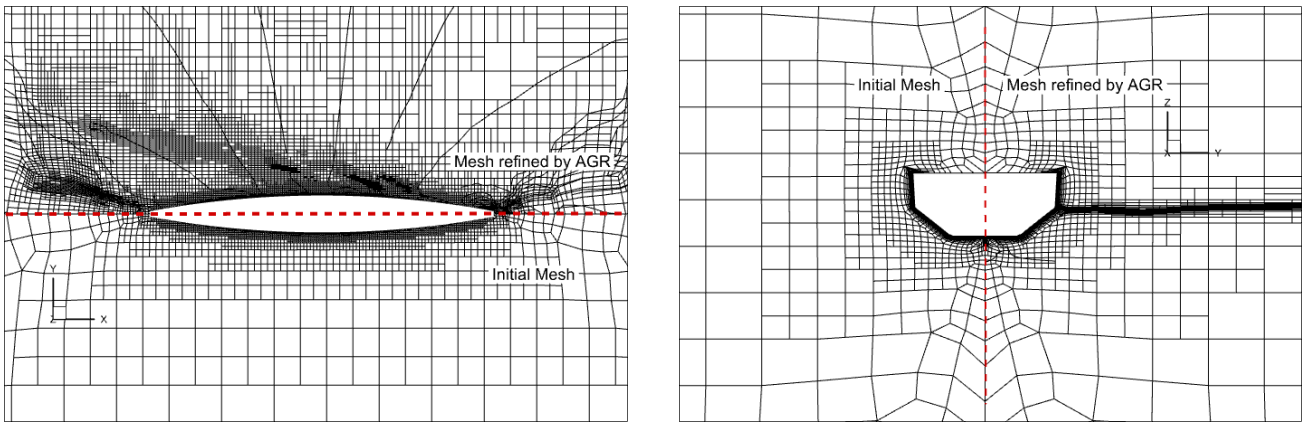

(a) Mesh on the free surface. **(b)** Mesh at mid-section of the boat.

Figure 5.25: Oscillating-surge hull mesh before and after AGR at $T_{rH}/L = 0.20$.

The spatial and temporal comparisons are treated separately because changing the mesh and changing the time step affect different aspects of the numerical solution. The AGR figure illustrates the spatial refinement applied in the unsteady calculation, while the force comparison in Figure 5.23 examines the effect of temporal discretisation at fixed spatial resolution.

5.3.4 Bare-hull discussion

The resistance calculations provide the baseline for the subsequent paddle-hull comparison, while the oscillating-surge cases characterise the bare-hull force response to the prescribed unsteady advance in the absence of paddle forcing. The mesh and time-step comparisons further show that the high-frequency content of the computed hull-force history is sensitive to temporal resolution.

The selected viscous formulation and MS+PH refinement criterion apply to the bare-hull resistance calculations. They do not imply that the later Euler paddle-hull case represents a viscous hull solution, nor can the bare-hull force histories be used to isolate the paddle-induced contribution to the hull load.

The resistance curve established here is used later as the reference resistance at the corresponding advance speed. In Section 5.4, the paddle-hull force statistics are compared with this baseline to assess the relation between the peak paddle load and hull resistance. A separate comparison considers whether the combined cycle-averaged thrust of a full crew is sufficient to overcome the predicted hull resistance.

5.4 Type 3 simulation: CFD of paddle and hull interaction

The Type 3 case places one prescribed paddle beside the hull at $T_{rH}/L = 0.20$ (Chapter 4, Table 4.10, case 21). Both bodies follow the prescribed advance motion. The case uses Euler flow modelling and one refinement threshold only. No matched viscous paddle-hull configuration or paddle-hull grid series was run. The reported loads apply to the single run only and have no paddle-hull discretisation-uncertainty estimate.

The comparison also cannot separate wake interaction, pressure transmission, boundary-layer effects, or the change in immersion caused by the combined configuration. The flow visualisations and force histories are used only to describe the computed response [21, 28].

AGR mesh

Figure 5.26 illustrates the adaptive grid refinement (AGR) for the Type 3 paddle-hull configuration using a refinement threshold of 0.20. The mesh is locally refined around the moving paddle, overset-grid interface, hull waterline, and disturbed free surface, while coarser cells are retained farther away. This concentrates spatial resolution in the regions most relevant to the paddle-hull interaction. The corresponding standalone-paddle refinement is shown in Figure 5.14 in Section 5.2.

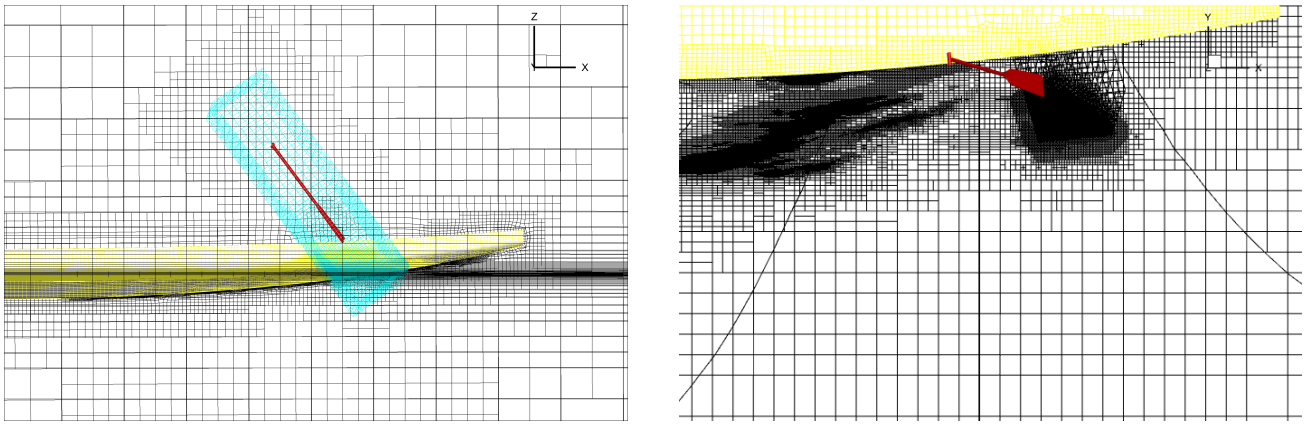

(a) Overset grid (x–z view). **(b)** Free surface (top view).

Figure 5.26: AGR for the paddle-hull configuration.

5.4.1 Phase definition and stroke-start detection

Type 3 simulations begin with a 15 s acceleration phase (Chapter 4, Section 4.5.2) to establish the hydrodynamic state, followed by approximately three full paddle strokes over a total interval of approximately 2.5 s. The post-acceleration analysis time is defined as

$$t' = t - 15, \tag{5.12}$$

where t' is the time elapsed since the end of the acceleration phase and t is the absolute simulation time.

The stroke phase is defined relative to the detected stroke-start time t_{start} as

$$\tau_c = 100\frac{t - t_{\text{start}}}{T_s} \quad [\%], \tag{5.13}$$

where τ_c is the stroke phase, T_s is the detected stroke period, and t_{start} is the start time used as the phase reference. The phase is not reset after each stroke, so the three simulated strokes remain separate and can be identified individually in the force history.

Hull forces are reported as magnitudes and are therefore positive throughout, consistent with the convention adopted in Section 5.3. Paddle immersion is represented by the paddle-tip elevation z_{tip}, as described in Section 5.4.2.

5.4.2 Paddle force, immersion, and wetted area in the paddle-hull configuration

The standalone-paddle simulation uses its native stroke-time coordinate, whereas the paddle-hull simulation is represented using the shifted time $t' = t - 15$. For direct comparison, the two datasets are aligned

using stroke phase rather than absolute simulation time. The comparison intervals are defined using Equation (5.13), thereby ensuring that corresponding portions of the paddle stroke are compared.

Paddle immersion is characterised by the paddle-tip elevation z_{tip}. This quantity is reconstructed using the paddle-frame lever arm

$$\mathbf{r}_{\text{tip}}^{B} = (0, -0.988, 0)\ \text{m}, \tag{5.14}$$

defined in Equation (4.33) (Section 4.5.6), and rotated into the inertial frame using the Cardan rotation sequence of Equation (4.31) (Section 4.5.6). Stroke progress is indicated in the figures using phase markers at 0%, 20%, 40%, 60%, and 80%.

The paddle-hull flow-interaction analysis addresses three principal questions. First, how the paddle-normal force differs between the standalone and paddle-hull configurations. Second, how paddle immersion relates to force generation throughout the stroke. Third, how the computed hull-force history compares with the boat-alone reference. These comparisons do not isolate a unique physical mechanism or establish a propulsive force balance.

Table 5.7 reports the peak, RMS, impulse, and conditional-positive mean of the paddle-normal force using the measures defined in Equation (4.34) (Section 4.5.6), each evaluated with the same time-weighted definitions used for Table 5.5 and the GCI series of Table 5.4. These quantities constitute the supported quantitative statistics used for comparison in this chapter.

Figure 5.27 compares the paddle-normal force F_z^B for two configurations, (a) the standalone paddle and (b) the paddle in the presence of the hull. Differences in the force response are quantified through the peak and RMS values reported in Table 5.7. Changes in the force envelope, phase, and oscillatory structure provide qualitative support for the hydrodynamic modification associated with the presence of the hull.

Figure 5.28 compares paddle-tip elevation z_{tip}, paddle-normal force F_z^B, and instantaneous wetted area $S_w(t)$ for the standalone and paddle-hull configurations. The comparison establishes whether peak force occurs near maximum immersion or during paddle entry and exit, and whether force magnitude follows wetted area or instead reflects additional effects associated with the instantaneous flow state and paddle motion.

Qualitative pressure-field context for the drive phase is provided by the side-view pressure fields of Figure 5.36, whose second panel ($t' \approx 0.328$ s, that is $\tau_c \approx 40\%$) falls within the force interval containing the paddle-hull peak reported in Table 5.7. The pressure distribution on the paddle and hull illustrates the instantaneous pressure asymmetry associated with paddle loading and the corresponding pressure response of the hull.

Table 5.7: Time-aligned standalone and paddle-hull-configuration paddle-force statistics.

Metric	Paddle	Paddle+hull	Difference [%]
Peak F_z^B [N]	107.249	137.813	28.50
RMS F_z^B [N]	37.232	46.622	25.22
Impulse I_z^B [N s]	15.114	20.302	34.33
Conditional mean $\overline{F_z^{B+}}$ [N]	38.235	44.288	15.83

Note on RMS weighting. Because the solver uses Courant-controlled time stepping, the sampling density is not uniform in time, so substantially more samples are logged while the paddle is heavily loaded (where the time step is smaller) than during the lightly loaded portion of the stroke, so an unweighted per-sample average $\sqrt{\langle F^2 \rangle}$ would over-represent the high-force region. The RMS values reported above therefore use the time-weighted definition of Equation (4.34) (Section 4.5.6), $F_{\text{RMS}} = \left[\frac{1}{t_b - t_a}\int_{t_a}^{t_b} F^2\,\mathrm{d}t\right]^{1/2}$, consistent with every other RMS value in this chapter, including Table 5.5 and the GCI series of Table 5.4.

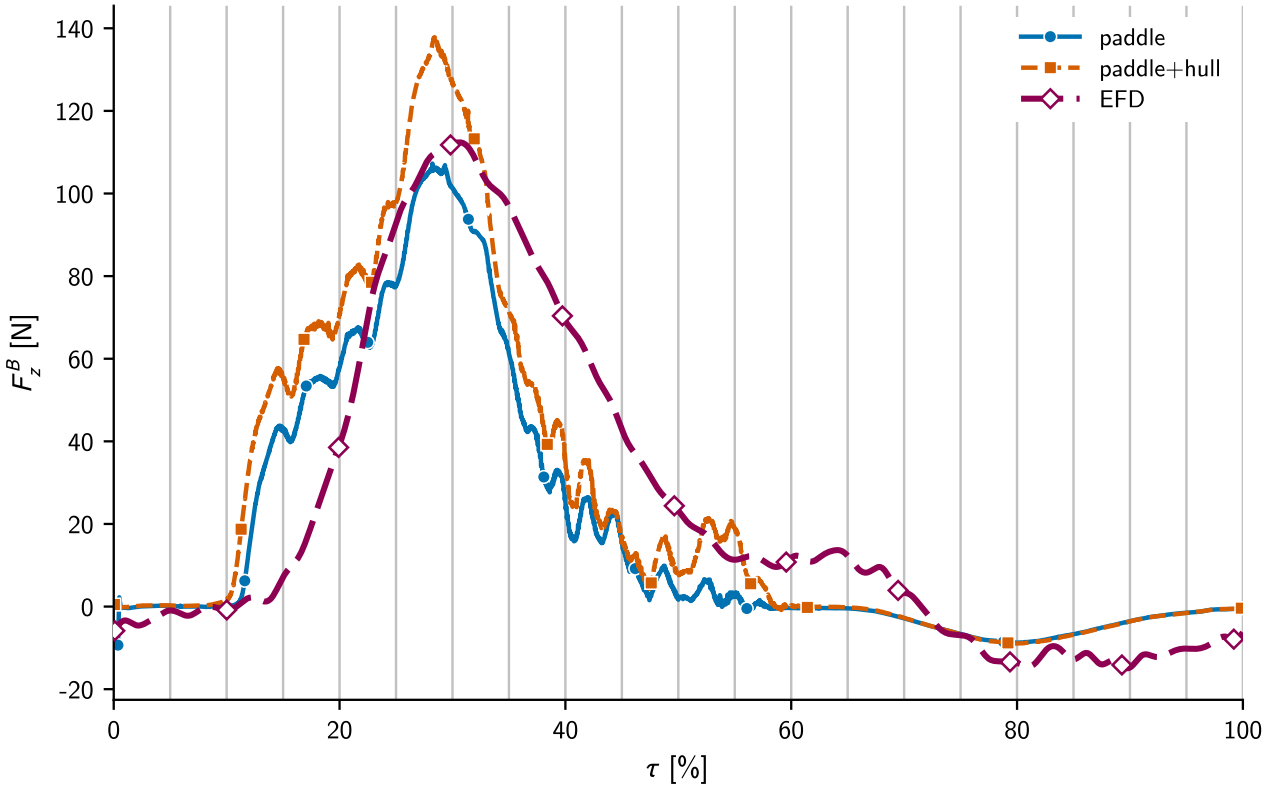

Figure 5.27: Aligned paddle-normal force with and without the hull.

The hull axial force $F_x(\text{Boat})$ exhibits two characteristic features over the plotted stroke history. The first is a recurring peak near the catch phase ($\tau_c \approx 0\%$), associated with paddle entry and the corresponding acceleration transient. The second is a larger, non-repeating peak at shifted time $t' \approx 0.902$ s, corresponding to approximately 110% of the stroke period for $T_s \approx 0.82$ s. This latter event therefore occurs after the nominal completion of the first stroke and is not representative of a periodic steady-cycle maximum.

The two force extrema occur under distinct instantaneous flow conditions. Their associated pressure, free-surface, and mass-fraction fields are presented in Figures 5.35–5.37. Because the paddle-hull simulation was performed at a single grid resolution, these extrema are reported as observed single-grid responses rather than grid-convergence-verified quantities.

The flow structure surrounding the paddle-hull system is examined using complementary front and top views at eight instants spanning the stroke, $\tau_c \approx 5\%, 10\%, 30\%, 35\%, 55\%, 60\%, 80\%$, and 95% (Equation (5.13)). Figure 5.29 presents the first four instants, covering the approach and drive up to just past peak force. Figure 5.30 presents the remaining four, covering the interval either side of release through recovery. For each instant, the standalone paddle is compared directly with the paddle-hull configuration. The front view provides information on paddle position, free-surface elevation, and transverse flow structure.

Figure 5.31 presents the corresponding top views. These show the horizontal wake development, paddle trajectory, and relative position of the hull and paddle wake. In the paddle-hull sequence the paddle-generated disturbance is convected downstream from the paddle path and reaches the adjacent hull region. The later frames show that this wake no longer occupies a flow field independent of the hull. It intersects the hull-side free-surface and pressure disturbance before leaving the domain. This is direct qualitative confirmation of paddle-hull interaction. It does not quantify the separate contributions of vorticity, radiated pressure, or wave elevation to the hull-force signal.

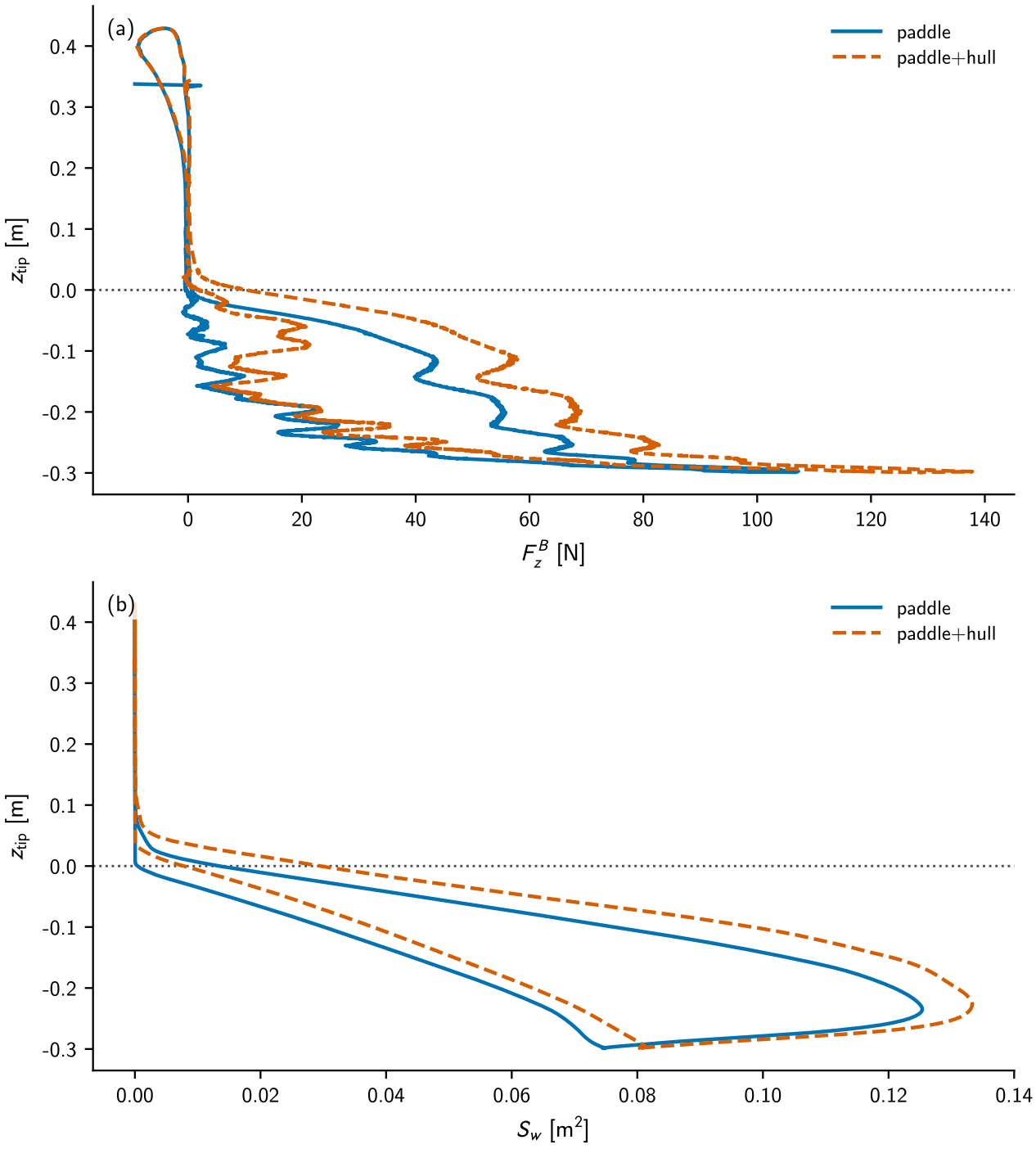

Figure 5.28: Paddle-tip elevation against paddle-normal force (upper panel) and wetted area (lower panel), comparing the standalone paddle with the paddle-and-hull computation.

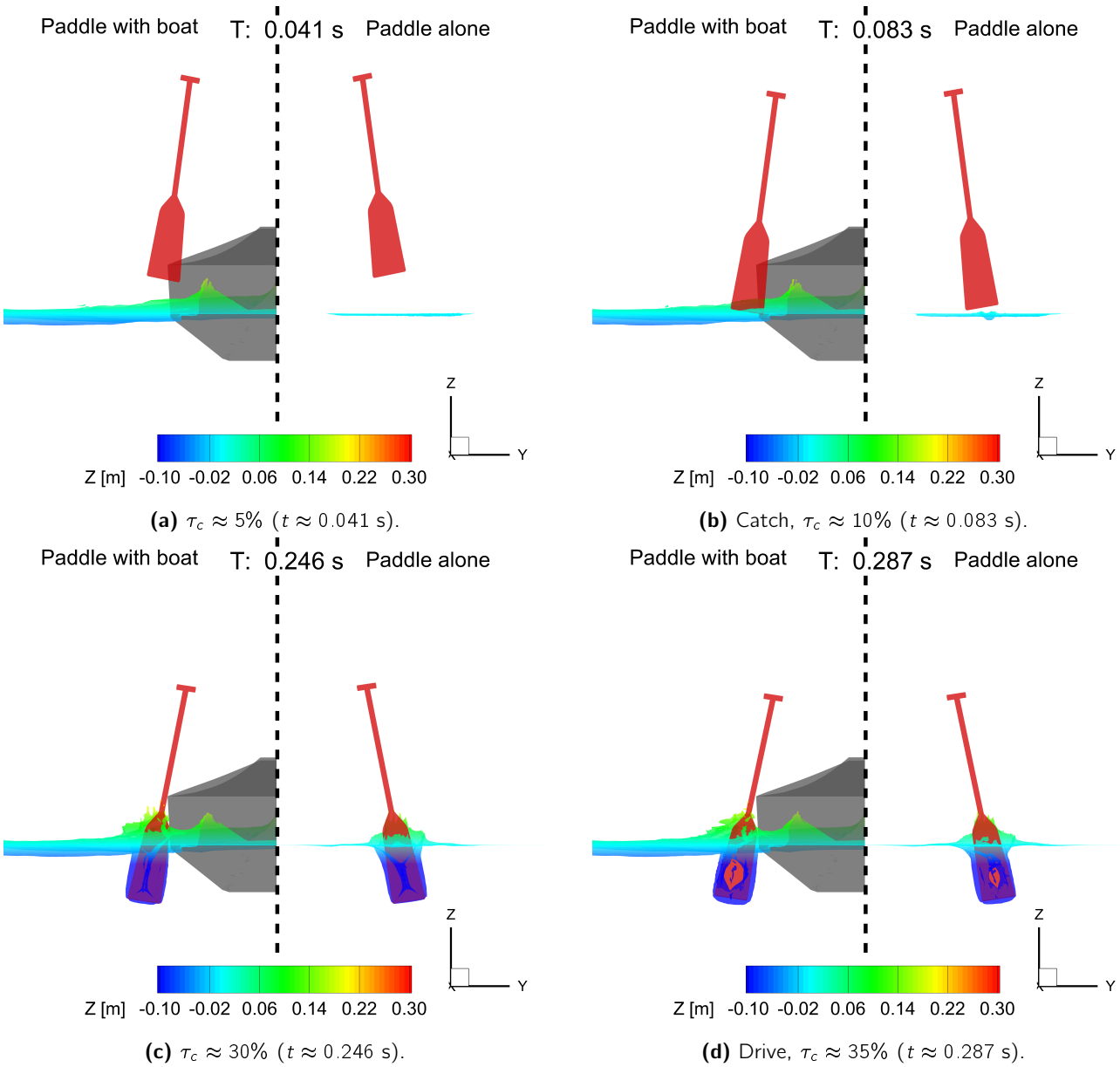

(a) $\tau_c \approx 5\%$ ($t \approx 0.041$ s). **(b)** Catch, $\tau_c \approx 10\%$ ($t \approx 0.083$ s).

(c) $\tau_c \approx 30\%$ ($t \approx 0.246$ s). **(d)** Drive, $\tau_c \approx 35\%$ ($t \approx 0.287$ s).

Figure 5.29: Front-view standalone and paddle-hull states from approach through drive.

5.4.3 Hull pressure-force comparison for standalone-versus-paddle-hull

The paddle-hull simulation contains paddle-generated pressure disturbances, wake-induced flow, and free-surface deformation absent from the boat-alone simulation. The following comparison places the two computed hull responses side by side without assigning a force difference to one mechanism.

Two configurations are considered, (1) the Type 3 paddle-hull simulation, in which the paddle and boat undergo prescribed forward motion, and (2) the Type 2 fixed-step boat-alone simulation, in which the boat undergoes oscillating surge without the paddle (Section 5.3, Section 5.3.3). Both histories are analysed from $t = 15$ s onward, following completion of the acceleration phase. The comparison should nevertheless be read as qualitative context. Type 3 uses Euler flow modelling and Courant-controlled stepping, whereas the selected Type 2 reference uses k–ω SST, and the paddle-hull simulation has no grid-convergence series.

The comparison considers the magnitude and temporal variation of the hull axial force in the two configurations, including the differences in their force histories. The two simulations use different configurations and therefore do not provide a controlled basis for attributing the observed differences to a specific

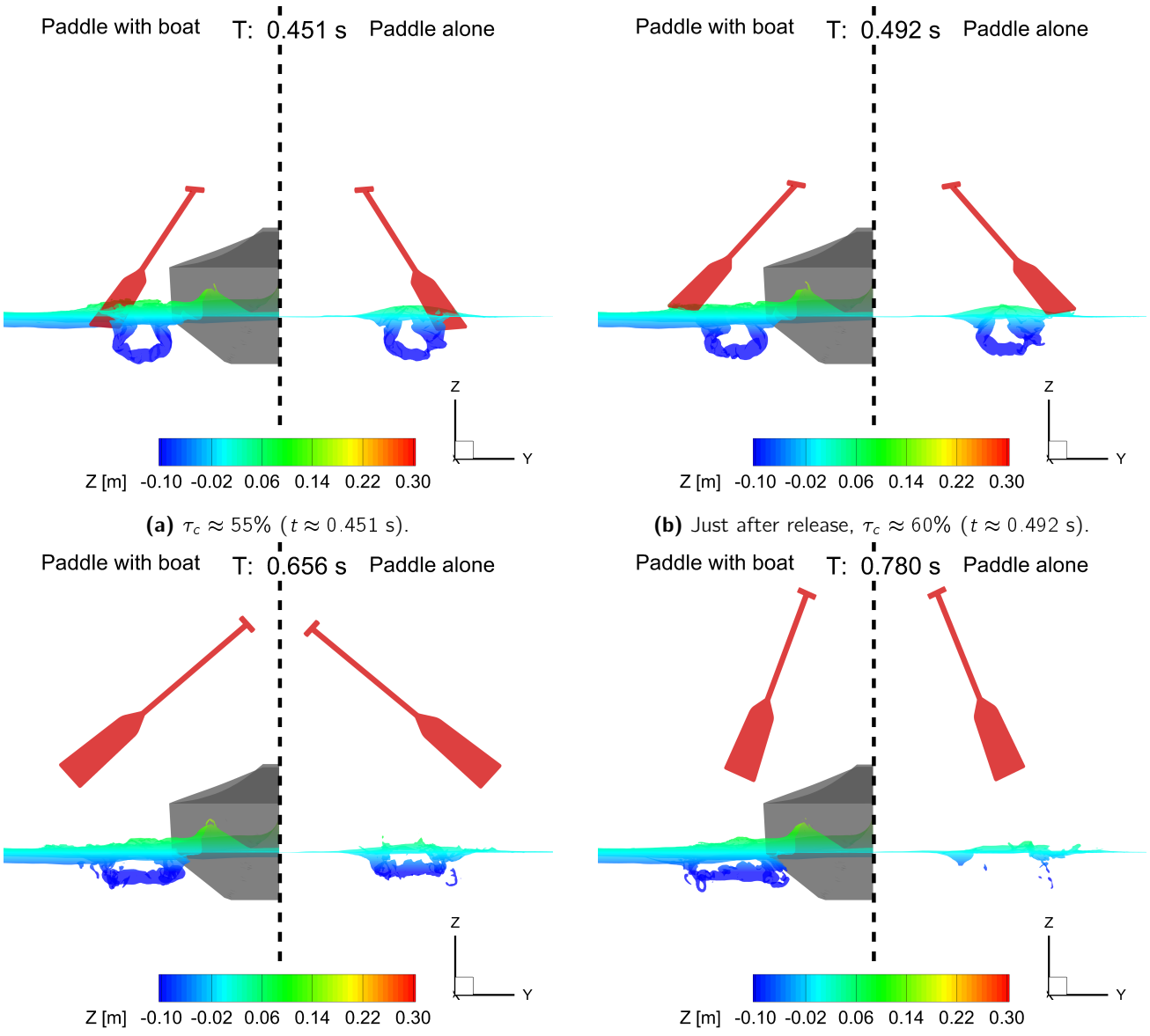

(a) $\tau_c \approx 55\%$ ($t \approx 0.451$ s).

(b) Just after release, $\tau_c \approx 60\%$ ($t \approx 0.492$ s).

(c) Recovery, $\tau_c \approx 80\%$ ($t \approx 0.656$ s).

(d) Late recovery, $\tau_c \approx 95\%$ ($t \approx 0.780$ s).

Figure 5.30: Front-view comparison of standalone and hull-adjacent paddle flow from late drive, through release, to late recovery.

cause. Figure 5.32 compares the paddle-normal force F_z^B with the hull axial force $F_x(\text{Boat})$ to examine their relative timing during the stroke.

Figure 5.33 compares paddle-tip elevation with the paddle and hull forces for the standalone and paddle-hull configurations, showing how force generation varies with paddle immersion.

Figure 5.34 compares the hull pressure-force component R_P between the standalone and paddle-hull cases to identify differences in the magnitude and temporal evolution of the hull loading.

To provide flow-field context for the force spikes identified in the time-series results, three complementary visualisations are examined at the same selected instants. The selected times correspond to the hull force-spike events, allowing the force response to be considered alongside the instantaneous free-surface and pressure fields.

Figure 5.35 presents top-view free-surface elevation at six instants distributed over the three simulated strokes. The images show the spatial development of the free-surface disturbance associated with the paddle and its interaction with the existing hull-wave system.

Figures 5.36 and 5.37 provide corresponding side-view pressure and free-surface mass-fraction fields.

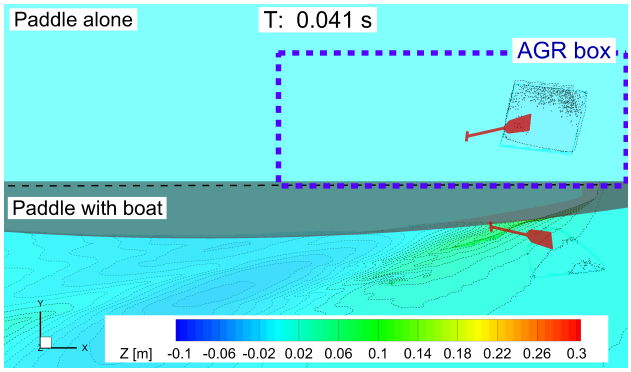

(a) $\tau_c \approx 5\%$ ($t \approx 0.041$ s).

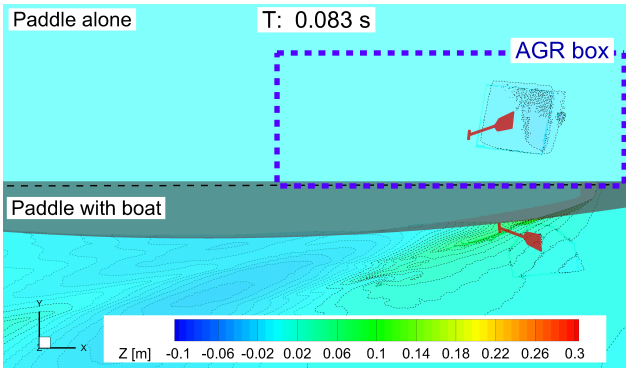

(b) Catch, $\tau_c \approx 10\%$ ($t \approx 0.083$ s).

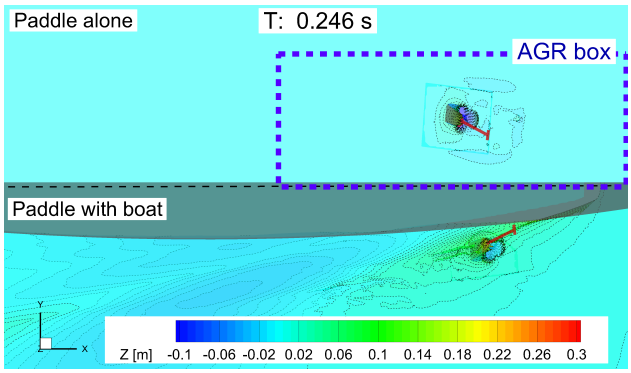

(c) $\tau_c \approx 30\%$ ($t \approx 0.246$ s).

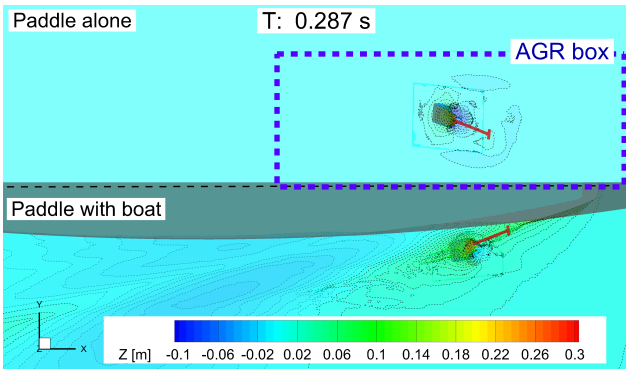

(d) Drive, $\tau_c \approx 35\%$ ($t \approx 0.287$ s).

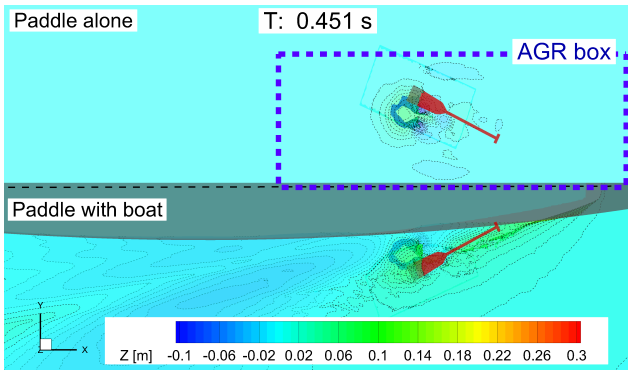

(e) $\tau_c \approx 55\%$ ($t \approx 0.451$ s).

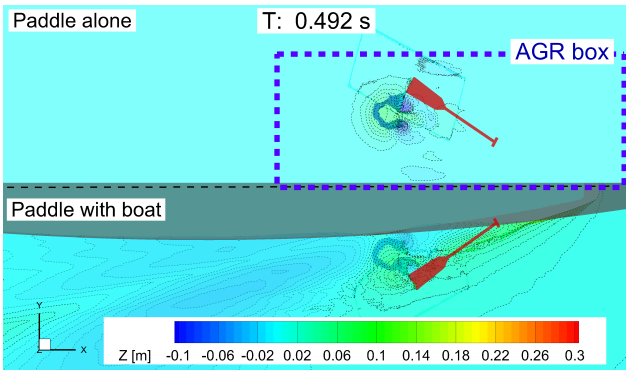

(f) Just after release, $\tau_c \approx 60\%$ ($t \approx 0.492$ s).

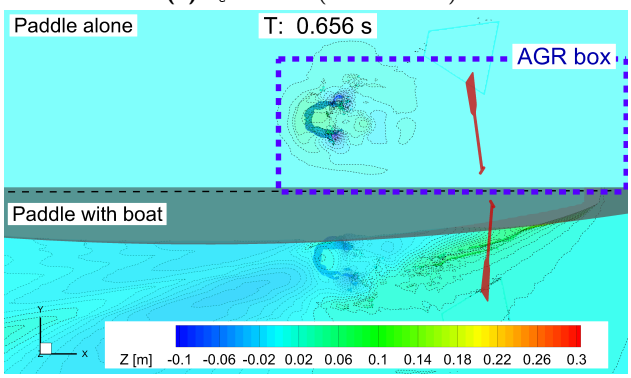

(g) Recovery, $\tau_c \approx 80\%$ ($t \approx 0.656$ s).

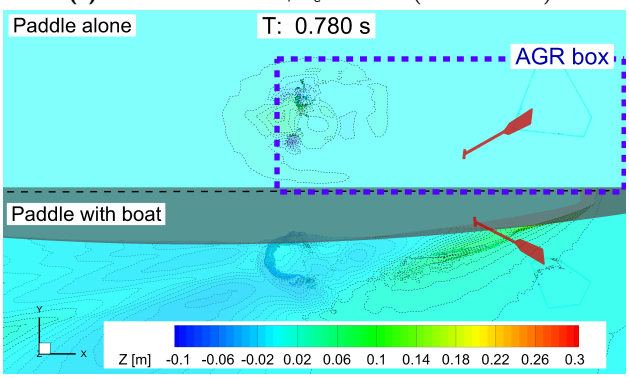

(h) Late recovery, $\tau_c \approx 95\%$ ($t \approx 0.780$ s).

Figure 5.31: Top-view comparison of standalone and hull-adjacent paddle wakes over the same eight stroke instants as Figures 5.29 and 5.30.

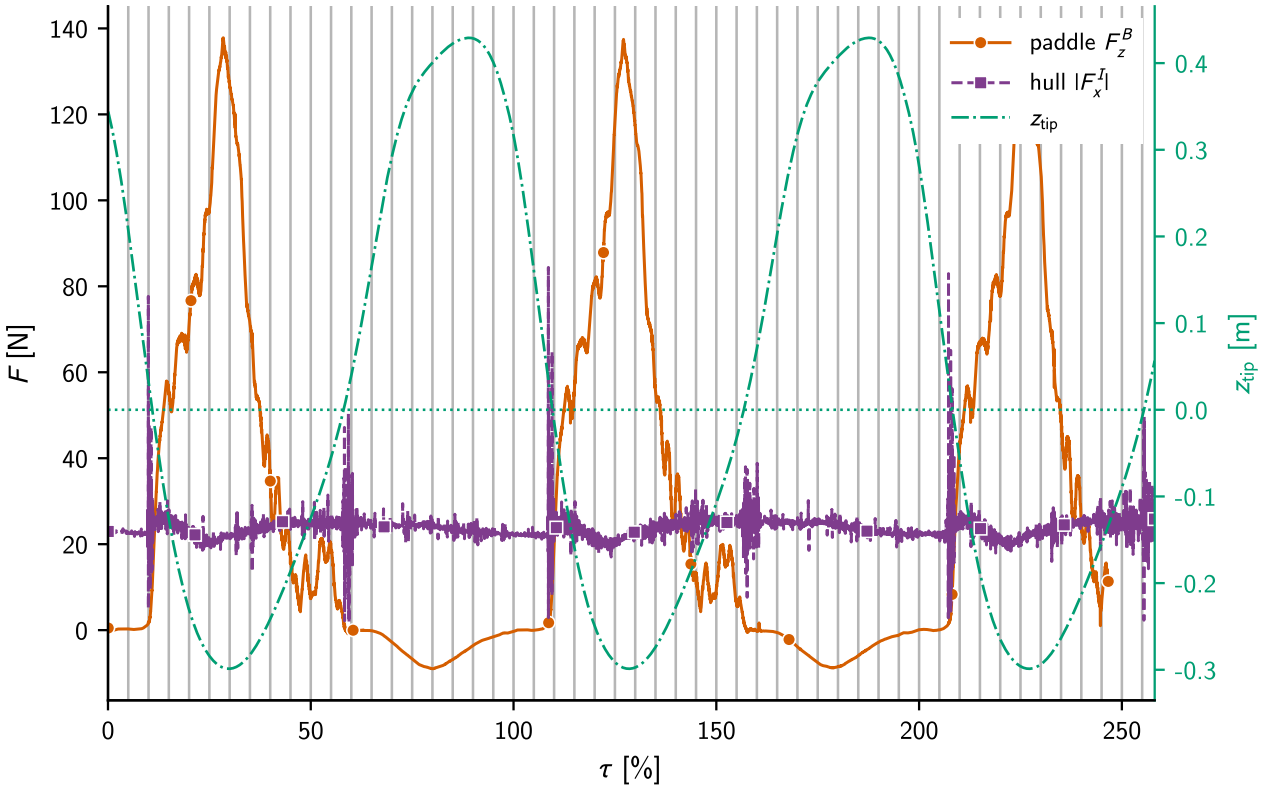

Figure 5.32: Paddle force and positive hull resistance in the paddle-hull configuration, using all available stroke data, with vertical lines marking five-percent phase intervals.

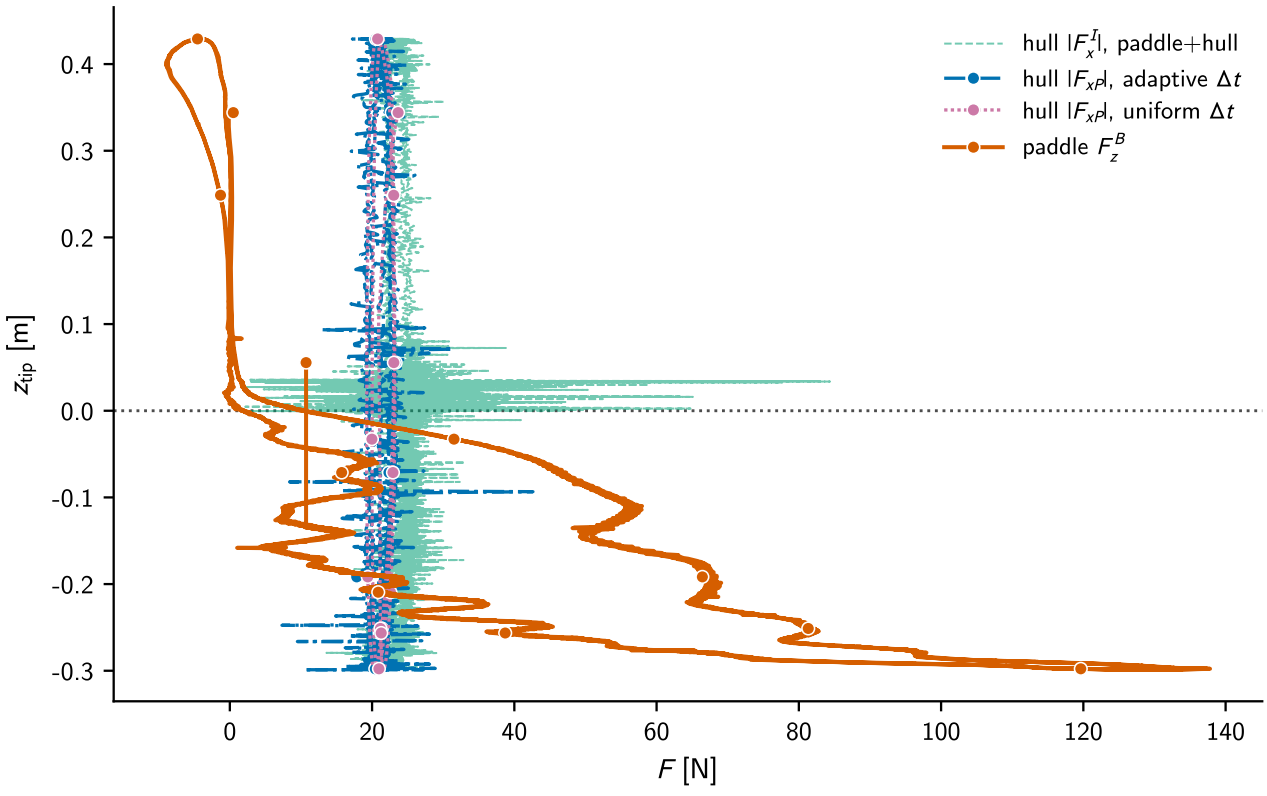

Figure 5.33: Paddle-tip elevation against paddle and hull force for all available paddle-hull-configuration stroke data.

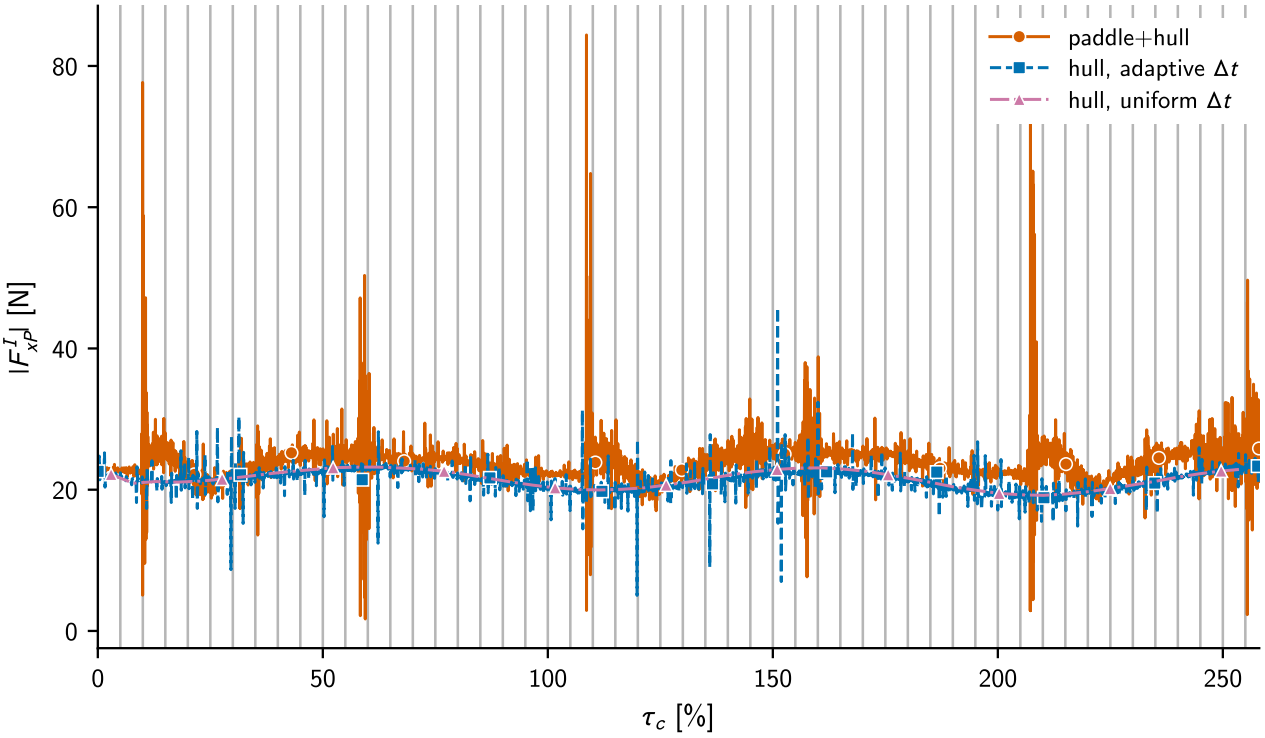

Figure 5.34: Hull pressure-force comparison for standalone and paddle-hull configurations.

The pressure plots show the instantaneous pressure distribution on the paddle and hull, while the mass-fraction plots identify the air–water interface and the extent of local submergence and free-surface deformation.

For the hull, the pressure distribution indicates how the hull loading changes during the paddle stroke. The mass-fraction fields provide additional geometric context for interpreting the instantaneous paddle immersion and free-surface state.

A recurring feature of the hull-force spikes identified above is that they occur near catch and release, that is, when the paddle-tip elevation $z_{\text{tip}}(t)$ is close to the free surface and the paddle immersion is near zero (Figure 5.33). At near-zero immersion the paddle geometry, its overset-grid interface, and the hull waterline are in close geometric proximity. The multisurface–flux-component-Hessian AGR criterion used for the paddle-hull configuration (Section 3.6.1, Equation (3.18)) responds to this proximity by adding refinement on the hull surface in the vicinity of the paddle, not only on the paddle and its wake [21–24]. The resulting local change in cell size and overset donor cells at the paddle-hull interface is one mechanism for the hull-force spikes, independent of any underlying hydrodynamic transient. In addition to this proximity-driven refinement effect, the paddle wake itself, once shed and convected toward the hull, modifies the local pressure and free-surface state seen by the hull, so that the force signal also changes through wake–hull interaction, as shown in the top-view free-surface development of Figure 5.35 and the paddle-and-hull force comparison of Figure 5.32. The pressure and mass-fraction fields of Figures 5.36 and 5.37 provide the corresponding local flow context for each spike instant. Neither mechanism is isolated from the other in the present single-grid simulation, and both are reported as flow-field-supported observations rather than a quantitatively separated force decomposition.

5.4.4 Numerical scope and limits of the paddle-hull configuration

For both the paddle-hull and boat-alone simulations, the analysis begins at $t = 15$ s, following completion of the acceleration phase. The displayed time coordinate is shifted according to $t' = t - 15$. The time-step axis is shown on a logarithmic scale to capture the full range of the Courant-controlled time-step response.

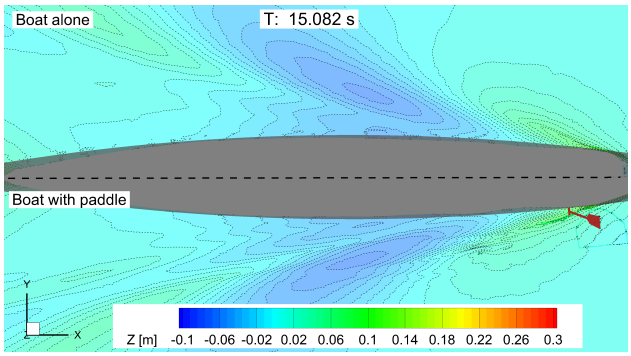

(a) $\tau_c \approx 10\%$ ($t \approx 0.082$ s).

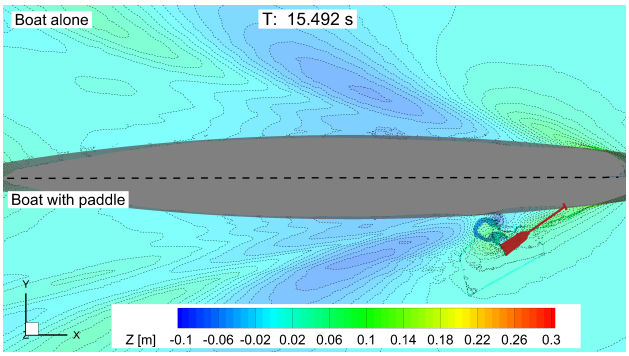

(b) $\tau_c \approx 60\%$ ($t \approx 0.492$ s).

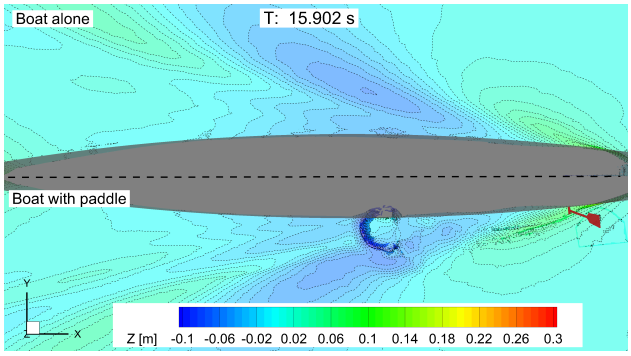

(c) $\tau_c \approx 110\%$ ($t \approx 0.902$ s).

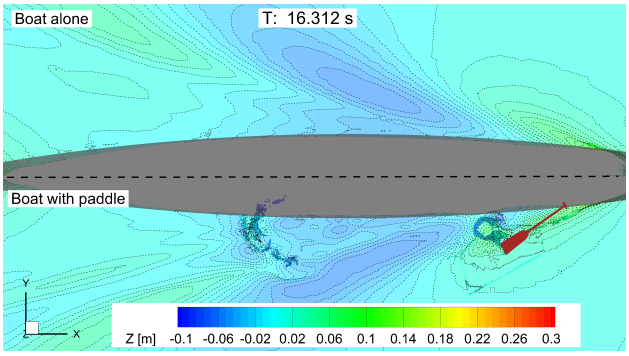

(d) $\tau_c \approx 160\%$ ($t \approx 1.312$ s).

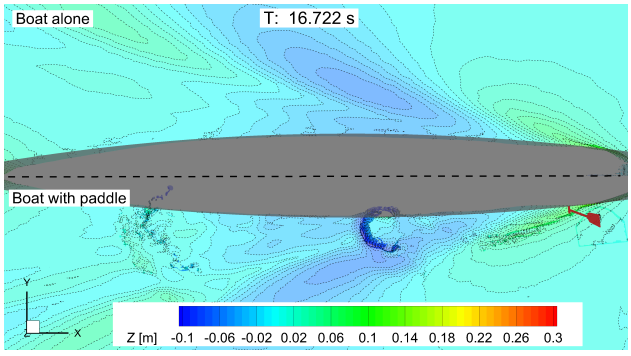

(e) $\tau_c \approx 210\%$ ($t \approx 1.722$ s).

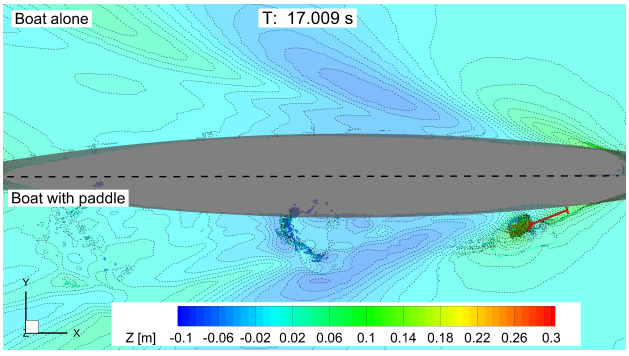

(f) $\tau_c \approx 245\%$ ($t \approx 2.009$ s).

Figure 5.35: Top-view free-surface contours at six paddle-hull boat-force spikes.

Figure 5.38 compares the cell-count and time-step histories for the paddle-hull and standalone configurations.

Table 5.8: Spatial and temporal workload descriptors over the common post-acceleration interval.

Case	Mean cells [10^6]	Peak cells [10^6]	Median Δt [ms]
paddle+hull	1.766	2.634	0.186
paddle	0.644	0.929	0.192
hull, adaptive dt	0.521	0.549	0.695

The time-step histories identify the paddle as the active temporal constraint. The standalone paddle and paddle-hull cases have median accepted steps of 0.192 and 0.186 ms, respectively, a difference of only 3.1%. Removing the paddle raises the adaptive hull median to 0.695 ms. The paddle-hull case therefore does not take smaller steps because the hull has been added. It needs the step required to transport the moving paddle, its overset interface, and the sharply deformed free surface.

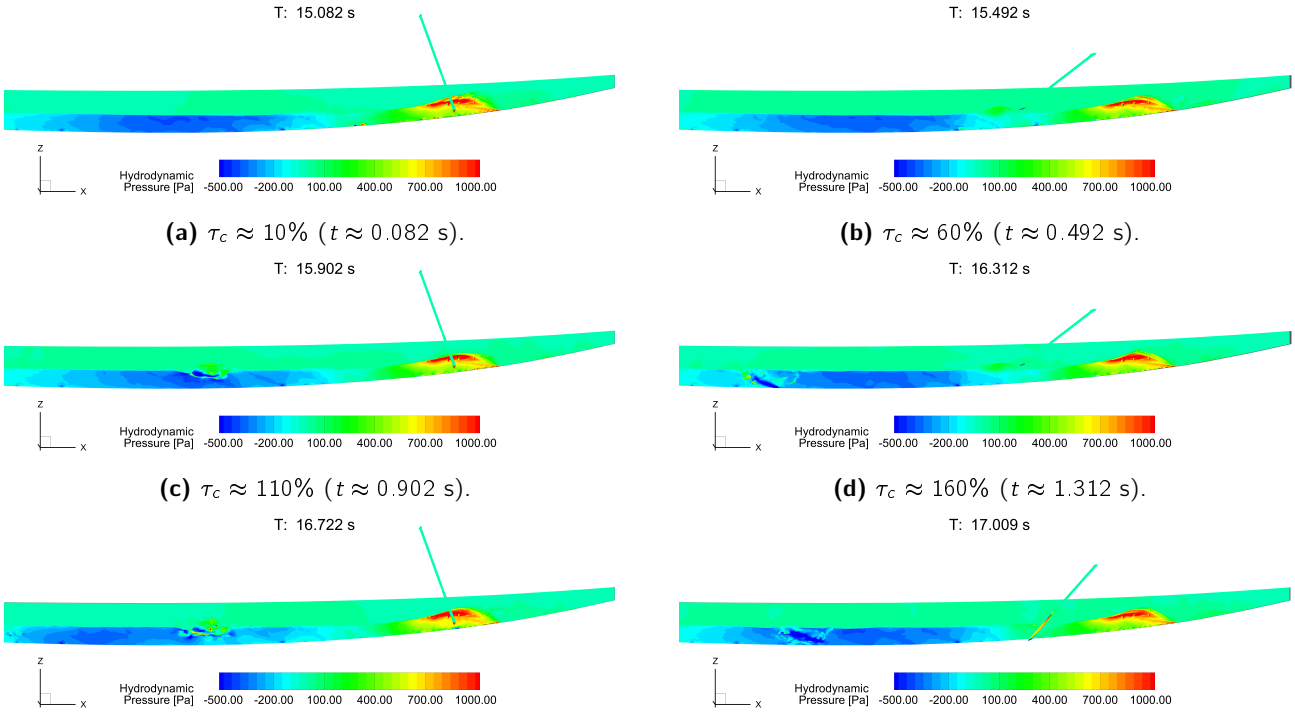

(a) $\tau_c \approx 10\%$ ($t \approx 0.082$ s). **(b)** $\tau_c \approx 60\%$ ($t \approx 0.492$ s).

(c) $\tau_c \approx 110\%$ ($t \approx 0.902$ s). **(d)** $\tau_c \approx 160\%$ ($t \approx 1.312$ s).

(e) $\tau_c \approx 210\%$ ($t \approx 1.722$ s). **(f)** $\tau_c \approx 245\%$ ($t \approx 2.009$ s).

Figure 5.36: Paddle and hull pressure at six paddle–hull boat-force spikes.

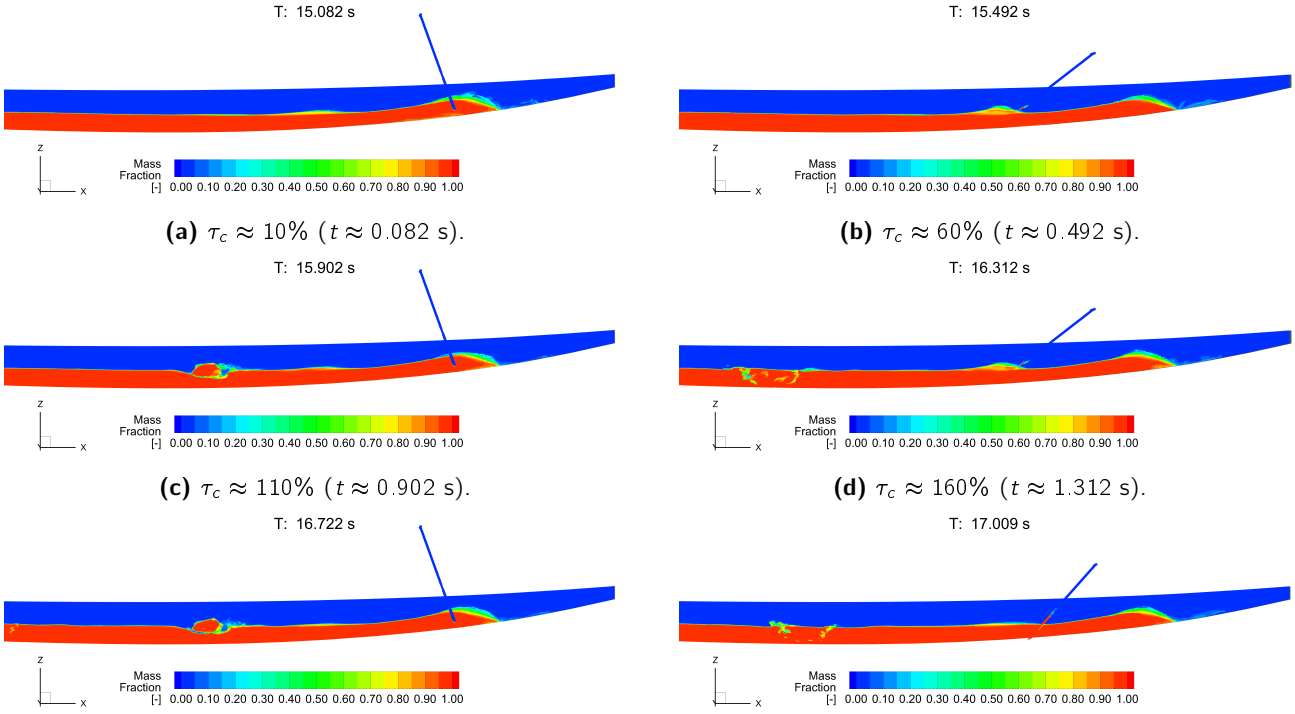

(a) $\tau_c \approx 10\%$ ($t \approx 0.082$ s). **(b)** $\tau_c \approx 60\%$ ($t \approx 0.492$ s).

(c) $\tau_c \approx 110\%$ ($t \approx 0.902$ s). **(d)** $\tau_c \approx 160\%$ ($t \approx 1.312$ s).

(e) $\tau_c \approx 210\%$ ($t \approx 1.722$ s). **(f)** $\tau_c \approx 245\%$ ($t \approx 2.009$ s).

Figure 5.37: Side-view free-surface contours at six paddle-hull boat-force spikes.

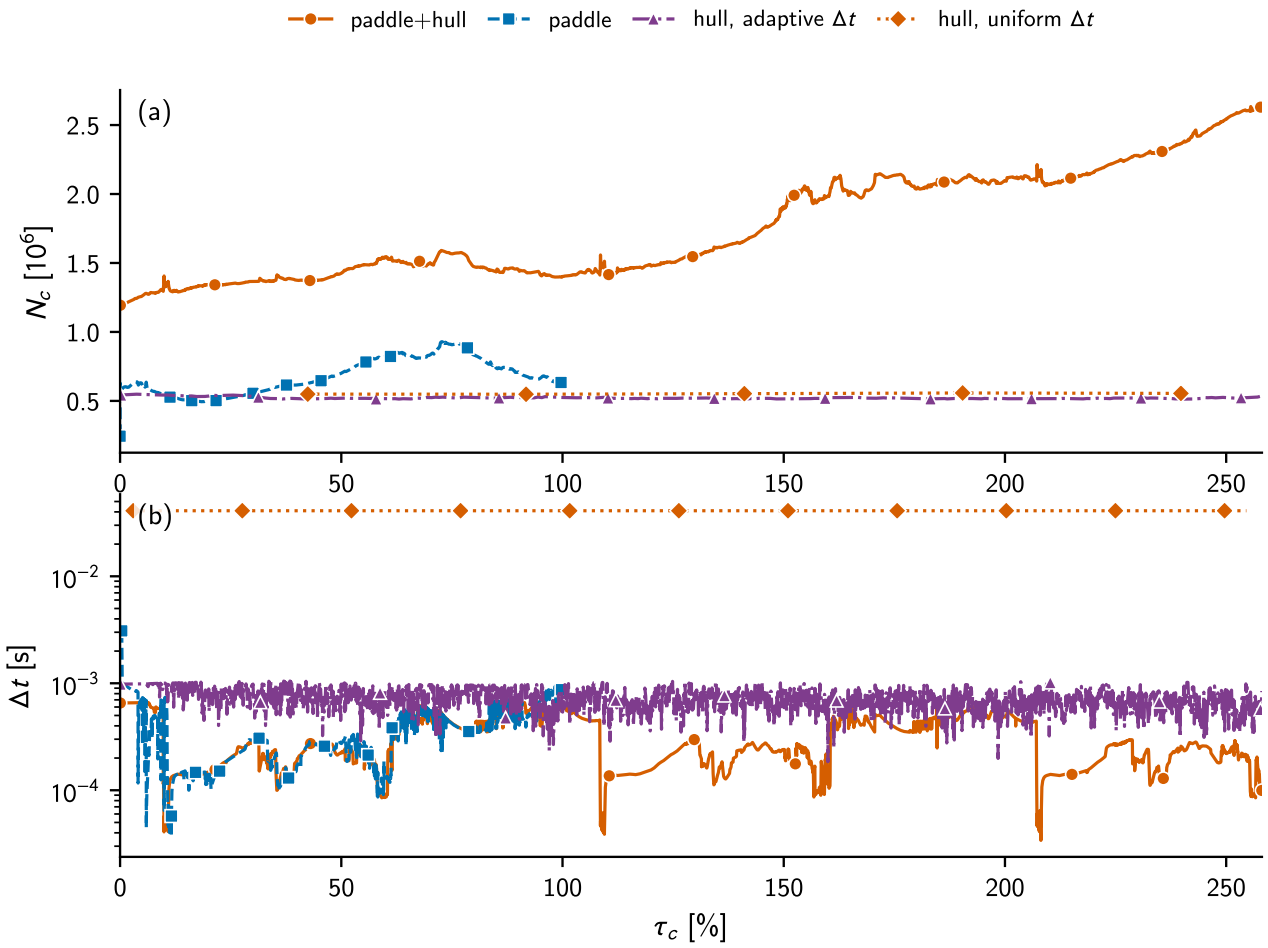

Figure 5.38: Cell-count and time-step histories for the paddle-hull and standalone cases.

This behaviour is consistent with Robert et al. [5], who found that the compressive free-surface scheme in a realistic rowing-blade simulation imposed a restrictive interface Courant limit. They accelerated their cases with volume-fraction sub-cycling. The present test run found no useful reduction in cost or change in the resolved load/interface history, so the paddle and paddle-hull configurations use no sub-cycling. The nearly coincident time-step histories in Figure 5.38 show that this decision affects two paddle-controlled cases in the same way. The paddle–hull case contains 1.77 million cells on average and reaches 2.63 million, compared with 0.64 and 0.93 million for the standalone paddle. As the paddle wake is convected downstream, it remains within the computational domain and continues to fall within the adaptive grid-refinement criterion when the paddle begins the next stroke. AGR therefore refines the wake from the preceding stroke while also resolving the free surface and paddle region of the current stroke. The refined portion of the domain consequently grows over successive strokes rather than returning to its initial size, increasing the average cell count by a factor of 2.74. The time-step size remains nearly unchanged, so the higher computational cost of the paddle–hull simulation arises primarily from the additional cells required to resolve the convecting paddle wake. The cell-count histories indicate this increase in relative cost, although the actual wall-clock time also depends on the number of solver iterations. The computational cost of all simulated cases is reported in Table A.1 in the appendix.

5.4.5 Paddle-hull flow interaction, discussion and scope

The standalone-paddle Euler case is used as the reference for comparison with the paddle-hull configuration because both use the same prescribed paddle motion and advance speed, with the nearby hull being the

main difference. The timing of the force development remains almost unchanged. The time from water contact to peak force differs by less than 0.3% of the stroke period, or less than 2 ms, showing that the presence of the hull does not noticeably shift the phase at which the paddle reaches its maximum load.

The main differences appear in the force magnitude. The peak paddle-normal force increases by 28.5%, from 107.2 N to 137.8 N, while the RMS force increases by 25.2% (Table 5.7). The conditional-positive mean increases by 15.8%, whereas the propulsive impulse increases by 34.3%, from 16.36 N s to 21.52 N s. The larger increase in impulse is partly explained by the longer period over which the paddle remains wetted, with the paddle-in-water ratio increasing from 43.0% to 47.6% (Table 5.5). The force-development rate also increases from 576 to 702 $\mathrm{N\,s^{-1}}$, showing that the force rises more rapidly in the paddle-hull case.

These results indicate that the nearby hull increases the paddle load in two ways. It increases the force level and also increases the duration over which the paddle remains loaded. Both effects contribute to the 34.3% increase in propulsive impulse.

The front-view flow-field comparisons already presented in Section 5.4.2, Figures 5.29 and 5.30, offer a specific mechanism for the increased paddle load. The prescribed paddle kinematics, and therefore the paddle-tip elevation $z_{\mathrm{tip}}(t)$ of Equation (4.32) (Section 4.5.6), are identical between the standalone and paddle-hull runs, since both are driven by the same reconstructed trajectory and advance law. What differs is the free surface the blade meets. In the standalone case the blade enters a free surface fixed at the calibrated datum $z_{\mathrm{fs}} = 0$ (Section 5.1.4), whereas in the paddle-hull case the local free surface at the paddle location is displaced by the hull's own divergent wave system, so that the local elevation $z_{\mathrm{fs}}^{\mathrm{loc}}(t)$ departs from the flat datum. The effective blade immersion is therefore

$$d_{\mathrm{eff}}(t) = z_{\mathrm{fs}}^{\mathrm{loc}}(t) - z_{\mathrm{tip}}(t), \tag{5.15}$$

which reduces to the standalone immersion $d(t) = -z_{\mathrm{tip}}(t)$ only when $z_{\mathrm{fs}}^{\mathrm{loc}} = 0$. Because $z_{\mathrm{tip}}(t)$ is unchanged between the two cases, an increase in effective immersion requires $z_{\mathrm{fs}}^{\mathrm{loc}}(t) > 0$ at the paddle location. This is consistent with the free surface visibly raised and disturbed around the blade in the paddle-hull frames of Figures 5.29 and 5.30, relative to the corresponding standalone frames at the same stroke phase.

The greater effective immersion increases the wetted area presented to the flow at a given stroke phase and is consistent with the higher paddle-in-water ratio (47.6% against 43.0%, Table 5.5) and with the higher force level reported above.The present simulation is consistent with this mechanism, with a locally elevated free surface producing greater blade immersion and higher load at matched stroke phase in the paddle–hull configuration. However, the present setup uses prescribed surge motion, an Euler formulation, a calibrated vertical reference, and a single paddle–hull grid. These limitations prevent a reliable calculation of propulsive efficiency, a unique separation of the different force contributions, or an estimate of numerical uncertainty for the paddle-hull case.

Crew-thrust order-of-magnitude check using the propulsive cycle mean. The peak comparison above says nothing about whether a crew can maintain the modelled speed continuously, because a single paddle does not load continuously. The prescribed oscillating-surge advance law (Equation (4.16), Section 4.4) varies the boat speed between approximately 11 and 12 $\mathrm{km.h^{-1}}$ over each stroke rather than holding a fixed value, and it produces zero forward-driving force whenever it is out of the water. The appropriate quantity for that question is the cycle-averaged propulsive force $\overline{F}_{\mathrm{prop}}$ of Equation (4.44) (Section 4.5.6), which credits zero force for the unloaded portion of the stroke instead of either restricting the average to the loaded duration, as the conditional-positive mean $\overline{F_z^{B+}}$ does, or omitting the zero-clipping altogether, as the plain impulse rate I_z^B/T_s does. This metric is defined and evaluated independently of the Gomory/Galipeau literature descriptors of Section 4.5.6, for the reason given in Section 4.5.6. Restricting the same zero-clipped integral to the detected catch-to-end-of-drive window instead recovers Gomory's propulsive impulse rate $\dot{I}_{\mathrm{prop}}$ (19.69 N standalone, 25.90 N paddle-hull, Table 5.5), and the close agreement between the two independently computed values is a consistency check on both, not a second, unrelated result. Evaluated over the full prescribed stroke, $\overline{F}_{\mathrm{prop}} = 19.8$ N for the standalone paddle and 26.0 N for the paddle-hull

configuration, both well below the peak values above, as expected since $\overline{F}_{\text{prop}}$ alone accounts for the paddle-in-water ratio of only 43.0% (standalone) and 47.6% (paddle-hull, Table 5.5). For the majority of the cycle the paddle contributes no forward-driving force, and $\overline{F}_{\text{prop}}$ is diluted by that unloaded portion of the stroke exactly as a continuous thrust-versus-resistance balance requires.

Multiplying the paddle-hull value by a ten-paddler crew gives an illustrative combined propulsive force of $10 \times 26.0 = 260$ N. Because the advance speed oscillates between approximately 11 and 12 km.h^{-1} rather than holding a fixed value, the calm-water resistance to compare against also spans a range over the same interval, from 137.7 N at 11 km.h^{-1} to 171.8 N at 12 km.h^{-1} (Table 5.6). The illustrative combined thrust therefore exceeds the calm-water resistance across the modelled speed range, by a margin of about 89% at the lower end of the range and about 51% at the upper end. Read as an order-of-magnitude check rather than a self-propulsion prediction, this is consistent with a crew of that size being able to maintain the modelled speed. The combined cycle-averaged thrust is not merely of the same order as the resistance it must overcome, it exceeds it with margin across the oscillating-surge range, which is the direction expected for a successfully self-propelled hull. The comparison carries no stronger claim than that. It assumes ten paddle positions each reproduce the single modelled paddle-hull interaction, with no allowance for along-hull variation in local wake and pressure field, no stroke-phase offset between paddlers, no coupling of the resulting thrust back into hull motion or added resistance, and no allowance for the resistance increase that a self-propelled (rather than towed, prescribed-motion) hull would actually see. No interaction between one paddler and another is modelled, and in practice each paddler faces a different free-surface state shaped by the wake left by the paddlers ahead of them, so the comparison is indicative only and cannot represent the along-hull variation in loading that a full crew would actually produce. The present single-paddle, single-stroke cases cannot, on their own, resolve the crew-level thrust balance to better than this order-of-magnitude level. Chapter 6 returns to this point as a target for future work.

Chapter 6

Conclusions and future work

6.1 Conclusions

This thesis applied high-fidelity CFD, already established across industry and, at LHEEA, for rowing [3–5], to dragon-boat paddling. The work examined how free-surface deformation, flow unsteadiness, and paddle-hull interaction shape the hydrodynamic force on a dragon-boat paddle blade during a measured stroke. Four case groups were considered. The first involved a standalone-paddle series comparing an inviscid Euler formulation against a viscous k–ω SST closure on a four-level Euler grid-refinement sequence. The second consisted of a bare-hull calm-water resistance sweep from 7 to 13 km,h^{-1}. The third involved a bare-hull oscillating-surge series with four spatial refinement levels and, a comparison between Courant-controlled and uniform time stepping. The fourth considered a paddle–hull configuration placing one paddle beside the hull under the same prescribed kinematics used for the standalone paddle. These results were compared with each other and, for the standalone paddle, with a phase-averaged on-water force history built from one athlete's five most consistent strokes. A single athlete and a single repeatable trajectory kept the comparison controlled and well documented, rather than adding the complexity of stroke-to-stroke and athlete-to-athlete variability to the same study. Within that scope, the computed flow reproduces the catch, drive, and exit phases that dominate a real dragon-boat stroke, providing a consistent basis for future comparisons of athlete technique.

Flow unsteadiness, expressed through the added-mass reaction to blade acceleration, is a defining feature of the standalone-paddle load. Because the pressure field satisfies an elliptic Poisson equation under the incompressible idealisation used here, that reaction tracks the acceleration field without a resolvable phase lag. Figure 5.16 shows the force and angular-acceleration fluctuations overlapping while the blade is wetted and decoupling the instant it is not, direct numerical confirmation of this mechanism rather than a general force-kinematics correlation over the whole cycle. The dominant force peak coincides with a small angular acceleration, so the velocity-dependent quasi-static term governs it. The smaller force ripples that follow, and the loss of force response the instant the blade leaves the water, carry the added-mass signature instead, since that term needs both blade acceleration and a submerged surface to react against. A purely quasi-static force model, which omits the acceleration-dependent term by construction, would reproduce the catch and drive-phase peak but miss this behaviour near blade entry and exit.

Viscosity plays a secondary role in the peak and root-mean-square paddle-normal load. Removing it changes these two quantities by 2.74% and 1.55%, matching the pressure-dominated, largely inviscid character Leroyer et al. [3] reported for an oar blade under comparable conditions. Its effect concentrates instead near blade exit. The paddle kinematics and geometric immersion duration are identical between the viscous and Euler runs, yet the viscous solution separates from the blade earlier, cutting the effective paddle-in-water ratio from 43.0% to 36.3%. That earlier separation compresses a nearly unchanged propulsive impulse, differing by only 0.9%, into a shorter drive phase, producing a 27% difference in average drive force despite a peak-force difference under 3%. Viscosity was found to leave the overall load magnitude largely unchanged but shorten the window over which the blade drives the boat forward.

The calm-water resistance sweep gives the reference hull loading used throughout the rest of this chapter. Resistance rises from 49.63 N at 7 km.h^{-1} to 229.92 N at 13 km.h^{-1}, while the frictional share falls from 82.48% to 58.37% as wave-making resistance grows with speed.

The oscillating-surge series adds two further bare-hull checks, one spatial and one temporal, neither a formal discretisation-uncertainty study. The spatial check compares the hull-force history across four threshold levels, $T_{rH}/L = 0.20$, 0.15, 0.10, and 0.05, and establishes the force signal's sensitivity to spatial resolution. It does not extend the paddle's grid-convergence-index treatment to the hull. The temporal check compares Courant-controlled adaptive stepping against a uniform time step at fixed spatial resolution and finds that the uniform time step produces a smoother force history with reduced fluctuations. That difference has a specific numerical cause. The compressive volume-of-fluid interface stays sharp only while it crosses about one cell or less per time step, and a uniform step large enough to violate that limit pushes the boundedness limiter toward its diffusive branch. The same large step also weakens the momentum-interpolation coefficient that couples pressure and velocity in the collocated formulation. Since the reported hull force is the pressure integral over the wetted surface, both effects smooth the resolved force before it reaches that integral. The uniform-step calculation looks steadier because the numerics filter part of the interface dynamics, not because the underlying hull response is intrinsically steadier, consistent with the mechanism Leroyer et al. [3] identified in their free-surface-resolved oar computation.

This finding is specific to the bare-hull oscillating-surge case and does not carry over to the paddle or paddle-hull configurations. Both already run with Courant-controlled adaptive time stepping throughout, the same scheme identified above as the more accurate of the two, so no equivalent fixed-step comparison applies to them. The standalone-paddle and paddle–hull configurations have median time steps of 0.192 and 0.186 ms, respectively, differing by only 3.1%. In contrast, the bare-hull configuration has a median adaptive time step of 0.695 ms. The paddle motion, not the hull, sets the active temporal constraint in both cases, and both already resolve it at the finer, Courant-controlled resolution that this section identifies as the more accurate choice. The paddle–hull configuration shows how the nearby hull alters the blade loading. The peak and RMS paddle-normal forces increase by 28.5% and 25.2%, respectively, while the propulsive impulse, which is particularly sensitive to the duration of loading, increases by 34.3%. This increase results from both a higher instantaneous force level and a longer loading interval, with the paddle-in-water ratio increasing from 43.0% to 47.6%. Because the prescribed blade kinematics are identical in the two configurations, the change is attributed to the modified local free-surface environment. The hull's divergent wave system raises the local free surface at the blade location, increasing the effective blade immersion relative to the standalone case at the same stroke phase, as also indicated by the front-view flow-field comparisons.

Hull-force spikes recur near catch and release, when the blade immersion is close to zero. Two features accompany the observed increase in cell count. Adaptive refinement responds to the geometric proximity of the blade, overset interface, and hull surface at these instants, while the paddle-generated disturbance subsequently reaches and interacts with the hull. Both features are identified from the flow field on a single paddle–hull grid. The changed immersion history and the absence of a matched viscous grid-refinement series prevent their individual effects from being quantified. The numerical peaks observed in the paddle–hull force history therefore remain unresolved and should be addressed in future work through dedicated sensitivity and grid-refinement studies.

The paddle–hull configuration uses Euler flow modelling, so its hull force contains no viscous contribution. Comparison with the boat-alone reference therefore uses only the reference pressure component, R_P (Section 5.4.3), rather than the total resistance, because the viscous component of the reference case has no counterpart in the inviscid paddle–hull simulation. The full calm-water resistance curve, including both pressure and viscous contributions, is reserved for the separate thrust-versus-resistance comparison below, where the physically relevant quantity is the total resistance that must be overcome.

Because a single blade drives the boat forward only while wetted, the physically relevant load for a continuous thrust balance is not the peak force but the cycle-averaged propulsive force, over the whole stroke period with zero substituted whenever the blade is unloaded (Section 4.5.6). This cycle mean is 19.8 N for the standalone paddle and 26.0 N for the paddle-hull configuration, both far below the peak

because the blade carries load for under half the stroke period. Scaled to an indicative ten-paddler crew, the combined paddle-hull cycle-mean thrust, 260 N, exceeds the total calm-water resistance across the modelled speed range, by about 89% at 11 km.h^{-1} and about 51% at 12 km.h^{-1}. Read strictly as an order-of-magnitude check rather than a self-propulsion prediction, this margin is consistent with a crew of that size maintaining the modelled speed. The comparison assumes every paddle position reproduces the single modelled paddle-hull interaction. It ignores interaction between paddlers, any stroke-phase offset between them, any coupling of the resulting thrust back into hull motion or added resistance, and the different free-surface state each paddler in practice faces from the wake left by paddlers ahead. It still provides a concrete, quantitative motivation for extending the present single-paddle framework to multi-paddle, crew-level simulations.

The only formal discretisation-uncertainty estimate in this thesis comes from the standalone-paddle Euler series, 0.45% for peak force and 0.11% for RMS force on the finest grid (Section 4.5.7), small enough that the viscous and paddle–hull effects reported above, each several times larger, substantially exceed the mesh sensitivity observed in this study. No comparable estimate exists for the bare hull, the viscous paddle case, or the paddle-hull configuration. The bare-hull spatial comparison checks the influence of four threshold levels on the force signal rather than establishing a discretisation uncertainty, and the paddle-hull configuration runs on a single grid.

The comparison against the measured on-water force history is calibration-informed rather than independently validated, because the trajectory's vertical datum was set by matching the computed and measured peak loads, while the inertial measurements alone could not determine this datum. Within that limit, the completed workflow reproduces the catch, drive, and exit structure of a measured dragon-boat stroke, resolves the added-mass and free-surface mechanisms a quasi-static model would miss, and reaches an encouraging level of agreement with the measured force history. This supports the central premise of the thesis that a transient, free-surface CFD workflow based on field-measured kinematics can provide flow information unavailable from on-water instrumentation alone, with the associated numerical uncertainty explicitly assessed rather than left unexamined. Appendix F reports a separate proof-of-concept structural coupling between ISIS-CFD and a geometrically exact beam solver, verified independently of the CFD results above and taken up again below as the basis for a future flexible-paddle extension.

6.2 Future work

The paddle–hull configuration requires a formal grid-convergence uncertainty estimate. This would require at least four spatial refinement levels with an inviscid paddle, using zero shear stress on the paddle surface, coupled to the viscous hull. Only with such a refinement series can the 28.5% peak-force and 34.3% impulse differences be reported with an associated uncertainty, as already done for the standalone-paddle series. Neither the standalone-paddle nor the paddle–hull configuration requires a matching temporal study, as both already use Courant-controlled adaptive stepping governed by the paddle motion, while the bare-hull comparison assessed the effect of the two time-stepping approaches.

The order-of-magnitude comparison between crew thrust and calm-water resistance motivates a specific extension toward a multi-paddle, crew-averaged model. Several prescribed paddle motions could be phased both with the stroke cycle and relative to one another to assess whether the crew-averaged thrust inferred from the present single-paddle loads can sustain the target speed against the computed resistance curve. A first step would extend the present framework to a full-crew simulation with prescribed motion for each paddler, applying the same kinematic approach used here at each crew position. Subsequently, the boat surge could be solved dynamically rather than imposed, with the resulting motion driven by the combined thrust generated by the paddles through the same dynamic coupling library used to transfer loads to BeamDyn in Appendix F. A stable load–motion exchange accounting for added-mass effects [26] would then remove the prescribed-surge assumption and allow the framework to predict self-propelled motion rather than the prescribed-surge response considered throughout this thesis.

The next measurement campaign should remove the force calibration from the trajectory validation.

Paddle position, orientation, force, and boat motion need one hardware-synchronised clock. Two calibrated cameras and a surveyed volume fixed to the boat can supply an independent blade path, and a boat-mounted GNSS/INS unit can replace the manually fixed heading. Measuring the free surface near the blade gives immersion directly, letting the added-mass and quasi-static decomposition proposed above be checked against measured kinematics instead of only computed ones. The force sensor needs static and dynamic calibration before and after each trial, and two working paddle sensors across several athletes would separate stroke variability from sensor error, supplying the population of strokes that the present single-athlete, single-stroke study does not attempt to represent.

The reconstruction, meshing, and solution workflow documented in Chapter 4 takes a phase-averaged six-degree-of-freedom paddle trajectory as its only case-specific input, so the same numerical environment can simulate a different athlete's stroke, or a different technique from the same athlete, once the corresponding inertial and force data exist, without further development. Once that population of strokes exists, a direct, comparative CFD assessment of paddling technique across athletes follows as the natural next study rather than a new development effort. Beyond that, the model can extend to multiple strokes, the dynamically coupled hull motion described above, and flexible-paddle coupling. Appendix F already reports the structural verification work completed toward that last step.

Bibliography

[1] Cadence Design Systems, Inc. FINE/Marine 12.1 User Guide. Software documentation, 2024. Document build 202402061531.

[2] International Dragon Boat Federation. History & culture. https://www.dragonboat.sport/about-us/history-culture/, 2026. Accessed: 19 August 2026. Cites nearly 50 million participants in China, over 300,000 in the UK and Europe, 90,000 in Canada and the USA, and organised competition in over 60 countries.

[3] Alban Leroyer, Sophie Barré, Jean-Michel Kobus, and Michel Visonneau. Influence of free surface, unsteadiness and viscous effects on oar blade hydrodynamic loads. *Journal of Sports Sciences*, 28(12):1287–1298, 2010.

[4] Alban Leroyer, Sophie Barré, Jean-Michel Kobus, and Michel Visonneau. Experimental and numerical investigations of the flow around an oar blade. *Journal of Marine Science and Technology*, 13(1):1–15, 2008.

[5] Yoann Robert, Alban Leroyer, Sophie Barré, Patrick Queutey, and Michel Visonneau. Validation of CFD simulations of the flow around a full-scale rowing blade with realistic kinematics. *Journal of Marine Science and Technology*, 24(4):1105–1118, 2019.

[6] Ernst Jan Grift, Mark J. Tummers, and Jerry Westerweel. Hydrodynamics of rowing propulsion. *Journal of Fluid Mechanics*, 918:A29, 2021.

[7] Alastair Campbell Ritchie and Mohammad Faizal Bin Selamat. Comparison of blade designs in paddle sports. *Sports Technology*, 3(2):141–149, 2010.

[8] Suzi R. Ho, Richard Smith, and Damien O'Meara. Biomechanical analysis of dragon boat paddling: A comparison of elite and sub-elite paddlers. *Journal of Sports Sciences*, 27(1):37–47, 2009.

[9] Joseph Alexander Gomory. The biomechanics of dragon boat paddling. Master's thesis, Victoria University, Melbourne, Australia, 2018. Research Master thesis, https://vuir.vu.edu.au/39512/.

[10] Cameron Galipeau. The on water instrumentation of a sprint canoe paddle. Master's thesis, McMaster University, Hamilton, Canada, 2018.

[11] Nicholas Caplan, Anna Coppel, and Trevor Gardner. A review of propulsive mechanisms in rowing. *Proceedings of the Institution of Mechanical Engineers, Part P: Journal of Sports Engineering and Technology*, 224(1):1–8, 2010.

[12] Dana Morgoch, Cameron Galipeau, and Stephen Tullis. Sprint canoe blade hydrodynamics – modeling and on-water measurement. *Procedia Engineering*, 147:299–304, 2016.

[13] Stephen Tullis, Cameron Galipeau, and Dana Morgoch. Detailed on-water measurements of blade forces and stroke efficiencies in sprint canoe. In *Proceedings of the 12th Conference of the International Sports Engineering Association*, volume 2, page 306, 2018.

[14] Anna Coppel, Trevor N. Gardner, Nicholas Caplan, and David M. Hargreaves. Simulating the fluid dynamic behaviour of oar blades in competition rowing. *Proceedings of the Institution of Mechanical Engineers, Part P: Journal of Sports Engineering and Technology*, 224(1):25–35, 2010.

[15] Andrew Sliasas and Stephen Tullis. Numerical modelling of rowing blade hydrodynamics. *Sports Engineering*, 12(1):31–40, 2009.

[16] Andrew Sliasas and Stephen Tullis. The dynamic flow behaviour of an oar blade in motion using a hydrodynamics-based shell-velocity-coupled model of a rowing stroke. *Proceedings of the Institution of Mechanical Engineers, Part P: Journal of Sports Engineering and Technology*, 224(1):9–24, 2010.

[17] Paul D. Groves. *Principles of GNSS, Inertial, and Multisensor Integrated Navigation Systems*. Artech House, Boston, 2nd edition, 2013.

[18] Sebastian O. H. Madgwick. An efficient orientation filter for inertial and inertial/magnetic sensor arrays. Technical report, University of Bristol, 2010.

[19] Patrick Queutey and Michel Visonneau. An interface capturing method for free-surface hydrodynamic flows. *Computers & Fluids*, 36(9):1481–1510, 2007.

[20] Alban Leroyer and Michel Visonneau. Numerical methods for RANSE simulations of a self-propelled fish-like body. *Journal of Fluids and Structures*, 20(7):975–991, 2005.

[21] Jeroen Wackers, Ganbo Deng, Alban Leroyer, Patrick Queutey, and Michel Visonneau. Adaptive grid refinement for hydrodynamic flows. *Computers & Fluids*, 55:85–100, 2012.

[22] Jeroen Wackers, Ganbo Deng, Emmanuel Guilmineau, Alban Leroyer, Patrick Queutey, and Michel Visonneau. Combined refinement criteria for anisotropic grid refinement in free-surface flow simulation. *Computers & Fluids*, 92:209–222, 2014.

[23] Jeroen Wackers, Ganbo Deng, Clémence Raymond, Emmanuel Guilmineau, Alban Leroyer, Patrick Queutey, and Michel Visonneau. Adaptive grid refinement for ship resistance computations. *Ocean Engineering*, 250:110969, 2022.

[24] Jeroen Wackers, Ganbo Deng, Emmanuel Guilmineau, Alban Leroyer, Patrick Queutey, Michel Visonneau, Alexandro Palmieri, and Alfredo Liverani. Can adaptive grid refinement produce grid-independent solutions for incompressible flows? *Journal of Computational Physics*, 344:364–380, 2017.

[25] Luís Eça and Martin Hoekstra. A procedure for the estimation of the numerical uncertainty of CFD calculations based on grid refinement studies. *Journal of Computational Physics*, 262:104–130, 2014.

[26] Camille Yvin, Alban Leroyer, Michel Visonneau, and Patrick Queutey. Added mass evaluation with a finite volume solver for applications in fluid structure interaction problems solved with co simulation. *Journal of Fluids and Structures*, 81:528–546, 2018.

[27] James Diebel. Representing attitude: Euler angles, unit quaternions, and rotation vectors. Technical report, Stanford University, 2006.

[28] Ganbo Deng, Patrick Queutey, Emmanuel Guilmineau, Alban Leroyer, Michel Visonneau, and Jeroen Wackers. Ship maneuvering simulation with CFD approach. In *25ème Congrès Français de Mécanique*, Nantes, France, 2022.

[29] Ismail B. Celik, Urmila Ghia, Patrick J. Roache, Christopher J. Freitas, Hugh Coleman, and Peter E. Raad. Procedure for estimation and reporting of uncertainty due to discretization in CFD applications. *Journal of Fluids Engineering*, 130(7):078001, 2008.

[30] Florian R. Menter. Two-equation eddy-viscosity turbulence models for engineering applications. *AIAA Journal*, 32(8):1598–1605, 1994.

[31] C. W. Hirt, A. A. Amsden, and J. L. Cook. An arbitrary Lagrangian–Eulerian computing method for all flow speeds. *Journal of Computational Physics*, 14(3):227–253, 1974.

[32] John J. Craig. *Introduction to Robotics: Mechanics and Control*. Pearson/Prentice Hall, Upper Saddle River, NJ, 3rd edition, 2005.

[33] GLiCID. Cluster Phileas and GLiCID Computing Facility. Online technical description, 2026. Accessed 10 August 2026.

[34] WitMotion Shenzhen Co., Ltd. WT9011DCL Bluetooth 5.0 9-Axis AHRS IMU Sensor: Datasheet and User Manual. Manufacturer datasheet used in the HKUST investigation, 2023.

[35] SciPy developers. scipy.interpolate.CubicSpline — SciPy reference guide. https://docs.scipy.org/doc/scipy/reference/generated/scipy.interpolate.CubicSpline.html, 2024. Periodic boundary condition used for phase-averaged resampling.

[36] International Canoe Federation. Icf competition rules: Dragon boats. https://www.canoeicf.com/sites/default/files/2025_icf_competition_rules_dragon_boats_final.pdf, 2025. Accessed: 10 August 2026.

[37] Long Liu, Hui-Hui Wang, Sen Qiu, Yun-Cui Zhang, and Zheng-Dong Hao. Paddle stroke analysis for kayakers using wearable technologies. *Sensors*, 21(3):914, 2021.

[38] Long Liu, Sen Qiu, ZheLong Wang, Jie Li, and JiaXin Wang. Canoeing motion tracking and analysis via multi-sensors fusion. *Sensors*, 20(7):2110, 2020.

[39] Daniel Geneau, Drew Commandeur, Ryan Brodie, Ming-Chang Tsai, Matt Jensen, and Marc Klimstra. The determination of on-water rowing stroke kinematics using an undecimated wavelet transform of a rowing hull-mounted accelerometer signal. *Sensors*, 24(18):6085, 2024.

[40] Johan Wahlström and Isaac Skog. Fifteen years of progress at zero velocity: A review. *IEEE Sensors Journal*, 21(2):1139–1151, 2021.

[41] Dewey H. Hodges. *Nonlinear Composite Beam Theory*. American Institute of Aeronautics and Astronautics, Reston, VA, 2006.

[42] Qi Wang, Jason Jonkman, Michael Sprague, and Bonnie Jonkman. BeamDyn user guide and theory manual. Technical report, National Renewable Energy Laboratory, Golden, CO, 2016.

[43] Qi Wang, Michael A. Sprague, Jason Jonkman, Nick Johnson, and Bonnie Jonkman. BeamDyn: a high fidelity wind turbine blade solver in the FAST modular framework. *Wind Energy*, 20(8):1439–1462, 2017.

Appendix A

Computational cost summary

Table A.1 reports the computational cost and maximum cell count of the simulations analysed in Chapter 5.

Table A.1: Core-hour usage summary of the analysed CFD simulations, ordered according to the computational matrix.

Sr. No.	Simulation Name	Cores	Wall time [h]	Core hours	Maximum cells ($\times 10^6$)
Type 1, Single paddle (domain B0)					
Paddle grid-convergence series					
1	blade_inviscid_0.20	48	3.45	165.7	0.93
2	blade_inviscid_0.15	48	4.12	197.7	1.01
3	blade_inviscid_0.10	48	12.40	595.2	1.87
4	blade_inviscid_0.05	96	23.72	2277.0	6.00
Viscous paddle					
5	blade_viscous_0.20	48	9.67	464.0	1.00
Type 2, Boat alone (domain B1)					
Boat resistance					
6	boat_resistance_1.944ms	12	3.21	38.6	0.29
7	boat_resistance_2.222ms	12	2.77	33.2	0.30
8	boat_resistance_2.500ms	12	3.12	37.5	0.31
9	boat_resistance_2.778ms	12	3.63	43.6	0.32
10	boat_resistance_3.056ms	12	3.88	46.6	0.32
11	boat_resistance_3.333ms	12	4.89	58.7	0.33
12	boat_resistance_3.611ms	12	5.37	64.5	0.34
Boat oscillating surge, adaptive					
13	boat_adaptdt_0.20	48	9.65	463.4	0.59
14	boat_adaptdt_0.15	48	10.47	502.6	0.68
15	boat_adaptdt_0.10	48	17.00	816.1	0.82
16	boat_adaptdt_0.05	48	40.91	1963.8	1.60
Boat oscillating surge, fixed					
17	boat_uniformdt_0.20	48	0.15	7.2	0.57
18	boat_uniformdt_0.15	48	0.15	7.0	0.61
19	boat_uniformdt_0.10	48	0.25	12.2	0.75
20	boat_uniformdt_0.05	48	0.60	28.9	1.41
Type 3, Paddle-hull (domain B2)					
Paddle-hull					
21	blade_with_boat_0.20	48	117.16	5623.9	2.63
			Total	**13447.4**	

Appendix B

IMU processing and validation results

The figures in this appendix document the checks used during trajectory reconstruction. Figures B.1 and B.2 compare the reported quaternion and Euler attitude representations. Figures B.3–B.7 show the gravity and magnetometer checks. Figures B.8 and B.9 document the left-sensor failure that led to its exclusion. The phase-averaged statistics of the stroke are shown in Table B.2.

B.1 Sensor quality and data conditioning

The reconstruction accepts the magnetometer reading only if its magnitude remains stable over the trial. The coefficient of variation is

$$\mathrm{CV}_H = 100\,\frac{\sigma(\|\mathbf{H}\|)}{\mu(\|\mathbf{H}\|)}\,[\%], \quad \text{reliable if } \mathrm{CV}_H < 5\%, \tag{B.1}$$

where H_X, H_Y, H_Z are the raw magnetometer channels (µT), $\|\mathbf{H}\| = \sqrt{H_X^2 + H_Y^2 + H_Z^2}$ their combined magnitude, and CV_H the coefficient of variation (%).

Isolated deviations in Euler-angle channels are flagged using the finite-difference rate

$$\dot{\vartheta}_i = \frac{\vartheta_i - \vartheta_{i-1}}{t_i - t_{i-1}}, \quad |\dot{\vartheta}_i| > n_\sigma\,\sigma(\dot{\vartheta}), \tag{B.2}$$

where ϑ_i is the logged Euler angle at sample i (deg), $\dot{\vartheta}_i$ its finite-difference rate (deg/s), and $\sigma(\dot{\vartheta})$ the rate's standard deviation over the trial. The threshold is set to $n_\sigma = 6$ for catalogue detection and $n_\sigma = 4$ for the summary event count, with a minimum separation of 20 samples enforced between successive detections.

Over a static window $[t_1, t_2]$ where the sensor is at rest, the earth-frame acceleration should equal gravity. The residual magnitude is

$$\bar{\mathbf{a}} = \frac{1}{N}\sum_{t_i \in [t_1, t_2]} \mathbf{R}_{ES,i}\,\mathbf{a}_i^S, \quad r_g = \|\bar{\mathbf{a}} - [0, 0, g]^T\|, \tag{B.3}$$

where $\bar{\mathbf{a}}$ is the mean rotated acceleration over N static-window samples (m/s^2), g gravitational acceleration (m/s^2), and r_g the residual magnitude (m/s^2).

Evaluated over the static window (33.25 to 33.75 s) of the right paddle, the mean rotated acceleration is $\bar{\mathbf{a}} = (-0.23, 0.55, 9.75)$ m/s^2 against the expected $(0, 0, g) = (0, 0, 9.81)$ m/s^2, giving a residual magnitude $r_g = 0.60$ m/s^2, or 6.1% of g. This residual sets the floor on the gravity-compensated acceleration used throughout Sections 4.3–4.4. It is small relative to the peak in-stroke accelerations, which are of order several m/s^2, but is not zero, and is reported here as the residual bias that a perfectly executed rotation and gravity removal would not eliminate, attributable to residual sensor bias/misalignment and to the paddle not being perfectly stationary over the nominally static window (Figure B.5).

A centred moving average with window length $w = 200$ samples tracks slow bias in the earth-frame vertical channel

$$\overline{a}_z(t_i) = \frac{1}{\min(w, N)} \sum_{j=i-\lfloor w/2 \rfloor}^{i+\lfloor w/2 \rfloor} a^E_{z,j}, \tag{B.4}$$

where $a^E_{z,j}$ is the earth-frame vertical acceleration at sample j (m/s^2), and $\overline{a}_z(t_i)$ the rolling mean centred at sample i (m/s^2), compared against g over the whole trial.

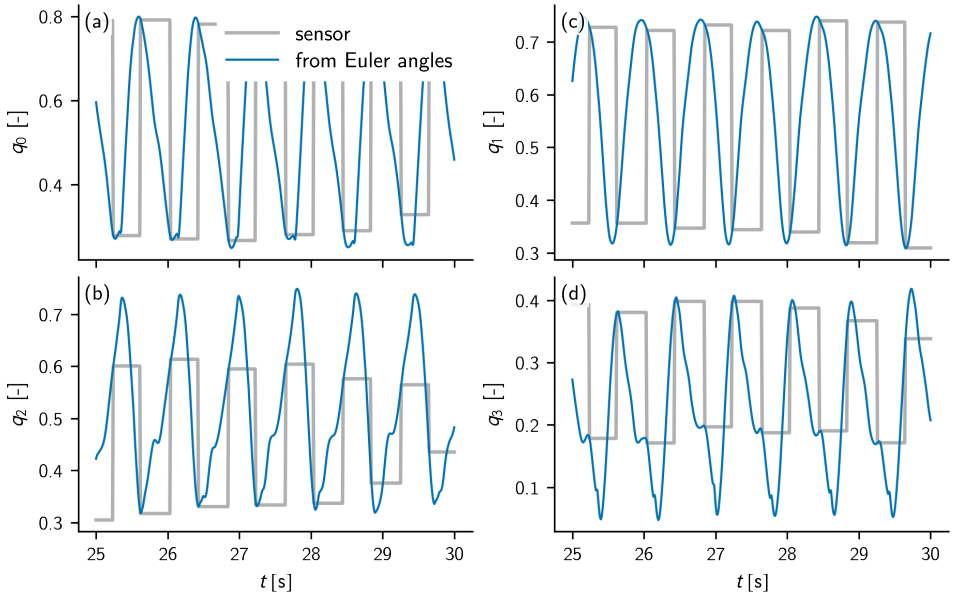

Figure B.1: Reconstructed and sensor-reported quaternions, checked for the double-cover consistency distance e_q.

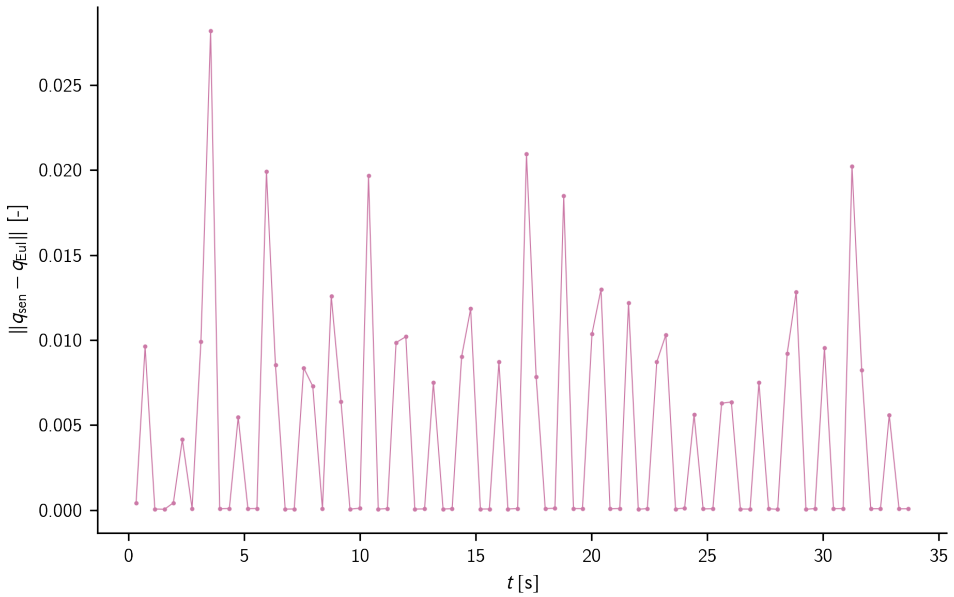

Figure B.2: Consistency between the quaternion- and Euler-angle-derived attitude, confirming the two representations agree.

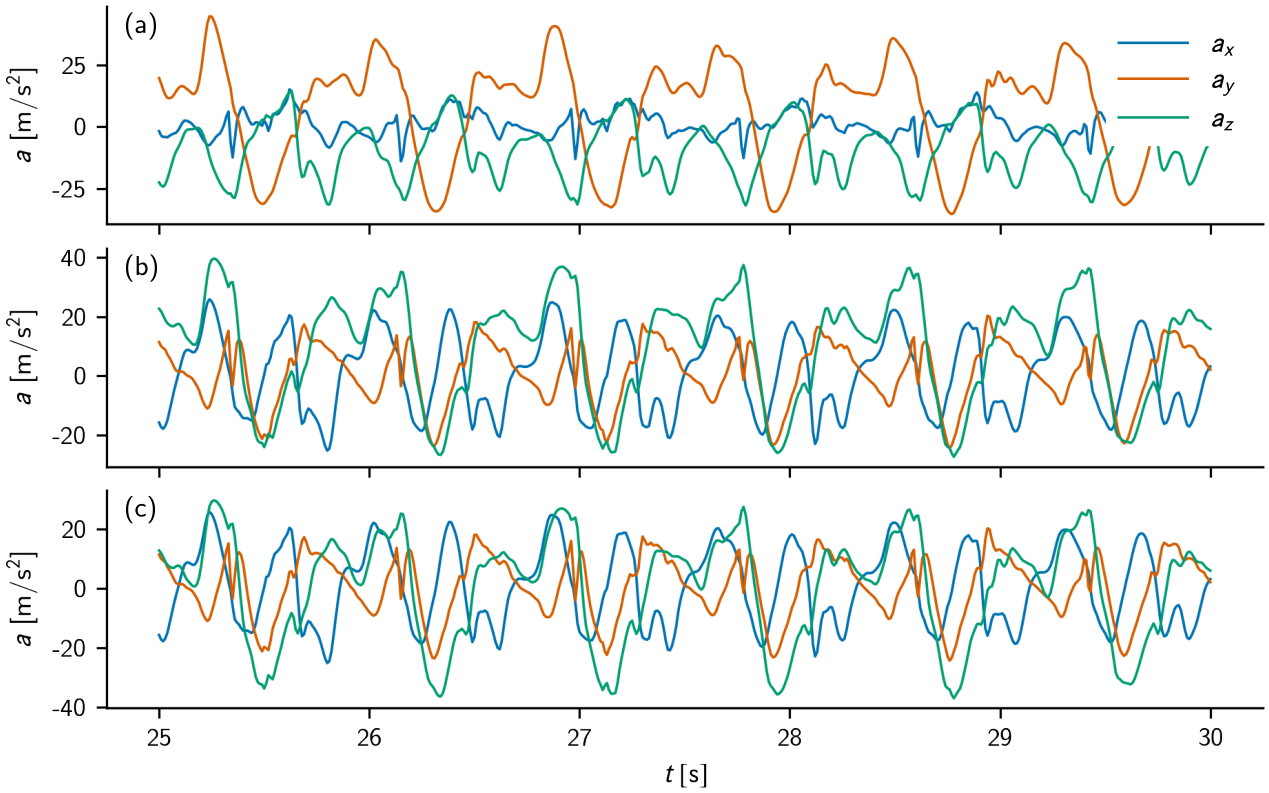

Figure B.3: Gravity-compensation stages, from raw specific force to the earth-frame acceleration used in the trajectory integration.

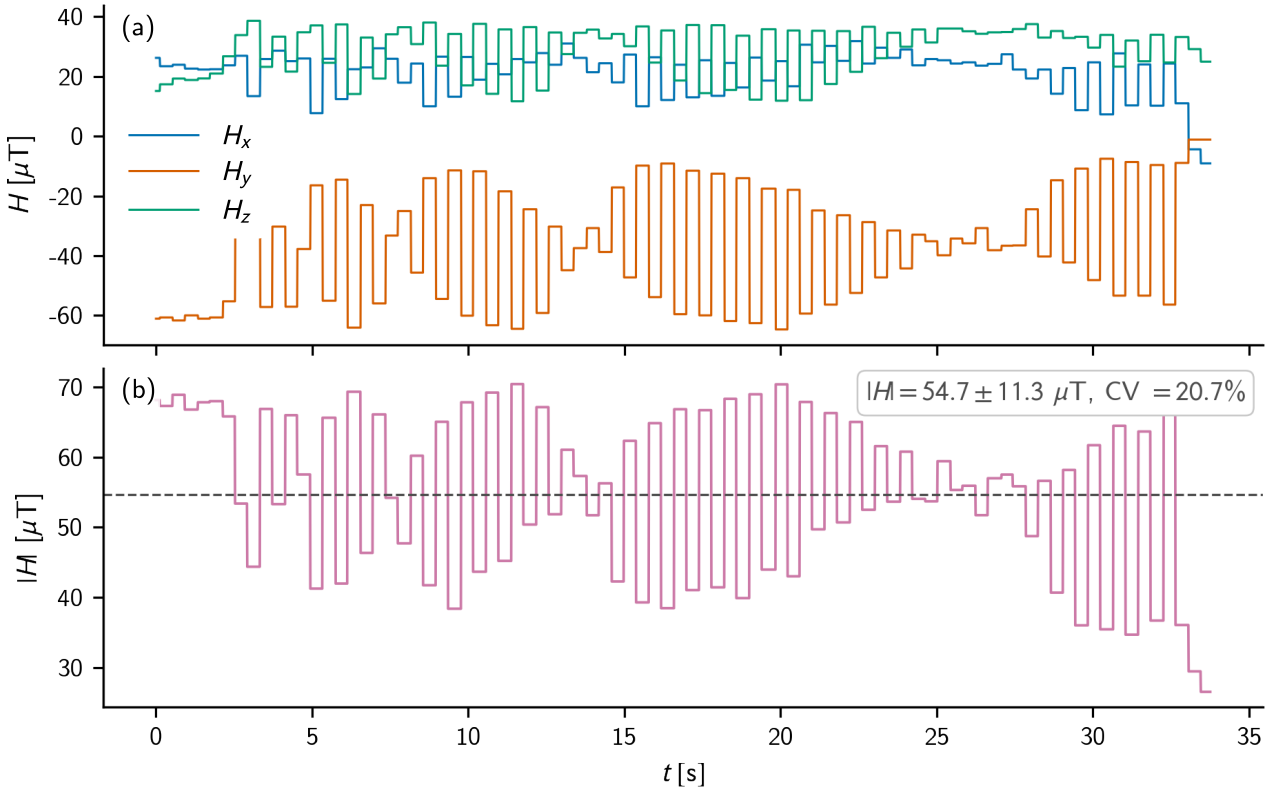

Figure B.4: Sensor-frame magnetometer components, used to evaluate the magnitude coefficient of variation CV_H of Equation (B.1).

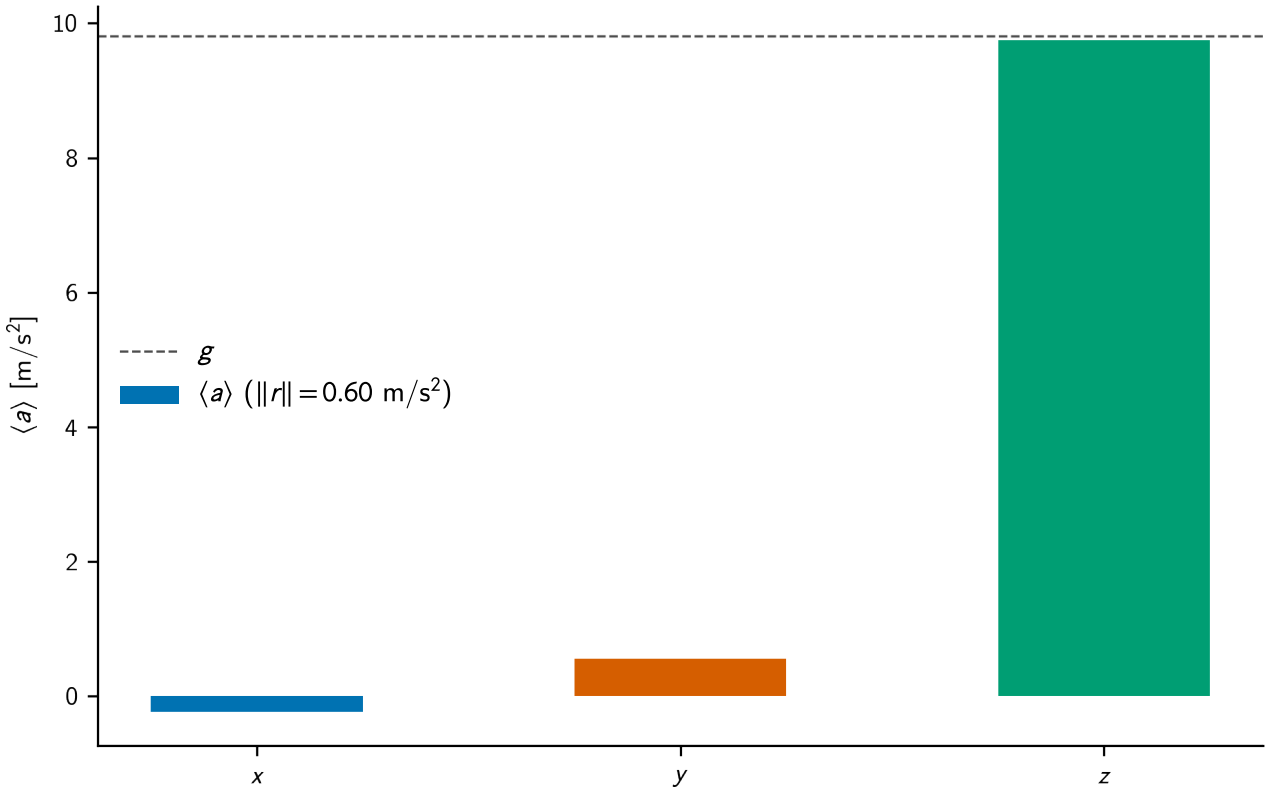

Figure B.5: Static gravity-compensation residual over the reference window, quantifying the bias floor r_g of Equation (B.3).

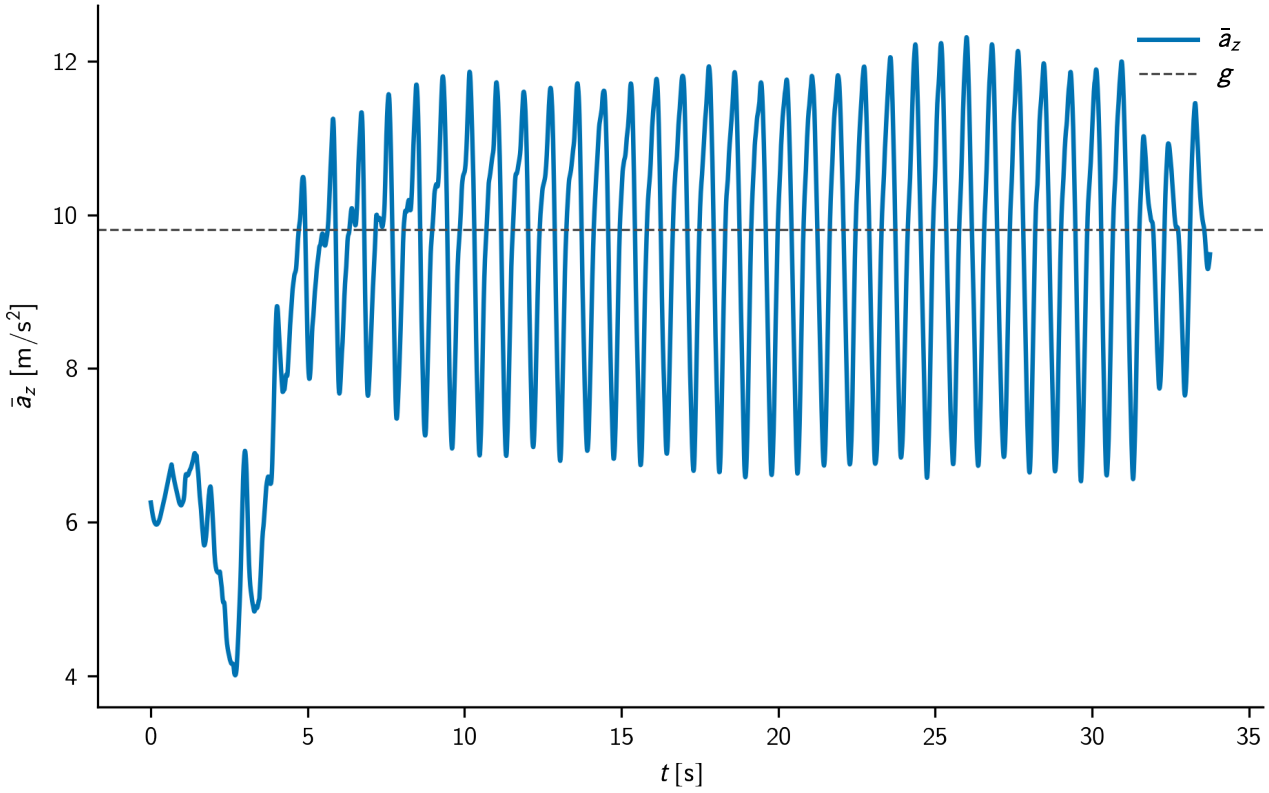

Figure B.6: Earth-frame vertical acceleration and low-frequency bias, tracked with the rolling mean of Equation (B.4).

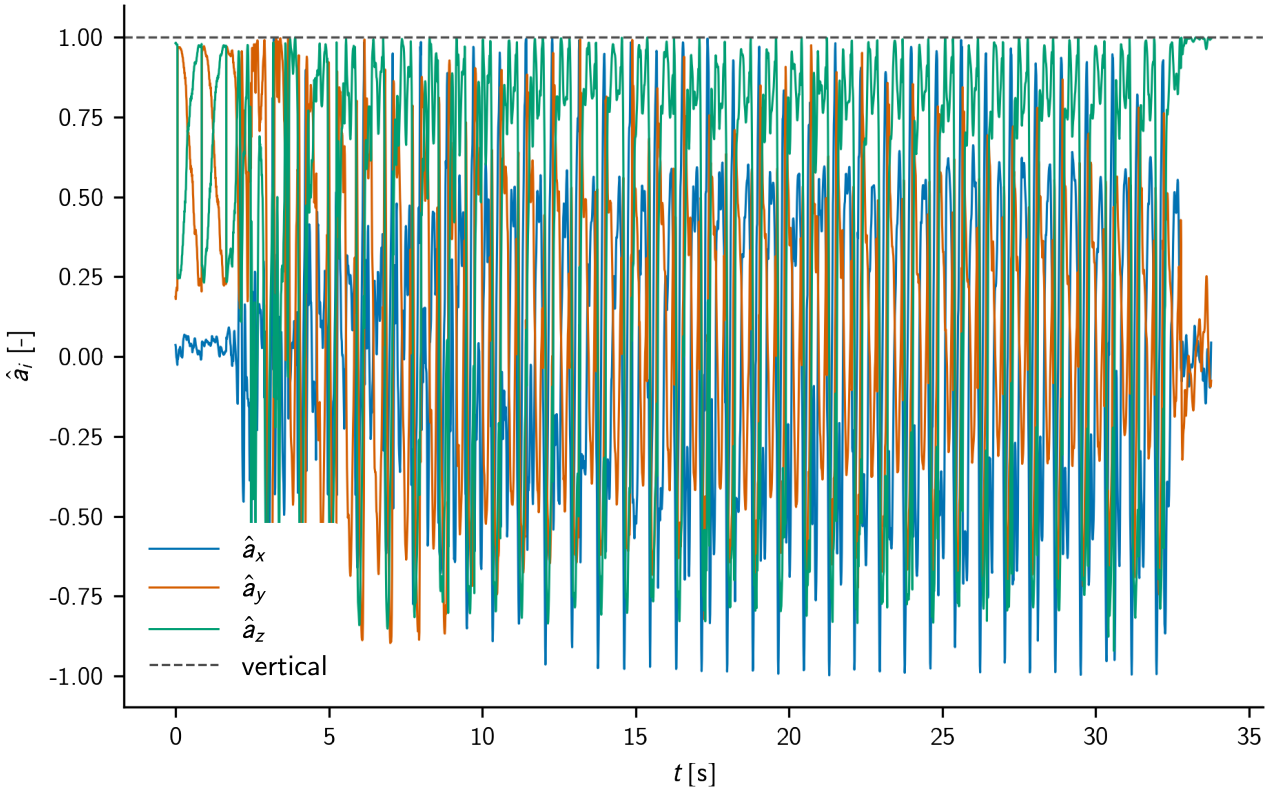

Figure B.7: Gravity-compensated specific-force direction, used to check the attitude correction before integrating the trajectory.

B.2 Left-sensor failure pattern

Table B.1 summarises the attitude-rate glitch counts (threshold $n_\sigma = 4$, Equation (B.2)) and the worst single deviation on each Euler-angle channel, comparing the excluded left paddle against the selected right paddle over the full trial. The detection *count* is consistently five to twenty times higher on the left sensor, which is the more diagnostic statistic, because the right sensor's few detections are isolated instances of legitimate large-amplitude stroke rotation exceeding the statistical rate threshold (its single roll deviation, 180.0°, occurs during ordinary paddle motion, not a reset), whereas the left sensor's repeated detections are the jerk-and-reset behaviour described in Section 4.4, where the logged angle snaps toward zero within one or two samples independently of the stroke phase.

Table B.1: Left- versus right-sensor attitude-rate glitch pattern over the full trial ($n_\sigma = 4$ threshold). "Worst deviation" is the logged angle at the most severe detected glitch on that channel.

Channel	Glitch count [-]		Worst deviation [deg]	
	Left	Right	Left	Right
Roll ϕ (angleX)	30	5	111.7	180.0
Pitch θ (angleY)	26	1	72.2	25.8
Yaw ψ (angleZ)	14	1	44.0	5.6

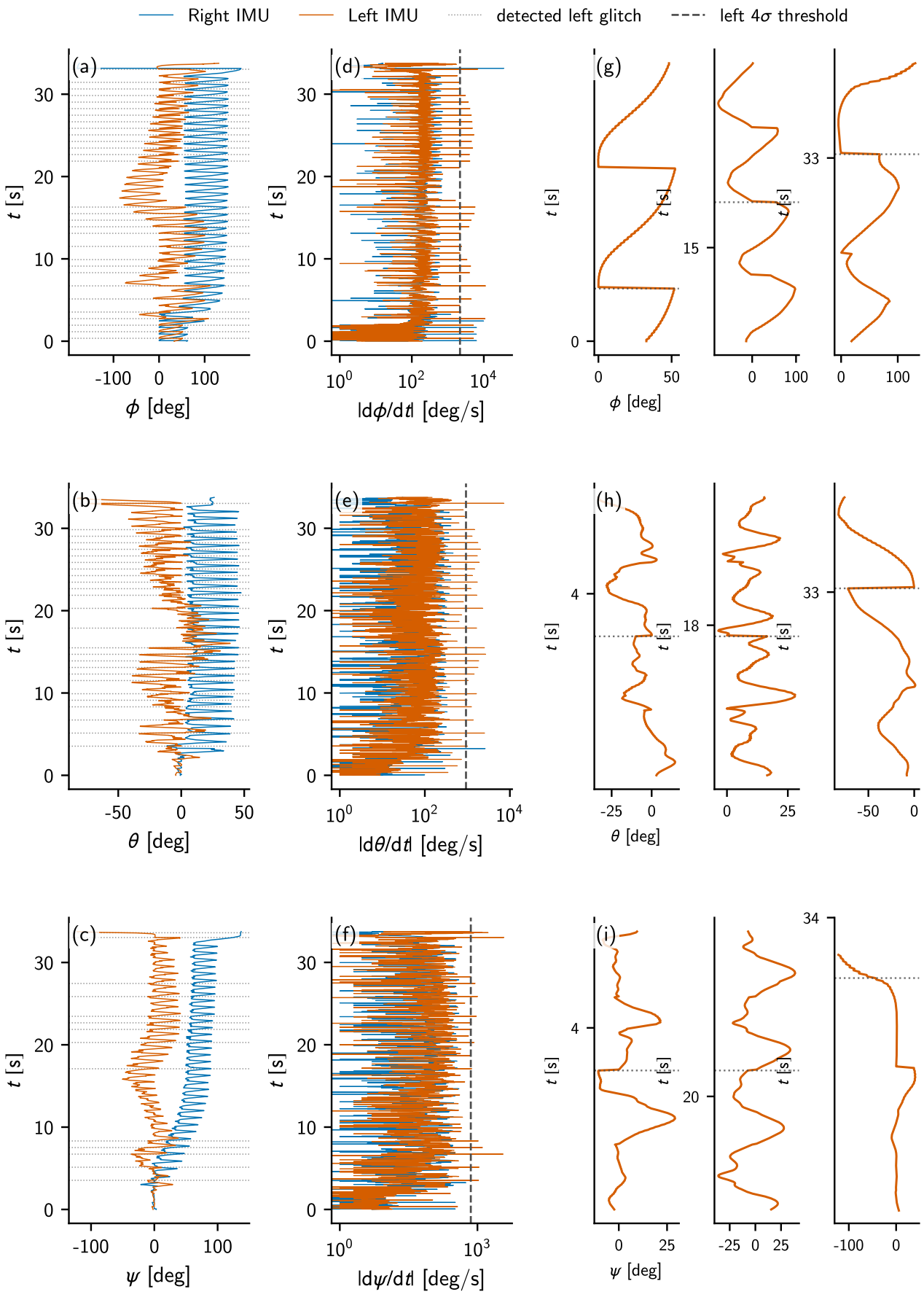

Figure B.8: Left-IMU Euler-angle glitches and detection thresholds, showing the jerk-and-reset pattern used to identify the sensor malfunction.

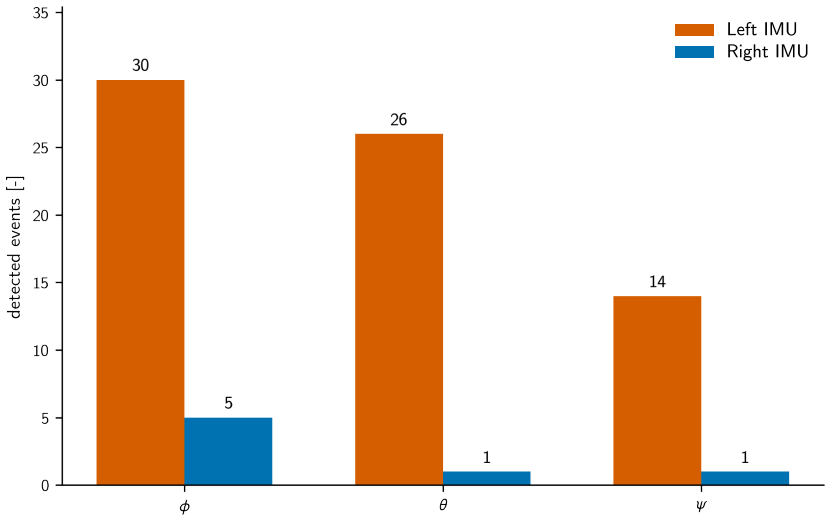

Figure B.9: IMU attitude-rate glitch counts, comparing the left- and right-sensor detection rates behind Table B.1.

B.3 Stroke-to-stroke variability of the selected paddle signal set

Table B.2 reports the variability of every signal used for phase averaging. Five stroke intervals were resampled onto the common phase grid. The representative-value bounds are the minimum and maximum of the phase-averaged history. The two standard-deviation columns quantify the inter-stroke spread at each phase location, where their mean summarises the typical spread and their maximum identifies its largest local value. The final two columns give the extrema over all resampled strokes, a descriptive range rather than an uncertainty bound on a single measurement.

Table B.2: Phase-resolved variability of the signals used for the representative stroke.

Signal	Unit	Min.	Max.	Mean SD	Max. SD	Overall Min.	Overall Max.
ϕ	deg	55.346	150.636	1.214	2.094	54.814	151.696
θ	deg	3.579	44.660	1.180	2.607	1.693	45.941
ψ	deg	58.751	96.532	1.139	1.780	57.843	98.250
a_x	$\mathrm{m\,s^{-2}}$	-20.611	21.065	2.013	5.286	-25.290	24.825
a_y	$\mathrm{m\,s^{-2}}$	-22.664	16.888	1.519	7.070	-24.402	20.620
a_z	$\mathrm{m\,s^{-2}}$	-34.857	25.172	2.094	4.507	-37.084	27.588
F_p	N	-14.938	112.390	8.047	30.627	-20.166	128.077

Appendix C

Immersion-depth sensitivity

C.1 Immersion-depth and advance speed sensitivity of the peak paddle-normal force

Section 5.2 uses $z = -0.8$ m as a working vertical datum. The sensitivity analysis reported here supported that choice. They vary $|z|$ over $\{0.65, 0.70, 0.80, 0.90\}$ m and use constant inflow or oscillating surge over the available speed range. The set has no grid-convergence control or fixed parametric matrix and is therefore used for calibration only.

Figure C.1 shows the full comparison of peak force across the tested immersion depths and advance conditions. The runs are not grid-converged and are used only to select the working vertical datum and advance-condition range for the main CFD calculations. Table C.1 lists the corresponding peak forces, while the $z_{fs} = -0.80$ m subset used in the main calculations is reported in Table 5.2.

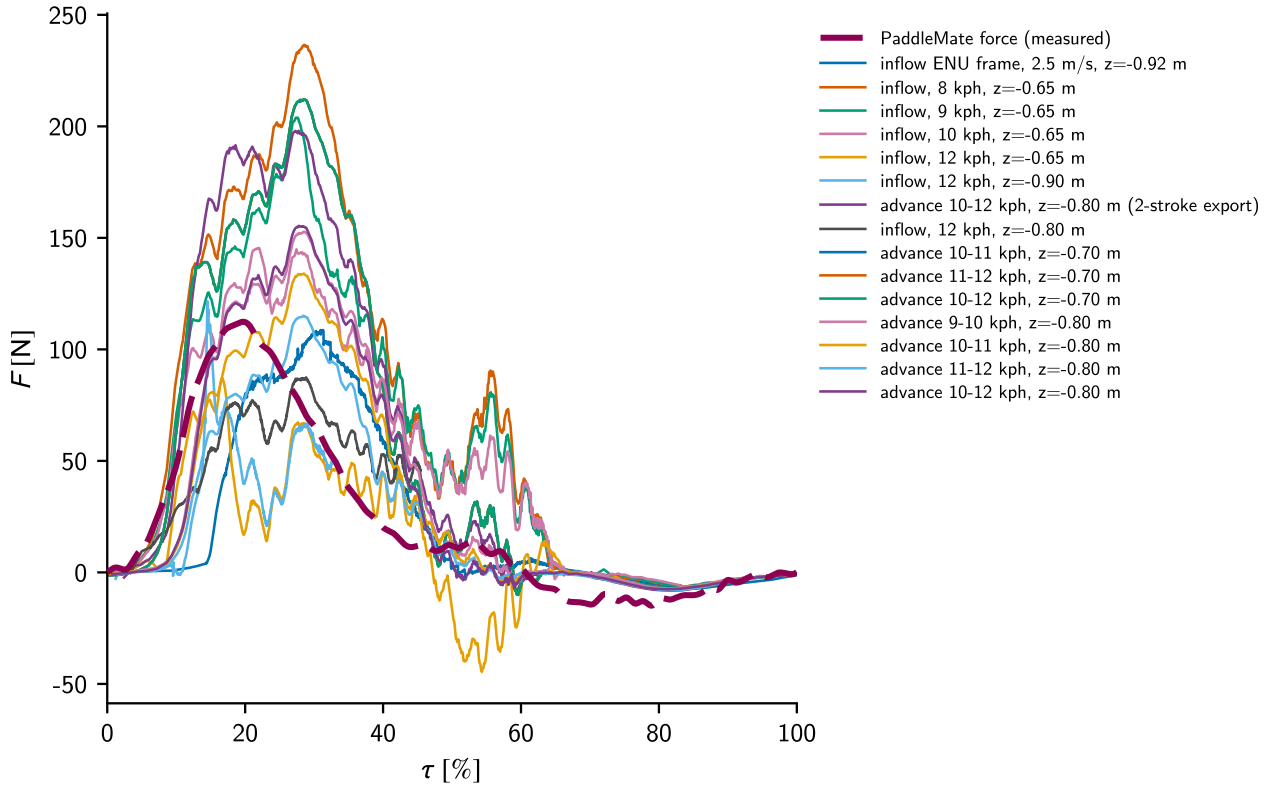

Figure C.1: Peak paddle-normal force across exploratory immersion-depth and inflow-speed cases.

Table C.1: Peak paddle-normal force over one settled stroke, exploratory immersion-depth and inflow-speed CFD runs, versus the measured PaddleMate peak.

Case	Condition	Speed	z_{fs} [m]	Peak force [N]
PaddleMate (measured)	measured	-	-	112.4
inflow ENU frame, 2.5 m/s, z=-0.92 m	inflow	2.5 m/s	-0.92	108.7
inflow, 8 kph, z=-0.65 m	inflow	8 kph	-0.65	236.5
inflow, 9 kph, z=-0.65 m	inflow	9 kph	-0.65	203.9
inflow, 10 kph, z=-0.65 m	inflow	10 kph	-0.65	145.5
inflow, 12 kph, z=-0.65 m	inflow	12 kph	-0.65	87.3
inflow, 12 kph, z=-0.90 m	inflow	12 kph	-0.90	121.6
advance 10-12 kph, z=-0.80 m (2-stroke export)	advancing	10-12 kph	-0.80	198.0
inflow, 12 kph, z=-0.80 m	inflow	12 kph	-0.80	87.5
advance 10-12 kph, z=-0.70 m	advancing	10-12 kph	-0.70	212.0
advance 9-10 kph, z=-0.80 m	advancing	9-10 kph	-0.80	152.7
advance 10-11 kph, z=-0.80 m	advancing	10-11 kph	-0.80	134.0
advance 11-12 kph, z=-0.80 m	advancing	11-12 kph	-0.80	115.1
advance 10-12 kph, z=-0.80 m	advancing	10-12 kph	-0.80	155.4

Appendix D

Supplementary results

D.1 Grid convergence of the blade-force impulse and positive-mean metrics

This section reports the blade-force impulse and conditional positive-mean grid-convergence metrics omitted from the main peak and RMS comparison in Section 5.2. Both use the least-squares procedure of Eça and Hoekstra [25] (uncertainty form in Equation (3.23)). Figure D.1 shows the resulting convergence assessment.

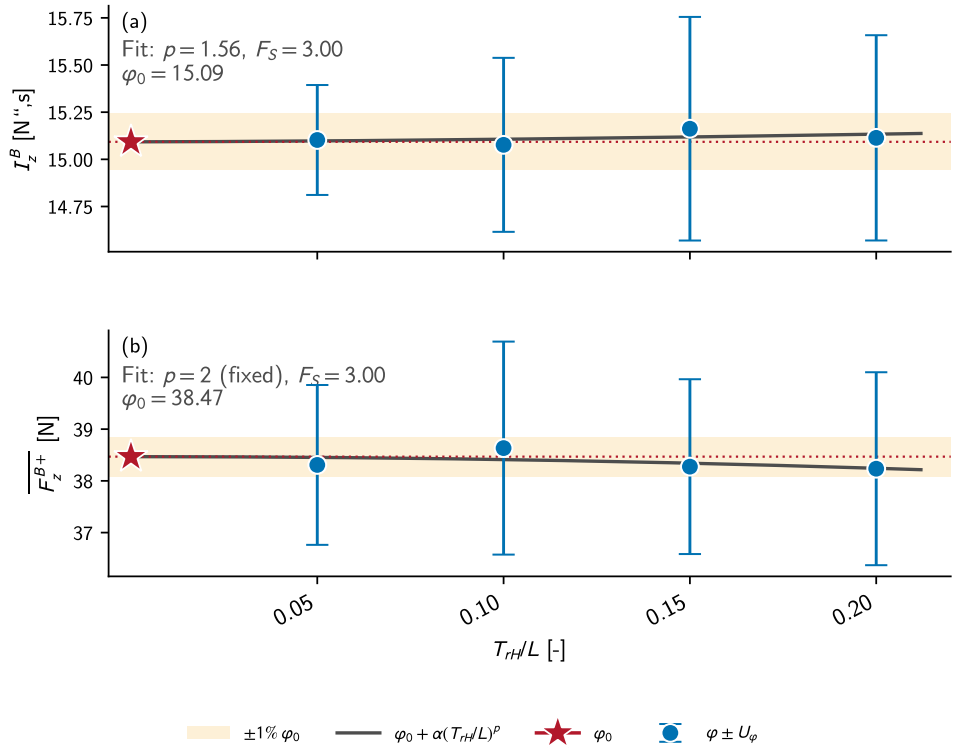

Figure D.1: Grid-convergence assessment of the blade-force impulse and positive mean, the two metrics omitted from the main peak and RMS comparison of Chapter 5.

D.2 Boat heave and pitch during the oscillating-surge and paddle–hull cases

This section reports the boat heave T_z and pitch R_y time histories for the oscillating-surge and paddle-hull cases introduced in Section 5.3.3 and Section 5.4, for reference only. They are not discussed further in the body text. Both figures restrict the displayed history to $t \geq 15$ s and show each series relative to its own value at the start of that window, $t = 15$ s, the same convention used for the force comparison of Figure 5.23.

Figure D.2 sweeps the four T_{rH}/L mesh levels of the oscillating-surge bare-hull case, uniform time step and adaptive time step in separate columns, heave in the top row and pitch in the bottom row. Figure D.3 compares the boat motion at the one T_{rH}/L level common to all three oscillating-surge and paddle-hull cases, $T_{rH}/L = 0.20$. The three cases are the paddle-hull case, the bare hull with adaptive time step, and the bare hull with uniform time step.

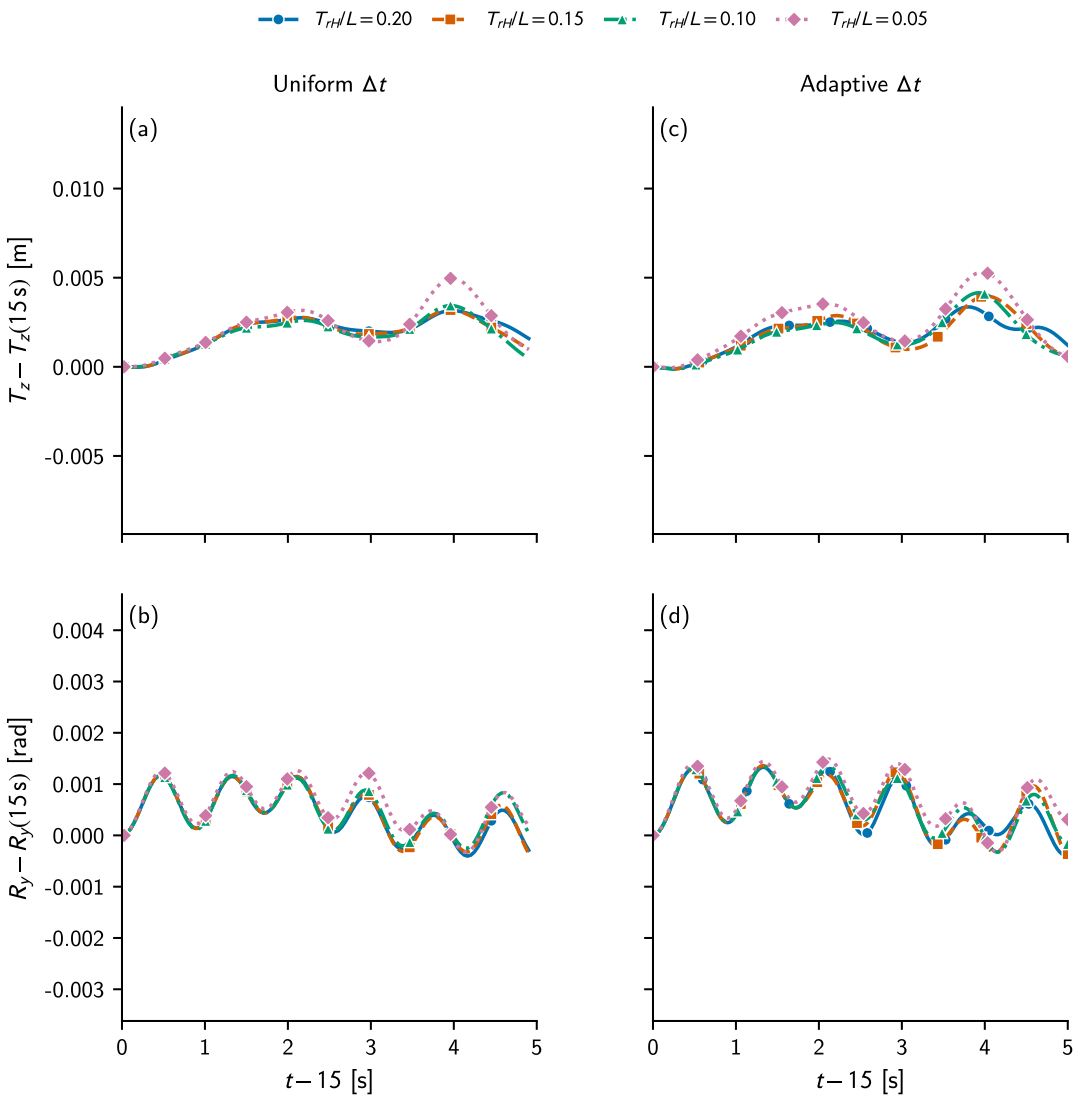

Figure D.2: Boat heave T_z (top) and pitch R_y (bottom) relative to their value at $t = 15$ s, oscillating-surge bare-hull case, uniform time step (left) and adaptive time step (right), across the four T_{rH}/L mesh levels.

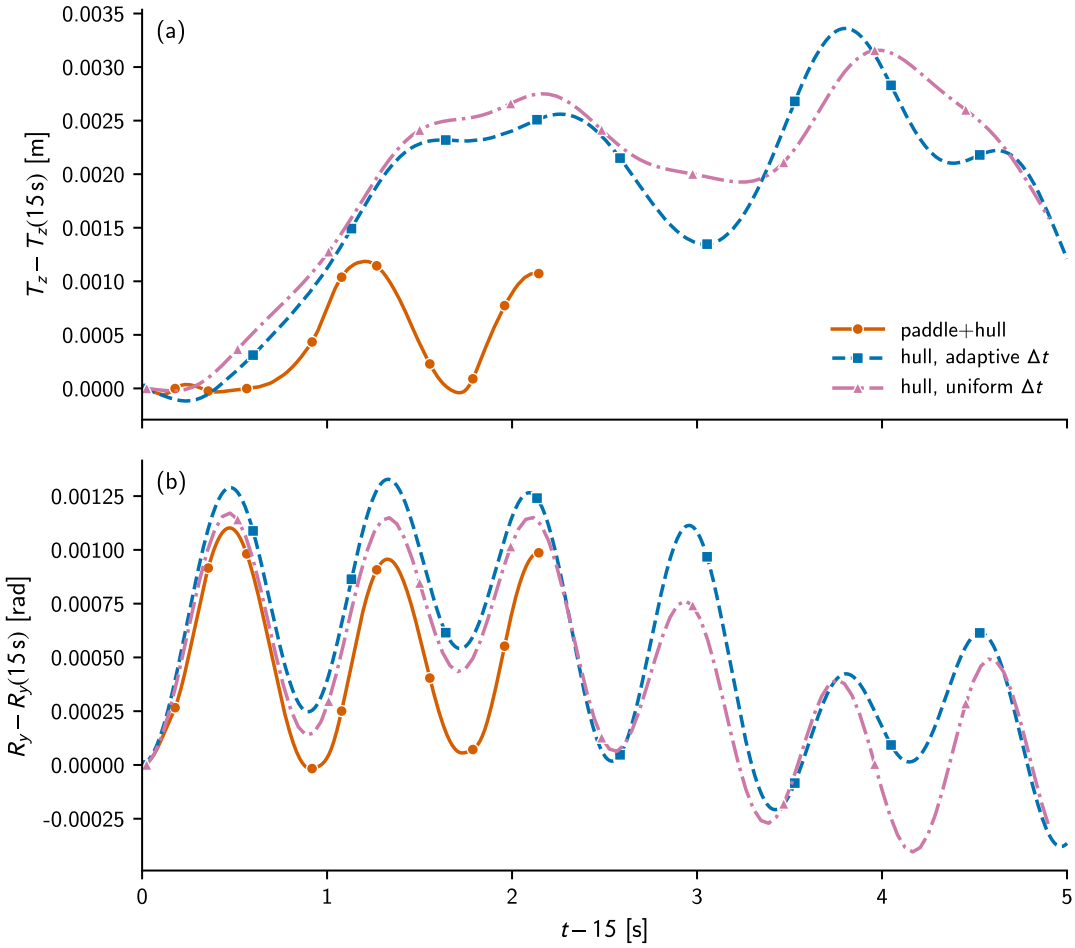

Figure D.3: Boat heave T_z (top) and pitch R_y (bottom) relative to their value at $t = 15$ s, at $T_{rH}/L = 0.20$, for the paddle-hull case, the bare hull with adaptive time step, and the bare hull with uniform time step.

D.3 Supplementary standalone-paddle

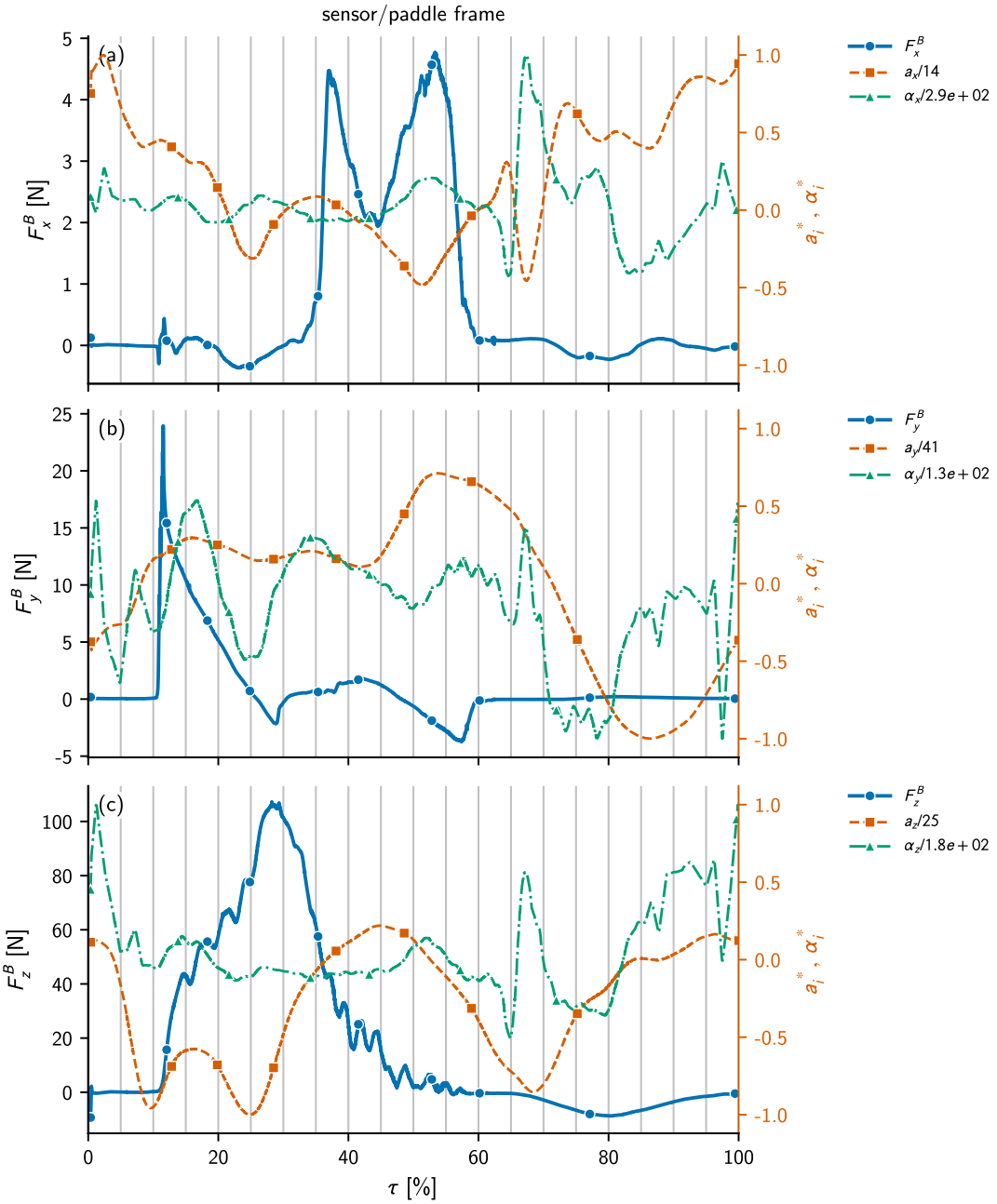

Figure D.4: Paddle force and normalised acceleration in the sensor/paddle frame, supplementing the force-acceleration discussion of Section 5.2.3.

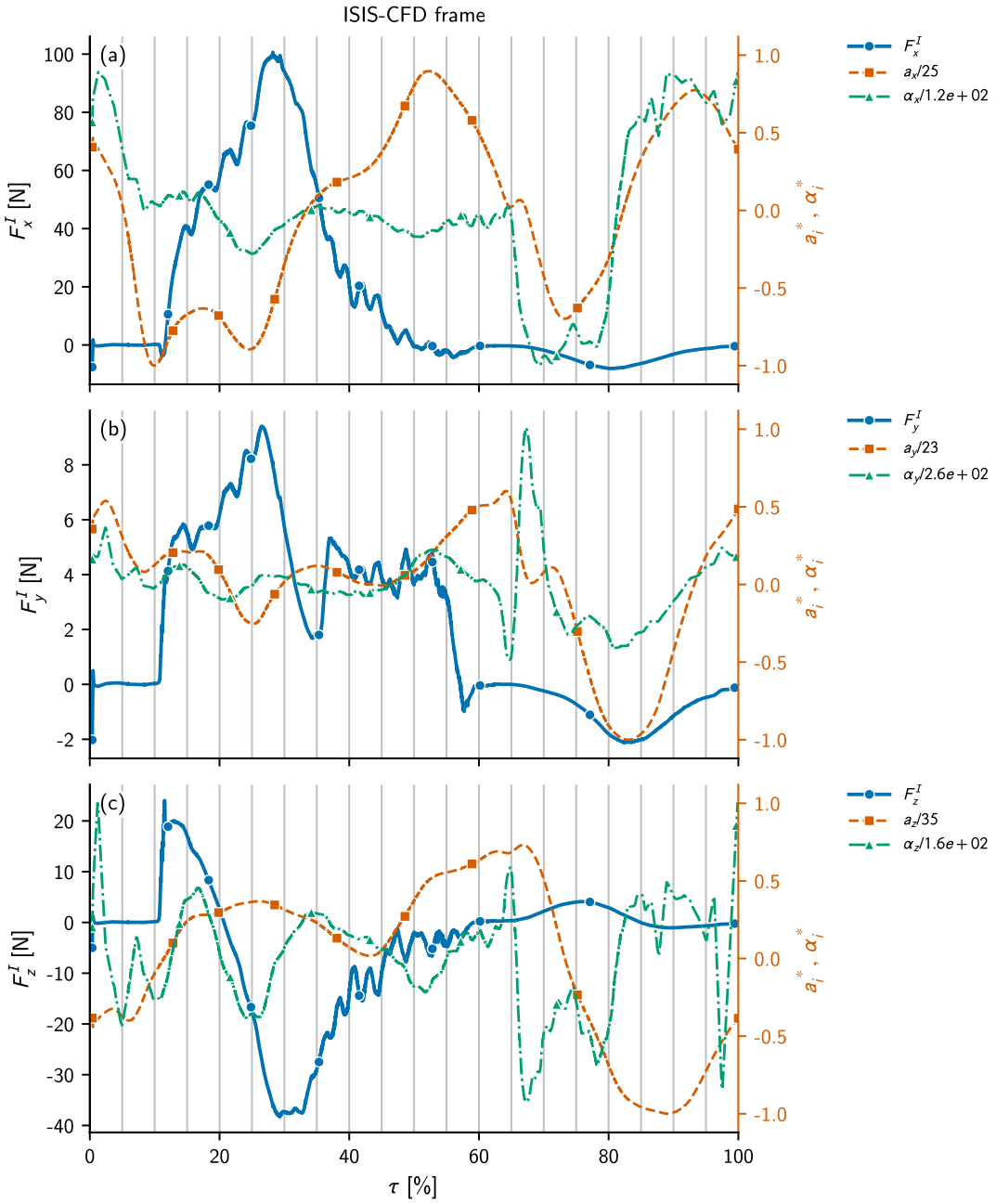

Figure D.5: Paddle force and normalised acceleration in the ISIS-CFD frame, the fixed-frame version of Figure D.4.

Appendix E

IMU error-propagation derivations

This appendix collects the multi-step derivation whose final results the body chapters quote, cross-referenced to its point of use.

E.1 IMU attitude and integration-uncertainty propagation

This section summarises the first-order uncertainty propagation used to assess the reconstructed trajectory and motivate the endpoint-drift correction, following the linearized error-propagation framework commonly used for IMU/INS systems [17].

For an Euler angle $\vartheta \in \{\phi, \theta, \psi\}$ evaluated from the attitude solution, first-order propagation of uncorrelated gyroscope and accelerometer noise gives

$$\sigma_\vartheta^2 = \sum_{k=1}^{3} \left(\frac{\partial \vartheta}{\partial \omega_k} \right)^2 \sigma_g^2 + \sum_{k=1}^{3} \left(\frac{\partial \vartheta}{\partial f_k} \right)^2 \sigma_a^2. \tag{E.1}$$

The sensitivities are evaluated at the instantaneous attitude estimate. Manufacturer specifications for the selected sensor give approximately $\sigma_g = 0.05^\circ\,\mathrm{s}^{-1}$ and $\sigma_a = 0.005 g$. These values describe sensor-level uncertainty rather than an independently measured trajectory-error bound.

The following derivation addresses the additional velocity and position drift introduced by double integration.

Velocity error growth. Let the discrete acceleration measurement at sample i carry a zero-mean, uncorrelated error ϵ_i, with $\mathbb{E}[\epsilon_i] = 0$ and $\mathbb{E}[\epsilon_i \epsilon_j] = \sigma_a^2 \delta_{ij}$ (Kronecker delta). Trapezoidal integration over n samples of duration Δt accumulates the error linearly,

$$e_v(n) = \Delta t \sum_{i=1}^{n} \epsilon_i. \tag{E.2}$$

Since the ϵ_i are uncorrelated, the variance of the sum is the sum of the variances,

$$\mathrm{Var}[e_v(n)] = \Delta t^2 \sum_{i=1}^{n} \mathrm{Var}[\epsilon_i] = \Delta t^2 \, n \, \sigma_a^2, \tag{E.3}$$

so that the standard deviation of the velocity error grows as

$$\sigma_v(n) = \sigma_a \, \Delta t \, \sqrt{n}. \tag{E.4}$$

Position error growth. Each velocity sample v_i inherits the accumulated error up to that point, $e_v(i) = \Delta t \sum_{k=1}^{i} \epsilon_k$. Trapezoidal integration of the velocity error over n steps gives the position error

$$e_x(n) = \Delta t \sum_{i=1}^{n} e_v(i) = \Delta t^2 \sum_{i=1}^{n} \sum_{k=1}^{i} \epsilon_k. \tag{E.5}$$

Exchanging the order of summation, each ϵ_k is counted once for every $i \geq k$, i.e. $(n - k + 1)$ times,

$$e_x(n) = \Delta t^2 \sum_{k=1}^{n} (n - k + 1)\, \epsilon_k. \tag{E.6}$$

Using $\mathrm{Var}[\epsilon_k] = \sigma_a^2$ and independence again,

$$\mathrm{Var}[e_x(n)] = \Delta t^4 \sigma_a^2 \sum_{k=1}^{n} (n - k + 1)^2 = \Delta t^4 \sigma_a^2 \sum_{m=1}^{n} m^2 = \Delta t^4 \sigma_a^2 \, \frac{n(n+1)(2n+1)}{6}, \tag{E.7}$$

using the standard identity $\sum_{m=1}^{n} m^2 = n(n+1)(2n+1)/6$, so that

$$\sigma_x(n) = \sigma_a \, \Delta t^2 \sqrt{\frac{n(n+1)(2n+1)}{6}}. \tag{E.8}$$

For large n, Equations (E.4) and (E.8) give the unconstrained random-walk growth rates $\sigma_v \propto n^{1/2}$ and $\sigma_x \propto n^{3/2}$.

Bound achieved by the periodic endpoint-drift correction. The endpoint-drift removal subtracts a linear ramp so that the corrected signal vanishes at both stroke endpoints t_0 and t_1 (sample indices 0 and N), $v^c(t_0) = v^c(t_1) = 0$. Writing the uncorrected error at the end of the stroke as $e_v(N)$, with standard deviation $\sigma_v(N)$ from Equation (E.4), the corrected error at an interior sample n is

$$e_v^c(n) = e_v(n) - \frac{t_n - t_0}{t_1 - t_0} \, e_v(N). \tag{E.9}$$

Because $e_v(n)$ and $e_v(N)$ are built from a common (overlapping) set of ϵ_i, they are correlated, and bounding the variance of Equation (E.9) by the triangle inequality on standard deviations (rather than propagating the exact covariance) gives

$$\sigma_v^c(n) \leq \sigma_v(n) + \frac{n}{N} \sigma_v(N). \tag{E.10}$$

Since $\sigma_v(n) = \sigma_v(N)\sqrt{n/N} \leq \sigma_v(N)$ for $0 \leq n \leq N$, and $n/N \leq 1$ over the same range, Equation (E.10) is itself bounded by

$$\sigma_v^c(n) \leq 2\, \sigma_v(N), \qquad 0 \leq n \leq N, \tag{E.11}$$

in place of the unconstrained $n^{1/2}$ growth of Equation (E.4). The identical construction applied to the position integral bounds the corrected position error at $\sigma_x^c(n) \leq 2\, \sigma_x(N)$, replacing the unconstrained $n^{3/2}$ growth of Equation (E.8). Both bounds are enforced once per stroke by construction (the ramp subtraction), rather than estimated from the noise model at run time.

Attitude-error bound at the blade tip. For a small attitude perturbation $\delta\boldsymbol{\vartheta}$ about the true attitude, the perturbed rotation matrix is, to first order, $R_{ES}^{\text{pert}} \simeq (\mathbf{I} + [\delta\boldsymbol{\vartheta}]_\times) R_{ES}$, following the standard small-angle rotation-error construction [27, 32], where $[\cdot]_\times$ denotes the skew-symmetric cross-product matrix. The resulting error in the reconstructed paddle-tip position (Equation (3.11)) is

$$\delta\mathbf{x}_{\text{tip}} = R_{ES}^{\text{pert}} \mathbf{r}_{\text{tip}}^S - R_{ES} \mathbf{r}_{\text{tip}}^S \simeq [\delta\boldsymbol{\vartheta}]_\times R_{ES} \mathbf{r}_{\text{tip}}^S. \tag{E.12}$$

Since $\|[\delta\boldsymbol{\vartheta}]_\times \mathbf{v}\| = \|\delta\boldsymbol{\vartheta}\|\,\|\mathbf{v}\| \sin\gamma$ for the angle γ between $\delta\boldsymbol{\vartheta}$ and $\mathbf{v}$, and R_{ES} preserves vector norms (it is a rotation),

$$\|\delta\mathbf{x}_{\text{tip}}\| \leq \|\delta\boldsymbol{\vartheta}\|\,\|\mathbf{r}^S_{\text{tip}}\|, \tag{E.13}$$

with equality approached when the rotation-error axis $\delta\boldsymbol{\vartheta}$ is perpendicular to the lever arm $R_{ES}\mathbf{r}^S_{\text{tip}}$.

The periodic endpoint correction applied here is a stroke-cycle analogue of the zero-velocity-update (ZUPT) technique used in foot-mounted pedestrian inertial navigation, where a detected stance phase provides a known zero-velocity instant at which unbounded double-integration drift is reset rather than allowed to accumulate [40]. A paddle stroke has no interval of true zero velocity, and the construction above instead exploits the periodicity of the stroke, constraining the corrected velocity and position to return to the same value at each cycle boundary. This result is evaluated numerically for the representative stroke in Section 5.1.8.

Appendix F

BeamDyn and ISIS-CFD coupling proof of concept

The preceding chapters treat the paddle as a rigid body with prescribed motion. This appendix reports a proof-of-concept coupling between a structural beam solver and ISIS-CFD, establishing the groundwork for a future flexible-paddle extension. It does not simulate a flexible dragon-boat paddle under CFD-generated loading and does not change the CFD results of Chapter 5.

The structural solver is BeamDyn, a geometrically exact beam formulation following Hodges [41], discretised with Legendre-spectral finite elements and distributed as a structural module within the NREL FAST/OpenFAST simulation framework [42, 43]. BeamDyn and ISIS-CFD were connected through an in-house coupling interface exchanging structural state and load between the two solvers.

F.1 Benchmark and verification cases

Two beam geometries were used, both a cantilever of length 1 m and square 1 cm cross-section with material properties representative of a slender composite paddle shaft. The straight beam, mounted with no Cardan offset, was loaded independently in tension, bending, and torsion, and separately driven through a prescribed root rotation, alone and combined with a following torsion moment. The curved beam is a quarter-circle arc of 1 m radius, loaded in-plane and out-of-plane at the tip and driven through a prescribed rotation. This standalone structural benchmark does not exercise the coupling interface. The 45° Cardan-offset configuration is instead part of the separate kinematic verification campaign below, which also repeats the curved-beam check on a 45° arc rather than the 90° quarter circle used here. Every case has a closed-form reference solution against which the simulated response is compared. The full analytical derivations are given in Section F.3. Figure F.1 shows the two beam configurations and the loads applied to each.

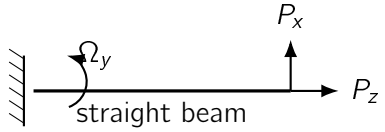

(a) Straight cantilever with prescribed rotation, follower torsion, and tip loads.

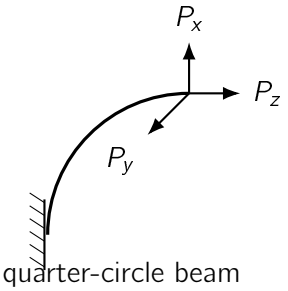

(b) Curved cantilever with tip loads in local coordinates.

Figure F.1: BeamDyn benchmark configurations. The labels denote the local loading directions used in the archived tests.

The straight-beam cases reproduce their closed-form target to four significant figures. Of the three curved-beam cases, the out-of-plane load agrees with its closed-form target to within one per cent, while the two in-plane cases differ by 13–18%, attributed to the geometrically exact solver's own shear flexibility, which is absent from the classical shear-rigid closed-form target used for these two cases (Section F.3). Table F.1 reports the calibration result for each case.

Table F.1: BeamDyn benchmark results compared with closed-form reference responses.

Case	Simulated response	Reference	Difference
Straight rotation, root reaction F_z^{root}	0.023 664 N	0.023 663 N	0.002%
Straight follower torsion, tip twist	4.5257×10^{-3} rad	4.5257×10^{-3} rad	0.00003%
Curved beam, P_y tip load	1.061×10^{-5} m	1.221×10^{-5} m	13.1%
Curved beam, P_z tip load	2.200×10^{-5} m	2.693×10^{-5} m	18.3%
Curved beam, P_x tip load	4.259×10^{-5} m	4.305×10^{-5} m	1.05%

The same beam geometries were subsequently exercised through the coupling interface in a kinematic verification mode. In this configuration, the fluid-force channel of the coupling dynamic library was set to zero, while the driving root rotations were prescribed analytically through BeamDyn's GUI-configured input. This allowed the coupling implementation, axis-frame transformation, and added-mass transfer to be verified independently of any converged flow solution. Eleven cases were run across three configurations. The first is the straight beam with no Cardan offset, four cases, tension, torsion, rotation, and rotation combined with torsion. The second is the straight beam with a 45° Cardan yaw offset, the same four cases plus additional prescribed pitch- and roll-axis rotations, six cases in total. The third is a 45° curved arc, one rotation case. All 264 logged added-mass components across these eleven cases matched within tolerance. Where a case additionally applies a driving tension or torsion load rather than a rotation alone, that load is applied through the same coupling dynamic library used to deliver fluid loads to BeamDyn. Section F.4 reports the full eleven-case matrix, and Section F.7 reports the full component-by-component comparison for the Rotation case of the straight beam at its 45° Cardan offset and of the curved arc, giving the fluid-side local value, the value BeamDyn reports in the global frame, and the value predicted by rotating the local tensor into that frame, at the first and last node and at both the initial and final time step.

F.2 Coupling frame convention

BeamDyn's own formulation requires the undeformed beam reference line along its local Z axis, whereas the paddle shaft is the ISIS-CFD X axis in the fluid frame (Section 3.2 shows paddle along Y). The coupling interface therefore applies the fixed axis transformation of Table F.2 between the two frames, used unchanged for every configuration in this appendix.

Table F.2: Fixed axis convention between the ISIS-CFD (fluid) frame and the BeamDyn (beam) frame, read as $\mathbf{x}_{\text{BeamDyn}} = \mathbf{R}\,\mathbf{x}_{\text{ISIS-CFD}}$ with $\mathbf{R}$ the matrix of table entries.

	BeamDyn X	BeamDyn Y	BeamDyn Z
ISIS-CFD X	0	0	1
ISIS-CFD Y	1	0	0
ISIS-CFD Z	0	1	0

Because this rotation is fixed, it is applied identically for every configuration. BeamDyn's own conven-

tion keeps its reported root orientation free of the beam's Cardan offset, the fixed yaw at which the whole beam is mounted for a given case, so that offset is absent from what BeamDyn itself reports and is reintroduced separately, together with the prescribed rotation, only when the local added-mass tensor is mapped into the fluid-side global frame for comparison. Removing the initial Cardan offset from the beam's own reported frame in this way keeps the axis convention of Table F.2 identical across the straight 0°, straight 45° Cardan, and curved configurations, with only the case-specific orientation differing between them.

For the coupling exercise, the origin was additionally placed at the IMU location on the shaft and paddle was aligned towards ISIS-CFD X rather than the initial configuration used throughout the rest of this thesis (Section 3.2). Figure F.2 defines this convention and the corresponding paddle dimensions. Because this geometric rotation was applied to the sensor frame itself, the reconstructed paddle kinematics used to drive the coupled beam were updated to the rotated frame accordingly.

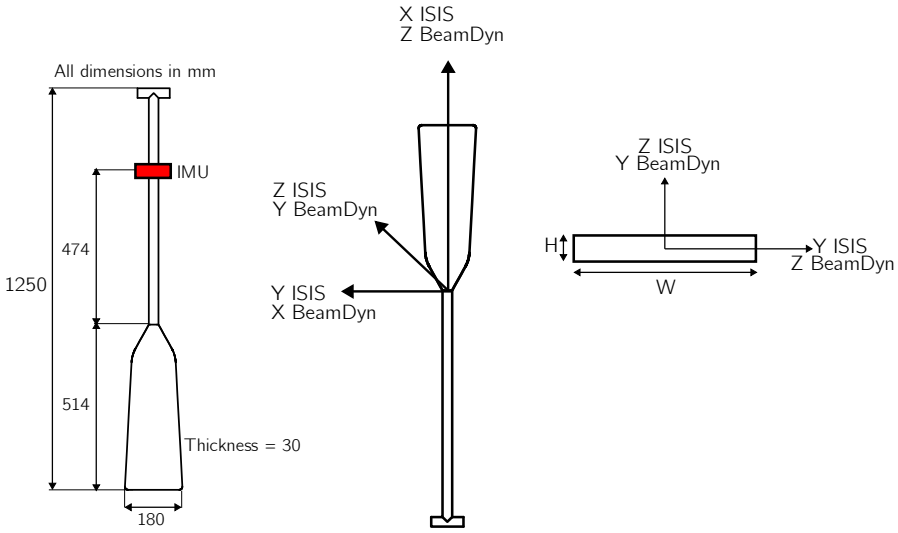

Figure F.2: Paddle dimensions and axis correspondence between the ISIS-CFD and BeamDyn frames, origin at the IMU location on the shaft, used for the coupling exercise.

The coupling dynamic library that delivers fluid loads to BeamDyn indexes the global-frame force components as channels 1, 2, and 3, corresponding to the ISIS-CFD global F_x, F_y, and F_z. Table F.2 defines the fixed mapping from these indexed components to the corresponding BeamDyn local-frame loads, so the force mapping follows directly from the established kinematic convention without requiring a separate mapping scheme.

A flexible-paddle case, in which the computed hydrodynamic pressure field drives the coupled beam directly, is left for future work, although the verification reported here suggests it may not be strictly necessary before the coupling can be trusted for other purposes. The benchmarking and verification campaign reported in this appendix, covering closed-form structural verification, kinematic frame transfer, and added-mass transfer, is not specific to the dragon-boat paddle and can support the coupling of other fluid-structure interaction problems using the same two solvers.

The remaining sections of this appendix give the supporting closed-form derivations, the full verification matrix, the benchmark and frame-transfer figures, and the component-by-component added-mass tables

referenced above. None of this is a flexible-paddle hydrodynamic result.

F.3 Closed-form reference solutions

The straight-beam cases are loaded independently in tension, bending, and torsion through tip loads, each with its own closed-form target,

$$\delta_{\text{axial}} = \frac{P\ell}{EA}, \qquad \delta_{\text{bend}} = \frac{P\ell^3}{3EI}, \qquad \theta_{\text{twist}} = \frac{T_m\ell}{GJ}, \tag{F.1}$$

where P is the applied tip load, T_m the applied torsion moment, and ℓ the beam length.

For the quarter-circle arc cantilever of radius R, parametrised by $\varphi \in [0, \pi/2]$ measured from the fixed root, a tip load applied tangentially at the free end produces a local bending moment $M(\varphi) = -PR(1 - \sin\varphi)$ and no torsion, giving a tip deflection in the load direction of

$$u_y = \left(\frac{3\pi}{4} - 2\right)\frac{PR^3}{EI}, \tag{F.2}$$

while a tip load applied radially, with local bending moment $M(\varphi) = -PR\cos\varphi$ and likewise no torsion, gives

$$u_z = \frac{\pi}{4}\,\frac{PR^3}{EI}. \tag{F.3}$$

An out-of-plane tip load produces both a local torque $T(\varphi) = PR(1 - \sin\varphi)$ and a local bending moment $M(\varphi) = -PR\cos\varphi$, so bending and torsion compliance both contribute to the tip deflection,

$$u_x = PR^3\left[\frac{\pi}{4}\,\frac{1}{EI} + \left(\frac{3\pi}{4} - 2\right)\frac{1}{GJ}\right]. \tag{F.4}$$

The applied tip load for every case was confirmed to four significant figures against the solver's own static root reaction rather than assumed from the run configuration.

F.4 Full verification case matrix

Table F.3 lists all eleven kinematic verification cases run through the coupling interface, across the three configurations introduced in Section F.1 above. The pure-rotation cases drive BeamDyn through its own GUI-configured input with the coupling's fluid-force channel zeroed. The cases marked with a dagger additionally apply a tension or torsion load through the coupling dynamic library itself, exercising the same load path used to deliver fluid loads to BeamDyn. Only the Rotation case of the curved beam is tabulated component-by-component in Section F.7. The remaining cases are not separately tabulated there. Their purpose is to exercise the coupling load and rotation paths listed here.

Table F.3: Full eleven-case kinematic verification matrix. Cases marked † additionally inject a tension or torsion load through the coupling dynamic library rather than relying on prescribed rotation alone.

Configuration	Case	Load path
Straight, no Cardan offset	Tension (axial, 1000 N)	† dynamic library
	Torsion (0.5 N m)	† dynamic library
	Rotation (yaw, $0 \rightarrow \pi/2$)	GUI-configured
	Rotation + torsion	† dynamic library
Straight, 45° Cardan offset	Tension (axial, 1000 N)	† dynamic library
	Torsion (0.5 N m)	† dynamic library
	Rotation (yaw)	GUI-configured
	Rotation + torsion	† dynamic library
	Rotation (pitch)	GUI-configured
	Rotation (roll)	GUI-configured
Curved, 45° arc	Rotation	GUI-configured

F.5 BeamDyn benchmark response histories

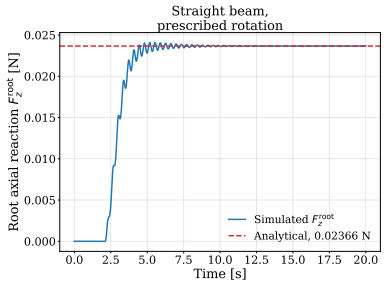

(a) Straight beam under prescribed rotation.

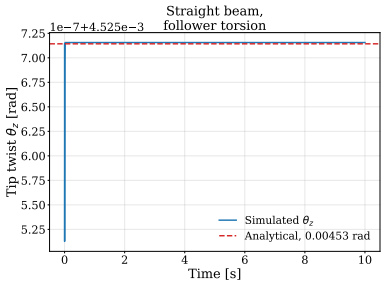

(b) Straight beam under follower torsion.

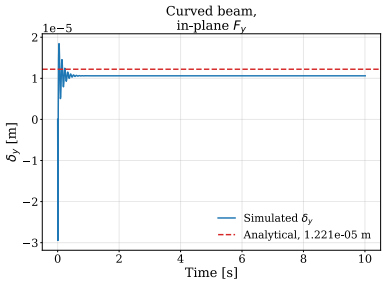

(c) Curved beam under tip load P_y.

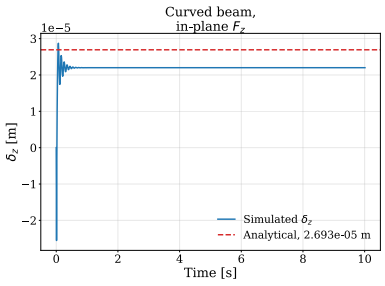

(d) Curved beam under tip load P_z.

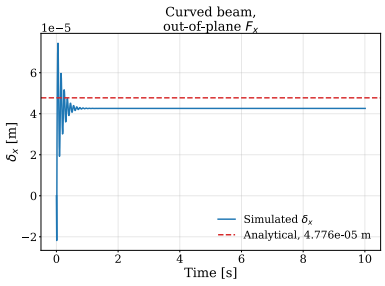

(e) Curved beam under tip load P_x.

Figure F.3: BeamDyn benchmark response histories for the straight and curved beam configurations. The transient responses converge toward their corresponding closed-form static solutions.

F.6 ISIS-CFD–BeamDyn frame-transfer illustrations

The local tip frame in the following figures indicates the orientation used to transfer the added-mass components between coordinate systems.

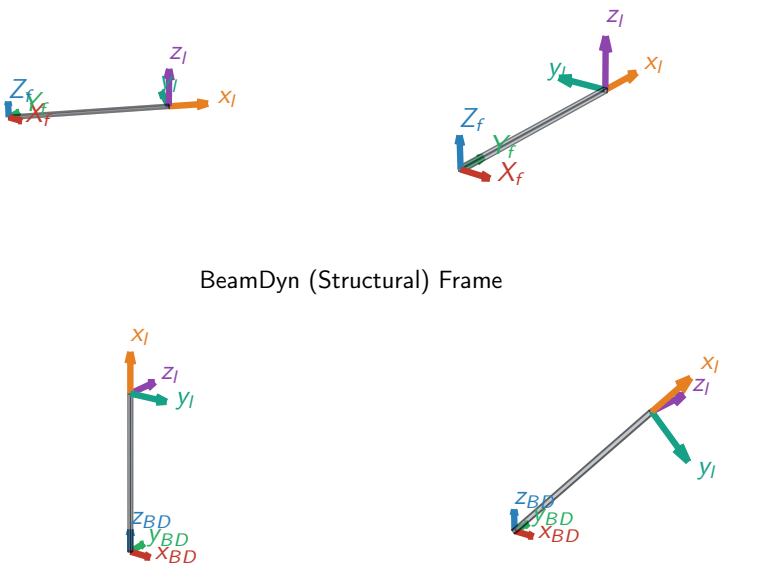

Figure F.4: ISIS-CFD–BeamDyn frame-transfer check for the straight beam at the initial orientation.

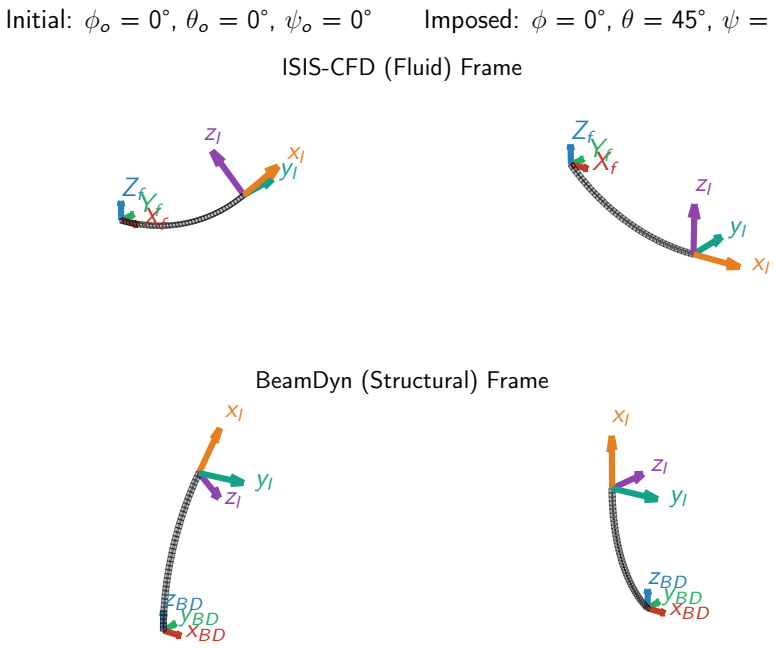

Figure F.5: ISIS-CFD–BeamDyn frame-transfer check for the curved beam at the initial orientation.

F.7 Added-mass verification table

For the curved beam at its 45° in the Rotation case, every logged added-mass component is compared directly. Three values appear for each component, the fluid-side value in its own local axes (ISIS-CFD), the value BeamDyn reports in the global frame (BeamDyn), and the value obtained by rotating the local tensor into the global frame with the node's own orientation, $M_{\text{global}} = \mathbf{R}\, M_{\text{local}}\, \mathbf{R}^{\mathsf{T}}$ (Predicted). Each is reported at the first and last beam node, at the initial and final time step. Cell colour marks which local axis, or axis pair, the rotation's weights say a global component is made of.

Table F.4: Added mass coefficient comparison – Curved Beam, 45°, Rotation.

		First node			Last node		
Time step	Comp.	ISIS-CFD	BeamDyn	Predicted	ISIS-CFD	BeamDyn	Predicted
Initial	Tx	2.979×10^{-7}	1.751×10^{-6}	1.751×10^{-6}	3.153×10^{-7}	1.479×10^{-6}	1.479×10^{-6}
	Ty	1.751×10^{-6}	1.745×10^{-6}	1.745×10^{-6}	1.479×10^{-6}	9.210×10^{-7}	9.210×10^{-7}
	Tz	1.745×10^{-6}	2.979×10^{-7}	2.979×10^{-7}	1.524×10^{-6}	9.178×10^{-7}	9.178×10^{-7}
	Rx	7.803×10^{-13}	3.902×10^{-14}	0.000×10^{0}	3.212×10^{-12}	1.606×10^{-13}	0.000×10^{0}
	Ry	–	3.902×10^{-14}	4.689×10^{-27}	–	1.682×10^{-12}	1.602×10^{-12}
	Rz	–	7.803×10^{-13}	7.803×10^{-13}	–	1.690×10^{-12}	1.610×10^{-12}
Final	Tx	2.979×10^{-7}	1.751×10^{-6}	1.751×10^{-6}	3.153×10^{-7}	1.479×10^{-6}	1.479×10^{-6}
	Ty	1.751×10^{-6}	1.021×10^{-6}	1.021×10^{-6}	1.479×10^{-6}	1.524×10^{-6}	1.524×10^{-6}
	Tz	1.745×10^{-6}	1.021×10^{-6}	1.021×10^{-6}	1.524×10^{-6}	3.153×10^{-7}	3.153×10^{-7}
	Rx	7.803×10^{-13}	3.902×10^{-14}	0.000×10^{0}	3.212×10^{-12}	1.606×10^{-13}	0.000×10^{0}
	Ry	–	4.097×10^{-13}	3.902×10^{-13}	–	1.606×10^{-13}	5.551×10^{-18}
	Rz	–	4.096×10^{-13}	3.902×10^{-13}	–	3.212×10^{-12}	3.212×10^{-12}

The table contains 24 logged components, comprising six components at each of the first and last beam nodes for the initial and final time steps. The translational components show the expected transformation between the local and global frames, while the rotational components provide the corresponding comparison for the rotational added-mass terms. The results support the implemented coordinate transformation and added-mass transfer. They do not, however, assess numerical stability under fluid loading or validate the behaviour of a flexible paddle in water.